Design, realization and electrical characterization of " Solar-blind " ultraviolet photodetectors based on new alloys BAlGaN

Hussein Srour

Laboratoire Matériaux Optiques Photonique et Systèmes
Unité de recherche commune à l'Université de Lorraine et Supélec
EA 4423

Conception, réalisation et caractérisation de photodétecteurs ultraviolets "solar-blind" à base de nouveaux alliages BAlGaN

présenté dans le cadre de l'école doctorale EMMA pour l'obtention

du titre de Docteur de
l'Université de Lorraine

Monsieur Hussein SROUR

le 16 Mai 2012 devant le jury
composé de

Laurent BECHOU, Pr., LIMS, UMR 5218 Université de Bordeaux I . . . . . Rapporteur
Zakaria DJEBBOUR, Dr., LGEP, UMR 8507 Université de Versailles . . . . . Rapporteur
Ali SOLTANI, MCF, IEMN, UMR 8520, Université de Lille . . . . . Examinateur
Badreddine ASSOUAR, CR HDR, IJL, UMR 7198 Université de Lorraine / CNRS . . . . . Examinateur
Philippe CHRISTOL, Pr., IES, UMR 5214 Université de Montpellier . . . . . Examinateur
Guilhem ALMUNEAU, CR HDR, LAAS, CNRS Toulouse . . . . . Examinateur
Abdallah OUGAZZADEN, Pr., UMI GT CNRS 2958, Georgia Tech . . . . . Examinateur
Ali AHAITOUF, Pr., DGE, USMBA, FST-Fès, Maroc . . . . . Invité
Jean Paul SALVESTRINI, Pr., LMOPS, EA 4423 Université de Lorraine . . . . . Directeur de thése

Laboratory Optical Materials, Photonics, and Systems

Thesis for the degree of doctor of philosophy

Design, construction and electrical characterization of "Solar-blind" ultraviolet photodetectors based on new BAlGaN alloys

Hussein SROUR

Metz, FRANCE 2012

Table des matières

1 Semi-conducteurs de type III-N pour la détection UV **8**

1.1 Structures cristallographiques des nitrures III-N 9

1.2 Substrats pour l'épitaxie de matériaux nitrures III-N 11

1.3 Matériaux de type GaN 14

1.3.1 Propriétés mécaniques et optiques 15

1.3.2 Propriétés diélectriques et de transport 16

1.3.3 Défauts dans GaN 17

1.4 Alliages $Al_xGa_{1-x}N$ 19

1.4.1 Propriétés structurales 19

1.4.2 Propriétés électriques 21

1.5 Alliages $B_xGa_{1-x}N$ 21

1.5.1 Propriétés structurales et morphologiques 23

1.5.2 Propriétés électriques 27

1.5.3 Propriétés optiques 28

2 Photodétecteurs: les différents types et leurs caractéristiques générales 31

2.1 Caractéristiques des photodétecteurs 32

2.1.1 Efficacité quantique 32

2.1.2 Sensibilité 32

2.1.3 Réponse spectrale 33

2.1.4 Temps de réponse 33

2.1.5 Courant d'obscurité 35

2.1.6 Contraste UV-visible 37

2.1.7 Bruit dans les photodétecteurs 38

2.2 Photodétecteurs UV: état de l'art 39

2.2.1 Détecteurs photoconducteurs 39

2.2.2 Photodiodes PIN 42

2.2.3 Photodiodes à avalanche 43
2.2.4 Photodiodes barrière de Schottky 46
2.2.5 Photodétecteur Métal-Semiconducteur-Métal 49
2.2.6 Mécanisme de gain dans les photodétecteurs Schottky et métal-semiconducteur-métal 53

3 Réalisation du composant caractérisations 57
3.1 Introduction 58
3.2 Contacts métal-semiconducteur 58
3.2.1 Diagrammes de bande d'énergie 58
3.2.2 Mécanismes de transport 61
3.2.2.1 Emission au déla de la barrière 61
3.2.2.2 Théorie de l'émission thermoïonique 62
3.3 Réalisation du composant 68
3.3.1 Procédé de photolithographie 69
3.3.1.1 Préparation des échantillons et traitement chimique 71
3.3.1.2 Paramètres des résines photosensibles 71
3.3.2 Dépôt de métal 73
3.3.2.1 Evaporation sous vide 73
3.3.2.2 Dépôt par pulvérisation 75
3.3.2.3 Recuit thermique 76
3.3.3 Microcâblage 77
3.4 Caractérisation des dispositifs: mesures électriques 79
3.4.1 Contacts ohmiques 79
3.4.1.1 Principes de base de la formation du contact ohmique . . 79
3.4.1.2 Résistance de contact spécifique 80
3.4.1.3 Caractérisations 82
3.4.1.4 Structures TLM linéaires 83
3.4.1.5 Structures TLM circulaires 87
3.4.1.6 Méthode courant-tension (I-V) 88
3.4.2 Techniques Van der Pauw et Hall 90
3.4.3 Contacts Schottky 92
3.4.3.1 Choix des contacts métalliques 92
3.4.3.2 Hauteur de barrière et facteur d'idéalité 93
3.4.3.3 Mesures capacité-tension (cas de semiconducteur de type n) 93

3.5 Mesures électro-optiques 96
3.5.1 Mesures de la sensibilité 96
3.5.2 Mesures de photocourant resolues en temps 100

4 Composants référence à base de GaN et AlGaN 102
4.1 Contacts ohmiques 103
4.2 Contacts Schottky 109
4.3 Photodétecteur Schottky 119
4.4 Photodétecteurs MSM 121
4.4.1 Mesures des courants d'obscurité 122
4.4.2 Mesures de la sensibilité 123
4.4.3 Réponse spectrale 124
4.5 Conclusions 126

5 Photodétecteur à base de BAlGaN 127
5.1 Introduction 128
5.2 Contact ohmique sur BGaN 130
5.3 Diodes Schottky $B_xGa_{1-x}N$ 132
5.4 Photodétecteur Schottky à base de $B_xGa_{1-x}N$ 134
5.5 Photodétecteurs MSM à base de BGAN et BAlGaN 135
5.5.1 Caractérisation I-V 135
5.5.2 Dépendance en tension de la sensibilité 137
5.5.3 Dépendance en puissance optique de la sensibilité 139
5.5.4 Réponse spectrale 139
5.5.5 Temps de réponse 142
5.6 Conclusions 144

Contents

1 III-N based semiconductors for UV detectors **8**

1.1 Crystal structure of III-Nitrides 9

1.2 Substrates for nitride materials epitaxy 11

1.3 GaN based materials 14

1.3.1 Mechanical and optical properties 15

1.3.2 Dielectric and transport properties 16

1.3.3 Defects in GaN 17

1.4 $Al_xGa_{1-x}N$ alloys 19

1.4.1 Structural properties 19

1.4.2 Electrical properties 21

1.5 $B_xGa_{1-x}N$ alloys 21

1.5.1 Structural and morphological properties 23

1.5.2 Electrical properties 27

1.5.3 Optical properties 28

2 Photodetectors: the different types and their characteristics **31**

2.1 Photodetector characteristics 32

2.1.1 Quantum efficiency 32

2.1.2 Responsivity 32

2.1.3 Spectral response 33

2.1.4 Response time 33

2.1.4.1 Drift time of carriers 33

2.1.4.2 Junction capacitance effects 34

2.1.5 Dark current 35

2.1.6 UV-visible contrast 37

2.1.7 Noise in photodetectors 38

2.2 III-N UV photodetectors: state of the art 39

2.2.1 Photoconductive detectors . . . 39
2.2.2 P-I-N photodiodes . . . 42
2.2.3 Avalanche photodiodes . . . 43
2.2.4 Schottky Barrier Photodiodes . . . 46
2.2.5 Metal-Semiconductor-Metal Photodetector . . . 49
2.2.6 Gain mechanism in Schottky and Metal-Semiconductor-Metal photodetector . . . 53

3 Device processing and characterizations 57
3.1 Introduction . . . 58
3.2 Metal-semiconductor contacts . . . 58
3.2.1 Energy band diagrams . . . 58
3.2.2 Current transport mechanisms . . . 61
3.2.2.1 Emission over the barrier . . . 61
3.2.2.2 Thermionic emission theory . . . 62
3.3 Device processing . . . 69
3.3.1 Photolithography process . . . 70
3.3.1.1 Sample preparation and chemical treatment . . . 71
3.3.1.2 Photoresist parameters . . . 71
3.3.2 Metal deposition . . . 74
3.3.2.1 Vacuum evaporation . . . 74
3.3.2.2 Sputtering deposition . . . 75
3.3.2.3 Thermal annealing . . . 76
3.3.3 Wire bonding . . . 77
3.4 Device characterization: Electrical measurements . . . 79
3.4.1 Ohmic contacts . . . 79
3.4.1.1 Basic principles of ohmic contact formation . . . 79
3.4.1.2 Specific contact resistance . . . 80
3.4.1.3 Characterization . . . 82
3.4.1.4 Linear TLM . . . 83
3.4.1.5 Circular TLM . . . 87
3.4.1.6 Current-Voltage (I-V) method . . . 88
3.4.2 Van der Pauw and Hall effects . . . 90
3.4.3 Schottky contacts . . . 92
3.4.3.1 Choice of metal contact . . . 92

3.4.3.2 Barrier height and ideality factor 93
3.4.3.3 Capacitance-Voltage method (case of n-type) 94
3.5 Electro-optical measurements 96
3.5.1 Quantum efficiency measurements 96
3.5.2 Time resolved measurements of the photocurrent 100

4 GaN and AlGaN devices as a reference **102**
4.1 Ohmic contact 103
4.2 Schottky contact 109
4.3 Schottky photodetector 119
4.4 MSM photodetectors 121
4.4.1 Dark currents measurements 122
4.4.2 Responsivity measurements 123
4.4.3 Spectral response 124
4.5 Conclusions 126

5 BAlGaN UV Photodetector **127**
5.1 Introduction 128
5.2 Ohmic contact on $B_xGa_{1-x}N$ 130
5.3 $B_xGa_{1-x}N$ Schottky diodes 132
5.4 $B_xGa_{1-x}N$ Schottky photodetector 134
5.5 BGaN and BAlGaN superlattice MSM photodetectors 135
5.5.1 I-V characterization 135
5.5.2 Voltage dependence of the responsivity 137
5.5.3 Optical power dependence of the responsivity 139
5.5.4 Spectral response 140
5.5.5 Response time 142
5.6 Conclusions 145

Remerciements

Ce travail a été effectué au Laboratoire Matériaux Optiques, Photonique et Systèmes (LMOPS) de l'Université de Lorraine. Je tiens à exprimer mes plus sincères remerciements à tous ceux sans qui ce travail n'aurait été possible. Mes remerciements chaleureux et sincères s'adressent également à tous ceux qui m'ont fourni un soutien sans faille pour moi pendant mes années de doctorat.

Ainsi, je tiens, tout d'abord, à remercier mon professeur encadrant Jean-Paul Salvestrini. Cela a été un véritable honneur et un privilège d'être son doctorant. Les mots me manquent pour exprimer ma gratitude envers lui mais je lui en serai à jamais reconnaissant. Il m'a appris, consciemment et inconsciemment à la fois, comm la physique expérimentale doit être abordée et réalisée Sa supervision, ses conseils et ses orientations dans les travaux m'ont donné une confiance extraordinaire et m'ont encouragé tout au long de cette thèse. Je lui suis éternellement redevable en sa croyance dans mon potentiel et mes capacités à surmonter toutes les difficultés et les défis que j'ai pu rencontrer au cours de cette période de ma vie. Ses intuitions scientifiques, comparables à une oasis pleine d'idées et de passion scientifique, m'ont permis de réellement m'inspirer et de m'enrichir dans mon aspiration à travailler dans la recherche scientifique. Je ne peux oublier de rappeler sa joie et son enthousiasme pour la recherche qui m'ont touché et m'ont motivés pendant les périodes difficiles. Il sera toujours mon modèle. Je lui suis vraiment reconnaissant pour l'excellent exemple qu'il m'a fourni en tant que physicien et professeur de succès.

Je tiens à remercier tout les collègues et personnels pour le temps qu'ils ont pu me consacrer, leurs idées et leurs motivations afin que mes années passées en thèse m'ai apportées une expérience productive et stimulante.

Un remerciement spécial et sincère au groupe MOVPE, en particulier au Prof. Abdallah Ougazzaden, Simon GAUTIER et Tarek MOUDAKKIR, pour m'avoir fourni des échantillons sans lesquels tout ce travail n'aurait pu être possible.

La précieuse aide du Prof. Badreddine ASSOUAR en ce qui concerne l'accès à la salle blanche et sa large participation dans mes travaux expérimentaux ne peuvent être

omis : un grand merci encore. Je lui suis éternellement reconnaissant pour ses conseils sans faille, sa supervision et son soutien dans des moments parfois difficiles. Je tiens à noter son investissement concret : il fut toujours présent lorsque j'avais besoin de lui. J'ai vraiment apprécié être encadré par ce superviseur, modèle, scientifique passionné et ami.

Mes remerciements s'étendent également à Gwladys Lengaigne et Laurent Bouvot pour tous leurs conseils et leur partage de connaissance sur le travail en salle blanche.

Je suis profondément reconnaissant au professeur associé Ali AHAITOUF pour ses encouragements, ses conseils, son soutien généreux et pour la confiance dans mes capacités qu'il m'a attribué. Ses vastes connaissances et sa sagesse scientifique ont déclenché et nourri ma maturité intellectuelle que je vais bénéficierai à l'avenir.

Je voudrais aussi remercier ma collègue Sarah AMOR pour son soutien et de son aide sur de nombreuses expériences que j'ai effectué.

Un « special thank » à Mme Schreiber Cécile pour ses aides, ses conseils et ses soutiens qui m'ont vivement encouragé. Elle a toujours été là pour moi et m'a fournie une assistance dans de nombreuses situations : reconnaissant D'avoir pu être son collègue et son ami.

Mes remerciements sont également attribués à Frédéric Gentil et à tous mes collègues du laboratoire pour m'avoir fourni une très bonne et agréable atmosphère de travail. Leurs soutiens et leurs encouragements, perpétuellement rafraîchis, m'ont aidé et inspiré dans les moments difficiles. J'ai eu beaucoup de chance d'avoir rencontré ces collègues qui m'ont soutenu dans des moments toujours conviviales.

Un remerciement tout particulier au doctorant Mourad Bourezzou avec qui j'ai partagé des moments inoubliables et qui seront à jamais gravé dans ma tête. Il a toujours été là pour moi, dans les moments les plus difficiles également et je ne doute pas de travailler à l'avenir avec lui.

Parmi les autres doctorants, je tiens à citer Charles Ciret pour sa présence et ses aides mais également Hadrien Chaysnes pour sa bonne humeur et ses qualités d'ingénieur.

Pour cette thèse, je tiens évidemment à remercier les membres du comité de lecture pour leur temps, leur intérêt et leurs commentaires très utiles.

Enfin, je tiens à remercier ma famille qui mérite une mention très spéciale pour leur soutien éternel, leurs prières, leur amour et leurs encouragements. Mes parents m'ont élevé avec amour, m'ont permis d'être là où j'en suis dans la science et m'ont toujours soutenu dans toutes mes activités. A ma très chère soeur Khadija et à mes très chers frères Hassan et Ali qui m'ont énormément aidée et à qui je témoigne mon affection et ma profonde reconnaissance.

Je remercie pour la vie mon amour, mon épouse Fatima pour tout son soutien, sa

patience, sa fidélité durant les phases finales de cette thèse.

Pour finir, je tiens à remercier tout les personnes qui furent importante pour la réalisation réussie de ma thèse. Je m'excuse pour ceux que je n'ai pas pu citer dans ces remerciements mais qui sont dans mon coeur à jamais.

Acknowledgments

In this humble acknowledgment, I would like to convey my heartiest gratitude to all those without whom this work would have not been possible. My warm and sincere gratefulness to all those who provided endless support to me during my PhD years.

First and foremost, I want to thank my advisor Professor Jean Paul SALVESTRINI. It has been an honor and privilege to be his PhD student. Words fail to express my gratitude and appreciation to him. I will forever be thankful to him. He has taught me, both consciously and unconsciously, how good experimental physics is done. His supervision, advice and guidance from the very early stage of my PhD gave me extraordinary confidence and encouragement throughout the work. I am forever indebted to his belief in my potential and capabilities to overcome all the difficulties and challenges I faced during this period of my life. His truly scientist intuition has made him as a constant oasis of ideas and passions in science, which exceptionally inspire and enrich my growth as a student, a researcher and a scientist want to be. I appreciate all his contributions of time, ideas, and funding to make my phd experience productive and stimulating. The joy and enthusiasm he has for his research was contagious and motivational for me, even during the tough time in my PhD pursuit. He will forever be my role model and am thankful for the excellent example he has provided as a successful physicist and professor.

Accessing the clean room facility and performing most of the experimental work presented in this thesis would have never been possible without the support and help of Prof. Badreddine ASSOUAR. I am forever grateful for his endless advice, supervision, and support in the hardest of times. I am grateful to him in every possible way for being there for me whenever I needed him. I immensely thank him for being there as a supervisor, a passionate model of a scientist, and a friend.

I am deeply indebted to thank Associate Prof. Ali Ahaitouf for his encouragement, guidance, and generous support, and for his confidence in my capabilities. His wide knowledge and scientific wisdom have triggered and nourished my intellectual maturity that I will benefit from, for a long time to come.

One special thanks is to my favorite receptionist Ms Cecile Schreiber for her assistance in many ways and her advice, support and encouragement. She was always there for me and provided assistance to me in every way, I am grateful to have had her as a colleague and friend. Collective and individual thanks are also owed to my colleagues at the Supelec Institute for providing such a pleasant working atmosphere and whose support and encouragement always perpetually refreshed, helped and inspired me through the hard times. It was fortunate for me to have met such supportive and friendly colleagues.

For this dissertation, I would like to thank my reading committe members for their time, intereset and helpful comments and insightful questions.

Lastly, I would like to thank my family who deserve special mention for their inseparable support, prayers, love and encouragement. A special thanks to my parents who raisedme with a love for science and supported me in all my pursuits. A very huge and specialthanks for my loving, supporting, encouraging, and patient wife Fatima whose faithful support during the final stages of theis PhD is so appreciated. Thank you

support during the final stages of this PhD is so appreciated. Thank you

Finally, I would like to thank everybody who was important to the successful realization of my thesis and my apology for those whom I could not mention personally one by one.

Context and goals of the study

The detection of light is one of the most fundamental processes in the field of optics. The scientific exploration and technological use of optical radiation at any frequency is initially enabled and ultimately limited by the capabilities of the photodetector used. Sources, materials science and device design form the fundamental pillars on which devices for photodetection are built. Over the past decade, the ultraviolet (UV) region of the electromagnetic spectrum has been the focus of intense research. It is highly ionizing and activates many chemical processes on different types of materials and living beings. The UV spectrum is divided into four categories such as:

Near-ultraviolet (NUV) (400 nm - 300 nm) : Fluorescence is a luminescence phenomenon that is mostly found in cold bodies when the molecules are excited by incident photons. The relaxation of the excited molecules will trigger another photon emission at a longer wavelength than the incident photons. The energy difference between the absorbed and emitted photons ends up being molecular vibrations or heat. The fluorescence detection has been widely used in compound identification, such as biological-agent detection. The fluorescence generated by UV excited biological-agent often expands to NUV range with very weak intensity at the order of pW, i.e. 10^6 photons/sec. Low-level UV detection in the spectral range from 300 to 400 nm is used to identify the presence of a biological organism, to distinguish biological substances from non-biological substances and to differentiate common biological particles from harmful biological agents [1].

Mid-ultraviolet (MUV) (300 nm - 200 nm) : One of the most attractive applications in MUV range is solar-blind UV detection. The sun is the strongest irradiation source around us. Figure 1 shows the average solar irradiation at the top of the atmosphere and at the sea level on the earth. The cut-off wavelength of solar UV irradiance at the sea level of the earth is 280 nm, where the solar irradiance is less than 10^{-20} mW/m^2/nm, which corresponds to 6.1x10^{-5} photons/sec/nm/m^2. The

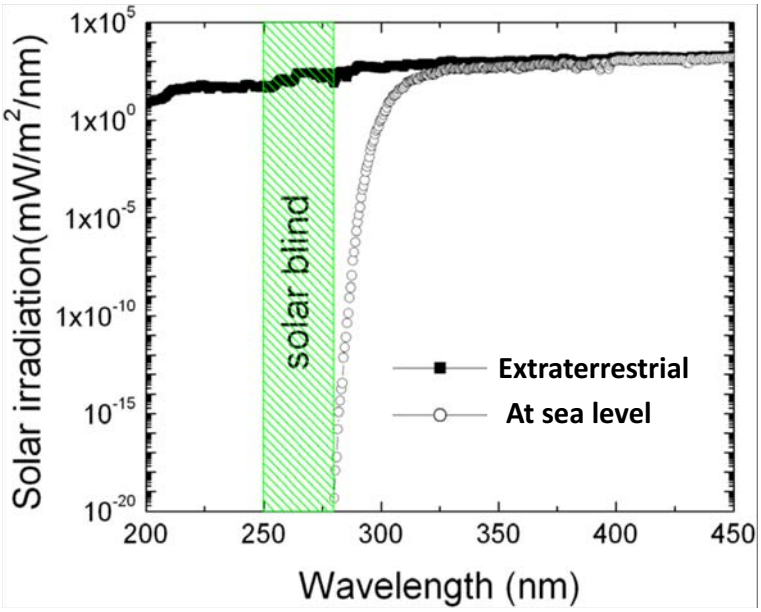

Figure 1: *Solar irradiation at the top of the atmosphere and at the sea level on the earth. The stratospheric ozone layer strongly absorbed the UV emission with the wavelengths from 200 nm to 290 nm [2].*

stratospheric ozone layer strongly absorbs the UV emission with the wavelengths from 200 nm to 280 nm [3], and only the light with the wavelength longer than 290 nm reaches the Earth's surface. Simultaneously the far UV emission from 110 to 250 nm is strongly absorbed by molecular oxygen and can only propagate a very short distance in air. At the extreme UV, atomic and molecular gases become strong absorbers. It is worthwhile to notice that, if the photodetection is carried out between 250 and 290 nm, it is practically free of the interference with the solar irradiation. Therefore, the UV spectrum from 250 to 290 nm is called "solar-blind" window. Solar-blind UV detectors are imperative, particularly for the military, because they enable air, sea, and ground equipment to detect and warn against the ground-to-air, air-to-air, air-to-ground, and ground-to-ground missile threats. The system, at the heart of which is a UV detector, must be able to detect and track extremely weak signals from rapidly moving threats, which necessitates operation in the solar-blind region of the spectrum, 260-290 nm. With visible blind UV detector, which has a high UV to visible rejection ratio, this window has been utilized for many other commercial applications such as in boilers, flame sensor and jet engines, though they may not require operation in the solar-blind region of the spectrum [4,5], and non-line-of-sight (NLOS) UV communications [1,6].

Far-ultraviolet (FUV) (200 nm - 100 nm) : FUV radiations are completely absorbed by the ozone layer extending from about 15 km to 30 km above earth's surface. To observe in the far-ultraviolet, telescopes must be in space above the atmosphere with special detectors. Furthermore, a biological application that uses detector technology developed by physicists is the measurement of circular dichroism (CD). CD measurements are performed in the UV region (180 nm to 240 nm) of the electromagnetic spectrum. Absorption in this region of the spectrum arises from electron transitions that can occur in the peptide bonds that hold the protein molecule together. CD is defined as the difference in absorption between left hand and right hand circularly polarized light as it passes through a solution of an optically active molecule. Proteins are optically active molecules and CD may be used to determine how various proteins fold and the time taken for a protein to adopt a certain configuration. Neuro-degenerative diseases such as Alzheimer's and Creutzfeldt-Jakob disease occur when certain proteins in the brain do not fold in the conventional way. By establishing how different proteins fold it may be possible to design drugs to treat diseases such as Alzheimer's. It is not possible to obtain good CD data below 190 nm using conventional UV sources such as deuterium lamps or xenon arc lamps due to strong UV absorption by both the protein sample and by oxygen in the air. However the high brightness offered by synchrotron radiation overcomes this limitation and enables CD measurements to be performed below 190 nm [7].

Extreme ultraviolet (EUV) (100-10 nm) : The region below the FUV portion, is called Extreme-UV because the atmosphere absorbs below 100 nm. Sometime, the following subdivisions may be also encountered such as: Ultraviolet-A (UVA) 300-320 nm, Ultraviolet-B (UVB) 320-280 nm, Deep-ultraviolet (DUV) 280-190 nm and Vacuum-ultraviolet (VUV) 190-10 nm [8]. However, the strongest and the most significant UV source around us is the sun. The solar EUV irradiance can change by a factor of two in a period of less than one hour and by one order of magnitude between solar minimum and solar maximum [9]. Absorption of this variable solar EUV radiation is the dominant source of energy for the heating and ionization of the earth's upper atmosphere and ionosphere, which causes phase delay of Global Position System (GPS), radio frequency and microwave communications and orbit shift of satellites in the low-earth-orbit due to the upper-atmospheric drag forces [1]. Detection of the solar EUV irradiation can provide information on the variations in the upper atmospheric density and in the ionospheric electron density, and has

great significance in monitoring, specifying and predicting the space environment. However, at such short wavelengths, UV radiation damage becomes a major concern for semiconductor detectors. Semiconductor detectors with high radiation hardness and small volume are highly desired. Another application is to detect man-made EUV sources such as in EUV photolithographic system. It is well known that the UV radiation is very harmful to life. Fortunately, the ozone layer absorbs the UV radiation with $\lambda <$ 280nm, which is called solar blind region. Therefore, there is no natural radiation for $\lambda <$280 nm within the atmosphere. Similarly, the radiation above the visible region of the electromagnetic spectrum is called the visible-blind region $\lambda <$ 400 nm because the human eye does not respond to the wavelengths smaller than 400nm [1].

The ability to detect UV radiation begins with the optical and electrical properties of candidate materials system, and the most technologically important materials are the semiconductors. The conventional UV photodetection is performed by photomultiplier tubes (PMTs), thermal sensors, and narrow band-gap semiconductor diodes. PMT displays high gain and low noise. However, PMT are made out of a vacuum tube and are very delicate because they require very high bias voltages, designed filters to operate at certain wavelength and are rather expensive. Thermal detectors such as pyrometers and bolometers are used in the calibration processes of UV detectors, but they are slow and their response is wavelength independent [10]. Solid state photodetectors are small in size, easy to fabricate, inexpensive, insensitive to magnetic fields, and their capability of high-speed operation makes them suitable for UV detection. Si, GaAs, and GaP have been used in the fabrication of UV detectors. Si was the first material ever used for UV photodetection because of its well established technology, but it display some limitations due to its narrow and indirect band gap. However, Si and other narrow band gap materials are suitable for devices operating in visible and infrared regions, because they suffer from radiation aging, as their band gap is far lower that the UV photon energies, and also require expensive filters as the case in PMTs [11]. From the aspect of semiconductor band gap theory, the wide-band gap semiconductors make it possible to realize a filter-free highly sensitive UV detection with lower noise when compared to PMTs or narrow band gap based detectors [12].

Up to date, Group III Nitrides semiconductor compounds encompass a range of materials such as gallium nitride, aluminum nitride and indium nitride, which are very promising materials for their potential use in emitters, detectors, and high power/temperature

electronic [13,14]. These materials and their ternary and quaternary alloys cover an energy bandgap range of 0.7-6.2 eV, suitable for band-to-band light generation with colors ranging from red (potentially) to ultraviolet (UV) wavelengths. Specifically, nitrides are suitable for such applications as surface acoustic wave devices [15], UV detectors [16,17], Bragg reflectors [18], waveguides, UV and visible light emitting diodes (LEDs) [19–21], and laser diodes (LDs) for digital data read-write applications [22]. III-Nitrides are a group of materials which have existed for the past decades and have been the subject of extensive research. Their discovery was initiated in 1907 when Fichter et al. [23] successfully synthesized AlN and InN [24] materials, followed by the successful synthesis of the GaN material in the 1930's by Johnson et al. and Juza et al. [25,26]. Initially, these materials did not draw much interest; they were made from polycrystalline materials and were not useful for semiconductor devices, and hence, limited research was conducted on them till the early 1990's when Masruska and Titjen demonstrated growing GaN on sapphire substrates by using chemical vapor deposition [27]. Ever since then, the III-nitrides, AlN, GaN, and InN, have become an important trio of semiconductors which have attracted much interest. At that time was believed the early unintentionally doped GaN was invariably n-type due to nitrogen vacancies. It was difficult to minimize the high n-type carrier concentration on the order of 10^{18} cm^{-3}, and the prospect of a production scale of GaN based device was dimmed due to the absence of a shallow acceptor. Nevertheless, the first blue, green, yellow and red light emitting diodes (LEDs) [28] were demonstrated using the earlier work on zinc-compensation. The further device development was stifled by the seemingly insurmountable problem of making conducting p-type GaN. The search for p-type GaN was not successful until Akasaki and Amano demonstrated this feat in 1989 [29]. This remarkable achievement was actually a result of two significant milestones. First the crystalline quality and the background n-type carrier density in unintentionally doped GaN films was significantly reduced by the use of low temperature AlN buffer layer [30,31]. Second, p-type GaN was demonstrated with Mg-doping followed by an ex situ low energy electron beam irradiation treatment [32]. These breakthroughs opened the door to the control of the material structural, electrical and optical properties.

On the other hand, because of the direct and tunable band gap, the III-Nitride materials have gained great interest for optoelectronic devices in both light detection and emission applications. From a physics perspective, the presence of electronic band gaps with energies comparable to those of photons makes the semiconductor an extremely capable material for detecting light. For example the direct, wide band gap of GaN makes it an attractive material for the UV light detection. At room temperature GaN wide

band gap (E_g) is approximately 3.39 eV, that corresponds to a cut-off wavelength λ_C of 365 nm [12]. We can conclude that any detector fabricated on GaN should, theoretically, exhibit no photoresponse to light with a wavelength greater than 365 nm. Therefore, GaN is an intrinsic blind of visible light and presents a significant advantage over Si UV detector. Another advantage or benefit that can be extracted from GaN is that by adding varying fractions of Al, forming the ternary alloy $Al_xGa_{1-x}N$ the band gap can be tailored from 3.39 eV (x_{Al}=0) to 6.2 eV (x_{Al}=1), corresponding to a cut-off wavelength which may be tuned between 365 nm and 200 nm to suite each unique application. Since the band gap of $Al_xGa_{1-x}N$ material covers the entire mid-UV and near-UV spectrum makes it also intrinsically visible blind. After the first successful demonstration of UV photodetectors [33, 34], various types of $Al_xGa_{1-x}N$ based photodetectors have been reported, such as the Schottky barrier [35, 36], p-i-n [37, 38], and MSM [39, 40] photodetectors. For III-Nitride photodiodes, the spectral response peaks are very close to the intrinsic absorption wavelength with a sharp cut-off edge, showing a high UV-visible rejection ratio. In addition, these devices are suitable for harsh environment applications due to the materials chemical and thermal stability. III-Nitride photodiodes are considered more suitable than other semiconductor for UV detections and have been studied extensively in the recent years. The materials quality and availability of large-area GaN and AlGaN active layers are currently considered as a key problem for the continuing development of improved GaN-based devices specially solar-blind ultraviolet (UV) photodetectors. In order to improve the GaN-based device quality, a tremendous technological effort is underway.

The work described in this thesis lies in this general frame work and has been carried out within a joint project (CNRS-PEPS) between the Laboratoire Matériaux Optiques, Photonique et Systèmes (LMOPS), the UMI GT-CNRS 2958 and IJL Lorraine. The aim of this project was to study the possibility to achieve UV photodetectors using BGaN and BAlGaN materials. These new alloys are expected, thanks to the boron incorporation, to decrease the residual doping and obtain a better lattice match with the substrate, leading to photodetectors with very low dark current. Furthermore, the excellent thermal and chemical stability of the BN band should yield a better behavior of the device in harsh environments. Finally, the boron incorporation should allow, as in AlGaN PD, the tuning of the wavelength cutoff. The PD structures which were chosen are twice: Schottky and MSM, both with circular and interdigited electrodes. GaN and AlGaN were first realized and characterized, in order to compare the performance of the new structure to these references.

Chapter I, gives an overview of the properties of the GaN, AlGaN and BGaN materials, and discusses the problem of the lack of lattice matched substrates as well as the different possible solutions to this issue.

Chapter II, addresses the state-of-the-art of the various types of photodetectors with special orientation toward UV and solar-blind detectors. Because noise and detectors are synonymous with each other, sources of the noise are discussed then followed by a discussion on the vital characteristics such as quantum efficiency and responsivity.

Chapter III, treats metal semiconductor structures and fabrication methods used for III-nitride-based devices to arrive at the desired configuration. Following a comprehensive discussion of current conduction mechanisms in metal semiconductor contacts, which are applicable to metal semiconductor system, it gives way to a discussion of ohmic and Schottky contacts, their technologies, and their characterizations. In particular, an ample discussion on the determination of ohmic contact resistivity is provided. Then it deals with the determination of carrier concentrations and mobility by capacitance-voltage and Hall measurements.

Chapter IV, focuses on the results obtained for the electrical and electroptical characterizations on GaN and AlGaN devices (Schottky diodes, Schottky and MSM PD). These results are considered as our reference and will be compared to those obtained with the new devices based on BGaN and BAlGaN materials.

Chapter V, discusses the results obtained on BAlGaN alloys of Schottky and MSM photodetectors.

Chapitre 1

Semi-conducteurs de type III-N pour la détection UV

Sommaire

1.1 Structures cristallographiques des nitrures III-N 9

1.2 Substrats pour l'épitaxie de matériaux nitrures III-N 11

1.3 Matériaux de type GaN 14

1.3.1 Propriétés mécaniques et optiques 15

1.3.2 Propriétés diélectriques et de transport 16

1.3.3 Défauts dans GaN 17

1.4 Alliages $Al_xGa_{1-x}N$ 19

1.4.1 Propriétés structurales 19

1.4.2 Propriétés électriques 21

1.5 Alliages $B_xGa_{1-x}N$ 21

1.5.1 Propriétés structurales et morphologiques 23

1.5.2 Propriétés électriques 27

1.5.3 Propriétés optiques 28

Chapter 1

III-N based semiconductors for UV detectors

Contents

1.1 Crystal structure of III-Nitrides 9

1.2 Substrates for nitride materials epitaxy 11

1.3 GaN based materials 14

1.3.1 Mechanical and optical properties 15

1.3.2 Dielectric and transport properties 16

1.3.3 Defects in GaN 17

1.4 $Al_xGa_{1-x}N$ alloys 19

1.4.1 Structural properties 19

1.4.2 Electrical properties 21

1.5 $B_xGa_{1-x}N$ alloys 21

1.5.1 Structural and morphological properties 23

1.5.2 Electrical properties 27

1.5.3 Optical properties 28

1.1 Crystal structure of III-Nitrides

The wide band gap III-nitride are compounds of binary, ternary and quaternary (Ga,Al,In,B)-N alloys. They are the basic materials for the semiconductor material class named nitrides: gallium nitride (GaN), aluminum nitride (AlN), indium nitride (InN), and boron nitride (BN). These III-nitride crystals can exist in three basic structures: rocksalt, zincblende (ZB) and wurtzite (Wz). The rocksalt cannot be produced by any epitaxial growth and its form is possible only under high pressures. The structural phase transition to rocksalt structure was experimentally observed at the following estimated pressure values 22.9 GPa for AlN [41], 52.2 GPa for GaN [42], and 12.1 GPa for InN [43]. Its space group is Fm $\bar{3}$m in the Hermann-Mauguin notation. The zincblende structure has a cubic unit cell, containing four group III elements and four nitrogen elements. Within the unit cell, the position of the atoms is identical to the diamond crystal structure. Its space group structure in the Hermann-mauguin notation is F$\bar{4}$3m. Each atom in the structure may be viewed as positioned at the center of a tetrahedron, with its four nearest neighbors defining the four corners of the tetrahedron. The stacking sequence for the (1 1 1) close-packed planes in this structure is AaBbCc. The wurtzite structure has a hexagonal unit cell and thus two lattice constants, c and a. It contains six atoms of each type. The space grouping for the wurtzite structure is P6$_3$mc in the Hermann Mauguin notation. In both cases of zincblende and wurtzite structure, each group III atom is coordinated by four nitrogen atoms, and each nitrogen atom is coordinated by four group III atoms. The main difference between these two structures lies in the stacking sequence of closest packed diatomic planes. The wurtzite structure consists of alternating biatomic close-packed (0 0 0 1) planes of Ga and N pairs, thus the stacking sequence of the (0 0 0 1) plane is AaBbAa in the (0 0 0 1) direction. Lowercase and uppercase letters stand for the two different kinds of constituents. The wurtzite and zincblende structures differ only in the bond angle of the second nearest neighbor as shown in figure 1.1. Figure 1.1(a) clearly shows, the stacking order of the Wz along the [0 0 0 1] c-direction is AaBb, meaning a mirror image but no in-plane rotation with the bond angles. In the zinc blende structure along the [1 1 1] direction, there is a 60° rotation that causes a stacking order of AaBbCc. The point with regard to rotation is illustrated in figure 1.1.b. The group terms of various commonly used planes of hexagonal semiconductors in two- and three-dimensional versions is presented in figures 1.2 and 1.3. The Wz group III nitrides lack an inversion plane perpendicular to the c-axis; thus, nitride surfaces have either a group III element (Al, Ga, or In) polarity (referred to as Ga-polarity) with a designation of (0 0 0 1) or (0 0 0 1)A plane or a N-

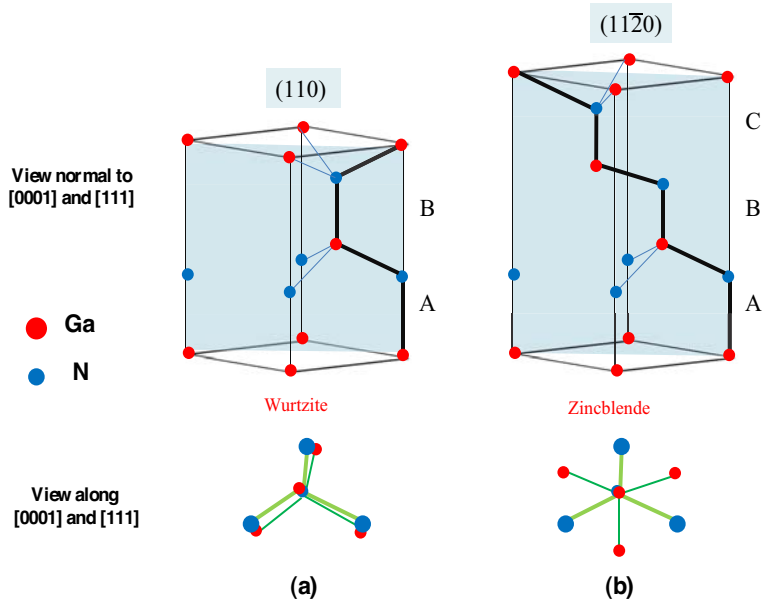

Figure 1.1: *Top figures depict the three-dimensional view. Bottom figures indicate the projections on the (0 0 0 1) and (1 1 1) planes for wurtzitic and cubic phases, respectively. Note the rotation in the zincblende case along the* $\langle 111 \rangle$ *direction. [44].*

polarity with a designation of $(000\bar{1})$ or (0 0 0 1)B plane. The distinction between these two directions is essential in nitrides because of their implications in the polarity of the polarization charge. Three surfaces and directions are of special importance in nitrides, which are (0 0 0 1) c-, $(11\bar{2}0)$ a-, and $(1\bar{1}00)$ m-planes and the directions associated with them, $\langle 0001 \rangle$, $\langle 11\bar{2}0 \rangle$, and $\langle 1\bar{1}00 \rangle$ as shown in figure 1.4. The (0 0 0 1), or the basal plane, is the most commonly used surface for growth. The other two are important in that they represent the primary directions employed in reflection high-energy electron diffraction (RHEED) observations in molecular beam epitaxial growth, apart from being perpendicular to one another. The cohesive energy per bond in the wurtzite form is 2.88 eV (63.5 kcal mol^{-1}), 2.2 eV (48.5 kcal mol^{-1}), and 1.93 eV (42.5 kcal mol^{-1}) for AlN, GaN, and InN, respectively [45]. The calculated energy difference ΔE_{W-ZB} between wurtzite and zinc blende lattice is small [46]: ΔE_{W-ZB} =-18.41 meV/atom for AlN, ΔE_{W-ZB} =-11.44 meV/atom for InN, and ΔE_{W-ZB} =-9.88 meV/atom for GaN. Wurtzite form is energetically preferable for all three nitrides compared to zinc blende, although the energy difference is small.

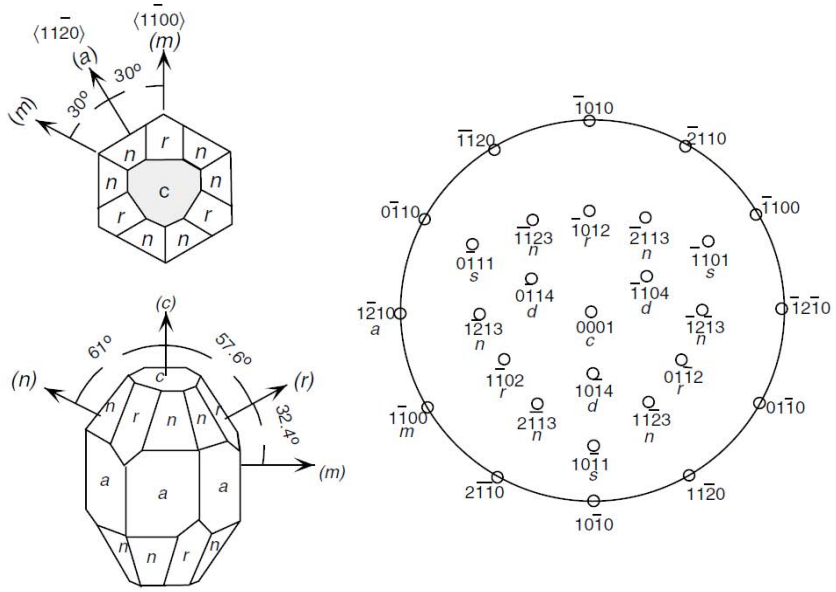

Common crystallographic planes in sapphire

Plane name	Miller index	d spacing
a	(11$\bar{2}$0)	2.379 Å
m	(10$\bar{1}$0)	1.375 Å
c	(0001)	2.165 Å
r	(1$\bar{1}$02)	1.740 Å
n	(11$\bar{2}$3)	1.147 Å
s	(10$\bar{1}$1)	1.961 Å

Angles between common planes

(0001) ^ (1$\bar{1}$02)	c ^ r	57° 35'
(0001) ^ (11$\bar{2}$3)	c ^ n	61° 11'
(0001) ^ (10$\bar{1}$1)	c ^ s	72° 23'
(0001) ^ (11$\bar{2}$1)	c ^	79° 37'
(0001) ^ (11$\bar{2}$0)	c ^ a	90° 00'
(0001) ^ (10$\bar{1}$0)	c ^ m	90° 00'
(1120) ^ (10$\bar{1}$0)	a ^ m	30 00'

Figure 1.2: *Labeling of planes in hexagonal symmetry [44].*

1.2 Substrates for nitride materials epitaxy

In spite of the interesting thermal, optical and electrical performance of this material devices produced, GaN materials suffer from numerous threading dislocations and lattice mismatch due to the lack of an appropriate substrate. Lattice mismatched substrates can lead to a substantial density of misfit and threading dislocations in the range of 10^6 and 10^{12} cm^{-2}. Selective epitaxy followed by coalescence such as epitaxial lateral overgrowth (ELOG) [47], is a promising method for reducing dislocations down to 10^6 cm^{-2}. Nearly every crystal-growth techniques, substrate-types, and orientations have been tried in an effort to grow high-quality group III-V nitride thin films. Researchers have successfully taken advantage of the hydride vapor phase epitaxy (HVPE), organometallic vapor phase epitaxy (OMVPE), and molecular beam epitaxy (MBE) techniques, which have yielded greatly improved film quality. The lack of native GaN substrates and difficulty with nitrogen incorporation were two main problems in all these epitaxial methods. The best alternatives now lie in the development of Al_2O_3, SiC, or AlN substrates. Interest in AlN substrates has increased recently owing to the closer lattice match over Al_2O_3, matched

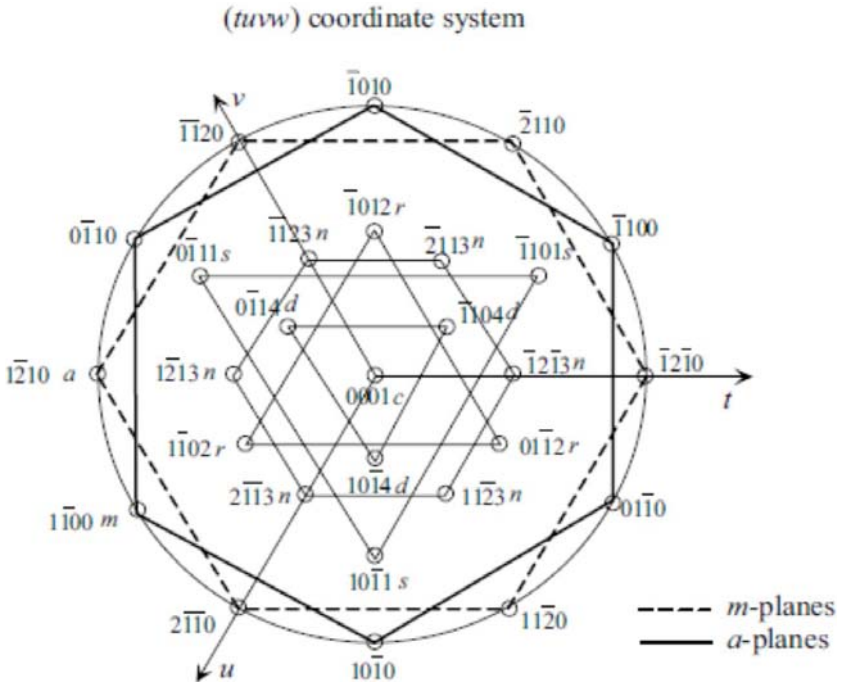

Figure 1.3: *Magnified view of labeling of planes in hexagonal symmetry in the (tuvw) coordinate system with w representing the unit vector in the c-direction. The lines are simply to show the symmetry only [44].*

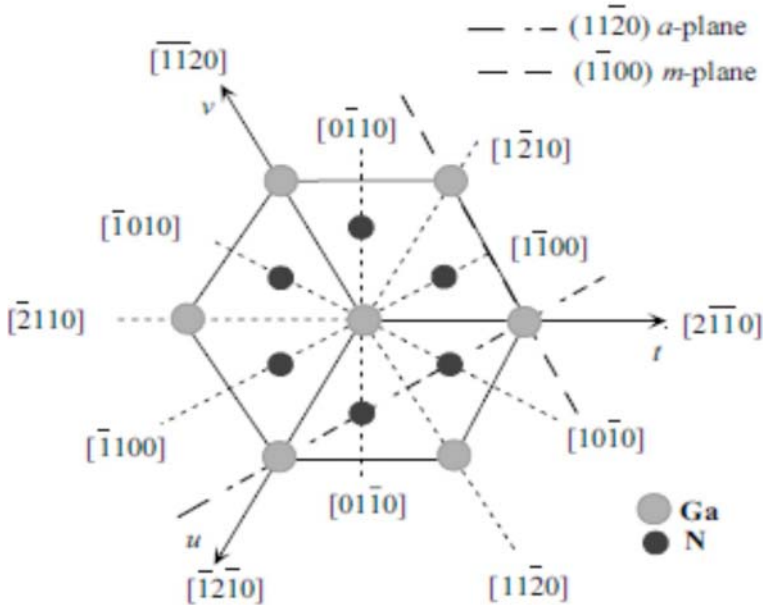

Figure 1.4: *The orientations which are commonly used in nitrides, namely the (11$\bar{2}$0)and (1$\bar{1}$00) planes and associated directions are shown as projections on the (0001) basal plane [44].*

stacking order, and high thermal conductivity [45]. As an alternative, the deposition of GaN on hexagonal silicon carbide (4H-SiC and 6H-SiC), with a lattice mismatch of ~3.4% [48] has paved the way for the fabrication of GaN/SiC films with lower threading dislocation densities. However, these techniques are not straightforward especially in the latter case where Ga has poor wetting on the SiC surface [49]. In addition, the high cost of growing good quality SiC substrates as well as the wide availability, the ease of handling and the easier pre-growth cleaning of Al_2O_3 has allowed it gains popularity as the substrate for depositing GaN films. The direct integration of GaN based optoelectronics with Si micro-electronics has been very difficult due to a lattice mismatch of ~17%, a thermal expansion coefficient incompatibility of ~56% and a poor nucleation of GaN on Si. Figure 1.5 gives a schematic illustration of the lattice mismatch of a GaN(0001) film onto

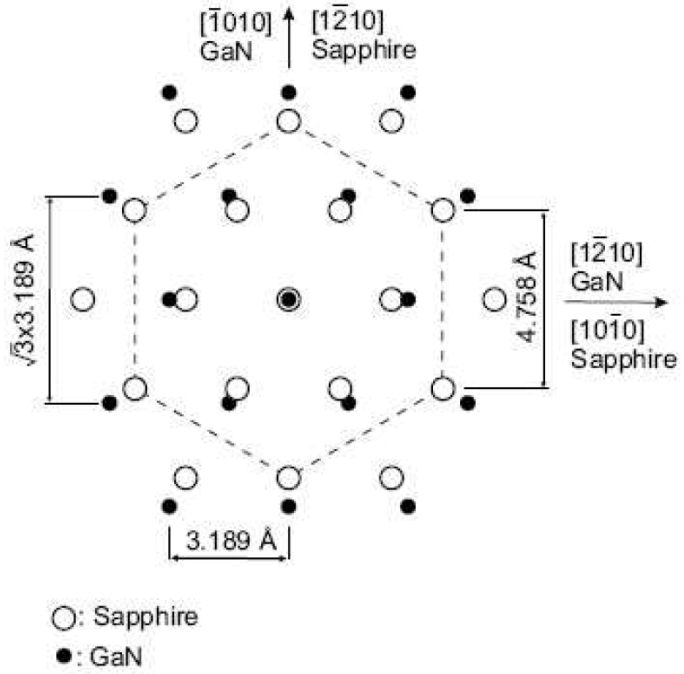

Figure 1.5: *Schematic illustration of the lattice mismatch for GaN(0001) grown onto an Al_2O_3(0001) surface [50]*

an Al_2O_3(0001) substrate, and table 1.1 compiles the resulting lattice-mismatch between the various III-N materials and substrates. The samples of GaN, AlGaN, and BGaN used in our current research, were properly grown and optimized by MOVPE leading to GaN films with dislocation densities in range of the 10^8 and 10^9 cm^{-2}. Sapphire is still the substrate of choice for growing GaN layers and has the advantage of ease of surface cleaning, interfacial adhesion, availability, chemical stability and thermal stability. Some of the techniques that have been explored for threading dislocation density reduction involve the

Table 1.1: Mismatch comparison for the III-N binary materials for [0001] directions at 300K [51].

Material substrate	GaN (%)	AlN (%)	InN (%)
GaN	0	2.3	10.6
AlN	2.4	0	12
InN	10.6	12	0
SiC	3.3	1.0	14
Al_2O_3	14.8	12.5	25.4
Si	16.9	18.7	7.6

patterning of substrates. Recently, selective area growth (SAG) [52]has been shown to be a powerful approach to lower Threading Dislocation Density TDDs. On the other hand SAG on the nano scale offers advantages such as a 3-D stress relief mechanism and extremely low defect density. Generally speaking, the quality of the epitaxial overgrowth is determined by the quality of the nucleation layer; however, the surface energy of the free surfaces during a lateral overgrowth phase can act as a sink for the threading dislocation density and trap them so they cannot propagate into the top layers of the film. Patterning substrates can maximize this behavior and reduce the density of dislocations in the upper layers of a thin film. Substrates are sometimes patterned by using masks with regions of nucleation in order to control the growth of GaN by SAG [53]. In this technology GaN is selectively nucleated at specific areas of the substrate and is grown laterally over the masked areas, it has been found to have significantly lower TDDs.

1.3 GaN based materials

Gallium nitride is the basic material of this material class which is typically used for all device layers requiring fast carrier transport with a high breakdown voltage. GaN is used as the channel material in various FETs and also as the base material in AlGaN/GaN Heterojunction Bipolar Transistors HBTs [54]. Most of the ohmic contact layers in any device incorporate binary n-doped and p-doped GaN. GaN can further be grown as a semi-insulating material with growth parameters close to those of the semiconducting layers. Second to GaN, AlN is the most important binary material in the III-N material family for electronic applications and is mostly used as its ternary compound $Al_xGa_{1-x}N$, e.g., in

barriers heterostructures. AlGaN can be considered as an insulator due to the high-band gap energy and the high-activation energy of donors. Binary AlN is usually grown as a nucleation layer to start the growth on SiC or sapphire substrates [55] and as an interlayer at the channel/barrier interface [56]. InN forms the third binary of the nitride family and both InAlN/GaN [57] as well as AlGaN/InGaN [58] heterostructures have been reported. Prior to 2001, InN and its compounds $In_xGa_{1-x}N$ and $In_xAl_{1-x}N$ were not yet widely used in electronic devices [59], and essentially, the early results suggested that wurtzite indium nitride had a band gap of approximately of 1.8-2.0 eV at room temperature. Both MBE and OMVPE techniques gradually gave way to more refined growth methods. The stoichiometry, however, has always been a pestering issue and will always remain so, which appears to have been one of the sources of controversy as to InN's true band gap following the longstanding value of about 1.89 eV. An inordinate number of reports adorned many reputable journals and filled the programs in technical meetings wherein researchers in great numbers argued that the true band gap of InN is actually 0.7-0.8 eV. In fact, lower values such as 0.65 [60] and 0.67 eV [61] have also been reported. The data of all III-N binaries are also compiled in table 1.2. One of the primary goals of solar cell design is to improve efficiency. InGaN is a material that has undergone extensive research since 2002 as a potential photovoltaic material. By varying the composition of In and Ga within InGaN, the band gap of this semiconductor material can be tuned. The band gap range of InGaN matches closely the visible solar spectrum frequencies. Hence, a high-efficiency solar cell can be potentially developed by having several InGaN junctions. Finding high-efficiency solar cell models is of great interest in space applications. By increasing the efficiency of photovoltaics, the number of solar panels is decreased. Therefore, the overall weight that needs to be launched into space is reduced. A cost-reduction can be achieved over the life of the space power system. Furthermore, InGaN-based PDs, with tunable direct band gap energy and sharp cutoff wavelength, offer an alternative and potentially better approach for detecting UV-A light [62].

1.3.1 Mechanical and optical properties

The crystal structure and the mechanical and thermal properties of GaN, AlN, and InN are discussed in a number of publications [63–68] respectively. Table 1.3 compiles the data on the mass density and compares the values of the hardness H and fracture toughness K_c. The Vickers hardness and fracture toughness of bulk GaN in comparison to other semiconductors are given in [69]. More recent results are presented in [70]. The absorption

Table 1.2: Material properties of binary compounds at 300K [51].

Material	GaN	AlN	InN	BN
Crystal structure	Wz	Wz	Wz	c
Lattice constant a_0 (Å)	3.189	3.112	3.533	2.534
Lattice constant c_0 (Å)	5.185	3.982	5.693	4.191
Band gap (Eg) (eV) 300K	3.39	6.22	0.8	6.4
Thermal expansion ($10^{-6}K^{-1}$) Δa/a	5.59	4.2	3.548	1.15
Thermal expansion ($10^{-6}K^{-1}$) Δc/a	3.17	5.3	5.760	-
Eff. e^--mass (m/m_0)	0.2	0.314	0.11	-
Thermal conductivity (WK^{-1} cm^{-1})	1.3	2.85	0.38	-

spectrum of GaN at room temperature and the absorption coefficient are presented in [71]. Overviews of further optical parameters of GaN such as the refractive index are given in [63, 72].

Table 1.3: Mass density, Vickers hardness H, refractive index and fracture toughness K_c of III-N comparing with other semiconductor materials [51].

Material	GaN	AlN	InN	BN	Si
Mass density (kgm^{-3})	6,100	3,230	6,810	3,480	2.33
H (GPa)	12	14	11.2	55-65	9
K_C ($MP_am^{1/2}$)	0.8	2.6	-	-	0.7
Index of refraction	$n_{(\lambda)}$=2.35,	2.1-2.2	2.9-3.05	-	3.42
at 300K	$n_{(\lambda)}$=2.85	of infrared	(λ=0.66-1 μm)		(λ=310nm)
α (x10^3cm^{-1})	130	5	100	1.8	6
at photon energy	4 eV	4 eV	3eV	13eV	2eV

1.3.2 Dielectric and transport properties

Compiling the basic dielectric properties, table 1.4 gives both the static and high-frequency dielectric constants. The dielectric constant of GaN is slightly lower than in silicon and GaAs (not shown). InN has the highest values of the three binary materials.

Table 1.4: Dielectric constants ϵ_r^t, ϵ_r^s and e^- saturated velocity of III-N and other semiconductor materials [51].

Material	GaN	AlN	InN	BN	Si
Crystal structure	Wz	Wz	Wz	c	
ϵ_r^t	9.5	8.5	15.3	7.1	11.9
ϵ_r^s	5.5	4.77	8.4	4.5	-
ν (10^7cm/Vs)	2.5	1.9	3.4	-	2.3
μ $cm^2V^{-1}s^{-1}$	990	135	3000	500	–
of (N_D) at 300K	(1x10^{17})	(1x10^{17})	(1x10^{17})	(N_A=5x10^{18})	–

1.3.3 Defects in GaN

The defects in crystals are typically classified by dimension. Zero-dimension (OD) or point defects include intrinsic point defects such as vacancies, interstitials, antisite defects and impurity-point defect complexes. Extended defects include linear defects (dislocations) and planar defects (grain boundaries, interfaces, stacking faults and micro-cracks). The three dimension (3D) defects include precipitates, holes (including nanopipes) and surface hillocks and pits (so called pinholes). The density of the intrinsic point defects in GaN could be very high and they may significantly affect the physical properties of the material [73]. The common extended defects in GaN and related compounds are dislocations and stacking faults. The formation of defect levels in GaN is strongly dependent on the growth conditions, temperature, Ga to N ratio and growth technique. Unintentionally doped GaN is nominally n-type and can have electron concentrations as high as 10^{18} cm^{-3}. This auto-doping of GaN is attributed to the formation of shallow donor levels with activation energies ranging from 30-40 meV [74, 75]. Theoretical calculations have shown that nitrogen vacancies may be shallow hydrogen like donors in GaN [75,76]. These nitrogen vacancies are thought to be responsible for the unintentional n-type doping of GaN. A further deeper V_N (nitrogen vacancies) level is also believed to exist with an energy level $\sim$ 120 meV from the conduction band. The Ga vacancy forms a shallow acceptor level 0.14 eV above the valence band. There are more than 30 recognized defect levels in GaN, some of which are shown in figure 1.6. All native defects in GaN, with the exception of the N vacancy and Ga vacancy create deep defect levels in the band gap. The nitrogen antisite, N on Ga site, and gallium antisite, Ga on N site, introduce levels close to the middle of the band gap. Both antisites occur in low concentrations as a result

of the high energy required to form them [77]. A deep level at 0.5 eV above the valence band is formed by the neutral Ga interstitial while the neutral N interstitial introduces two closely spaced deep acceptor levels at an energy level $\sim$ 1 eV separated by $\sim$ 0.06 eV [78]. Unintentional impurities such as oxygen, carbon, and hydrogen, present during the growth of GaN also introduce deep levels within the band gap. N-type conductivity in

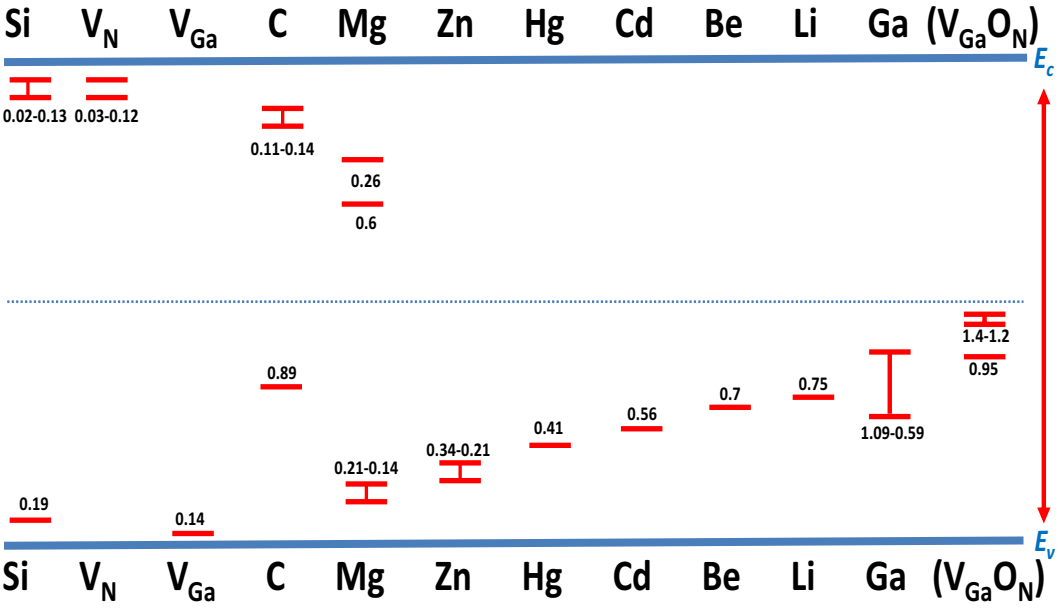

Figure 1.6: *Selected defect levels in GaN. V_{Ga} and V_N denote Ga and N vacancies respectively. Ga is a Ga atom on an N atom site (that is a Ga antisite)* [7].

GaN is usually achieved by Si doping. P-type conductivity in GaN has been successfully achieved by Mg doping. Thermal annealing or electron beam irradiation is required to activate the Mg acceptors. Threading dislocations (TDs) in GaN also have an important role to play in crystal growth. The densities of TDs for GaN epilayers grown on sapphire can be as high as 10^{10} cm^{-2}. These threading dislocations are a direct result of the lattice and thermal expansion coefficient mismatch between sapphire and GaN. There has been a range of conflicting theoretical and experimental results reported on the electrical activity and role of TDs in GaN [79]. First principle calculations suggest that edge TDs are electrically inactive while other theoretical predictions suggest that different types of edge TDs (open core, full core, Ga and N vacancy structures) introduce numerous electronic states in the band gap. Progress of understanding the electrical activity of both edge and screw TDs in GaN has been limited because of the difficulty in distinguishing the effects of impurities and point defects from the intrinsic properties of the dislocation core.

1.4 $Al_xGa_{1-x}N$ alloys

1.4.1 Structural properties

$Al_xGa_{1-x}N$ is the most important ternary compound, as the lattice-mismatch relative to GaN can be effectively controlled for nearly all material compositions. A distinction may be required for wurtzite and zincblende AlGaN materials, as the zincblende material has a transition from a direct to an indirect semiconductor [80]. The ternary alloys of wurtzite and zinc blende polytypes of GaN with AlN form a continuous alloy system with a wide range of band gap and a small change in the lattice constant. An accurate knowledge of the compositional dependence of the barrier as well as material is a requisite in attempts to analyze heterostructures in general and quantum wells (QWs) and superlattices in particular. The barriers can be formed of AlGaN or AlN, and while dependent on the barrier material, the wells can be formed of GaN or AlGaN layers. The compositional dependence of the lattice constant, the direct energy gap, and electrical and cathodoluminescence CL properties of the AlGaN alloys were measured by Yoshida et al. and Khan et al. [81, 82]. On the structural side, namely the calculated lattice parameter of this alloy, predictions indicate that Vegard's law applies [83, 84]:

$$a_{Al_xGa_{1-x}N}(\text{Å}) = 3.1986 - 0.0891x \qquad and \qquad c_{Al_xGa_{1-x}N}(\text{Å}) = 5.2262 - 0.2323x \quad (1.1)$$

By bringing to bear various tools such as high-resolution x-ray diffraction (HRXRD), the experimental data for various AlGaN support the applicability of Vegard's law in that the experimental data are within about 2% of those predicted by linear interpolation, Vegard's law.

$$a_{Al_xGa_{1-x}N}(\text{Å}) = (3.189 \pm 0.002) - (0.086 \pm 0.004)x \quad (1.2)$$

and

$$c_{Al_xGa_{1-x}N}(\text{Å}) = (5.188 \pm 0.003) - (0.208 \pm 0.005)x \quad (1.3)$$

However, the bond lengths exhibit a nonlinear behavior, deviating from the virtual crystal approximation. Essentially, the nearest neighbor bond lengths are not as dependent on composition as might be expected from the virtual crystal approximation. The ensuing investigations to pin down the compositional dependence of the band gap of this important alloy continued with conflicting results. These are discussed below following the presentation of an empirical expression used to relate the band gap to composition.

The compositional dependence of the principal band gap of $Al_xGa_{1-x}N$ can be calculated from the following empirical expression providing that the bowing parameter, b, is known accurately:

$$E_g(x) = xE_g(AlN) + (1-x)E_g(GaN) - bx(1-x) \tag{1.4}$$

where E_g(GaN) = 3.39eV, E_g(AlN) = 6.1eV, x is the AlN molar fraction, and b is the bowing parameter. An earlier compilation by Amano et al. [85] already pinpointed the discrepancy in the reported bowing parameters. For example, Yoshida et al. [86] concluded that, as the AlN mole fraction increases, the energy band gap of $Al_xGa_{1-x}N$ deviates upward, implying a negative value for the bowing parameter b. This contrasts the data of Wickenden et al. [87] that support a vanishing bowing parameter b. Koide et al. [88] observed that the bowing parameter is positive and that the band gap of the alloy deviates downward indicating a positive value for the bowing parameter. Figure 1.7 shows the value of AlGaN band gap versus the composition, yielding a bowing parameter of b=1.0 eV for the entire range of alloy compositions. To determine the bowing parameter accurately,

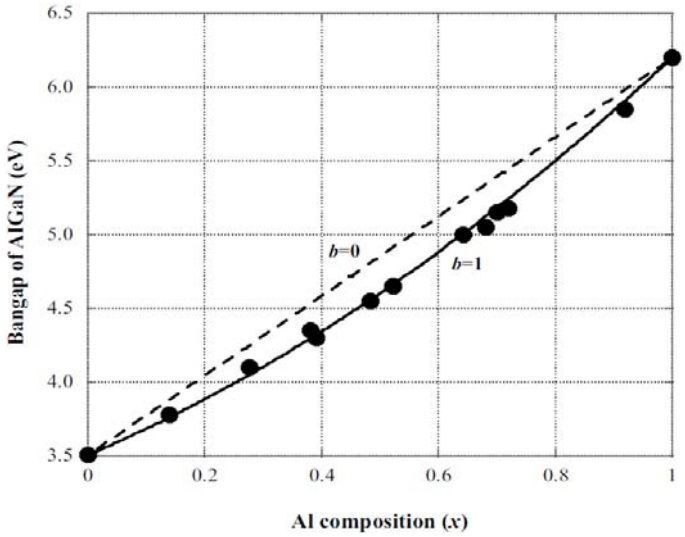

Figure 1.7: *Experimental data of energy band gap of AlGaN 0≤ x ≤1 , plotted as a function of Al composition (solid circle), and the least squares fit (solid line) giving a bowing parameter of b=1.0 eV. The dashed line shows the case of zero bowing [44].*

as investigations expanded so did the dispersion in the bowing parameters ranging from -0.8 eV (upward bowing) to +2.6 eV (downward bowing), as compiled by Yun et al. [89]. Much of this spread emanates from the likely dispersion in the quality of $Al_xGa_{1-x}N$, thus erroneous determination of its band gap and to a lesser extent its lattice parameter.

1.4.2 Electrical properties

Hall measurements for n-$Al_{0.09}Ga_{0.91}N$ demonstrated a carrier concentration of 5x10^{18}cm^{-3} and a mobility of 35 cm^2 V^{-1} s^{-1} at 300 K [90]. This measurement did not reveal any temperature-dependent mobility of n-$Al_{0.09}Ga_{0.91}N$. Other Hall measurements [91] on Mg-doped p-$Al_{0.08}Ga_{0.92}N$ grown by MOVPE, however, addressed the temperature dependence of the mobility [91]. They indicate that the hole mobility decreases with increasing temperature, reaching a value of about 9 cm^2 V^{-1} s^{-1} for a doping density of 1.48x10^{19}cm^{-3}. This low mobility is ascribed to a high carrier concentration and the intergrain scattering present in the samples. While the lattice constant was studied, it was observed to be almost linearly dependent on the AlN mole fraction in AlGaN. Until recently, the resistivity of unintentionally doped AlGaN was believed to increase so rapidly with increasing AlN mole fraction that AlGaN became almost insulating for AlN mole fractions exceeding 20%. As the AlN mole fraction increased from 0 to 30%, the n-type carrier concentration dropped from 10^{20} to 10^{17} cm^{-3} and the mobility increased from 10 to 30 (cm^{-2} .V^{-1} s^{-1}). An increase in the native defect ionization energies with increasing AlN may possibly be responsible for this variation. Our knowledge of the doping characteristics of AlGaN is still incomplete. For example, it is not known how the dopant atoms such as Si and Mg respond to the variation of the AlN mole fraction in AlGaN. However, it was suggested that as the AlN mole fraction increases, the dopant atom moves deeper into the forbidden energy band gap. AlGaN with an AlN mole fraction as high as 50-60% may be doped by both n- and p-type impurity atoms. The ability to dope a high mole fraction AlGaN, especially when low-resistivity p-type material is required, is important because it may otherwise restrict the overall characteristics of devices such as laser diodes. A low AlN mole fraction in AlGaN has been considered sufficient for acceptable optical field confinement. However, this must be addressed before the potential of AlGaN with respect to the other wide band gap semiconductors is fully realized.

1.5 $B_xGa_{1-x}N$ alloys

Recently a solution has been proposed by our group [92–95] to decrease the large lattice mismatch between GaN and Al_2O_3 and GaN and SiC substrates, which is to use a new materials system, known as the quaternary $B_xAl_yGa_{1-x-y}N$ (BAlGaN) system [92,96,97]. The advantages of incorporating boron are: its small ionic radius, being smaller than that of gallium (Ga) and aluminium (Al), which would help in the effective reduction in the size

of the system's crystalline lattice. Characteristics of these new alloys are similar to those on InGaN and AlGaN materials and the main advantage of this system is that there are solution compositions that are lattice matched to 6H-SiC and AlN. Add-on that SiC and AlN exhibit high thermal conductivities. Besides unlike the AlGaN based devices grown on sapphire, cleaving the BGaAlN based devices grown on SiC and AlN occurs along the cleavage planes. This discovery by Sakai et al. [98] was, in principle, the basis for the possibility of ternary BGaN and BAlN with quaternary BAlGaN materials to agree with underlying substrates of AlN and 6H-SiC. Based on their studies, a 5% composition of boron in BAlN is required to obtain a lattice matching with the AlN substrate, while 8 and 17% of boron in BGaN is required for its matching on AlN and 6H-SiC substrates, respectively. A corresponding adjustment of the bandgap energy between 3.6 and 6.2 eV would be required for the quaternary BAlGaN to match with the AlN lattice, while that of 3.8 to 6.2 eV would be required for it to match with the 6H-SiC [99]. An overview of the material band gap is illustrated in figure 1.8. It is well known that most of the

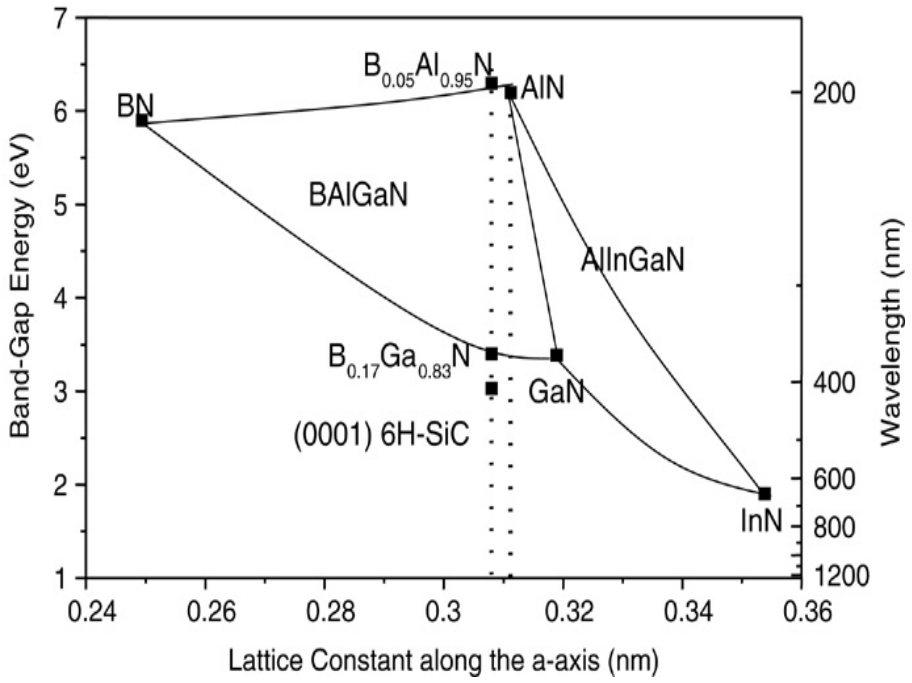

Figure 1.8: *Comparison of III-N semiconductors band gap energy at T=300K as a function of lattice constant with III-V semiconductors.*

semiconductor compounds used today in electronic and optical devices exhibit miscibiltiy gap in a wide range of compositions. BGaAlN materials are no exception as few studies indicate and hence this might limit incorporation of B in large amounts [100–102], but the epitaxial layers are made stable due to coherency strain [103]. Besides, these materials

offer the possiblity of using quaternary BAlGaN alloys in UV range and hence lead to more degrees of freedom in designing sophisticated device structures in the short wavelength range.

1.5.1 Structural and morphological properties

Orsal et al. [104] have shown that the surface morphology of the $B_xGa_{1-x}N$ layers changes drastically with the TEB/III ratio and with the layer thickness. SEM measurements were performed on different BGaN samples that varied in their thickness. This was essential to study the relationship between the thickness of the sample and the TEB/III ratio, the results of which are presented in figure 1.9. A drastic change in surface layer

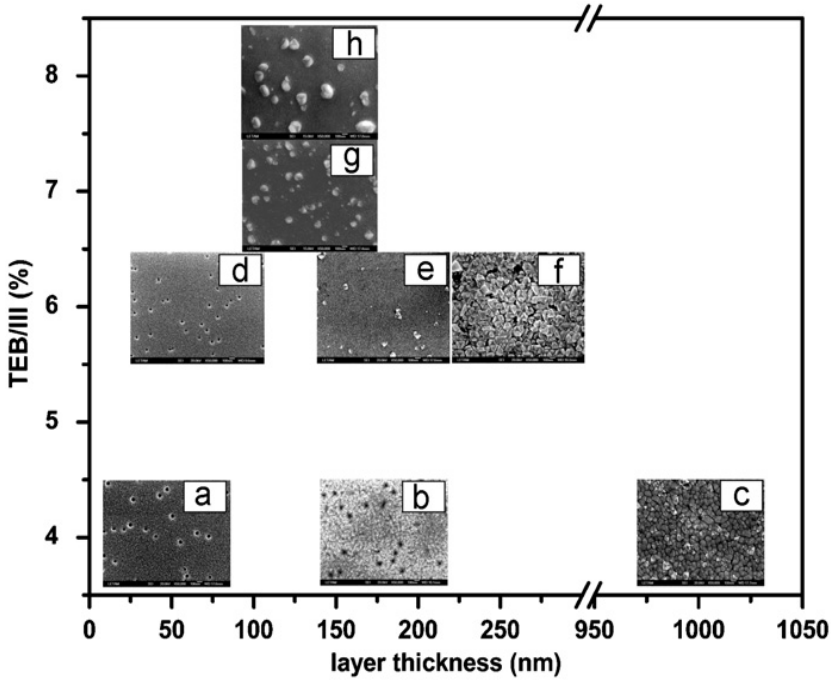

Figure 1.9: *BGaN surface images taken with SEM. Each of the figures represents different BGaN thicknesses grown with various TEB/III ratios [104].*

morphology was seen when TEB ratios increased from 4 to 8%. At 4% TEB/III (Figure 1.9 (a) and 1.9 (b)), SEM images showed an homogeneous surface composed of a matrix of small crystallites and numerous V-defects which are known to form when threading dislocations intersect the epilayer surface. When the ratio was increased to 8%, V-defects were fully covered in small and large crystallites with polygonal shape (figure 1.9 (g) and 1.9 (h)). Therefore, both the thickness of the film and the TEB/III ratio play an important role. While a TEB/III ratio of 4% showed no large crystallites over a broad

range of film thicknesses, a 1 μm layer thickness showed extra and different crystallites emerging on the surface when compared to the 175 nm layer. For BGaN of 50 nm thickness grown with a TEB/III ratio of 6% (figure 1.9 (d)), no change in morphology is seen compared to 4% TEB/III ratio. However, for TEB/III ratio of 6%, an increase in film thickness from 50 to 250 nm lead to filling of the V-defects and to the formation of large polygonal crystallites. The size and density of these crystallites increase with the thickness until the matrix is fully covered (figure 1.9 (f)). This suggests that both components play an important role and the effect seen is largely based on a combination of both. Ougazzaden et al. [93] has studied the surface morphology of BGaN monolayer and BGaN superlattice by using AFM, HRXRD and SIMS. It has been shown that to obtain smooth surface morphology of BGaN layers and to avoid plastic relaxation in the presence of high TEB/III ratio, thin superlattice of BGaN/GaN were grown. From figure 1.10 (b), it is evident that indeed multi-layer samples show less cracks and smoother surface providing extra evidence that the formation of layer cracking (figure 1.10 (a)) is indeed related to relaxation of strain due to higher boron effect. This relation between strain and boron content in BGaN layers was further investigated by using high resolution X-ray diffraction with (0002) reflection. Figure 1.11 illustrates this effect showing the plot

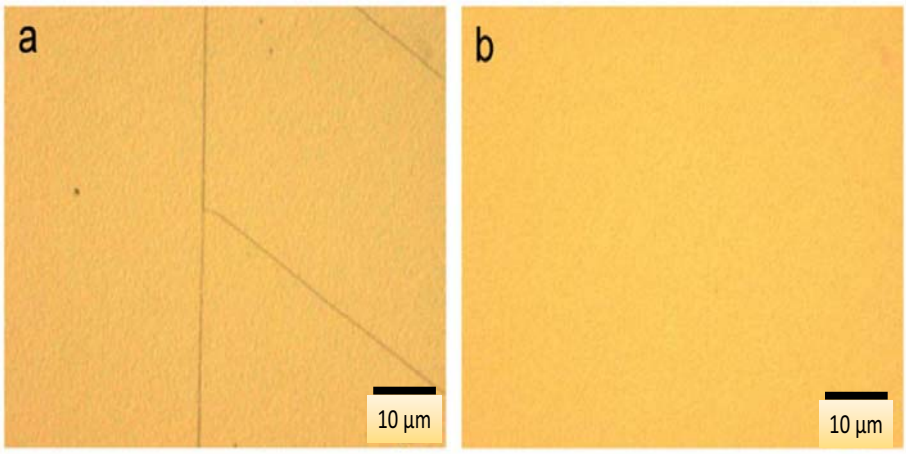

Figure 1.10: *(a) Nomarsky optical contrast microscopy image of thick relaxed strain BGaN layer. The marker line represents 10 mm. (b) Nomarsky optical contrast microscopy image of 20/20nm of BGaN/GaN multi layer [93].*

of BGaN/GaN at different TEB/III ratios where it is clearly that the shift in the BGaN peak towards higher tensile strain with increasing TEB/III ratio is enhanced as a result of the boron incorporation in GaN material. The lines in figure 1.12 represent the optimum thickness between good and degraded surface areas as a function of the TEB/III ratio

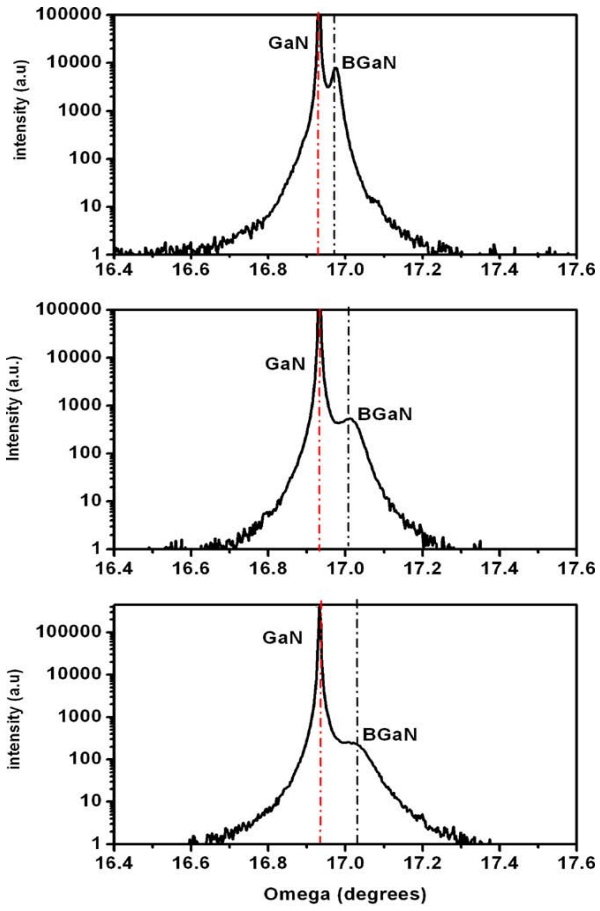

Figure 1.11: *HRXRD rocking curves of three BGaN films grown on 4-m-thick GaN layer. The shift of the BGaN peak increases from top to the bottom spectrum with boron incorporation [93].*

for two growth pressures of 600x10^2 Pa (450 Torr) and 133x10^2 Pa (100 Torr). For a given TEB/III ratio the intensities of the optical reflectometry peaks during the growth are strong and stay unchanged with increasing thickness up to an optimum thickness after which the reflectometry signal suddenly degrades down to the background noise signal. This degradation is related to an enhanced surface roughness beyond an optimum thickness. Decreasing growth pressure from 600x10^2 Pa (450 Torr) to 133x10^2 Pa (100 Torr) allows to extend the area of good surface morphology with both thicker layers and higher TEB/III ratio.

In order to study the distribution of boron on the substrate, SIMS analysis was carried out for a monolayer and a BGaN superlattice thin film. Figure 1.13 , shows the concentration of boron and gallium as a function of the layer depth for a BGaN monolayer. The anti-phase boron profile against gallium is consistent with what is expected from III-III-V

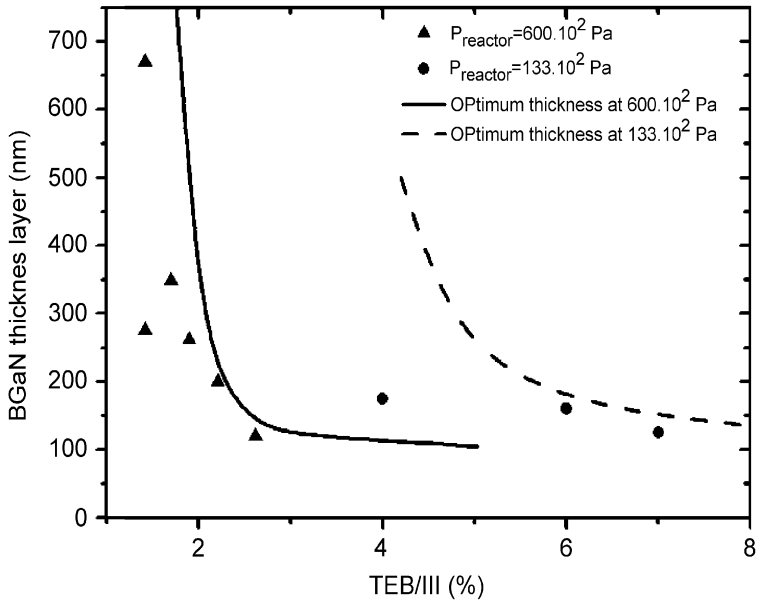

Figure 1.12: *Mapping of BGaN surface morphology as a function of TEB/III ratio for two different growth pressures. The lines delimitate good (left side) and poor (right side) morphology regions [93].*

alloys which shows that the boron element is well incorporated into the Ga site. Figure

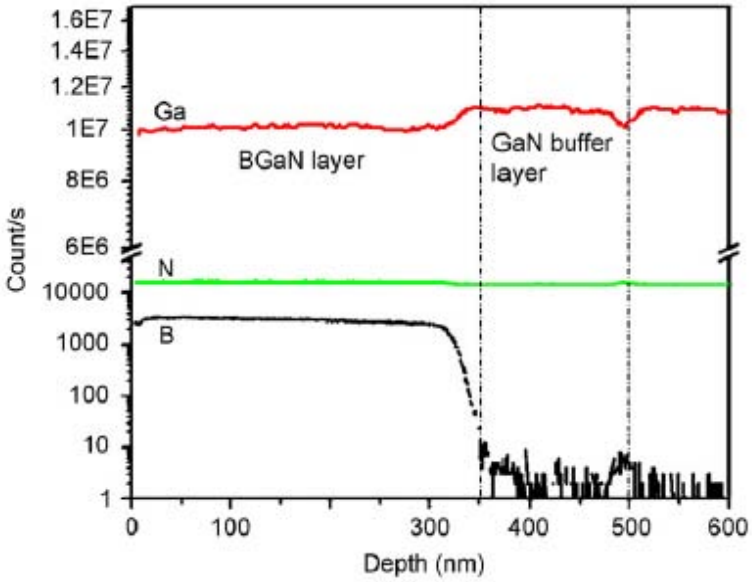

Figure 1.13: *SIMS profile of 350nm BGaN monolayer grown on GaN substrate [93].*

1.14 shows the resulting profile of boron concentration of 10 peaks and 10 valleys which were respective of the 10 layers of BGaN and GaN. The antiphase oscillations of boron and gallium in the BGaN/GaN multilayers is characteristic of III-III-V alloys.

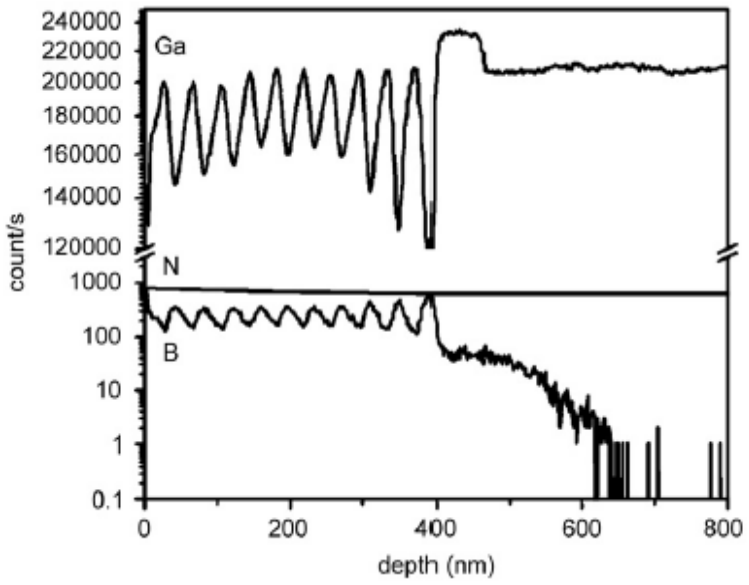

Figure 1.14: *SIMS profile of BGaN superlattice of 10 periods of 20/20nm BGaN/GaN [93].*

1.5.2 Electrical properties

The studies of electrical and structural properties realized by our research team on $B_xGa_{1-x}N$, show that it was possible to incorporate up to 4% of boron in GaN without any phase separation [105]. It is important to emphasize that this growth was conducted under special and original epitaxy conditions in a T-shaped growth chamber, one of the very few types of reactors available in the world. Baghdadli et al. [106] shows that the electrical resistivity is strongly related to the boron incorporation in BGaN alloy, while the mobility increases up to 290 cm^2/Vs with increase of boron content up to 1.75 % as shown in figure 1.15. The high carrier concentration in BGaN with boron composition less than 0.3% is attributed to background shallow donors such as silicon or oxygen commonly observed for MOVPE grown GaN layers [107]. Stampfl et al. [108] have observed a strong decrease in carrier concentration for AlGaN alloy, which may be related to a decrease in the density of dopants or an increase in their activation energy or an incorporation of a compensating native defect. This could be the same for the BGaN alloys for which increasing in resistivity with respect to boron composition in BGaN can be explained by either a change in the ionized impurity or dislocation scattering.

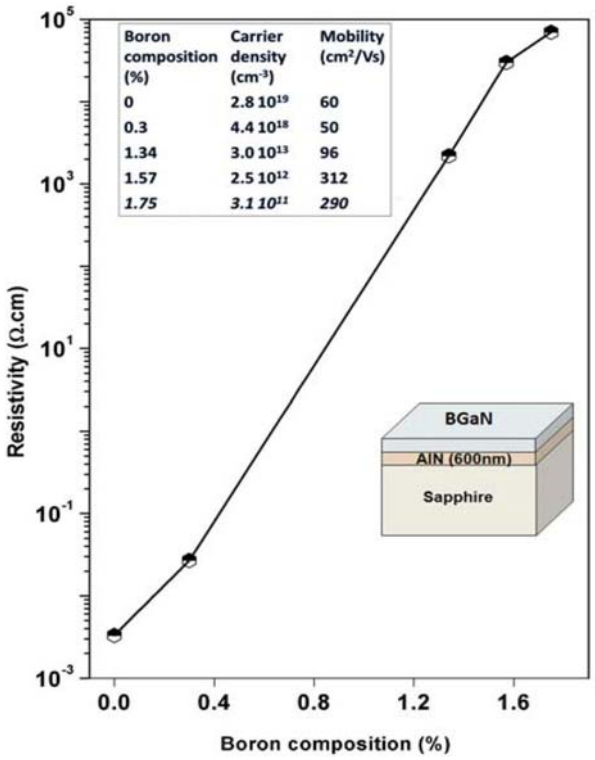

Figure 1.15: *Dependence of the electrical resistivity on boron composition in BGaN alloy at room temperature. Inset table shows the carrier density and mobility dependence on boron content with layers thickness varies from 0.3 μm to 0.6 μm [106].*

1.5.3 Optical properties

Polyakov [109] in 1997 initially observed the luminescence of BGaN materials by cathodoluminescence when working on GaN samples with implanted and annealed boron atoms. In the following years 1998 and 1999, this feature was also observed by Gupta et al. [110] and Wei et al. [111] with BGaN material epitaxied by MBE and MOVPE respectively. Based on the literature, in the absence of any boron composition (x_B= 0%), a GaN material reference has a luminescence band gap of 3.4 eV at room temperature. An increase in boron composition to x_B= 1.5%, as measured by X-ray diffraction, increased the luminescence of BGaN to 3.43 eV. According to the Vegard's law, the measured gap increases monotonically with the increase of boron concentration. A summary is presented in table 1.5. Honda et al. [113] have shown that the energy gap of ternary BGaN is greater than that of GaN for low boron composition (up to 1%), while the effective mass is close to that of GaN. Nevertheless, these unique results were obtained for very small range of composition of boron and the change in the observed gap is very small (1.5 nm between the GaN and the BGaN with 1% boron). Ilyasov et al. [114] have simulated a parameter

Table 1.5: BGaN band gap values as deduced from photoluminescence measurements [112].

Author	Conditions	Boron (%)	Band gap (eV)	Layer thickness
Gupta [110]	λ= 325nm, T= 300K	1.5 %	3.43	-
Wei [111]	λ= 325nm, T= 10K	1.5 %	3.465	-
Honda [113]	λ= 325nm, T= 20K	1 %	3.45	2 μm

of curvature of 3 eV using the Local Coherent Potential Approximation model. This value would reduce the energy band gap for low incorporation of boron. Other factors, such as the refractive index of the material used, were also modulated by the concentration of boron incorporated. Watanabe et al. [115] have measured the wavelength dependence of the refractive indices of BGaN and BAlN in the ultraviolet range. A strong dependence of the refractive index on boron composition have been evidenced and is shown in figure 1.16. The variation of the refractive index given in figure 1.16 corresponds to:

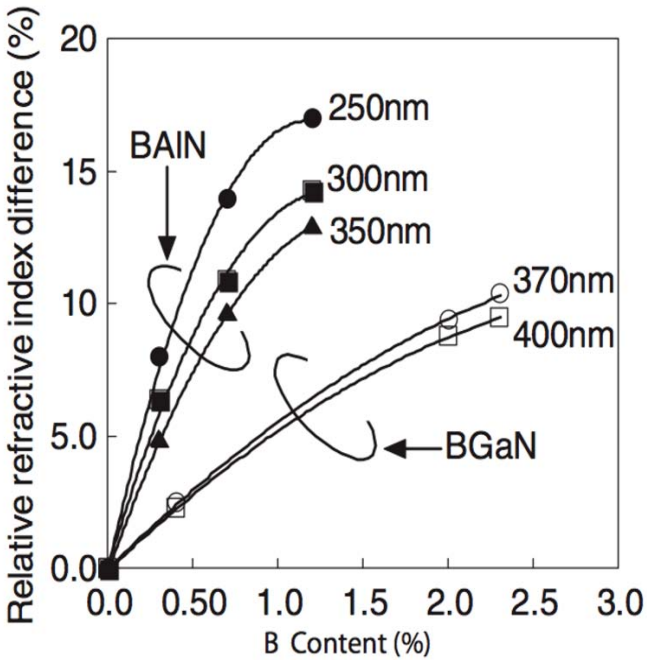

Figure 1.16: *Refractive index versus boron composition [112].*

$$\Delta \sim \frac{n_2 - n_1}{n_1} \tag{1.5}$$

where n_1 is the index of the top layer containing boron and n_2 the index of the layer below. The binary structures being examined are BAlN/AlN and BGaN/GaN.

Recently, Ougazzaden et al. [105] have reported on the band gap variation with a significant bowing parameter (C=9.2±0.5 eV) of the BGaN thin films. Absorbance spectra $\alpha^2(\lambda)$, are shown in figure 1.17, in the case of more disordered BGaN layers with a tail of absorbance below the band gap, the uncertainty of this approach is too high for precise measurements of the bowing parameter. The band gap absorption approach is decoupled in two contributions, which originate from the disorder and the composition-induced renormalization of the band gap.

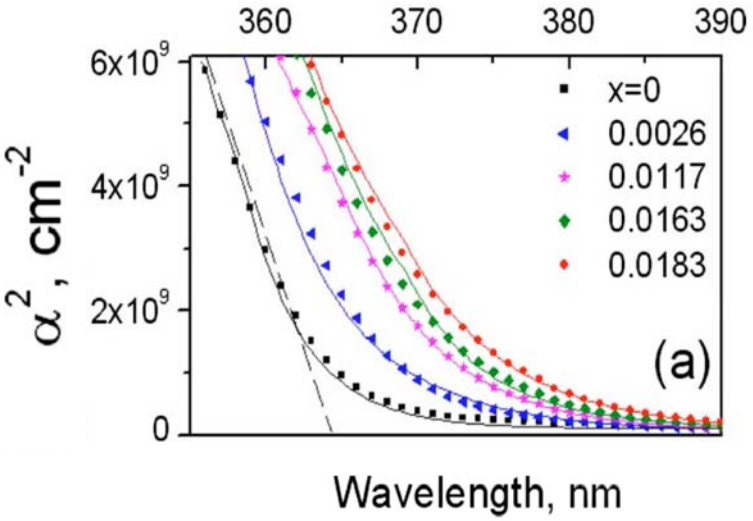

Figure 1.17: *Absorbtion coefficient versus wavelength [112].*

Chapitre 2

Photodétecteurs : les différents types et leurs caractéristiques générales

Sommaire

2.1 Caractéristiques des photodétecteurs 32

2.1.1 Efficacité quantique 32

2.1.2 Sensibilité 32

2.1.3 Réponse spectrale 33

2.1.4 Temps de réponse 33

2.1.5 Courant d'obscurité 35

2.1.6 Contraste UV-visible 37

2.1.7 Bruit dans les photodétecteurs 38

2.2 Photodétecteurs UV: état de l'art 39

2.2.1 Détecteurs photoconducteurs 39

2.2.2 Photodiodes PIN 42

2.2.3 Photodiodes à avalanche 43

2.2.4 Photodiodes barrière de Schottky 46

2.2.5 Photodétecteur Métal-Semiconducteur-Métal 49

2.2.6 Mécanisme de gain dans les photodétecteurs Schottky et métal-semiconducteur-métal 53

Chapter 2

Photodetectors: the different types and their characteristics

Contents

2.1 Photodetector characteristics 32

2.1.1 Quantum efficiency 32

2.1.2 Responsivity 32

2.1.3 Spectral response 33

2.1.4 Response time 33

2.1.5 Dark current 35

2.1.6 UV-visible contrast 37

2.1.7 Noise in photodetectors 38

2.2 III-N UV photodetectors: state of the art 39

2.2.1 Photoconductive detectors 39

2.2.2 P-I-N photodiodes 42

2.2.3 Avalanche photodiodes 43

2.2.4 Schottky Barrier Photodiodes 46

2.2.5 Metal-Semiconductor-Metal Photodetector 49

2.2.6 Gain mechanism in Schottky and Metal-Semiconductor-Metal photodetector 53

2.1 Photodetector characteristics

A number of important characteristics are commonly used to describe photodetector performances. These characteristics are quantum efficiency, response speed, dark current, UV visible rejection ration and responsivity. These performance characteristics indicate how a photodetector responds to an input of light energy. The choice of a particular photodetector depends on the requirements of a specific application. We will discuss these characteristics in the following.

2.1.1 Quantum efficiency

The quantum efficiency of a photodetector is defined as a very important parameter because it is a measurement of how efficiently the photons are converted to current. It is just another way of measuring effectiveness of the basic radiant energy in producing electrical current in a detector. It can be either internal η_0 or external η_{ext}. In a well designed photodetector, nearly all photons penetrating the semiconductor are absorbed and result in carrier generation followed by efficient carrier collection. If all of these processes were done perfectly, the internal quantum efficiency η_0 for this photodetector would be unity. The η_{ext} quantum efficiency depends on a number of factors like the absorption coefficient of the material and the thickness of the absorbing region and it is a measure of how many photons are detected or counted by the device. It is also a wavelength dependent quantity and is expressed conventionally as:

$$\eta_{ext}(\lambda) = (1 - r)(1 - e^{-\alpha(\lambda)d}) \tag{2.1}$$

where r is the reflection coefficient from the front surface, $\alpha(\lambda)$ is the absortion coefficient and d is the layer thickness. Efficiency increases with the increase of the absorption layer thickness. However, thick layers cause longer carrier transit times. Therefore, the detector is slower. This phenomenon is called the efficiency-bandwidth trade off. Furthermore, efficiency drops rapidly when λ becomes larger than the corresponding band gap wavelength [116,117].

2.1.2 Responsivity

The responsivity R_λ of a photodetector is essentially a measure of the effectiveness of the detector for converting electromagnetic radiation into electrical current. It is the ratio of

its output electrical signal I_p to the input optical signal P_λ [118]:

$$R_\lambda = \frac{I_p}{P_\lambda} = gq(\frac{\lambda\eta_{ext}}{hc}) = g\frac{q}{hc}\lambda\eta_{ext} \tag{2.2}$$

where, R_λ is expressed in A/W, h is the Planck's constant, c is the velocity of light, g is the gain (photoconductive gain) and q is the electric charge. In the UV spectral region of interest, the responsivity varies from 0.16 AW^{-1} at 200 nm to 0.294 AW^{-1} at 365 nm for an ideal quantum efficiency η_{ext}=1 and a gain g=1 [119].

2.1.3 Spectral response

The plot of absolute responsivity as a function of wavelength gives the spectral response of the detector. The long wavelength cut-off of the spectral response is determined by the absorption coefficient or band gap of the semiconductor. A short wavelength cut-off is observed because the value of absorption coefficient α is very large in most semiconductors and all the incident optical energy is absorbed near the surface. Except for shorter wavelengths there is high-energy absorption that requires an electron from the valence band to reach the conduction band where the density of states is low. However, these excited electrons cannot be accommodated and hence the responsivity drops.

2.1.4 Response time

There are two main factors which limit the speed of response of photodiodes: these arise from the finite transit time of carriers across the depletion region and from the RC time constant associated with the electrical parameters of the diode and its external circuitry.

2.1.4.1 Drift time of carriers

In very high electric fields the drift velocities of carriers in semiconductors tend to saturate. Thus provided the field within the depletion region exceeds the saturation velocity v_{sat}. Consequently they take a time τ_{drift} to traverse the depletion region of width w. where

$$\tau_{drift} = \frac{w}{v_{sat}} \tag{2.3}$$

During the whole of the time that the carriers are moving across the depletion region a current must be flowing through the external circuit. Thus if a very short duration pulse of radiation is absorbed within the depletion region then an output signal extending over a time τ_{drift} will be observed. Typical values for the saturation velocities are of the order of $10^6 Vm^{-1}$.

2.1.4.2 Junction capacitance effects

In a p-i-n photodiode we may assume a similar expression of the capacitance of an abrupt junction (see equation 3.49) where w is now the width of the i region. Although junctions are rarely abrupt in practice, it will remains true that junction capacitance decreases with increasing reverse bias. Figure 2.1 shows a photodiode equivalent circuit. In operation,

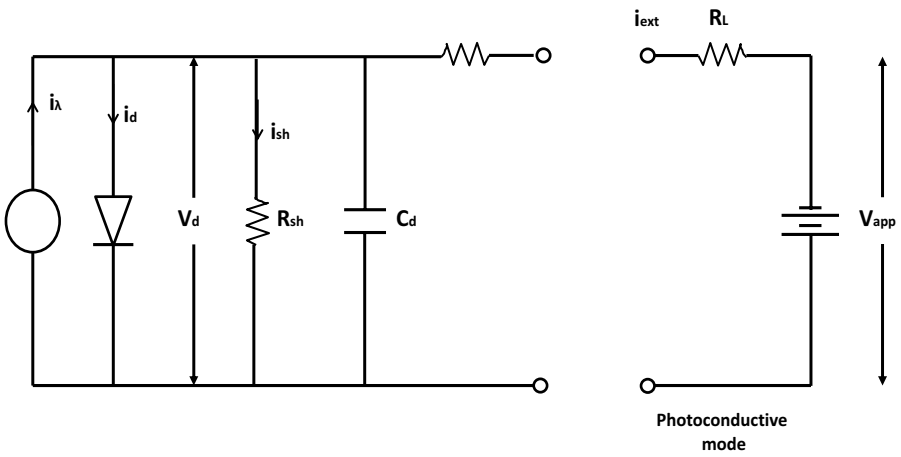

Figure 2.1: *Photodiode equivalent circuit [120].*

the photodiode can be represented by a photogenerated current source i_λ feeding into an ideal diode. The internal cell characteristics are better modeled by the introduction of a shunt resistor R_{sh}, a shunt capacitor C_d and a series resistor R_s. In the photoconductive mode, and external bias V_{app} is applied in conjunction with series load resistor R_L. The current flowing through R_L is monitored by measuring the voltage across it. We see from figure 2.1 that at high frequencies the diode capacitance acts as shunt across the output resistance network and reduces the output. Usually $R_{sh} \gg R_L$ and $R_s \gg R_L$, hence as far as the diode photocurrent i_λ is concerned, the diode capacitance C_d is in parallel with the load resistor R_L. If the i_λ is amplitude modulated at frequency f then the output voltage of the device is given by:

$$V_0 = \frac{i_\lambda R_L}{(1 + 4\pi^2 f^2 C_d^2 R_L^2)^{1/2}} \tag{2.4}$$

The electrical bandwidth Δf_{el} is defined as the frequency range over which the output is above $1/\sqrt{2}$ of its maximum value. Thus in the present instance $4\pi^2 \Delta f_{el}^2 C_d^2 R_L^2 = 1$, where $\Delta f_{el}^2 C_d^2$ is given by:

$$\Delta f_{el} = \frac{1}{2\pi R_L C_d} \tag{2.5}$$

The bandwidth may obviously be improved by reducing C_d. Inspection of equation 3.49 shows that this may be achieved by decreasing the diode area and increasing the thickness

of the i region. Unfortunately both these courses of action have associated difficulties. There is obviously a limit on how small the diode area can be made without encountering problems associated with focusing on incident beam onto a small area. In addition increasing the width of the i layer will increase the value of τ_{drift} which will worsen the frequency response as far as carrier transit time is concerned. There will thus be an optimum value for the thickness of the i region which will result in maximum overall bandwidth. Now the response time associated with the detector RC network can be written τ_{RC}=$R_L C$ and the total response time, τ, including both transit effects and junction capacitance effects can be written as:

$$\tau^2 = \tau_{drift}^2 + \tau_{RC}^2 \tag{2.6}$$

when $\tau_{drift} \propto w$ and $\tau_{RC_d} \propto 1/w$ it is easy to show that τ is minimized when $\tau_{drift} = \tau_{RC}$. This is the normal design criterion for ensuring the fastest diode response.

It should be mentioned that carriers generated outside the high field regions may contribute to the output provided the electron-hole pairs manage to diffuse into the high field region before recombination takes place. The problem with this is that carrier diffusion is inherently a relatively slow process carriers to diffuse a distance d can be written as:

$$\tau_{drift} = \frac{d^2}{2D_c} \tag{2.7}$$

where D_c is the minority coefficient. Thus distances of the order of micrometers typically involve carrier diffusion times of the order of nanoseconds and so carriers generated outside the depletion region may thus cause a 'slow' tail to be present in the response as illustrated in figure 2.2.

2.1.5 Dark current

The dark current I_d is the leakage current that flows through the photodiode is in the absence of any optical signal and originates from thermally generated electron-hole pairs, while a reverse voltage is applied across the junction. The dark current is a result of four major effects, including diffusion current, generation recombination current, surface current, and avalanche current. The current-voltage characteristics of a photodiode with no incident light is similar in nature to the normal p-n junction. When the photodiode is forward biased, there is an exponential increase in the current. When a reverse bias is applied, a small reverse saturation current appears. The dark current can be expressed as follows:

$$I_d = I_s \left[\exp\left(\frac{qV}{nk_B T} \right) - 1 \right] \tag{2.8}$$

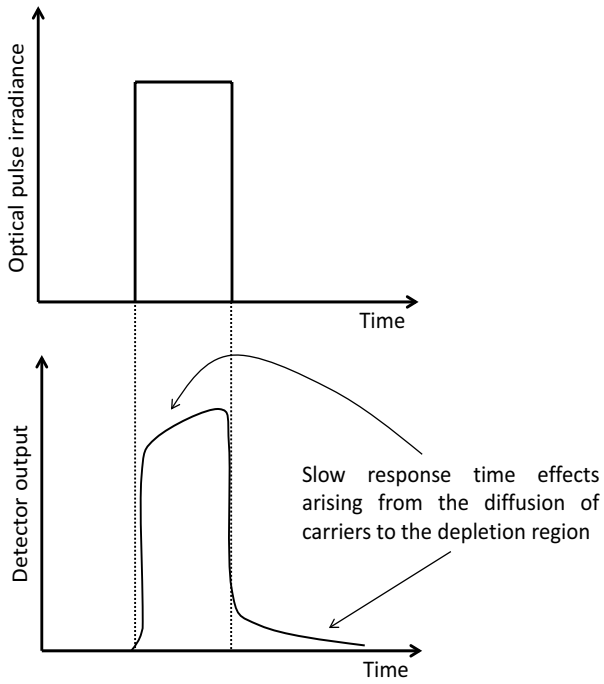

Figure 2.2: *Response of a p-n junction detector to a narrow optical pulse. The effects arising from the relatively long time it takes for carriers generated away from the depletion region to diffuse to the junction [120].*

where I_d is the photodiode dark current, I_s is the reverse saturation current, q is the electron charge, V is the applied bias voltage, k_B is the Boltzmann constant, and T is the absolute temperature.

The photodiode device produces a total current that is a sum of the photocurrent I_{ph} and the dark current I_d, and can be expressed by:

$$I_{total} = I_s \left[\exp\left(\frac{qV}{nk_BT} \right) - 1 \right] + I_{ph} \tag{2.9}$$

where I_{ph} is the photocurrent and I_{total} is the current across the junction. Figure 2.3 shows the characteristic I-V curves of the photodiode. It can be found that the generation of electron-hole pairs in a p-n junction shifts the reverse 'breakdown' characteristic toward the origin when illuminating the photodiode with optical radiation. As the applied reverse bias increases, there is a sharp increase in the photodiode current. The applied reverse bias at this point is referred to as breakdown voltage. The photodiode should be operated below the maximum applied reverse bias.

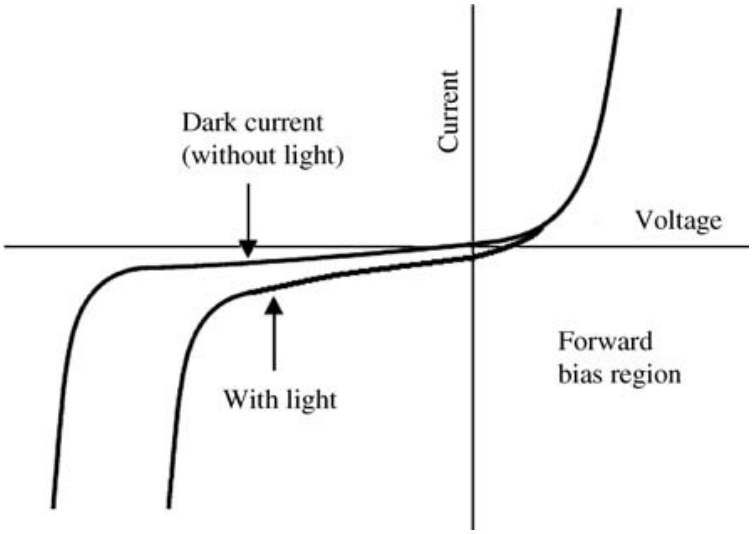

Figure 2.3: *Characteristic I-V curves of the photodiode.*

2.1.6 UV-visible contrast

The absorption of light is the fundamental effect governing the dependence of the spectral response of a photodetector as a function of the energy of the incident photons. In direct-band gap semiconductors, we therefore observe a dramatic transition in the value of the spectral response close to the band gap of the semiconductor material, dropping all at once to a very low value when we drop below the band gap. In the case of UV photodetectors, assigning an arbitrary limit to the wavelength of visible light of 400 nm, the UV-visible contrast which also known as UV-visible-rejection-ratio UVVRR is defined by the ratio $R_{imax}(\lambda = \lambda_G)/R_i$ ($\lambda = 400$ nm), where R_{imax} is the maximum value of the response coefficient at the wavelength λ_G of the band gap and R_i ($\lambda = 400$ nm) represents the value of the response coefficient at the limit of visible light. The UV-visible contrast is mostly limited by the two following factors [121]:

1. the presence in the band gap of the semiconductor of deep energy states which are electrically and optically active. These originate in particular from extended or localized defects in the crystal structure of the semiconductor, but can also be attributed to the presence of deep energy levels due to impurities, or deep levels caused by imperfections in the surface of the semiconductor;

2. in the case of Schottky junction photodetectors with semitransparent contacts, the effects of photo-emission of carriers by the metal.

2.1.7 Noise in photodetectors

As we have mentioned above, the output signal of a photodetector is an electrical signal. It means that it is not a strictly stable quantity over time, but fluctuates due to electrical noise. Noise it can be any undesired signal causing disturbances in the system that appears as a result of an action from outside the system. In order to compare the different noise mechanisms in different photodetectors, with different frequency bandwidths, it is convenient to use the concept of noise spectral density, which consists of normalizing the noise power to the frequency bandwidth considered:

$$Noise\ spectral\ density = \frac{\sqrt{\langle I_{noise}^2 \rangle}}{\sqrt{\Delta f}} \tag{2.10}$$

which is expressed in $\frac{A}{\sqrt{Hz}}$. It exists several contributions to the noise in photodetectors that will be briefly described in this sub-section.

Johnson noise

When the electrons collide with atoms or molecules in the matter, they constitute thermally-activated charge carriers through the conductor known as thermal or Johnson noise. The mean-square voltage of such noise can be calculated from:

$$\langle V_{noise}^2 \rangle_{Johonson} = 4k_B T R \Delta f \tag{2.11}$$

where k_B is the Boltzmann constant, T is the temperature of the conductor, R is its electrical resistance, and Δf is the frequency bandwidth of the noise.

Shot noise

In late 1918, Schottky showed that the random arrival of electrons on the collecting electrode of a vacuum tube was responsible for a so-called shot noise. This noise is present in all photons detectors due to the random arrival rate of photons from the source of radiant energy under measurement and background radiation. For example the shot noise in a p-n junction diode in the low operating frequency regime can be estimated by:

$$\langle I_{noise}^2 \rangle_{Shot} = 2q(I_D + 2I_0)\Delta f \tag{2.12}$$

where I_D=I_0(exp($\frac{qV_b}{KT}$)-1) and I_0 is the saturation current of the diode.

Generation-recombination noise

This noise can be understood by random processes of charge carriers in semiconductors associated with the creation and annihilation of electron-hole pairs in the material. This results in a random change of the voltage of the device, which is called generation-recombination (G-R) noise. For an intrinsic semiconductor with a moderate bias, this noise can be expressed as:

$$(V_{noise})_{G-R} = \frac{2V_b}{\sqrt{lwt}} \left(\frac{1+b}{bn+p} \right) \sqrt{\frac{np}{n+p} + \frac{\tau \Delta f}{1+\omega^2\tau^2}} \tag{2.13}$$

where V_b is the voltage bias, l is the length, w is the width, and t is the thickness of the device, b is the ratio of the motilities $\frac{\mu_e}{\mu_h}$, n and p are the electron and hole concentrations respectively, τ is the carrier lifetime in the semiconductor, ω is the angular frequency of operation, and Δf is the frequency bandwidth within which the noise is measured.

2.2 III-N UV photodetectors: state of the art

In this section we will give a brief presentation of the various types of photodetectors known but two photodetectors, the Schottky barrier and MSM photodiodes, will be the focus of great detail. These photodetectors are presented in figure 2.4. Photoconductive PD types are simple to fabricate, provide high gain and large noise. On the other hand, the p-i-n varieties which operates near zero bias offer high quantum efficiency, low-frequency noise, and high detectivity, but have a gain of unity. Avalanche photodiodes offer gain and low dark current, but with low-frequency and also high frequency noise as the avalanching process adds on additional statistical variations. Schottky barrier types PD operates near zero bias, have low-frequency noise and offer simple device structure. The metal-semiconductor-metal (MSM) varieties share much of the features of the Schottky barrier PD types, but requires bias voltage.

2.2.1 Photoconductive detectors

It is the simplest optical detector that exhibits an internal gain mechanism. Its operation is based on the photoexcitation of a specific region, which increases the conductivity. Photoconductors based on AlGaN typically consist of an epitaxial layer of AlGaN on sapphire, doped with silicon, with a thickness of 1 μm, onto which two ohmic contacts are attached as shown in figure 2.5. The electrical bias circuit includes a DC voltage source connected to the photoconductor, and the device is in series with a low-value load resistance. The

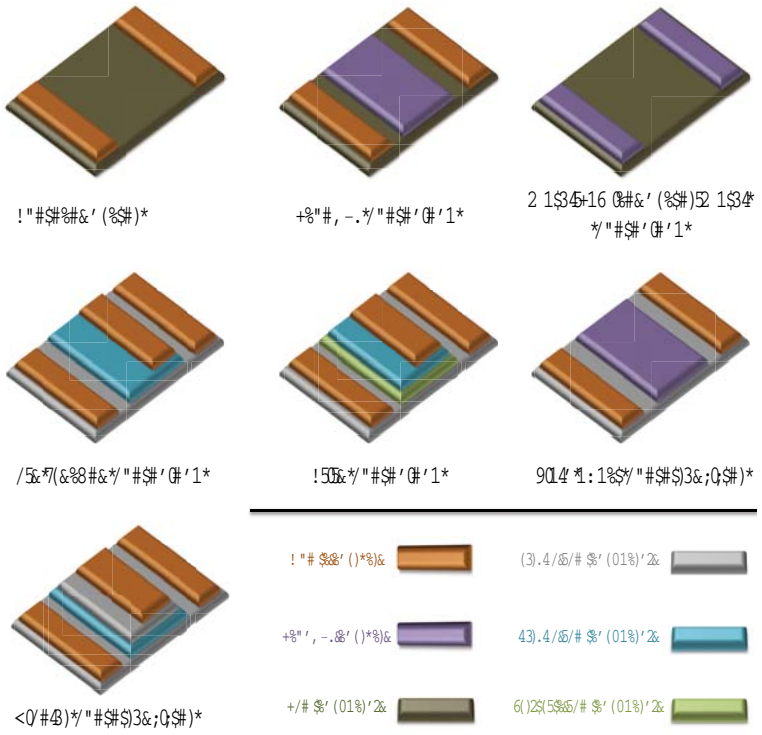

Figure 2.4: *Schematic structure of different types of photodetectors.*

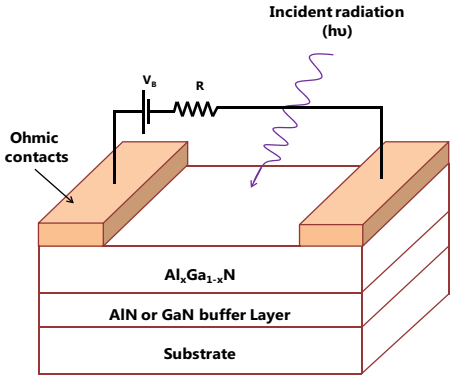

Figure 2.5: *Schematic structure of AlGaN-based photoconductor*

current induced in the device can be easily deduced from measurement of the voltage drop across the load resistance when the photoconductor is illuminated. Photoconductors based on GaN and AlGaN exhibit a gain under continuous illumination which can reach 10^5-10^6 and which strongly depends on the incident optical power. Its variation is a function which decreases in proportion to P^{γ} over a range of five decades, with $0.5 < \gamma < 0.95$, where P is the incident optical power [122]. The value of γ is a decreasing function of the electrical resistance of the layer, and decreases with temperature. The spectral

response of photoconductors based on $Al_xGa_{1-x}N$ exhibits a cutoff at 298 nm for x = 0.319 nm for x = 0.22 and 368 nm for x = 0.35. The UV/visible contrast is significantly smaller than the value obtained from a simple analysis based on the absorption coefficient of these materials. The mechanism which explains the variation of the spectral response of the photoconductor must therefore involve more than just the optical absorption of the semiconductor. In addition, a sub-linear dependence of the photocurrent is observed as a function of the power of the incident light. In the model developed by Garrido et al. [123], the photoconductor's responsiviy R_λ is the combination of two terms, one due to the photogenerated free carriers, Δn, and the other due to the modification by the light of the effective conducting crossection, ΔS. The responsiviy can be written as:

$$R_\lambda = \frac{qV_B\mu_e}{LP_{opt}}\left(S\Delta n + n\Delta S\right) \tag{2.14}$$

where q is the elementary charge of the electron, μ_e is the electron mobility, L is the distance between the contacts, S is the conductive cross-section, V_B is the bias voltage and n is the concentration of free carriers. The absorption of light produces a reduction of these depletion regions, leading to a modification of the conduction cross-section. Given that Δn can be expressed in the form [10]:

$$\Delta_n = \eta g\tau\frac{P_{opt}}{hc/\lambda} \tag{2.15}$$

where η is the quantum efficiency, g the photoconduction gain, τ the lifetime of the free carriers and hc/λ the photon energy. By substituting equation 2.15 into equation 2.14, it follows that:

$$R_\lambda = \frac{qV_B\mu_e}{L}\left(\frac{\eta(\lambda)g\tau S}{hc/\lambda} + \frac{n}{P_{opt}}\Delta S\right) \tag{2.16}$$

Depending on the detector size, material, doping and applied voltage, the photoconductive gain can vary from less than 1 up to 10^5. The spectral variation of the first term in this equation is given by $\lambda.\eta(\lambda)$. Since the quantum efficiency is a direct function of the absorption, this first term leads to a significant UV/visible contrast. However, experiments show that the dominant mechanism in these photodetectors is represented by the second term of equation 2.16. In other words, it depends strongly on the modification of the effective transverse conduction cross-section. This mechanism can also explain the high value of the spectral response for photon energies above the band gap energy: the energy levels responsible for the absorption of light in the visible region can originate either from point defects distributed homogenously within the semiconductor, either dopants or vacancies, or in extended defects associated with lattice discontinuities. If these defects

are electrically charged, they create a depletion region around them, which reduces the effective conduction cross-section of the device. Complete absorption of light through these defects can be treated as negligible, so that their presence has little effect on the absorption coefficient, and hence on the first term of equation 2.16. However, their effect on the photoconduction spectral response is large, since the electrical charge concentrated at these lattice discontinuities is modified by the light, which alters the effective transverse conduction cross-section.

2.2.2 P-I-N photodiodes

A p-i-n photodiode is a simple diode structure which consists in a p-n junction separated by an intrinsic or i-region with a thickness less or equal to $1/\alpha$, where, α is the optical absorption coefficient of the intrinsic region. Because of the very low density of free carriers in the i-region and its high resistivity, any applied bias is dropped almost entirely across this i-layer, which is then fully depleted at low reverse bias. The p-i-n diode has a "controlled" depletion layer width, which can be tailored to meet the requirements of photoresponse and frequency bandwidth. The absorption and carrier generation processes in a p-i-n photodiode are shown in figure 2.6. In the recent developments, one of the main

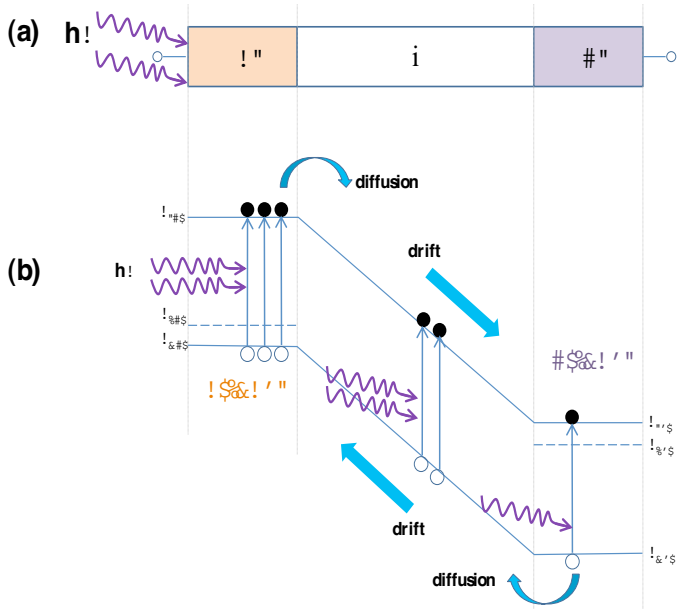

Figure 2.6: *(a) Schematic structure of a reverse-biased p-i-n diode, with the incident light arriving on the p-type side; (b) the absorption of photons creates electron-hole pairs in the ptype, n-type and the i-region where they then become spatially separated through the electric field across the space charge region.*

objectives relate to achieve true solar-blind operation and high quantum efficiencies, and to use device designs that would allow focal plane arrays. To achieve high performance p-i-n devices, high quality and high Al mole fractions ($\geq$0.4), with good n- and p-type conductivity layers and ohmic contacts are required. The use of higher Al mole fractions implies new difficulties in the ohmic contact technology, and higher series resistances are usually obtained. Solar-blind operation can be achieved using absorbing layers with Al mole fractions in the 40% range. Because of the lattice mismatch problems, cracks in the layers are usually present. For the p-type region, such compositions pose a severe problem to really achieve p-type conduction and ohmic contacting. High resistivity layers are usually obtained. At shorter wavelengths, photons are absorbed very close to the surface, and surface problems, band-bending effects, and electric field crowding problems (non-uniform spatial variations) tend to be present. To minimize such effects, the thinning of the p-type AlGaN, and the use of a semitransparent metal contact (Ni/Au) on top, to collect carriers more efficiently and to lower the series resistance, have been used [124]. In general, improvements in ohmic contacts to the p-type AlGaN layer are obtained by contacting on a p^+-GaN layer deposited on the p-type AlGaN region. By controlling the Al composition in the active region, peak responsivities in the 362 to 225 nm were reported. Such devices showed an UV/visible contrast up to six orders of magnitude, and peak responsivities of 0.20 AW^{-1} at 262 nm were obtained without applying bias as shown in figure 2.7 . Front and back illuminated structures were developed. A similar structure has been reported by Brown et al. [125], with an n-type $Al_{0.64}Ga_{0.36}N$ window and an absorbing layer with 0.47 Al mole fraction. A responsivity of 51 mA W^{-1} at 273 nm was achieved. Table 2.1 gives responsivity, UVRR, and current density recently reported in literature.

2.2.3 Avalanche photodiodes

The most basic structure of an avalanche photodiode is a p-i-n junction. An avalanche photodiode operates by converting each absorbed photon into a cascade of electron-hole pairs. It offers the combined advantages of a fast operation, high gain, and high sensitivity. As described in figure 2.8 the high electric field present in the i-region accelerates the photogenerated carriers until they reach a certain threshold energy (depending on the semiconductor material used), at which point they generate secondary electron-hole pairs across the band gap. These in turn gain energy from the field and create their own secondary pairs and so on. This gives rise to large currents flowing in the reverse-bias

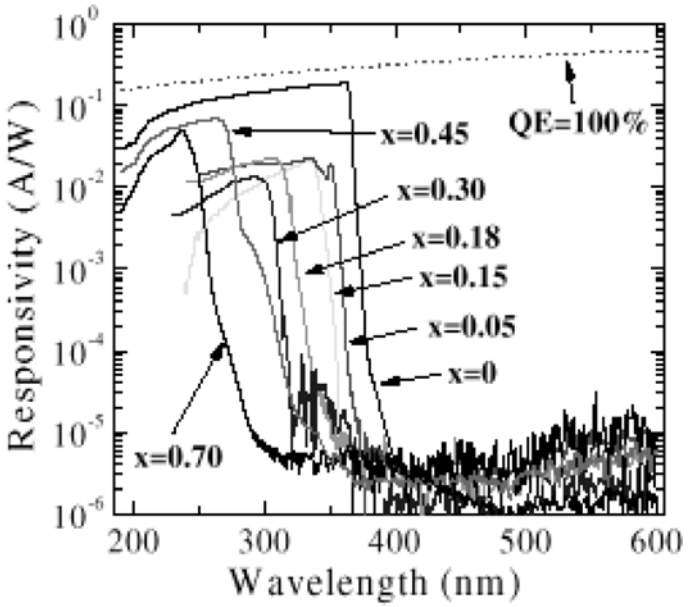

Figure 2.7: *Spectral responses of $Al_xGa_{1-x}N$ p-i-n photodiodes. The dotted line represents the theoretical limit for an external quantum efficiency of 100% [126].*

Table 2.1: Major progress of III-Nitride p-i-n photodiodes.

Materials	Type	Device area (μm^2)	Responsivity (A/W)	UVRR	Current Density I_d (A/cm^2)
GaN [127]	p-i-n	707	0.23 at 5V	–	7n at 5V
GaN [128]	p-i-n	–	0.11 at 0V (λ=365 nm)	1200	–
GaN [129]	p-i-n	31416	0.23 at -5V (λ=356 nm)	6700	–
$Al_{0.44}Ga_{0.56}N$ [130]	p-i-n	2.5x10^5	12x10^{-3} at (λ=270 nm)	10^6	4x10^{-10} at -5V

direction. This carrier generation process is known as the impact ionization process and is responsible for carrier multiplication, generating gain. This is the reason why the process is called avalanching. For a p-i-n junction, the photocurrent I_{ph} generated by the incident on the active region barely varies with the operating voltage. In contrast, for APDs, above a certain bias voltage the photocurrent I_{ph} grows steadily, reaching its maximum value when the bias voltage is equal to the breakdown voltage V_B of the junction. The

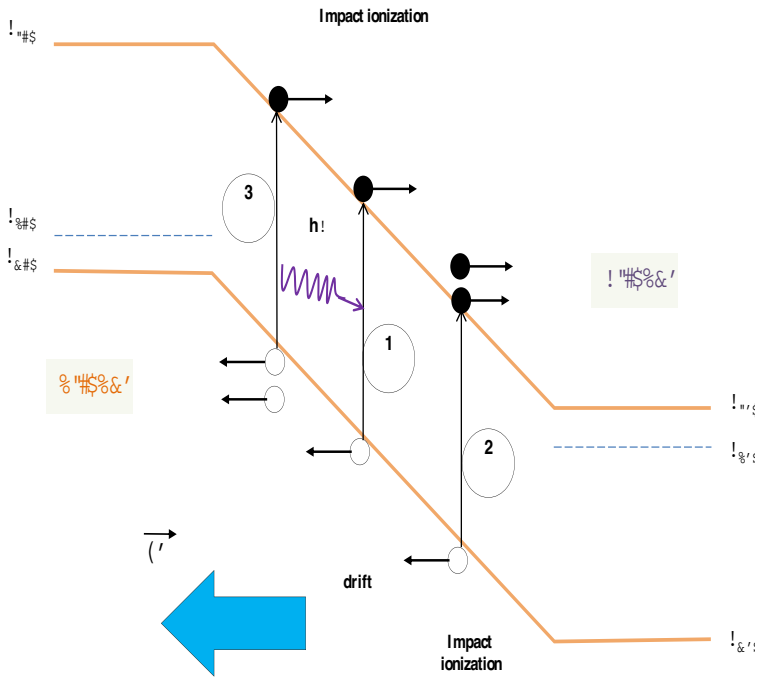

Figure 2.8: *Schematic representation of the multiplication process in an avalanche photodiode.*

gain M is given by:

$$M = \frac{I_{ph}(V)}{I_{ph}(V_0)} = \frac{I(V) - I_d(V)}{I(V_0) - I_d(V_0)} \tag{2.17}$$

where I_{ph}, I and I_d are respectively the photocurrent, the total current flowing across the junction, and the dark current. V and V_0 are the operating voltage and the reference voltage for which M=1 respectively. $I_{ph}(V)$ and $I_d(V_0)$ are the primary photocurrent and the primary dark current respectively.

Photodiodes based on GaN and AlGaN have a reduced density of dislocations, resulting in improved performance. Surprisingly, devices are operable even with large numbers of dislocations. In the case of avalanche photodiodes, a minimum dislocation density is required before gain can be obtained. The high electric field needed to initiate avalanche multiplication (greater than $\sim$1.6 MVcm^{-1}) simply cannot be reached in material with high dislocation density [131]. GaN-based avalanche photodiodes have been reported using material grown by MOVPE [132,133]. Figure 2.9 shows the room temperature I-V characteristics of a GaN avalanche photodiode. For low bias voltages, down to zero bias, The device diameter was 24 μm, and a low leakage current of about $\sim$ 2x10^{-11} A at a reverse bias of 5 V was obtained [132]. The responsivity of the device was independent of the voltage. A clear onset of the gain with respect to voltage is noted near 35 V, and a maximum gain of approximately 25 was achieved near the breakdown voltage of $\sim$

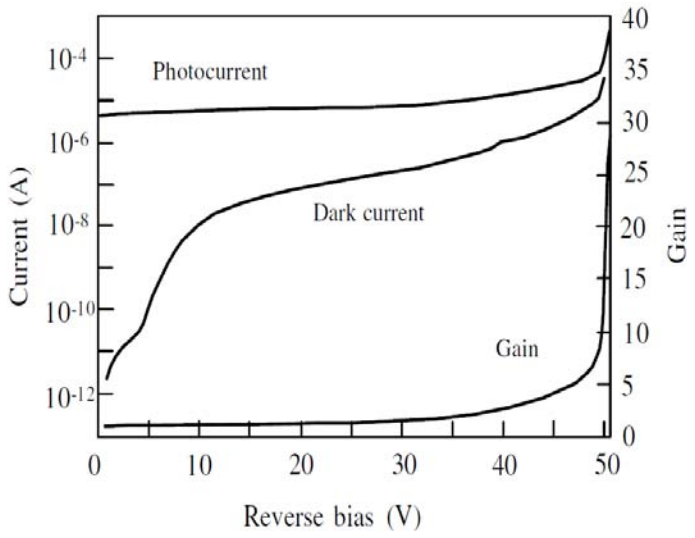

Figure 2.9: *Current-voltage and gain-voltage plots for a GaN avalanche photodector [132]*

48-50V, which led to the estimation that the breakdown field is about ~ 3.5 MVcm^{-1}.

2.2.4 Schottky Barrier Photodiodes

Schottky barrier photodiodes have been studied extensively and have found various applications. They are currently the most frequently used photodetectors in industry because of their efficiency and low cost. They are simple to fabricate, because they do not require p-type, and thus no high temperature diffusion processes. This give them some advantages over p-n junction photodiodes. Both planar and vertical structures are used for Schottky barrier photodiodes. The vertical structures device is good for attaining fast switching speed and having a high responsivity. Once the ohmic contact is deposited and annealed, the Schottky contact that typically uses Au, Pd or Pt is deposited. It is also possible to form two back-to-back Schottky contacts in the form of interdigitated metal fingers separated from each other by a few micrometers. This goes by the nomenclature of MSM detectors and will be discussed separately. The rectification arises from the presence of an electrostatic barrier between the metal and the semiconductor, which is due to the difference in work functions ϕ_m and ϕ_s of the metal and semiconductor, respectively, as shown in figure 2.10 for a n-type and a p-type semiconductor. The current transport across metal-semiconductor junctions is mainly due to the majority carriers, in contrast to p-n junctions where current transport is mainly due to minority carriers. It is now widely accepted that thermionic emission is the main process of carrier transport across

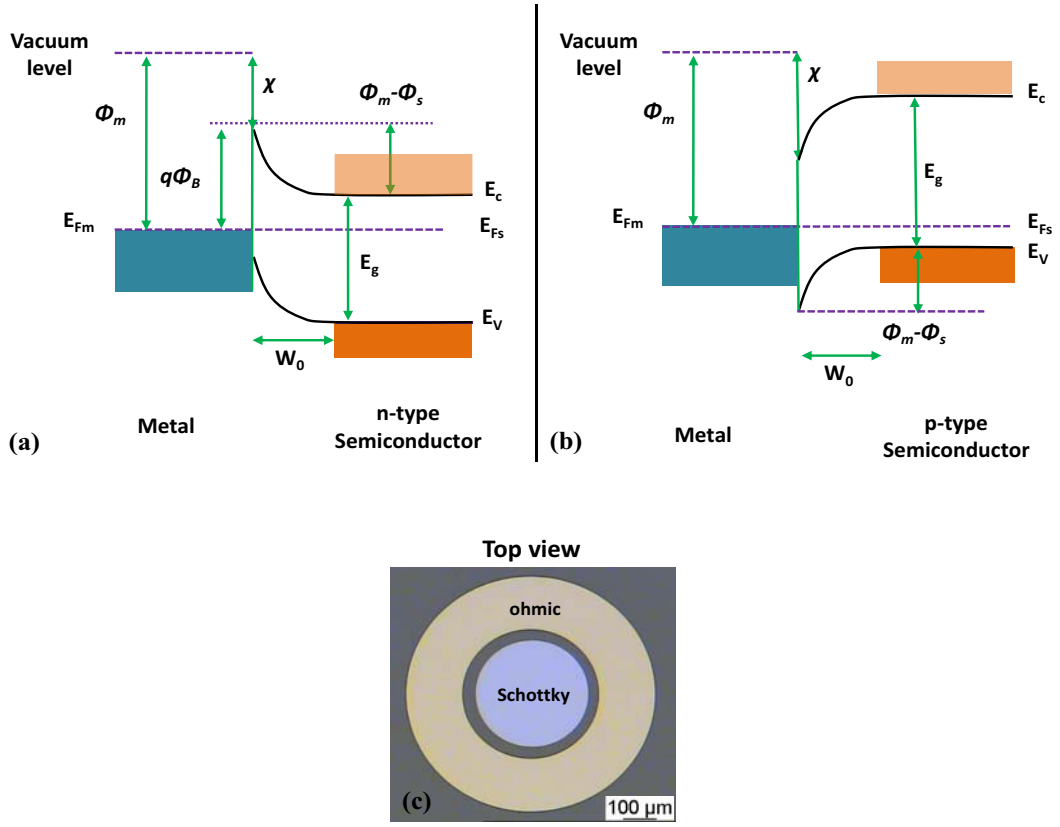

Figure 2.10: *Equilibrium energy band diagram of Schottky contacts: (a) metal-(n-type) semiconductor ($\phi_m > \phi_s$); (b) metal-(p-type) semiconductor ($\phi_m < \phi_s$). A Schottky contact is obtained in each case because the majority carriers in the semiconductor experience a potential barrier which prevents their free movement across the metal-semiconductor junction. (c) Optical top view image of Schottky diode after realization.*

Schottky barriers, and the current density is given by:

$$J = J_{s\to m} + J_{m\to s} = A^* T^2 e^{\left(-\frac{q\phi_{Bn}}{k_B T}\right)} \left[e^{\left(\frac{qV}{k_B T}\right)} - 1\right] J = J_{ST}\left[e^{\frac{qV}{k_B T}} - 1\right] \tag{2.18}$$

where A^* is richardson constant, T is the temperature. AlGaN-based Schottky barrier detectors are, at this point, somewhat less advanced than their GaN cousins. In spite of this, detectors fabricated with AlGaN (with the Al content up to 0.35) exhibited ultraviolet spectral response peaking at 280-290 nm with a responsivity of $0.1 \mathrm{AW}^{-1}$ [134, 135]. A very large drop in the below band gap response (four orders of magnitude) has been demonstrated, even in the absence of sophisticated postgrowth processing. This high UV-to-visible ratio was maintained even for AlGaN-based detectors on Si(1 1 1) substrates [136].

The normalized responsivity of $Al_xGa_{1-x}N$ Schottky barriers with AlN molar fraction

from the binary (representing no AlN) to 0.35 is shown in figure 2.11 Schottky barrier devices show a linear dependence of the photocurrent on the incident power over five orders of magnitude (from 10 mWm^{-2} to 2 kWm^{-2}) as shown in the inset of figure 2.11, which represents a welcome deviation from photoconductive varieties. Figure 2.11 a UV/visible contrast ratio of more than three decades is achieved. The cutoff wavelength shifts from 362 to 293nm as one traverse from GaN to $Al_{0.35}Ga_{0.65}N$. While the normalized responsivity is flat for wavelengths below the band gap, the absolute responsivity decreases with increasing AlN molar fraction, namely, 0.054, 0.045, 0.030, and 0.010 AW^{-1} for x= 0, 0.19, 0.26, and 0.35, respectively. The rapid drop in the responsivity for radiation below the band gap is indicative of the effect of the defects in the absorbing material only, in contrast with the results obtained in photoconductive detectors. Table 2.2 compiles the recent progress on Schottky barrier photodiodes. However, the typical dark current

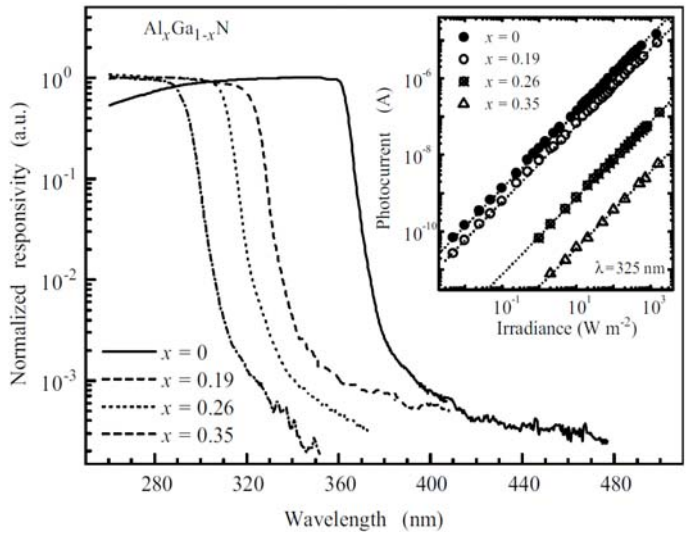

Figure 2.11: *Normalized room-temperature spectral response of $Al_xGa_{1-x}N$ Schottky barrier photodiodes for different values of the Al mole fraction. The inset shows the dependence of the photocurrent on the incident light power [137]*

density of the state-of-the art MSM photodiodes is still three orders higher than that of the p-n junction photodiodes due to the fundamental device limitation [12]. It is important to achieve a high Schottky barrier height at the metal-semiconductor interface for smaller leakage current and higher breakdown voltages. Most of the recent studies are focused on the metal-semiconductor interface studies, such as un-activated Mg-doped GaN layers [144, 145], interface states effects in Pt/n-GaN Schottky diodes [146] and dielectric/GaN heterojunctions [139]. Generally a large dark current is due to a high-density

Table 2.2: Comparing major progress of III-Nitride with ZnO, SiC, Diamond Schottky photodiodes

Materials	Responsivity (A/W)	UVRR	J_d (A/cm^2)
GaN/GaN [138]	0.09 at 0V (λ=360 nm)	2x10^6	—
GaN/Sapp. [139]	0.015 at 0V (λ=360 nm)	4x10^5	51x10^{-9}at -3V
AlGaN/Sapp. [140]	0.13 at -20V (λ=272 nm)	—	1x10^{-6}at 20V
AlInN/Sapp. [141]	0.14 at 0V (λ=230 nm)	—	12x10^{-6} at -5V
AlN/n-SiC [142]	0.12 at 0V (λ=200 nm)	1x10^4	1.27x10^{-8} at -50V
ZnO [143]	2.6x10^3 at 5V (λ=200 nm)	1x10^4	4x10^{-6} at -5V

threading dislocations and high background carrier concentration. To reduce the dark current, an insulation layer between the Schottky contact and the active layer can be used. Sang et al. [147] proposed to use a deposited CaF_2 layer on InGaN material. The dark current of the PD was reduced by six orders of magnitude compared with those without CaF_2 layer, with a value of the internal gain equal to 40. Using a less complex process, Lee et al. [148] used a thin low-temperature GaN cap layer on top of undoped GaN layer and below the Schottky contact. In this case, the dark current of the PD was reduced by four orders of magnitude compared with those without cap layer, but without any internal gain. In the context of this work, we took the initiative to use a BAlGaN alloy grown on both GaN and AlN templates in an attempt to fabricate a solar blind MSM PD on these materials. Instead of using the approach of insulation layer between the Schottky contact and the active layer, we aim to develop large internal gain MSM PD with reduced dark current based on GaN-type active layer with low electrical conductivity. To achieve this purpose, we show that, by using BGaN or quasi-alloy of BGaAlN superlattices (SL) as an active layer, the dark current can be lowered with keeping high DC internal gain (up to 10^5 for optical power in the nW range) and low time response (few tens ns) in AC regime. Moreover, thank to the boron incorporation, the UV cutoff wavelength can be also tuned.

2.2.5 Metal-Semiconductor-Metal Photodetector

In the past few years, MSM photodetectors became very popular in the field of optical communications because of their numerous advantages. One of its most advantageous properties results in extremely low capacitance, which matches the requirements of high-

speed performance very well. It is one of the simplest photodetectors in terms of epitaxial growth and fabrication, geometry convenience, speed, and not requiring p-n junctions. The lateral and planar structure of these devices consists of interdigitated back-to-back Schottky metal contacts on the top of an active layer. Therefore, compared to other photodetectors the MSM structure is an attractive candidate for UV photodetectors, due to its fabrication simplicity, need of a single active layer, low dark current, potential to achieve high quantum efficiency. It has been realized in materials such as AlGaN/GaN [149,150]. Furthermore, the fabrication process for MSM photodiodes is compatible with field effect transistors, which makes them suitable for integration in an optical detection and amplifier [151]. A typical schematic diagram of such an MSM structure, and the energy band diagram under applied bias is depicted in figure 2.12. When a bias voltage

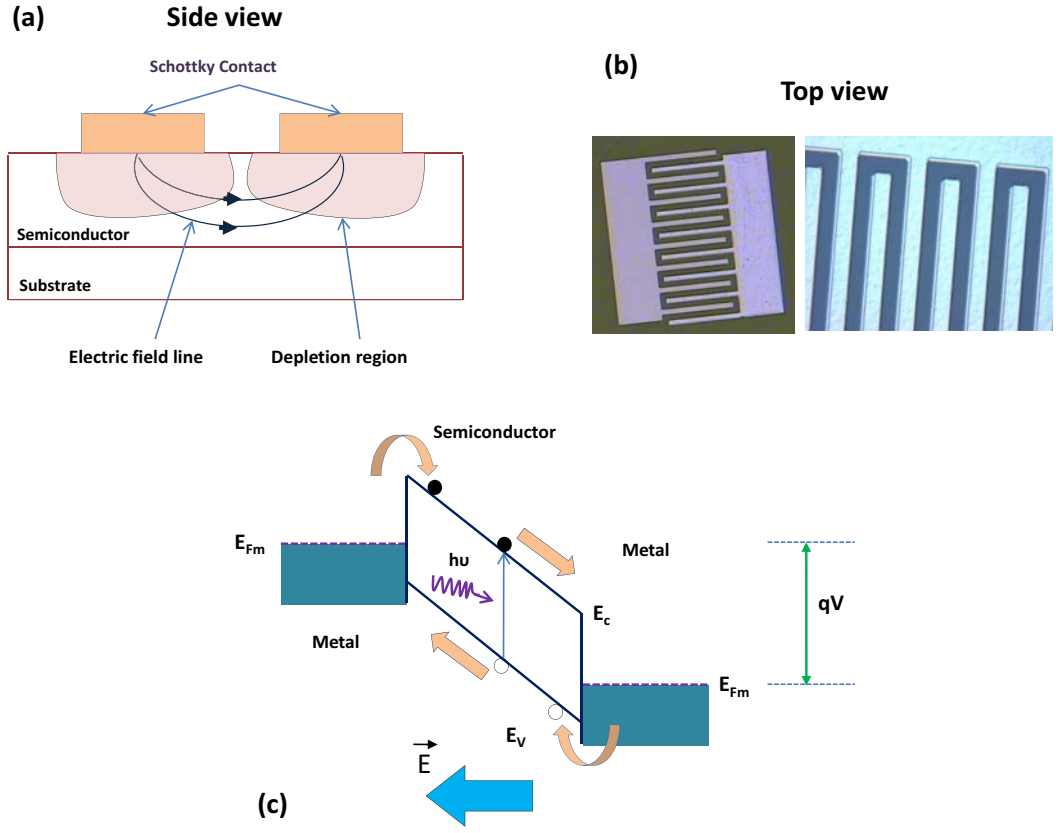

Figure 2.12: *Schematic representation of a typical MSM detector structure, (a) Side view, (b) Top view, (c) Energy band diagram of MSM photodiode under bias.*

is applied to the contact pads, one of the diodes is forward biased and the other is reverse biased. Since it is a unipolar device one of the junctions will always be reverse biased. Therefore, current is not allowed to pass in each direction [152]. As the applied voltage increases, the sum of space-charge regions also increases. At reach-through voltage, the

two depletion regions touch each other, so that the area between the electrodes become fully depleted. The maximum voltage that can be applied to the MSM structure is limited by the avalanche breakdown. When the semiconductor absorbs an incident photon (figure 2.12(c)), an electron-hole pair is created. The electron and the hole are spatially separated and accelerated under the influence of the applied electric field until they reach the metal contacts where they enter the biasing electrical circuit. The carriers are transported to the contact pads under the applied voltage. Thus, the device detects photons by collecting electric signals generated by photo-excited electrons and holes in the semiconductor, which drift under the electrical field applied between the fingers. Figure 2.13 shows the current-voltage characteristics of Schottky diodes obtained on two GaN MSM detectors, one having been fabricated by using a 1.5 mm thick and the other by using a 4.0 mm thick GaN grown by MOVPE on sapphire substrates, which exhibits Hall measured n-type carrier concentrations of about $6x10^{16}cm^{-3}$. At low voltage, Schottky diodes exhibited current densities in the mid-$10x10^{-6}Acm^{-2}$ range [153], with detectors fabricated on 4.0 mm thick GaN showing markedly improved I-V characteristics. The dashed line in figure 2.13 shows calculations assuming that the current transport is due to either thermionic emission [154] or thermionic fieldemission including tunneling currents [12], see chapter 3, for details. The MSM detector arena has been expanded to include AlGaN-based

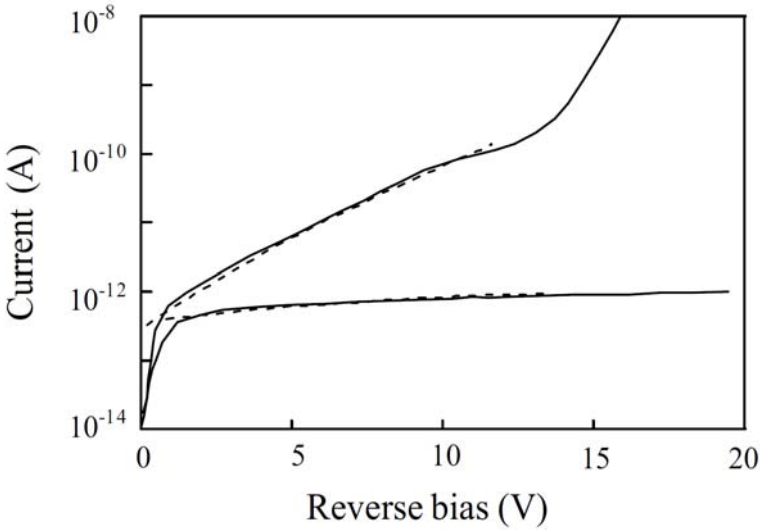

Figure 2.13: *Current-voltage characteristics of Schottky diodes fabricated on GaN epitaxial layers of different thicknesses. The upper curve is for the case of 1.5 mm thick GaN while the lower is for 4.0 mm thick GaN. The dashed lines represent calculations [153].*

photodiodes with two interdigitated Ni/Au Schottky contacts deposited on 1 mm thick

$Al_xGa_{1-x}N$ with unintentionally doped epitaxial layers, and 2, 4, and 7 mm finger widths and spacing [122]. The optical area of the devices investigated ranged from (250x250 μm^2) to (1x3 μm^2). The normalized spectral response of AlGaN MSM photodiodes for various AlN molar fractions and bias voltages is shown in figure 2.14. The responsivity is

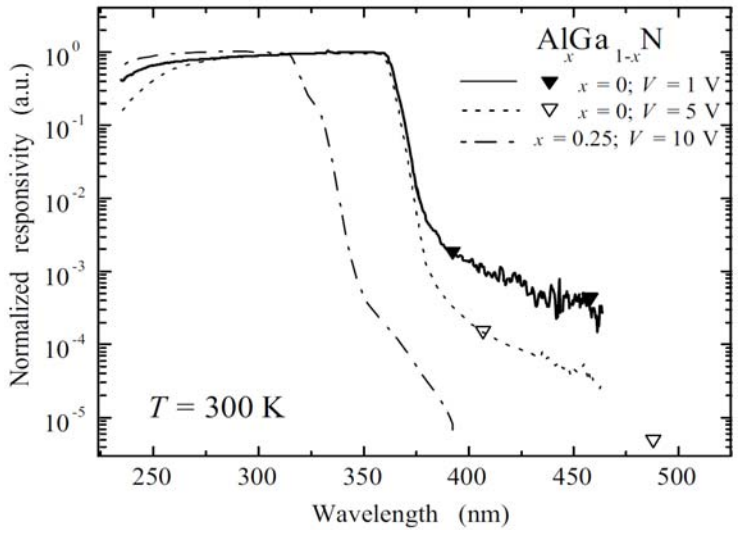

Figure 2.14: *Spectral response of AlGaN MSM photodiodes, measured under different bias. Triangles were obtained with the 458 and 488 nm lines of an Ar^+ laser [155].*

relatively flat over the band gap and the cutoff wavelength shifts to shorter wavelengths with increasing AlN molar fraction [155]. A UV/visible rejection ratio of four to five orders of magnitude is observed. The variation of the responsivity with bias has also been investigated for diodes of different sizes for excitation above the band gap, and the results are shown in figure 2.15. For $V_B < 2$V, the responsivity scales sublinearly with bias ($R_\lambda \propto V_B^{0.7}$), which fits the theoretical behavior expected for an MSM photodiode in the absence of gain and calculated from a one-dimensional model (solid line). An abrupt increase of the responsivity is observed between 2 and 5 V, indicative of a bias activated gain mechanism that saturates for higher bias voltages. This behavior is independent of the finger width and the gap spacing, as also shown in figure 2.15. The gain mechanism at high bias was also wavelength dependent [137]. For wavelengths corresponding to below bandgap response, the detectors follow the trend expected for an MSM photodiode in the absence of gain. Gain in interdigitated MSM photodiodes has been attributed to different mechanisms [157,158]. The most often suggested mechanism consists of electron tunneling enhanced by trap-mitigated hole accumulation at the cathode. Trapping at surface states or dislocations produces persistent photoconductivity effects and a sublinear behavior

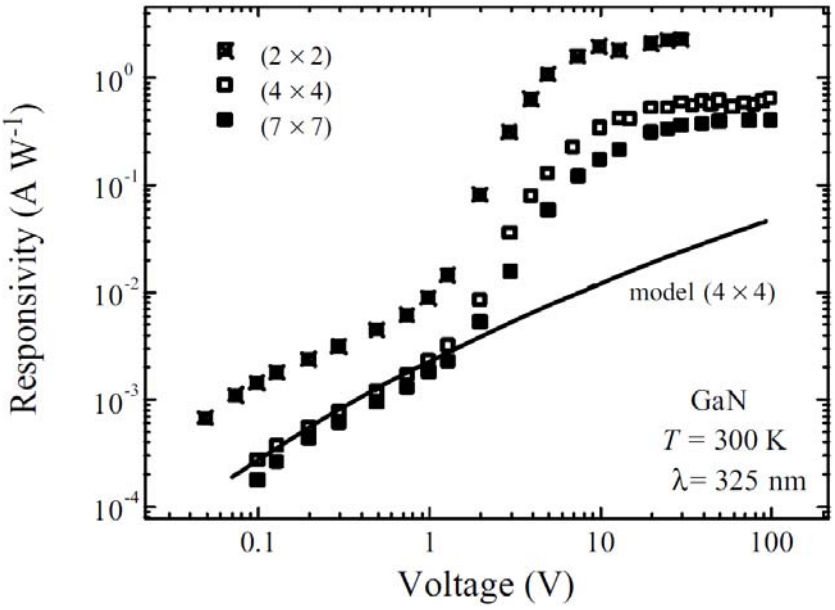

Figure 2.15: *Responsivity dependence on bias for GaN MSM photodiodes, measured with an excitation wavelength of 325 nm, which is above the band gap. Performances of three sizes of devices with finger widths and spacings of 2x2, 4x4, and 7x7 μm^2 in an active area of 250x250 μm^2 are shown. The model calculations of the responsivity for the 4x4 μm^2 active area are also shown with the solid line [137, 156].*

with optical power, degrading the spectral response.

Monroy et al. [159] reported that for a given detector area, there is an optimum finger separation for the maximum speed of response as shown in figure 2.16. The estimates agree well with experimental data of Carrano et al. [160] for 50x50 μm^2 devices with gap spacings of 2 and 10 mm.

2.2.6 Gain mechanism in Schottky and Metal-Semiconductor-Metal photodetector

As already shown in tables 2.2, 2.3 and 2.1 recently high-quality III-Nitride based MSM, Schottky barrier and p-i-n photodiodes have been reported. Photodiodes based on the Schottky-barrier junction, such as MSM and Schottky barrier photodiodes, have the advantages of high response speeds and simple fabrication processes that are compatible with Field Effect Transistor (FET) technology. Schottky and MSM PDs are not expected to exhibit gain, but internal photocurrent gain is sometimes observed in these photodetectors. While several physical mechanisms have been proposed for the explanation of

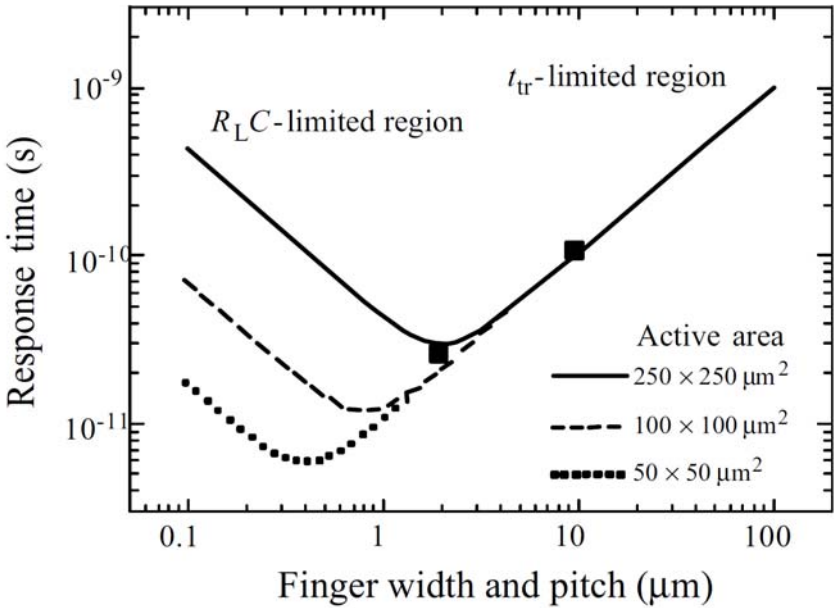

Figure 2.16: *Calculated time response of GaN MSM photodiodes as a function of finger separation for devices with various active areas. A saturation velocity v_{sat} of 107 cm s^{-1} is assumed [159]. The experimental data points are from Ref. [160].*

Table 2.3: Comparing the major progress of III-Nitride with ZnO, SiC, and Diamond MSM photodiodes.

Materials	Responsivity (A/W)	UVRR	J_d(A/cm^2)	Gain
GaN/Sapp. [144,161]	0.017 at -0.5V(λ=350nm)	1.44x10^4	—	—
GaN/Sapp. [161]	0.132 at 5V(λ=350nm)	—	2.5x10^{-3}(-10V)	—
GaN [162]	94 at 5V(λ=365nm)	—	3x10^{-7}	50
ZnO [163]	27x10^3 at 8V	300	50 (10V)	10^4
$Al_{0.25}Ga_{0.75}N$ [164]	70A/mW (100V)(λ=312nm)	10^4	5x10^{-8}	—
InGaN [165]	0.24 (λ=390 to 360 nm)	7.11x10^3	1.21x10^{-13}	—
$Mg_{0.4}Zn_{0.6}O$ [166]	1.3 at 3V(λ=320nm)	—	40x10^{-9}	—
SC-Diamond [167]	100 at 90V(λ=210nm)	1x10^6	8.8x10^{-6}	—
Al_2O_3/SiO_2/4H-SiC [168]	0.12 at 20V(λ=290nm)	—	7.5x10^{-6}A	—

such gain, most of the authors [147,162,163,169–175] attribute the gain phenomenon to the existence of trapping states at the active layer-metal interface, caused by long-lifetime traps located either within the barrier-enhancement layer or at the heterointerface. In

GaN-type materials, these traps are generally attributed to threading dislocations, having acceptor-like nature [147]. These interface states can trap photogenerated holes, thus reducing the Schottky barrier height (SBH) and producing a secondary photocurrent as shown in figure 2.17. Another theory is that when photogenerated holes are accumu-

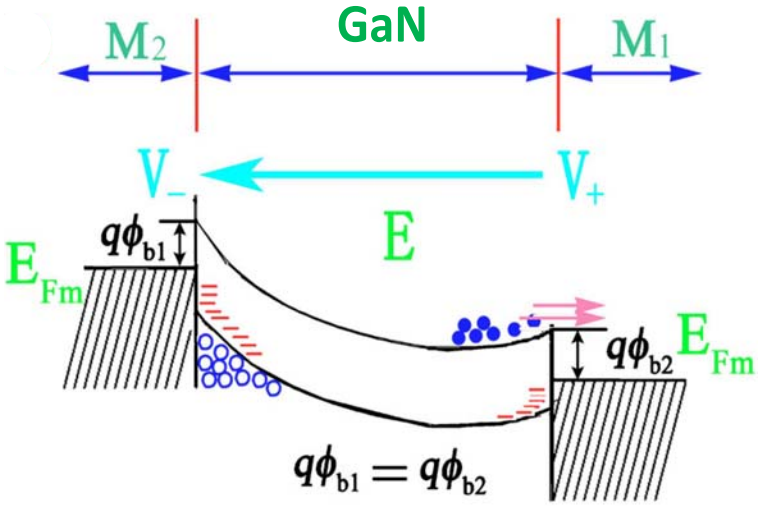

Figure 2.17: *Trapping states at the active layer-metal interface, which under illumination, can trap photogenerated holes, leading to a Schottky barrier height decrease* $\Delta\Phi_B$ *and producing a secondary photocurrent.*

lated at the valence-band peak near the cathode, these positive charges increase the field across the wide-energy-gap barrier-enhancement layer and induce a larger electron tunneling current. A similar effect can be true for electrons accumulated near the anode, and the hole tunneling current is enhanced. More recently, Katz et al. [162] reported on persistent photoconductivity in GaN Schottky photodetectors. Gain saturation and persistent photoconductivity were observed and modeled theoretically. The two effects were shown to be related and arising from the modification of Schottky barrier height from carrier trap-related effects at the Schottky junction interface. Under illumination, these interface states can trap photo-generated holes, leading to a Schottky barrier height (SBH) decrease $\Delta\Phi_b$ and producing a secondary photocurrent [162] I_λ^G:

$$I_\lambda^G = I_d e^{\frac{\Delta\Phi_b}{kT}}, \tag{2.19}$$

where I_d is the dark current in the structure, leading to a gain in the PD. This secondary current appears in addition to the "true" photocurrent generated by the photodetector

given by:

$$I_\lambda = q \times S \times P \left(1 - exp\left(-\alpha\sqrt{\frac{2\epsilon(V_{bi} - V)}{qN_D}}\right)\right) \tag{2.20}$$

where q is the electronic charge, S is the area of the contact, P is the optical power, α is the optical absorption coefficient at the corresponding excitation wavelength λ, V_{bi} is the built in potential of the diode, V is the external applied voltage and ϵ is the semiconductor dielectric constant. The total current I_{illum} produced by the device is then the sum of I_λ^G and I_λ, and thus, the responsivity R of the detector, according to equations 2.19 and 2.20, can be written as:

$$R = \frac{I_{illum} - I_d}{P} = \frac{\left(exp\frac{\Delta\Phi_b}{kT} - 1\right) I_d + I_\lambda}{P} \tag{2.21}$$

Figure 2.18 (a) and (b) shows the responsivity variation between the experimental and theocratical model of Schottky and MSM PDs respectivily. Normally, in Schottky diode the experimental responsivity variation obtained by Katz [162] is always expected, while for theoretical model responsivity in reverse bias is more candidate than in the forward bias. In contrary, for MSM both of experimental and theoretical are expected and our experimental work reveals a responsivity variation very closely to the experimental work obtained by Katz et al. [162].

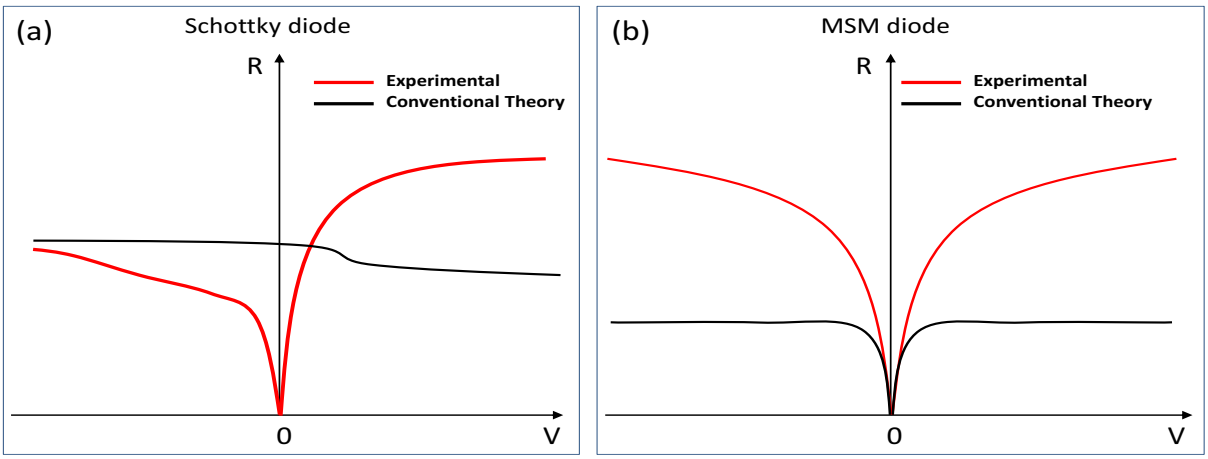

Figure 2.18: *Voltage dependence of the responsivity in Schottky and MSM PDs based on the model proposed by Katz et al. [162].*

Chapitre 3

Réalisation du composant caractérisations

Sommaire

3.1 Introduction 58

3.2 Contacts métal-semiconducteur 58

3.2.1 Diagrammes de bande d'énergie 58

3.2.2 Mécanismes de transport 61

3.3 Réalisation du composant 68

3.3.1 Procédé de photolithographie 69

3.3.2 Dépôt de métal 73

3.3.3 Microcâblage 77

3.4 Caractérisation des dispositifs: mesures électriques 79

3.4.1 Contacts ohmiques 79

3.4.2 Techniques Van der Pauw et Hall 90

3.4.3 Contacts Schottky 92

3.5 Mesures électro-optiques 96

3.5.1 Mesures de la sensibilité 96

3.5.2 Mesures de photocourant resolues en temps 100

Chapter 3

Device processing and characterizations

Contents

3.1 Introduction 58

3.2 Metal-semiconductor contacts 58

3.2.1 Energy band diagrams 58

3.2.2 Current transport mechanisms 61

3.3 Device processing 69

3.3.1 Photolithography process 70

3.3.2 Metal deposition 74

3.3.3 Wire bonding 77

3.4 Device characterization: Electrical measurements 79

3.4.1 Ohmic contacts 79

3.4.2 Van der Pauw and Hall effects 90

3.4.3 Schottky contacts 92

3.5 Electro-optical measurements 96

3.5.1 Quantum efficiency measurements 96

3.5.2 Time resolved measurements of the photocurrent 100

3.1 Introduction

The objective of this chapter is to provide an overview of the basic theory of metal-semiconductor contacts. First the energy band diagrams of both ideal and practical metal-semiconductor contacts will be considered. Second, the current transport processes, which govern the conduction properties of these contacts, will be discussed. Furthermore, we will address in detail the technological process used to fabricate the Schottky barrier and MSM photodetector. Finally, we will characterize the obtained devices by using electrical and optical measurements. All the information in this chapter is broadly referenced from [12,176–179]. The earliest systematic investigation on metal-semiconductor rectifying systems is generally attributed to Braun, who in 1874 noted the dependence of the total resistance of a point contact on the polarity of the applied voltage and on the detailed surface conditions [180]. The point-contact rectifier in various forms found practical applications beginning in 1904 [181]. In 1931, Wilson formulated the transport theory of semiconductors based on the band theory of solid [182]. This theory was then applied to metal-semiconductor contacts. In 1938, Schottky suggested that the potential barrier could arise from stable space charges in the semiconductor alone without the presence of a chemical layer [183]. The model arising from this consideration is known as the Schottky barrier. In 1938, Mott also devised a more appropriate theoretical model for swept-out metal-semiconductor contacts that is known as the Mott barrier. These models were further enhanced by Bethe in 1942 to become the thermionic-emission model which accurately describes the electrical behavior [184].

3.2 Metal-semiconductor contacts

3.2.1 Energy band diagrams

In this section we will consider the energy band diagrams of two limiting cases of the metal-semiconductor contact. The first limiting case is that of an ideal contact between a metal and a n-type semiconductor in the absence of surface states. The second limiting case is that of a practical contact between a metal and a n-type semiconductor, where a thin interfacial layer with an infinitely large density of surface states is present on the semiconductor surface. Figures 3.1 and 3.2 show the energy band diagrams for the first and the second limiting case respectively. Figure 3.1 (a) shows the flat band situation for a semiconductor without a surface layer and surface states. When a metal is

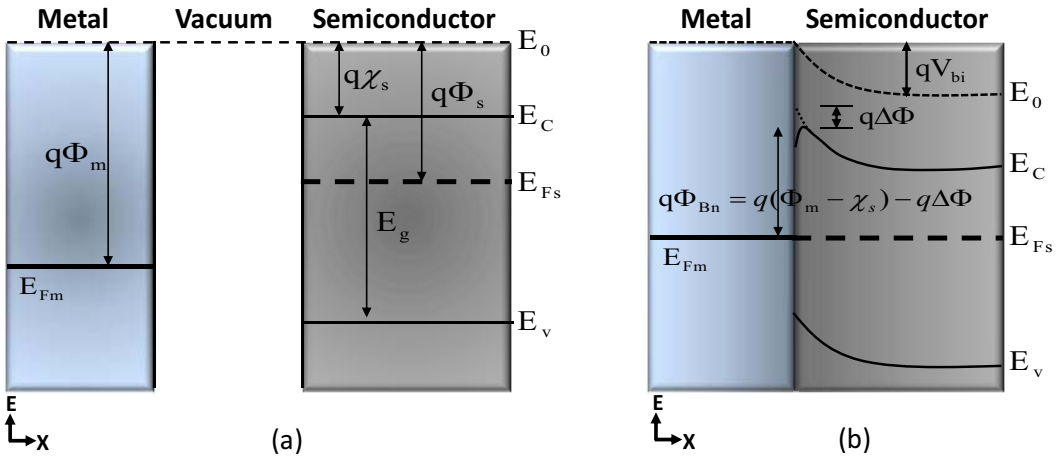

Figure 3.1: *Energy band diagrams of a metal-semiconductor contact without an interfacial layer and surface states before (a) and after (b) intimate contact under thermal equilibrium.*

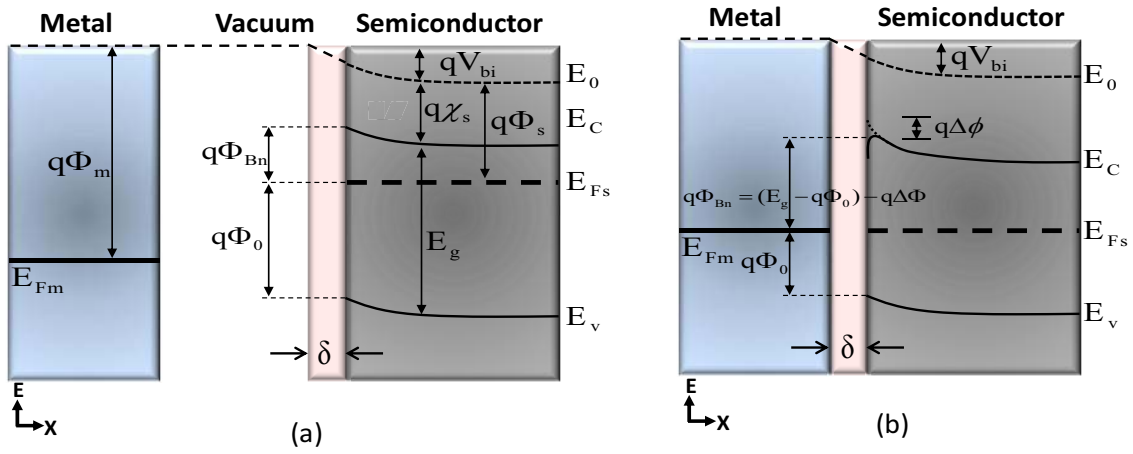

Figure 3.2: *Energy band diagrams of a metal-semiconductor contact with a thin interfacial layer δ and a large density of surface states before (a) and after (b) intimate contact under thermal equilibrium.*

placed in intimate contact with such a semiconductor, the conduction E_c and valence E_v energy bands have to bend in order to reach thermal equilibrium. In the case of thermal equilibrium (no external voltages are applied, no currents are induced, no temperature gradients are present), the Fermi levels in the metal and the semiconductor are at an equal level ($E_{Fm} = E_{Fs}$). Figure 3.1 (b) shows the barrier that has been formed at the metal-semiconductor interface after establishing thermal equilibrium. Figure 3.2 (a) shows the energy band diagram of a semiconductor with a thin surface layer e.g. a native oxide and a large density of surface states. If a metal is placed into contact

with such a semiconductor, the physics of the junction are not governed by the bulk properties of the metal and semiconductor material but by the properties of the surface boundaries and primarily those of the semiconductor surface [177]. The strong influence of the semiconductor surface is due to the surface states that are present inside the band gap. In this case it is possible to define a neutral level Φ_0 that represents the position of the Fermi level in the case that the semiconductor surface is electrically neutral. If the surface states below Φ_0 are empty the semiconductor surface will be positively charged and if surface the states above Φ_0 are filled the semiconductor surface will be negatively charged. If the Fermi level at the surface does not coincide with the neutral level Φ_0 there will be a net charge at the surface. This charge produces an electric field ($\vec{E}$) in the semiconductor which causes the energy bands to bend. If the surface charge is negative, as is the case for practical n-type $Al_xGa_{1-x}N$ layers [185], the energy bands will bend upwards towards the surface. As a consequence, the semiconductor material near the surface is already depleted before it has been brought into contact with the metal as can be observed in Figure 3.2 (a). This figure also shows that the energy levels of the surface states are occupied with electrons up to E_{Fs}, which in the case of an infinitely large density of surface states equals Φ_0, in order to establish thermal equilibrium between the surface states and the bulk of the semiconductor material. Figure 3.2 (b) shows the energy band diagram of such a practical metal-semiconductor contact.

If no surface states are present, the height of the potential barrier, which the electrons have to overcome if they flow from the metal into the semiconductor, is ideally equal to the difference between the metal work function Φ_m and the semiconductor electron affinity χ_s. Actually, the image-force-induced lowering of the barrier height in the case of an applied electric field $\vec{E}$, which is known as the Schottky effect, should also be taken into account. The value of the resulting barrier height Φ_{Bn} is then given by:

$$q\phi_{Bn} = q(\Phi_m - \chi_s) - q\Delta\Phi \tag{3.1}$$

where $\Delta\Phi$ represents the Schottky barrier lowering. In the case of a metal-semiconductor system $\Delta\Phi$ is given by [12]:

$$\Delta\Phi = \sqrt{\frac{qE}{4\pi\epsilon_0\epsilon_{r,s}}} \tag{3.2}$$

where E is the maximum electric field at the interface, ϵ_0 the permittivity of free space and $\epsilon_{r,s}$ is the relative permittivity of the semiconductor material. The observed change of the band gap of the semiconductor material at the metal-semiconductor interface compared to that in the bulk of the semiconductor could be explained by the distortion of the

periodicity of the potential function of the atoms near this interface. If the density of the surface states is infinitely large, the barrier height Φ_{Bn} and as a consequence the energy band diagram change only very little after placing the metal into intimate contact with the semiconductor. Thermal equilibrium between the two materials will be established by a small drop of the semiconductor Fermi level relative to that of the metal. The drop of E_{Fs} is small because the electrons, which are required for this process, are provided by the occupied surface states below E_{Fs}. In this case the Fermi level at the interface is "pinned" by the surface states at a value $q\Phi_0$ above the valence band E_v. The barrier height Φ_{Bn} is independent of the metal work function Φ_m and is entirely determined by the doping and surface properties of the semiconductor. If again the Schottky effect is taken into account, the resulting barrier height is given by [12]:

$$q\phi_{Bn} = q(E_g - q\Phi_0) - q\Delta\Phi \tag{3.3}$$

3.2.2 Current transport mechanisms

The current transport in metal-semiconductor contacts is mainly due to majority carriers, in contrast to p-n junctions where it is the minority carriers that are responsible of the transport. Figure 3.3 shows the four basic transport processes under forward bias for a metal-n-type semiconductor contact. The inverse processes occur under reverse bias. The mechanisms are [177]:

1. Emission of electrons from the semiconductor over the top of the barrier into the metal.
2. Quantum mechanical tunneling of electrons from the semiconductor through the barrier into the metal.
3. Recombination of electrons and holes in the depletion region.
4. Recombination of electrons and holes in the neutral region ("hole injection").

3.2.2.1 Emission over the barrier

The emission of electrons from the semiconductor over the top of the potential barrier into the metal can be described by two basic mechanisms, which in fact are two limiting cases. For high mobility semiconductors the transport can be adequately described by the thermionic emission theory. The transport in low mobility semiconductor material can

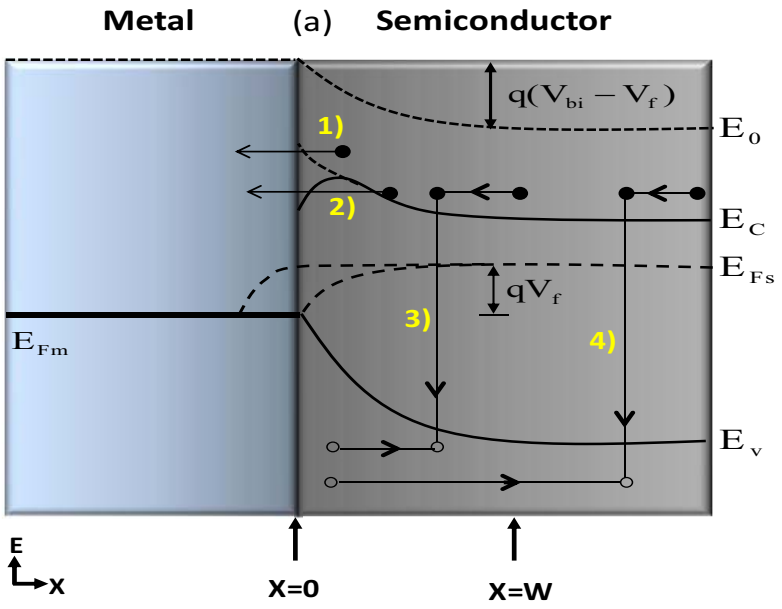

Figure 3.3: *Four basic transport processes under forward bias.*

be understood using the diffusion theory. In practice, the true behavior of the transport process will lie somewhere between these two extremes of the thermionic emission theory and the diffusion theory. This consideration has led to the development of the combined thermionic emission-diffusion theory. In the following subsection we will describe the thermionic emission theory combined with the effect of the image force on the current-voltage relationship and the tunneling through the barrier.

3.2.2.2 Thermionic emission theory

The thermionic emission theory by Bethe (1942) is derived from the assumptions [12] that:

- The barrier height $q\Phi_{Bn}$ is much larger than k_BT, where k_B is the Boltzmann factor and T is the absolute temperature.
- Thermal equilibrium is established at the plane that determines emission.
- The existence of a net current flow does not affect this equilibrium, so that the two current fluxes, one from the semiconductor to the metal and one from the metal to the semiconductor, can be superimposed.
- The current-limiting process is the actual transfer of the electrons across the interface between the semiconductor and the metal.

- The width of the region over which a k_BT drop in potential energy occurs at the barrier should be smaller than the electron mean free path.

According to these assumptions the shape of the barrier profile is immaterial and the current flow depends only on the barrier height. Hence, if the thermal energy of an electron is sufficiently high to surmount the potential barrier, this transport process is called thermionic emission. In the case of thermal equilibrium the electron flow from the semiconductor into the metal is equal to that from the metal into the semiconductor. As a consequence, the total current density $\vec{J}$ across the interface is equal to zero because the current densities in reverse and forward direction cancel each other out. If a forward bias voltage $V_f > 0$ is applied, the Fermi level in the semiconductor shifts to a higher energetic level with respect to the Fermi level in the metal by an amount of qV_f. As a result, the barrier height for electron flow from the semiconductor into the metal, which is determined by the built-in voltage V_{bi}, is lowered. The current density in forward direction is now larger than that in reverse direction because e1ectrons with smaller thermal energies can also surmount the potential barrier. If a reverse bias voltage $V_r < 0$ is applied, the Fermi level in the semiconductor shifts to a lower energetic level with respect to the Fermi level in the metal by an amount of qV_r. The barrier qV_f in the semiconductor is enlarged and the current density in forward direction falls below that in reverse direction. It has to be noted that the current density in reverse direction is independent of the polarity of the applied bias and remains constant because the barrier for e1ectrons flowing from the metal into the semiconductor $q\Phi_{Bn}$ remains unchanged. The total current density according to the thermionic emission theory is given by [12,177]:

$$J = J_s \left[exp\left(\frac{qV}{k_BT} - 1\right)\right] = A^*T^2 exp\left(-\frac{q\phi_{Bn}}{k_BT}\right)\left[exp\left(\frac{qV}{k_BT} - 1\right)\right] \tag{3.4}$$

$$J_s = A^*T^2 exp\left(-\frac{q\phi_{Bn}}{k_BT}\right) \tag{3.5}$$

$$\phi_{Bn} = -\frac{k_BT}{q} ln \frac{J_s}{A^*T^2} \tag{3.6}$$

where A^* is the Richardson constant, T the absolute temperature, q the electron charge, k_B is the Boltzmann's constant, ϕ_{Bn} is the barrier height to electron flow from the metal into the semiconductor, V the applied voltage across the barrier and J_s is the saturation current density according to the thermionic emission theory.

The current-voltage relationship predicted by the thermionic emission theory (equation 3.4) has the form of an ideal rectifier characteristic, provided that the barrier height is independent of bias. However, there are several reasons why the barrier height depends on

the electric field in the depletion region and hence on the applied bias. In particular, even in an ideal contact with no interfacial layer, the barrier height is reduced as a result of the image force by an amount $\Delta\Phi$ which depends on the bias voltage. If a forward bias voltage $V_f > 0$ is applied, the barrier height is larger than at zero bias. However, if a reverse bias voltage $V_r > 0$ is applied the barrier height is smaller than at zero bias. The effective barrier that e1ectrons have to surmount before they can reach the metal is therefore given by Φ_e=Φ_{Bn}-$\Delta\Phi$. Moreover, in the presence of an interfacial layer the barrier height Φ_{Bn} depends on the bias voltage. The bias dependence of Φ_e is very important with respect to the reverse current-voltage characteristics of a Schottky diode and it will consequently modify these current-voltage characteristics and is given by:

$$\Phi_e = (\Phi_e)_0 + \frac{\partial \Phi_e}{\partial V} V \tag{3.7}$$

with

$$(\Phi_e)_0 = (\Phi_{Bn})_0 - (\Delta\Phi)_0 \tag{3.8}$$

where $(\Phi_e)_0$, $(\Phi_{Bn})_0$ and $(\Delta\Phi)_0$ refer to the effective Schottky barrier height, the uncorrected barrier height and the image-force-induced barrier lowering at zero bias respectively. Assuming that Φ_e/V is constant, the effective barrier height is given by [186]:

$$\Phi_e = (\Phi_{Bn})_0 - (\Delta\Phi)_0 + \beta V \tag{3.9}$$

where the coefficient β is positive because Φ_e always increases with increasing forward bias. Inserting equation 3.9 in the current - voltage relationship of the ideal rectifier gives:

$$J = A^* T^2 exp\left(-\frac{q((\Phi_{Bn})_0 - (\Delta\Phi)_0 + \beta V)}{k_B T}\right)\left[exp\left(\frac{qV}{k_B T}\right) - 1\right] \tag{3.10}$$

$$J = J_s exp\left(-\frac{q\beta V}{k_B T}\right)\left[exp\left(\frac{qV}{k_B T}\right) - 1\right] \tag{3.11}$$

where

$$J_s = A^* T^2 exp\left(-\frac{q((\Phi_{Bn})_0 - (\Delta\Phi)_0)}{k_B T}\right) \tag{3.12}$$

Equation 3.11 can be written as:

$$J = J_s exp\left(\frac{qV}{nk_B T}\right)\left[1 - exp\left(-\frac{qV}{k_B T}\right)\right] \tag{3.13}$$

where

$$\frac{1}{n} = 1 - \beta = 1 - \frac{\partial \Phi_e}{\partial V} \tag{3.14}$$

n is called the ideality factor. If Φ_e/V is constant, n is still constant too. For values of V larger than $3k_BT/q$, equation 3.13 can be written as:

$$J = J_s \left[\exp\left(\frac{qV}{nk_BT}\right) - \exp\left(\frac{\left(\frac{1}{n} - 1\right) qV}{k_BT}\right) \right] \tag{3.15}$$

Equation 3.15 has the advantage that n can be determined experimentally by plotting ln[J/ (1 - exp(-qV/k_BT))] versus V. This graph should be a straight line with a slope of q/nk_BT if the ideality factor n is constant, even for $V < 3k_BT/q$ and for reverse bias [186]. In practice however, Φ_e/V is not constant and the plot of ln[1/ (1 - exp(-qV/k_BJ))] versus V is not linear. The ideality factor defined by equation 3.14 is in that case a function of the bias. However, it is still a useful concept which can be determined from the experimentally obtained current-voltage characteristic through the relationship:

$$n = \frac{q}{k_BT} \left[\frac{\partial \left(log\left(\frac{I}{1 - exp\left(\frac{qV}{k_BT}\right)} \right) \right)}{\partial V} \right]^{-1} \tag{3.16}$$

When the interface states are in equilibrium with the semiconductor, the interface states density is related to the ideality factor by [186]:

$$N_{ss} = \frac{\epsilon_o \epsilon_i}{\delta q^2}(n - 1) - \frac{\epsilon_o \epsilon_{SC}}{q^2\ W}, \tag{3.17}$$

where W is the depletion width, ϵ_i is the relative dielectric constant of the interfacial layer with a thickness δ larger than 3 nm (condition for equilibrium between the interface states and the semiconductor [186]). Figure 3.4 shows the current-voltage (J-V) characteristics of a Schottky diode under reverse and forward bias according to equation 3.13. Furthermore, it shows the dependence of the (J-V) characteristics on the ideality factor n. It can be observed that as n increases, the Schottky diode becomes increasingly leaky and shows better conduction in the reverse than in the forward direction. Tunneling through the barrier is the basic process under forward bias for a metal-n-type semiconductor contact. Depending on the circumstances it may be possible for electrons with energies below the top of the potential barrier to penetrate the barrier by tunneling. This tunneling process modifies the ordinary thermionic emission process in one of the two ways which are shown in figure 3.5. The energy band diagrams in the case of field emission (FE) and thermionic field emission (TFE) respectively. In the case of a very highly doped (degenerate) region of the semiconductor material near the surface (figure 3.5 (a)), at low temperature the current in the forward direction is due to the tunneling of e1ectrons with energies close to the Fermi energy in the semiconductor. This is known as field

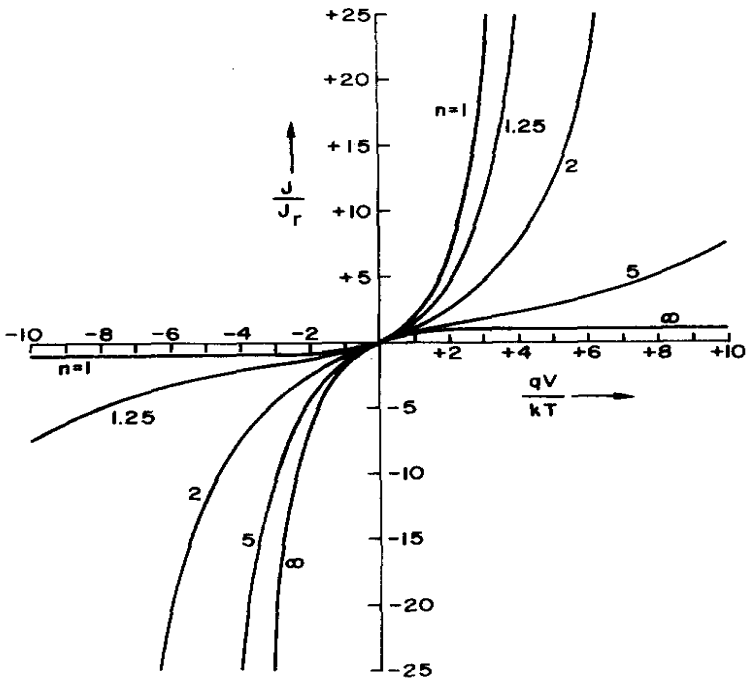

Figure 3.4: *Normalized current-voltage characteristic predicted by equation 3.15.*

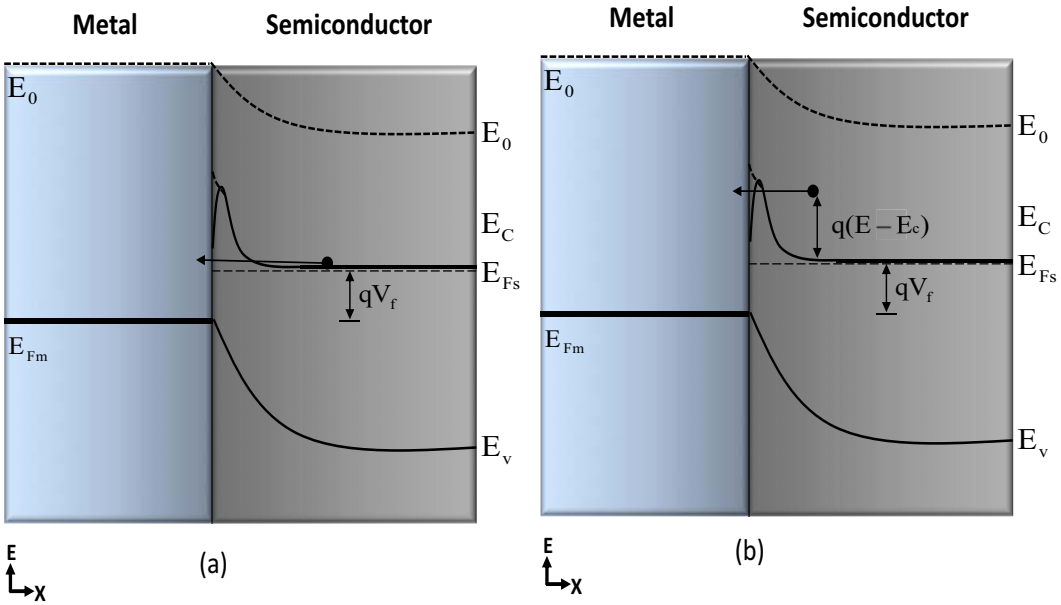

Figure 3.5: *Energy band diagrams in the case of field emission (FE) (a) and thermionic field emission (TFE) (b) under forward bias for a metal-n-type semiconductor contact.*

emission (FE). Field emission is of considerable importance with respect to ohmic contacts which usually consist of Schottky barriers on very highly doped semiconductor material. If the temperature is raised, electrons are excited to higher energies and the tunneling probability increases very rapidly because the electrons encounter a thinner and lower

potential barrier. In this case, electrons can tunnel through the barrier at a height E-E$_c$ above the bottom of the conduction band. This is known as thermally assisted tunneling or thermionic field emission (TFE). If the temperature is raised still further, a point is eventually reached in which virtually all of the electrons have enough energy to go over the top of the barrier. The effect of tunneling is then negligible and pure thermionic emission (TE) remains [12,186].

To arrive at a universal expression for the current densities in the different current transport mechanisms (TE, TFE and FE, respectively) we can use the ideality factor n introduced above. This universal equation is given by [178]:

$$J = J_s exp\left(\frac{qV}{nk_BT}\right)\left[1 - exp\left(-\frac{qV}{k_BT}\right)\right], \quad \begin{cases} n = 1 & \text{(TE) (a)} \\ 1 < n < 2 & \text{(TFE) (b)} \\ n \geq 2 & \text{(FE) (c)} \end{cases} \tag{3.18}$$

The conduction mechanisms for a metal-n-type semiconductor are illustrated in figure 3.6. For lightly-doped semiconductors the current flows as a result of thermionic emis-

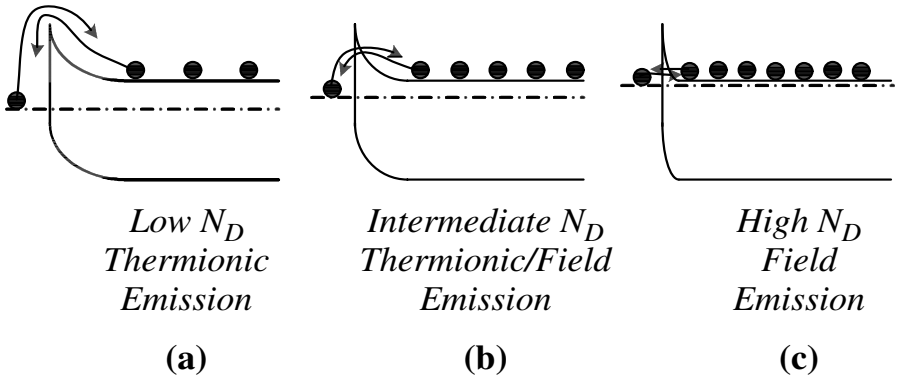

Figure 3.6: *Depletion-type contacts to n-type substrates with increasing doping concentrations. The electron flow is schematically indicated by the electrons and their arrows.*

sion (TE) shown in figure 3.6(a) with electrons thermally excited over the barrier. In the intermediate doping range thermionic-field emission (TFE) figure 3.6(b) dominates with carriers thermally excited to an energy where the barrier is sufficiently narrow for tunneling to take place. For high doping densities the barrier is sufficiently narrow at or near the bottom of the conduction band for the electrons to tunnel directly, known as field emission (FE) (direct tunneling dominates the current J_{tunn}) as shown in figure 3.6(c) [187], the three regimes can be differentiated by:

$$J_{TE} = A^*T^2 \times exp\left(-\frac{q(\Phi_e)_0}{k_BT}\right) \times exp\left(\frac{q(V-R_sI)}{nk_BT}\right) \times \left[1 - exp\left(\frac{q(V-R_sI)}{k_BT}\right)\right] \tag{3.19}$$

and

$$J_{TFE} = A^*T\frac{\sqrt{\pi E_{00}q(\Phi_e)_0 - V - \xi)}}{k_B\cosh(E_{00}/k_BT)} \times exp\left[\frac{q(V-R_sI)}{E_{00}\coth(E_{00}/k_BT)}\right] \times exp\left[-\frac{q\xi}{k_BT} - \frac{q((\Phi_e)_0 - \xi)}{E_{00}\coth(E_{00}/k_BT)}\right] \tag{3.20}$$

and

$$J_{FE} = AT^2\left(\frac{E_{00}}{k_BT}\right)^2\frac{\Phi_{Bn}-V}{\Phi_{Bn}}e^{\left(\frac{-2(q\Phi_{Bn})^{3/2}}{3E_{00}\sqrt{q\Phi_{Bn}-qV}}\right)} \tag{3.21}$$

where ξ is the Fermi level with respect to the conduction-band edge in an n-type semiconductor and with respect to the valence-band in a p-type semiconductor and E_{00} is the characteristic energy defined by:

$$E_{00} = \frac{qh}{4\pi}\sqrt{\frac{N}{\epsilon_{r,s}\varepsilon_0 m^*_{tun}}} = 1.86\times10^{-11}\sqrt{\frac{N(cm^{-3})}{\epsilon_{r,s}(\frac{m^*_{tun}}{m})}}[ev] \tag{3.22}$$

where h is planck's constant, N_D is the doping density, $\epsilon_{r,s}$ is the semiconductor dielectric constant, m^*_{tun} is the tunneling effective mass, and m the free electron mass. The effective barrier and ideality factor variations due to this tunneling effect are given respectively by [186, 188]:

$$\Delta\Phi_{tunn}(T) = (1.5\times E_{oo})^{\frac{2}{3}} \times V_{bi}^{\frac{1}{3}}(T) \tag{3.23}$$

and

$$n_{\text{tunn}}(T) = \frac{qE_{oo}}{k_BT}\coth\left(\frac{qE_{oo}}{k_BT}\right) \tag{3.24}$$

where V_d is the built-in voltage, $\hbar$ is the reduced Planck constant. Equation 3.22 is plotted in figure 3.7. A comparison of E_{00} to the thermal energy k_BT shows thermionic emission to dominate for $k_BT \gg E_{00}$, thermionic-field emission $k_BT \approx E_{00}$ and field emission for $k_BT \ll E_{00}$. For simplicity we have chosen the demarcation points on figure 3.7 as: for TE: $E_{00} \leq 0.5\ k_BT$, for TFE: $0.5\ k_BT < E_{00} < 5\ k_BT$, and for FE: $E_{00} \geq 0.5\ k_BT$. For practical matters it is generally assumed that if n is equal to unity, equation 3.18 (a) describes pure thermionic emission (TE). In the case of $1 < n < 2$, equation 3.18 (b) is assumed to describe thermionic field emission (TFE). Finally, in the case of $n \geq 2$, equation 3.18 (c) is assumed to describe field emission (FE) [178]. Hence, it can be concluded that if the thermionic field emission and field emission become increasingly dominant, the "ideality factor" will consequently increase.

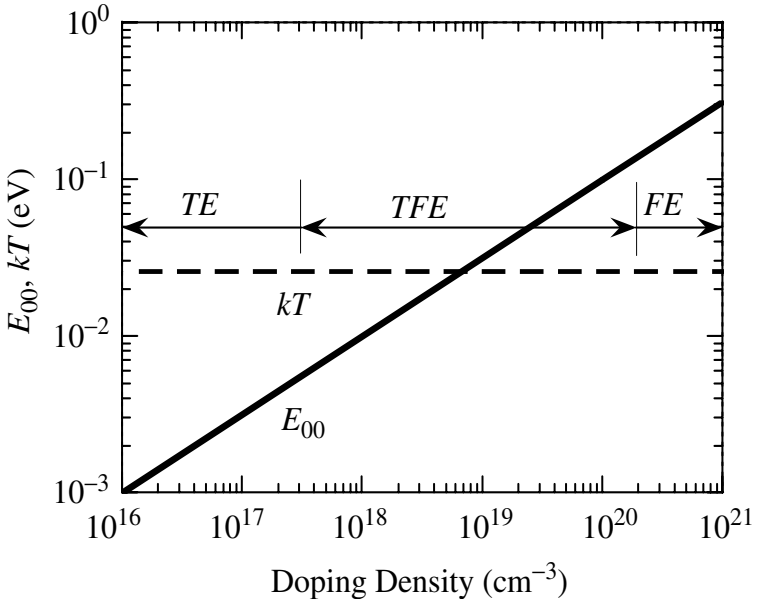

Figure 3.7: *E_{00} and k_BT as a function of doping density [187].*

3.3 Device processing

In this work, the ohmic contact used consists of four constitutive layers of (Ti/Al/Ti/Au-8/250/10/100 nm), and for schottky contact one layer of (Pt-150 nm). The primary contribution to the contact resistance is at the metal-semiconductor interface where tunneling and thermionic emission of the electrons must occur for the contact to be ohmic. It has been shown that Ti ions reacts with GaN to form TiN, leading to N vacancies in the GaN compound that acts as donors, thereby increasing the doping level at the metal-semiconductor interface. For having these contacts in geometrical form of interdigitated and circular photodiode, we need lithography process, surface chemical treatment, metal evaporation, mask, clean facilities and annealing at high temperature. In the following we will illustrate in details how we fabricate or build these photodiodes, for UV-PD applications, on GaN, BGaN, AlGaN, and BAlN-BGaAlN. As it is known the most important step in the lithographic process is the minimization of the defects, caused by particles either falling on the surface prior to epitaxy or during the steps of lithography. This is the reason why semiconductor processing is performed in ultra clean facilities, known as a cleanrooms, which uses sophisticated filtration such as filters employing laminar or turbulent air flow (figure 3.8) to remove airbone particulate. The cleanliness of a cleanroom is measured by the size and number of dust particles in a given volume of air. The photodetector fabrication was carried out in the Minalor Platform in the Institute Jean

Lamour (IJL) clean room facility (figure 3.9) at Nancy University.

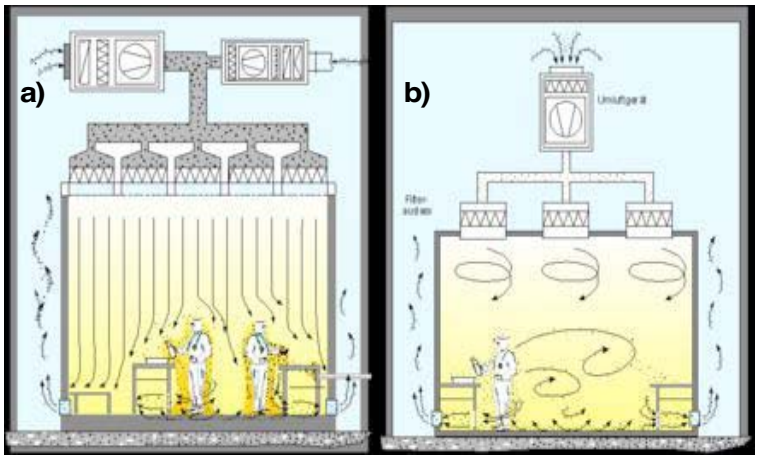

Figure 3.8: *a) Laminar air flow system, directly filter downward air in a constant stream towards filters located on walls near the cleanroom floor. b) Turbulent air flow which uses both laminar air flow hoods and non-specific velocity filters to keep air in a clearoom in constant motion*

Figure 3.9: *Minalor cleanroom facilities and equipments used in our device processing and fabrication. To the right is the "salle rouge" for doing lithography and to the left is the sputtering and thermal evaporator for doing metal deposition.*

3.3.1 Photolithography process

Nowadays several types of lithography techniques are used depending on the method used to activate the resist film. Currently the most widely used technique in microelectronics industry is the lithography which uses ultraviolet light and is called photolithography,

which is the same technique that we use in our process. To do so, the surface of the semiconductor must be carefully prepared prior to the resist deposition. In this section, we will describe in detail the photolithography method that we applied on our samples. We will address the sample preparation and chemical treatment used to clean the samples prior to any deposition, then followed by the photoresist implementation.

3.3.1.1 Sample preparation and chemical treatment

Surface preparation is an integral part of any fabrication or patterning process required in our experiments. Also it is one of the most important issues on semiconductor materials studies. The appropriate chemical etchants to clean the surface prior to the deposition of metal contact is the most important step, in particular for contacts. Figure 3.10(a) shows the effect of chemical treatment on the ohmicity of the contacts, where the current is significantly increased from 0.5 (before) to 2.5 (after) mA at 2V. Before processing the device fabrication on the samples, an optimized specific cleaning process is implemented for our experiments. This includes sample surface cleaning in acetone bath during 5 min to remove the presence of any organic residues, and unwanted inorganic as well, followed by isopropanol bath for 30 seconds, to remove acetone. It is well known that the nitrides materials form a thin film of GaO when exposed to air. The (1:2 HCL:H2O) etching during 5 minutes has been shown to be successful and effective in removing a large amount of the surface oxide as shown in figure 3.10(b). A one minute of de-ionized water rinse is the final step of the surface sample preparation and finally samples are blown dry with nitrogen flux.

3.3.1.2 Photoresist parameters

In the photolithography process, the resist is called photoresist, it is a photosensitive material, made of three main components: a resin or base material, a photo-active compound and an organic solvent. They are used to transfer the image of the mask to the wafer surface of oxides, metals, and semiconductors materials. It can be of either of two types: positive and negative photoresist depending on its chemistry which determines its property when exposed to light. They can be more or less easily dissolved using a developing solution, depending on the amount of light they have been exposed to. Our experiments required positive photoresist, since the choice of a positive or negative photoresist is determined by the subsequent sequence of processing steps to be performed. Let us illustrate all the steps that we pass through to fabricate a device by considering

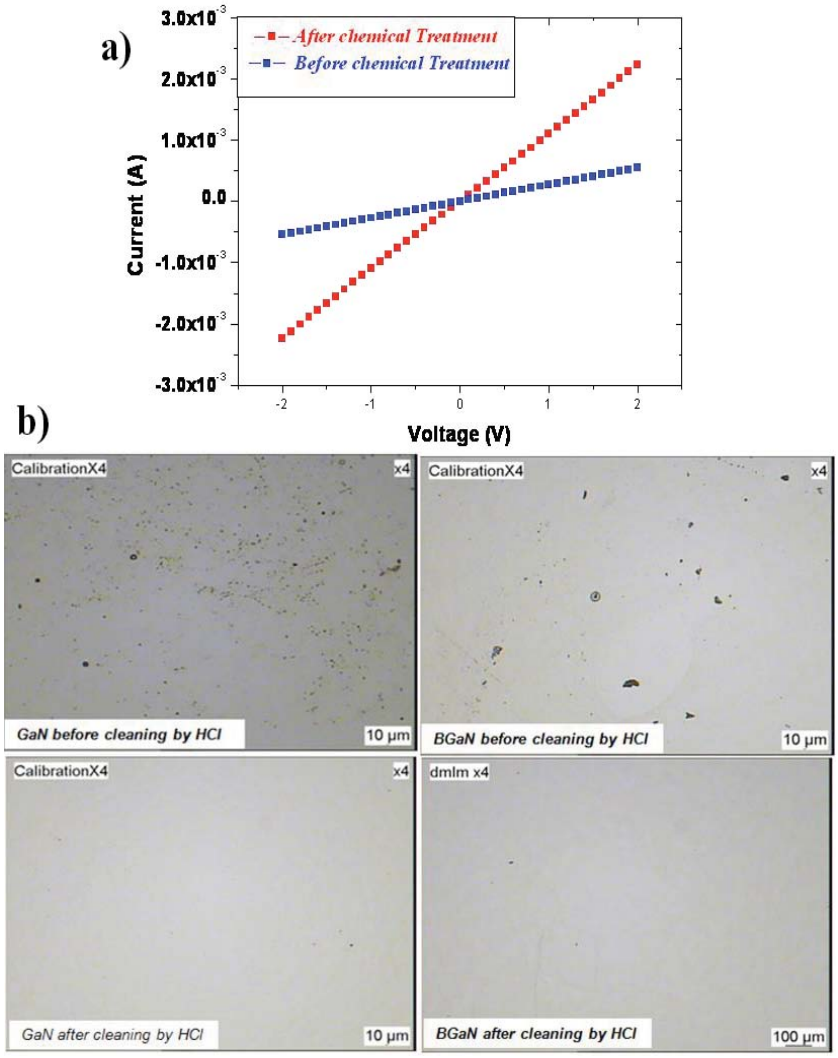

Figure 3.10: *Effect of the chemical treatment on the ohmicity, (a) I(V) characteristic of contacts before and after chemical treatment. (b) Effect of acetone and HCL on the surface before and after cleaning.*

an example applied to GaN, BGaN and AlGaN substrates. After the surface chemical treatment of the substrates, the substrate, is attached to a spindle using a vacuum chuck, a small puddle of a lift-off resist film (LOR3A) in a yellow light cleanroom environment, to avoid any white light (rich in ultraviolet) that can degrade the resist. The spindle is then spun rapidly; rotating the substrate at several thousand revolutions per minute for a given duration until the desired thickness of the photoresist film is achieved. Once the photoresist is applied, a prebake, or a softbake, step is performed at 140°C during 10 min. Softbaking is used to drive out the solvents present in the resist and to improve the adhesion. After the deposition of the first resist layer the same procedure is used for the deposition of a second layer of the photoresist (S1813) as shown in figure3.11(a) with a

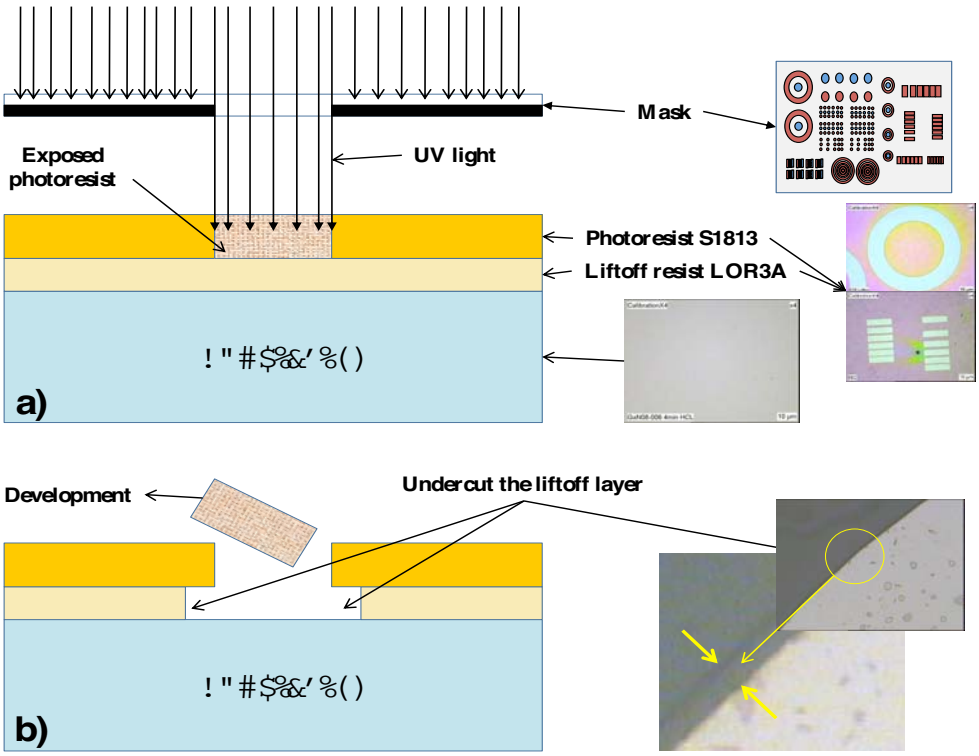

Figure 3.11: *Photolithography process sequence. When using positive resist, the exposed regions are dissolved in the developing solution, while the unexposed areas remain intact. (a) The positive photoresist is exposed using a source of intense ultraviolet light. (b) The wafer is removed from the alignment station and areas exposed are dissolved in a solution.*

softbake step at 115°C during 1 min. Once the lift-off resist (LOR3A) and photoresist (S1813) are deposited on the substrate and prebake is completed, the GaN, BGaN and AlGaN substrates are then ready for the mask alignment and exposure. In figure 3.11(a), the positive photoresist (S1813) is exposed using a source of intense ultraviolet light during 3 seconds which alters its chemical bonding to make it more soluble where it has been exposed. The wafer is removed from the alignment station and ready for etching. The etching process can be achieved through either chemical etching (known as wet etching), or physical etching (known as dry etching). In our process we used wet chemical etching figure 3.11(b). We immerse the wafer in a chemical developer solution for 80 sec. The exposed regions of the photoresist layer are dissolved in the developing solution, leaving the unexposed areas intact. In other words, for a photoresist, the light from the exposure step increases the solubility of the resist in the developing solution by depolymerizing the resist material.

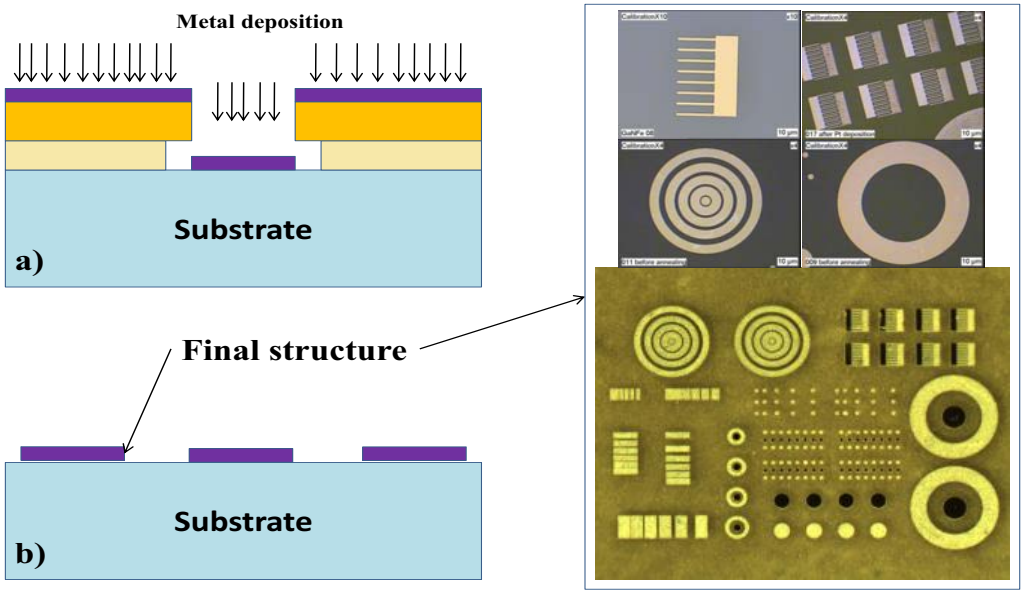

Figure 3.12: *(a) when the metal is deposited it will stick to the substrate. (b)The lift-off layer is removed the metal contact stuck to the substrate will remain.*

3.3.2 Metal deposition

3.3.2.1 Vacuum evaporation

In the steps illustrated in figure 3.12(a) and (b) when the metal contacts is deposited it will stick to the substrate and the photoresist is no longer needed, and removed by a chemical remover, while the metal contacts stuck to the substrate will remain. The result of the photolithographic process is shown in figure 3.12(b) while after the layer of resist has been removed, only the patterned layer of metal contacts is left as shown in the final structure, which is a real image of metal contacts on GaN substrate, consisting of four constitutive layers of metal (Ti/Al/Ti/Au-8/250/10/100 nm). The deposition of metal contact (Ti/Al/Ti/Au-8/250/10/100 nm) on GaN, BGaN and AlGaN substrate is commonly accomplished through vacuum deposition. Figure 3.13 shows a typical vacuum deposition system. It consists of a vacuum chamber, maintained at a reduced pressure by a pumping system. The shape of the chamber is generally a metal chamber that is made of stainless steel. The deposition system contains a wafer holder, a shutter, a thickness range monitor, heaters, and an ion gauge to monitor the chamber pressure. It is important to operate at a reduced pressure for a number of reasons. Any air or oxygen molecule in the vacuum chamber during the evaporation of aluminum, leads the metal to oxidize and as a

result aluminum oxide would form in the deposited film, causing non ideal performance. Reducing the pressure ensures that the concentration of residual oxygen molecules is small enough to minimize the oxidation reaction.

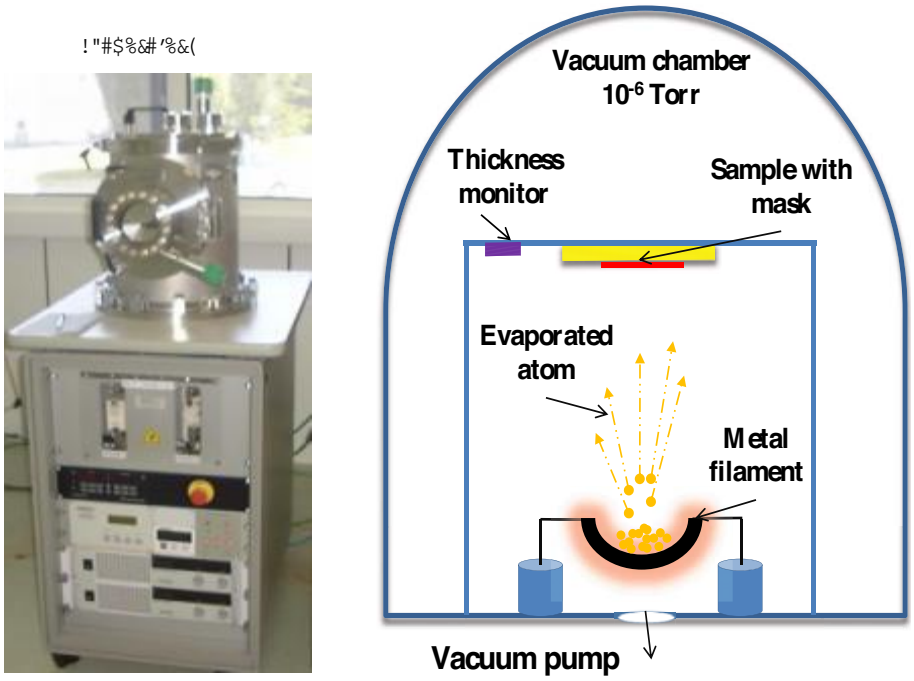

Figure 3.13: *Cross-section of a typical vacuum evaporation system which includes a vacuum chamber, a sample holder, a metal filament, and a thickness monitor.*

3.3.2.2 Sputtering deposition

After annealing, the first step of metal contact (Ti/Al/Ti/Au-8/250/10/100 nm) is achieved. Now for completing the device we need the second part of the metal contact which is Pt. For doing so, we used a sputtering deposition system as shown in figure 3.14. It contains a target of the Pt metal which is electrically grounded and serves as the cathode. Under vacuum conditions, argon gas is introduced into the chamber and is ionized into a positively charged ion. These ions are accelerated toward the cathode target. By impacting the target, enough metal atoms are dispersed such that they deposit onto the wafer surface. The main feature of the sputtering method is that the target material is deposited on the wafer. Sputtering has several advantages over other traditional evaporation techniques. For example, the composition of the deposited film is precisely determined by that of the target material, the step coverage is improved, and the sputtered films have a higher adhesion. As with the evaporation technique, a high quality film can only be obtained with a clean environment, clean chamber, pure source material and clean wafer surface.

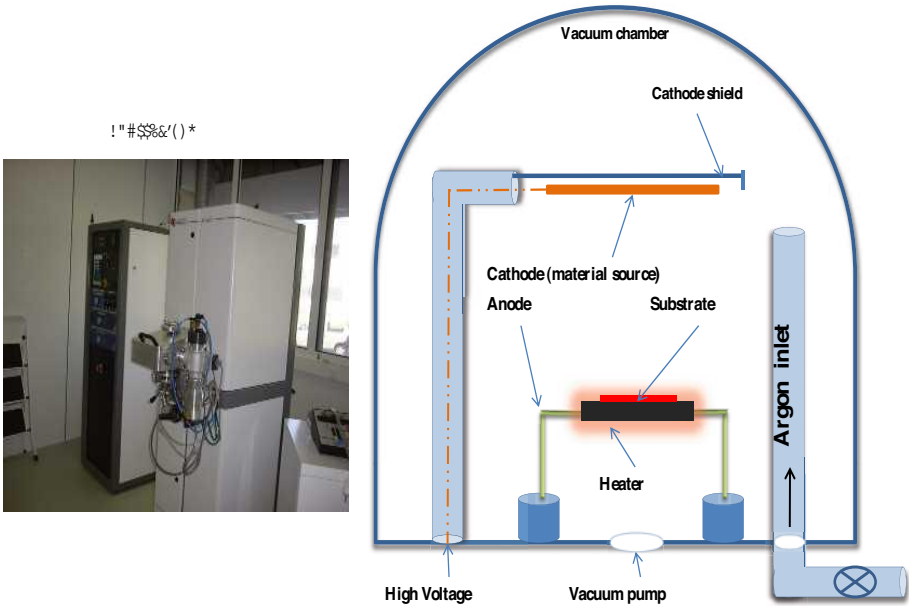

Figure 3.14: *Cross-section schematic diagram of a typical sputtering, which is enclosed in a vacuum chamber and includes the substrate which are placed on a heater, and a set of electrodes, one of which is made from the target material to be sputtered. Argon gas is supplied and ionized so that ions can impact the target to release atoms of the material to be deposited.*

3.3.2.3 Thermal annealing

Thermal annealing was performed with Rapid Thermal Processor (RTP). In RTP samples are subjected to high temperatures for a reasonably short period of time. The reaction chamber can be filled with gas, pumped down to vacuum or kept filled with room air during the annealing. The process gases vary according to the process. Typical process gases are inert, e.g., argon or nitrogen. Also oxygen can be used, if the process is used for oxidation. Figure 3.15(a) shows the Jipelec JetFirst 200C furnace that is used for Rapid Thermal Annealing (RTA) processing. Heating in Jipelec JetFirst 200C RTP is done with 18 infra red lamps as shown in figure 3.15(b). For measuring the process temperatures a pyrometer is used. Annealed sample is located on a susceptor and the pyrometer measure the temperature from the bottom of the susceptor. To achieve low resistance ohmic contact, it is necessary that Ti and Al diffuse in the semiconductor layer in order to form low resistance ohmic contacts. For this purpose a RTA is used. The resistivity of the contacts is highly sensitive to the annealing temperature. Contacts should be annealed for 30 s at 900°C. One example of the used annealing process is shown in figure 3.15(c). The ramp up rate was set to 10°C/s. After the ramp up the temperature was kept steady

for 30 s. The ramp down rate was limited in 10°C/s until 200°C reached. After the process ended, the chamber was purged with nitrogen.

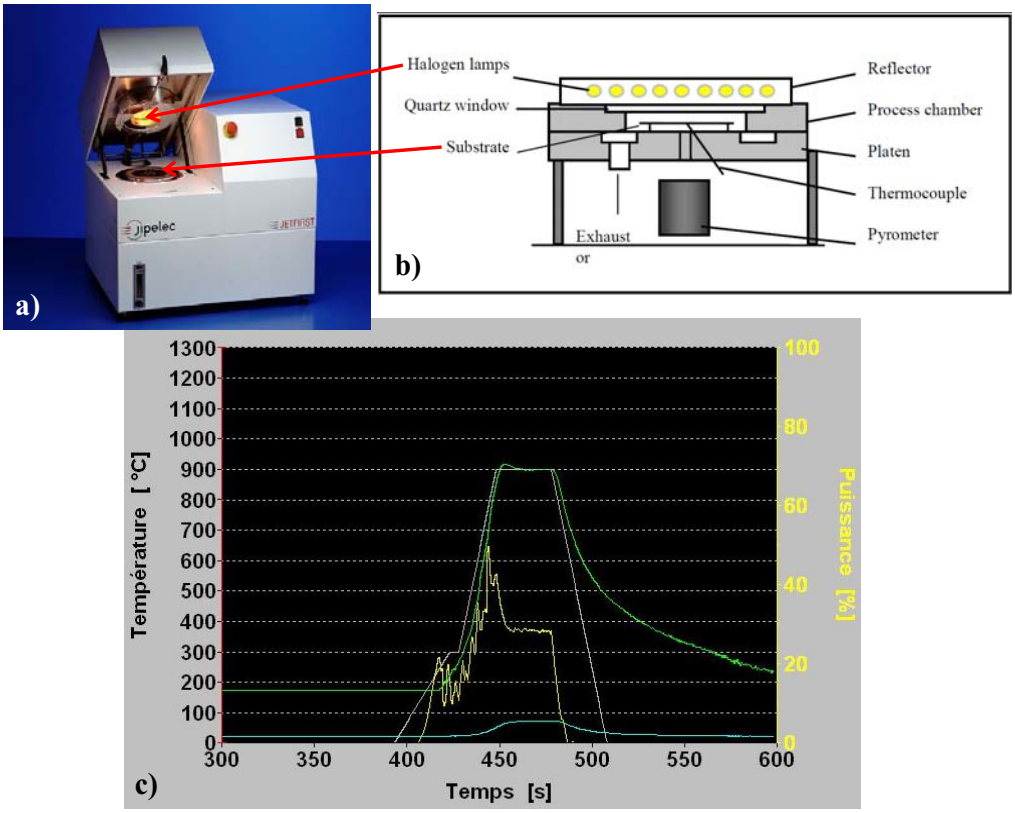

Figure 3.15: *General overview of the furnace (a), infrared halogen lamps heat up the substrate through a quartz window located on the topside of the process chamber (b). Temperature versus time profile, yellow line represent the power, green line represent the realtime temperature of the sample and the white line shows the rise, steady and fall time (c).*

3.3.3 Wire bonding

It is necessary to link the metal contacts which have microscopic sizes to a macroscopic electrical connector. The method used is called wire bonding. In this technique the bond is formed by pressure and mechanical vibration. In this case as the wire leaves the wedge, the tip is pushed against the surface and the vibration removes any existing oxide and allows the wire head to deform and flow under pressure at 70°C to create a strong bond. The wire used in our process was a gold wire with a diameter of 25 μm. Figure 3.16(a) illustrates the 6 simplified steps procedure for making an ultrasonic wire bonding between the metal contact pad and the sample holder with a typical wedge-type tool.

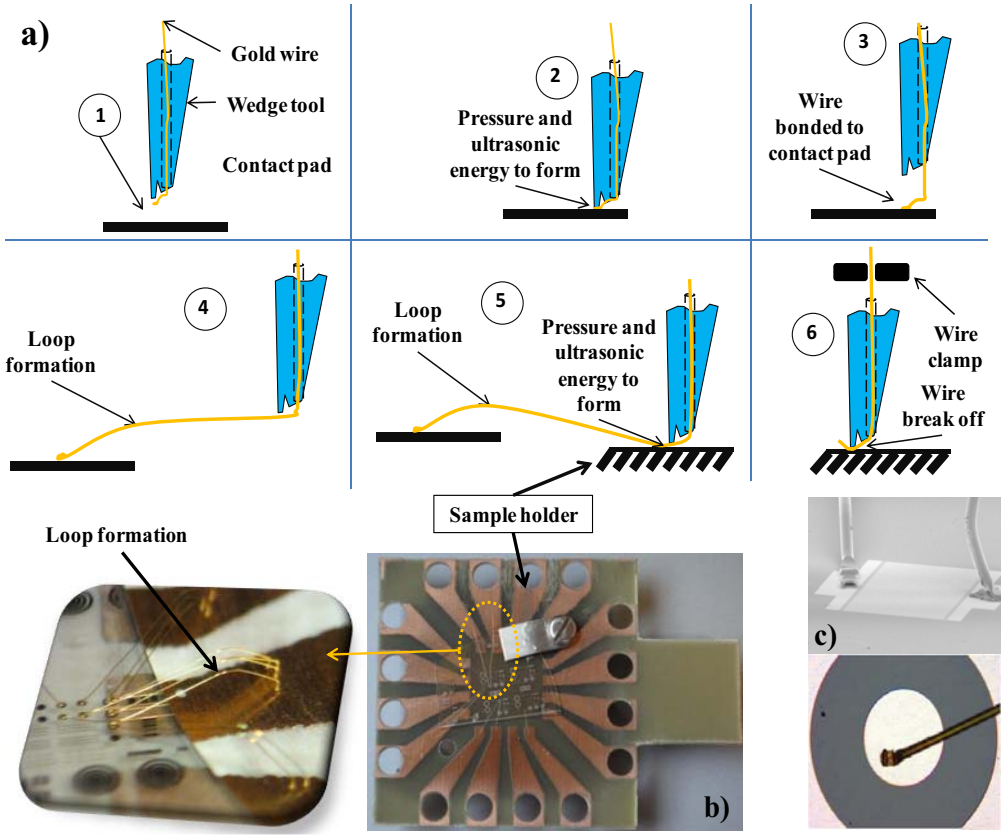

Figure 3.16: *Schematic diagrams showing the sequence in the ultrasonic wire bonding process (a). One of our samples connected to sample holder and ready for characterization (b), Example of wire bonded device viewed under electron and optical microscopy taken from our current work (c)*

1. Wire is located between the contact pad surface and the wedge tool.

2. The tool is lowered and presses the wire to the contact pad surface with a pre-determined force. Ultrasonic energy is applied for a preset time to make the first bond.

3. The wedge tool is raised while the wire is bonded to the contact pad.

4. The "workholder" or the wedge tool moves the second bonding site under the tool, the loop is formed, and the tool is lowered to its "second-search" position on the sample holder (sample holder shown in figure 3.16(b)).

5. The tool is lowered to the bonding pad, and the second bond is made.

6. A wire clamp (above the wedge tool) closes and pulls back on the wire to break it at the heel of the bond. The tool is then raised, and the end of the wire is fed

out underneath the tool until the end is located somewhat beyond the front of the tool (the tail length). The bonder is then ready to repeat the cycle. Figure 3.16(c) shows a bondable device taken by SEM and optical microscope.

3.4 Device characterization: Electrical measurements

In this section we will describe how we experimentally determine the ohmic and Schottky contact parameters. These measurement techniques fall in two categories, the current-voltage (I-V) method and the capacitance-voltage (C-V) method.

3.4.1 Ohmic contacts

This section deals with the first of the two limiting cases of metal - semiconductor contacts: the ohmic contacts. The term "ohmic contact" is generally used to refer to contacts for which the current - voltage characteristics are determined by the resistivity of the semiconductor material or by the behavior of the device to which they belong, rather than by the characteristics of the contacts themselves. The ideal contact would have an impedance which is negligible compared to that of the semiconductor material. In addition, the contact should not inject minority carriers and should be stable both electrically and mechanically. Ohmic contacts with very low contact resistances are needed to establish the connections between any semiconductor device or integrated circuit and the outside world. Furthermore, high quality ohmic contacts are essential for performing very accurate Van der Pauw/Hall measurements. We will start with an overview of the basic principles of ohmic contact formation. Next, the specific contact resistance ρ_c, which is the most important property of ohmic contacts, will be discussed. Finally, the Transmission Line Model (TLM), which is the most commonly used analysis technique to determine ρ_c, will be considered.

3.4.1.1 Basic principles of ohmic contact formation

The fabrication of ohmic contacts is still more an art than a science. Every laboratory tends to have its own favorite recipes which involve particular metal or alloy systems, particular deposition methods and particular forms of heat treatment. However, all these recipes appear to depend on one of the following three basic principles [186]:

1) If the semiconductor conforms approximately to the simple Schottky - Mott theory (Φ_{Bn}=Φ_m-χ_s) it should be in principle possible to obtain a contact with a negative barrier

height (which should behave as an ohmic contact) by finding a metal with a work function less than the work function of an n-type semiconductor or greater than the work function of a p-type semiconductor. Alternatively, if the barrier height is determined by Fermi level pinning, it occasionally happens that the pinning position is within the conduction band or valence band. In this case negative barrier heights should be obtainable on n-type or p-type semiconductors respectively. Unfortunately, there are very few metal semiconductor combinations with this property. However, if the barrier height is positive, but very small, the contact should have a low enough resistance to be effectively ohmic.

2) The vast majority of ohmic contacts depend on the principle of having a thin layer of very highly doped semiconductor material immediately adjacent to the metal-semiconductor interface. In that case, the depletion region is so thin that field emission takes place and the contact has a very low resistance at zero bias. The heavily doped layer may be formed by diffusion techniques or by ion implantation. Alternatively, the heavily doped region may result from the deposition and subsequent heat treatment of an alloy containing an element which acts as a donor or acceptor in the semiconductor. The heat treatment can be carried out in an ordinary furnace or by rapid thermal annealing (RTA). When heated, some of the semiconductor dissolves in the metal and on subsequent cooling it recrystallizes with a high concentration of the electrically active element in solid solution.

3) If the surface of the semiconductor material is damaged (e.g. by etching, chemical treatment,...), crystal defects may be formed near the surface which act as efficient recombination centers. If the density of these centers is high enough, recombination in the depletion region will become the dominant conduction mechanism and will cause a significant decrease in the contact resistance.

3.4.1.2 Specific contact resistance

The specific contact resistance ρ_c is the most important property of ohmic contacts. It provides the most systematic way to compare different metallization schemes with respect to the contact resistance. The specific contact resistance is due to the potential barrier at the metal- semiconductor interface and is defined by:

$$\rho_c = \left(\frac{\partial J}{\partial V} \right)^{-1}_{V=0} \tag{3.25}$$

where V is the voltage across the barrier and J is the current density through the barrier. The expression for the current density depends on the ruling current transport mechanism. The second basic principle of ohmic contact formation that has been described in previous

section is the most widely occurring. Hence, the current transport mechanisms that are of interest in ohmic contacts are thermionic emission (TE), thermionic field emission (TFE) and field emission (FE) respectively. Using the definition of ρ_c and equations 3.18 (a-c) that give the expressions for the current densities in the case of TE, TFE and FE respectively, the expressions for the specific contact resistance in each of these cases can be determined by [179]:

$$\begin{aligned}
&\rho_c \propto exp\left(\frac{q\Phi_{Bn}}{K_B T}\right) && \text{(TE) (a)} \\
&\rho_c \propto exp\left\{\frac{4\Pi\sqrt{m^*\epsilon\epsilon_{r,s}}}{h}\left(\frac{\Phi_{Bn}}{\sqrt{N_d}}\right) tanh\left[\frac{qh}{4\Pi K_B T}\sqrt{\frac{N_d}{m^*\epsilon\epsilon_{r,s}}}\right]\right\} && \text{(TFE) (b)} \\
&\rho_c \propto exp\left\{\frac{4\Pi\sqrt{m^*\epsilon\epsilon_{r,s}}}{h}\left(\frac{\Phi_{Bn}}{\sqrt{N_d}}\right)\right\} && \text{(FE) (c)}
\end{aligned} \tag{3.26}$$

The value of ρ_c in a given metal-semiconductor system is determined by the combination of the following three parameters [179]:

1. the potential barrier height Φ_{Bn},
2. the dopant concentration N_d (in the case of an n-type semiconductor), and
3. the temperature T.

The relative effect of these parameters in the various current transport mechanisms can be deduced from the exponential terms that contribute to ρ_c . Equation 3.26 (a) shows that in the thermionic emission process the specific contact resistance is independent of the dopant concentration N_d. In the case of a thermionic field emission tunneling mechanism (equation 3.26 (b)), $ln(\rho_c)$ varies nonlinearly with $N_d^{-1/2}$. It does vary linearly with $N_d^{-1/2}$, however, when a low-temperature tunneling process, known as field emission (equation 3.26 (c)), is the mechanism for current transport across the barrier.

In order to determine the specific contact resistance, the actual contact resistance R_c has to be measured. In the highly hypothetical case of a uniform current distribution over the contact area, the resistance of the metal-semiconductor contact R_c can be written as:

$$R_c = \frac{\rho_c}{A} \tag{3.27}$$

where A is the area of the metal - semiconductor contact. In reality however, the current density is seldom uniformly distributed across the contact area due to the voltage drop in the semiconductor. This phenomenon is referred as the current crowding effect. In practice, it is generally sufficient to mention that the current density is negligible beyond a certain distance from the front edge of the contact. This distance, which is also an

important property of ohmic contacts, is the so-called transfer length L_t. This quantity is related to the lateral distance required for current to flow into or out of the contact. The total current density passes through an imaginary plane at the edge of the contact, as shown in figure 3.17. A portion of this current density flows into the metal very near the edge of the contact while other portions enter the metal further from the edge. In the

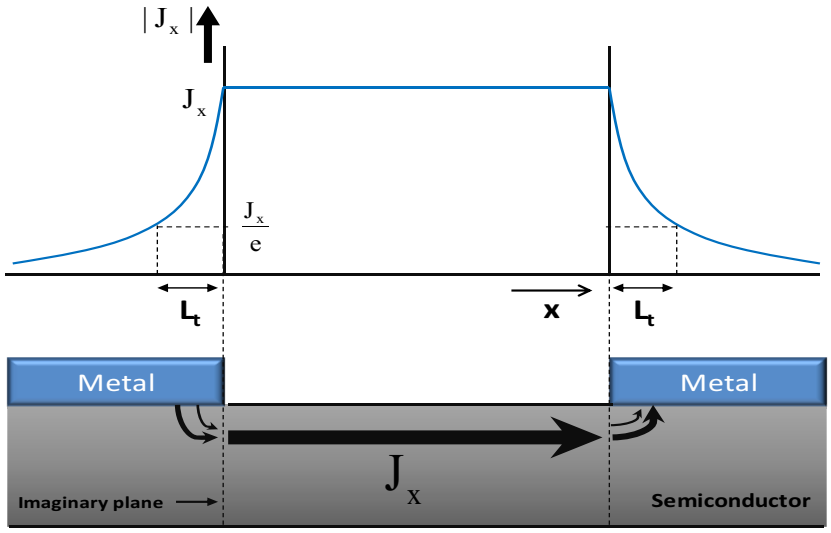

Figure 3.17: *Flow of the current density in a planar contact.*

case of a rectangular metal contact and if the contact length $d \gg L_t$ (electrically long), the effective contact area A_{eff} becomes $L_t x W_c$ where W_c is the contact width in the direction perpendicular to the current flow. For such a contact, the contact resistance is given by:

$$R_c = \frac{\rho_c}{A_{eff}} = \frac{\rho_c}{L_t x W_c} \tag{3.28}$$

Unlike the contact resistance R_c, the specific contact resistance ρ_c is unaffected by the current crowding effect and as mentioned before, ρ_c is determined by the barrier height, the doping concentration and the temperature [179]. In other words, unlike the contact resistance R_c, the specific contact resistance ρ_c is a unique, geometry independent characteristic of the metal-semiconductor interface.

3.4.1.3 Characterization

Transmission Line Model (TLM) was used by accessing the quality of contacts as well as electrical properties of all thin films used in our study. This model is the most widely used for obtaining the specific contact resistance, first proposed by Shockley [189]. Later this model has been refined and expanded by Murramann and Widmann [190], Reeves

and Harbison [191]. They used this method for obtaining both the semiconductor sheet resistance R_{sh}, and the specific contact resistivity ρ_c of contacts using rectangular and concentric contacts. A useful definition with regard to the latter modification is that of a quantity called the sheet resistance R_{sh}, which is given by [192]:

$$R_{sh} = \frac{\rho_c}{t} \tag{3.29}$$

where t is the thickness of the semiconductor layer used and R_{sh} has the dimensions of ohms, but it is universally given in the units "ohms per square" (Ω/sq). A "square" of material (W=Z) has an end-to-end resistance of R_{sh}. The sheet resistance can be usefully employed in calculations without any knowledge of the exact thickness of the conductive layer (which may be hard to measure accurately). More importantly, the concept of the sheet resistance is valid even when the resistivity of the conductive layer is not uniform. Besides considering the finite thickness of the conductive layer, alloying and sintering effects were included in the model by taking into account the difference in sheet resistances of the conductive layer beneath R_{sk} and outside the contact area R_{sh}. Finally, circular TLM (CTLM) has been developed [191] in order to simplify the fabrication procedure and achieve a more symmetrical current flow pattern by eliminating the edge effects that exist in the linear TLM (LTLM). In our study we will address LTLM method for calculating all the parameters R_{sh}, ρ_c and L_t.

3.4.1.4 Linear TLM

The simplest and most used configuration of the transmission length model is a linear array of ohmic contacts, all of the same size but placed at increasing distances d_i ($d_1 < d_2 < ... < d_i$), on the semiconductor surface. Because of the linear arrangement of the ohmic contacts, this configuration is often referred to as the linear transmission length model (LTLM). Figure 3.18 (a) shows a schematic diagram of the LTLM configuration. The figure also shows that the contacts have been isolated in order to restrict the current to flow only across the distances d_i and to prevent current spreading. This isolation can be obtained by etching away areas of the electrically active semiconductor material down to the semi-insulating substrate. Usually photolithography techniques are used to define the areas that should be etched away. As a result, the so-called "mesas" of the active semiconductor material are created. In this work we did not take into consideration the so-called "mesas" structure due to the complicated nature of this step and the lack of required mask. The linear TLM used in the current work consists of rectangular metal pads of length (Z), width (W), and spacing gap (d) placed at different distances with

the same area of each rectangular pad within the same pattern. As shown in figure 3.18 (b) the area of the rectangular pads are 300x150 μm^2 (pattern I), 300x80 μm^2 (pattern II-III), 150x100 μm^2 (pattern IV) and 150x50 μm^2 (pattern V), with spacing between the contacts equal to 10, 20, 30, 50 and 100 μm (pattern I and II) and 5, 10, 15, 20, and 25 μm (pattern III, IV and V). From figure 3.18 (c) the following equations describe the total

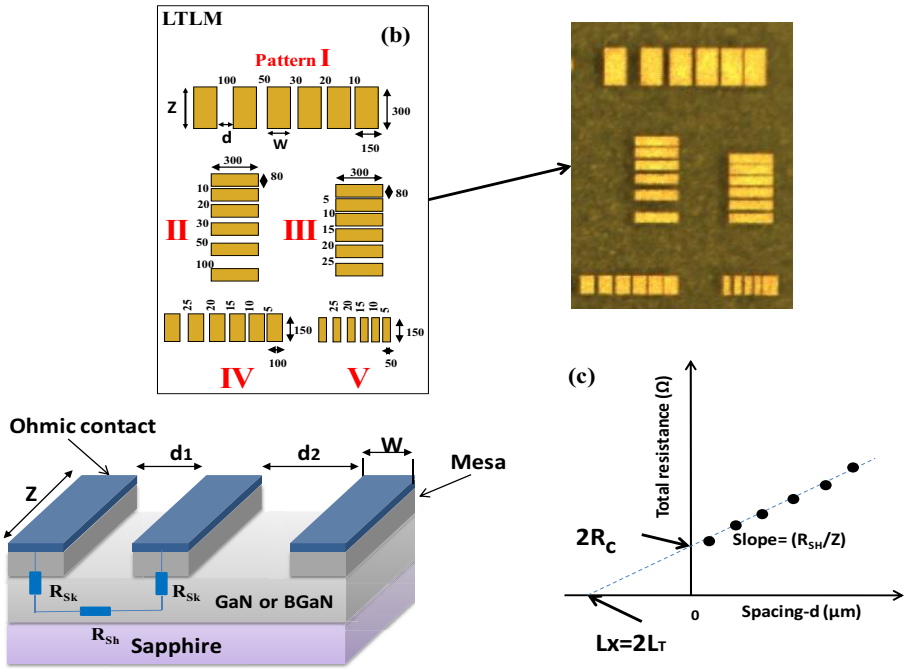

Figure 3.18: *Schematic diagram of a semiconductor material with contact pads prepared for LTLM analysis (a), schematic structure of all the pattern with the rectangular pads dimension (b).*

resistances R_1 and R_2 that correspond to the contact separations d_1 and d_2 respectively:

$$\begin{aligned} R_1 &= 2R_c + R_{sh}\left(\frac{d_1}{Z}\right) \\ R_2 &= 2R_c + R_{sh}\left(\frac{d_2}{Z}\right) \end{aligned} \tag{3.30}$$

where R_{sh} is the sheet resistance of the semiconductor material outside the contact area. In principle, the contact resistance R_c can be obtained by measuring the total resistances R_1 and R_2. Solving for R_c gives:

$$R_c = \frac{R_2 d_1 - R_1 d_2}{2\,(d_1 - d_2)} \tag{3.31}$$

However, the disadvantage of this procedure is that usually the contact resistance is small compared with that of the semiconductor material between the contacts ($2R_c \ll R_{sh}.\frac{d_1}{Z}$). In this case, R_c is determined from equation 3.31 as a small difference of large quantities

and thus is extremely sensitive to experimental errors in the values of R_1, R_2, d_1 and d_2. A somewhat better result can be obtained when the total resistance R_T (equation 3.32) is plotted as a function of the distance d between several pairs of the planar contacts.

$$R_T = 2R_c + R_{sh}\left(\frac{d}{Z}\right) \tag{3.32}$$

In this case, R_c is determined by a linear extrapolation of the experimental data to d=0, which is shown in figure 3.18 (c). Note that the external resistance of the measurement system, the probe resistance, is assumed to be negligible. Extraction of the specific contact resistance ρ_c from the contact resistance determined by the method described above requires that a certain model of the planar metal-semiconductor contact is adopted. A transmission line model is almost exclusively used for this purpose. It's validity is based on the fulfillment of the following conditions:

1. The current lines are normal to the metal-semiconductor interface.
2. The thickness of the metal and diffusion layers can be neglected.
3. The current-voltage characteristic of the contact is linear.

Among these three assumptions, only the third one can be verified directly by measuring the current-voltage characteristic of the metal-semiconductor contact. Figure 3.19 shows an equivalent circuit of the rectangular metal-semiconductor contact with approximately one-dimensional current flow pattern. The resistance R' and the conductance G' per unit

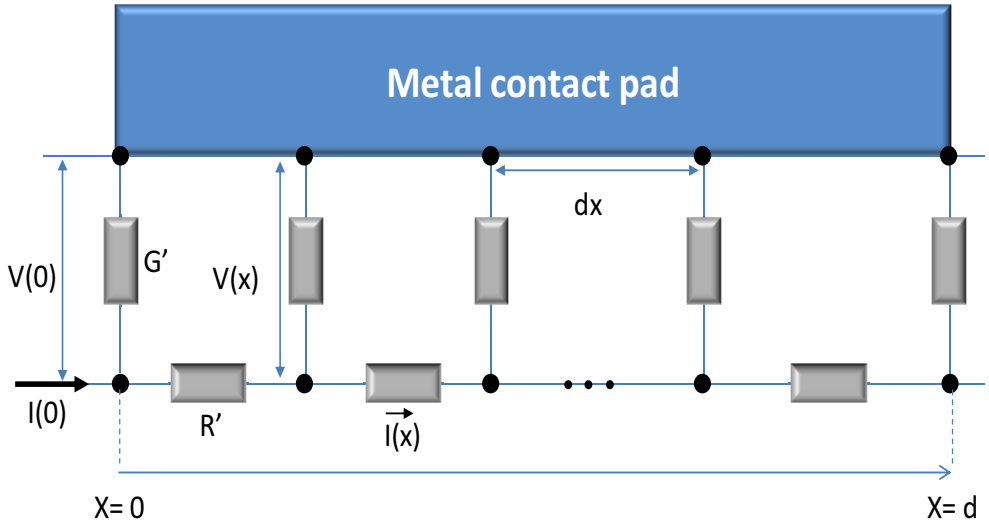

Figure 3.19: *Equivalent circuit of the rectangular metal-semiconductor contact pad.*

length of the contact, shown in Figure 3.19, can be written as:

$$R'=\frac{R_{sk}}{Z} \qquad and \qquad G'=\frac{Z}{\rho_c} \tag{3.33}$$

where R_{sk} is the resistance under the pad contact. The metal layer is considered to be equipotential, which, strictly speaking, is correct only when the metal sheet resistance $R_m \ll R_{sk}$. Then, the voltage drop in the semiconductor material between the contacts can be written as:

$$dV(x) = -RI'(x)\,dx \qquad and \qquad dI(x) = -V(x)\,Gdx' \tag{3.34}$$

where I(x) denotes the current in the semiconductor material between the contacts at a distance x from the front edge of the contact. A differential equation of the one-dimensional TLM follows from equation 3.34:

$$\frac{d^2V}{dx^2}-\frac{V}{L_t^2}=0 \qquad or \qquad \frac{d^2I}{dx^2}-\frac{I}{L_t^2}=0 \tag{3.35}$$

where the transfer length is defined as:

$$L_t=\frac{1}{\sqrt{R'G'}}=\sqrt{\frac{\rho_c}{R_{sk}}} \tag{3.36}$$

By introducing the current I_0 and the voltage V_0 at the input of the transmission line, the boundary conditions can be formulated as:

$$\begin{aligned} &V(0)=V_0 \\ &\texttt{and} \\ &I(0)=I_0 \qquad or \qquad \left[-\frac{1}{R'}\frac{dV(x)}{dx}\right]_{x=0}=I_0 \end{aligned} \tag{3.37}$$

The solution of equation 3.35 subject to these boundary conditions yields [44]:

$$\begin{aligned} &V(x)=V_0\cosh\left(\frac{x}{L_t}\right)-ZI_0\sinh\left(\frac{x}{L_t}\right) \\ &\texttt{where} \\ &Z=RL_t'=\frac{R_{sk}L_t}{Z}=\frac{\sqrt{\rho_c R_{sk}}}{Z} \end{aligned} \tag{3.38}$$

which denotes the characteristic resistance of the transmission line. The expression for the current I(x) follows from equations 3.34 and 3.38:

$$I(x)=-\frac{1}{R'}\frac{dV(x)}{dx}=I_0\cosh\left(\frac{x}{L_t}\right)-\frac{V_0}{Z}\sinh\left(\frac{x}{L_t}\right) \tag{3.39}$$

Returning to the equivalent circuit shown in figure 3.19, it has to be noted that I(x)= 0 for x>d. Hence, the current continuity requires that I(d)= 0 and according to equation 3.39:

$$\frac{V_0}{I_0}=Z\coth\left(\frac{W}{L_t}\right) \tag{3.40}$$

Since the imaginary separation between the semiconductor material between the contacts and the metal-semiconductor area is made at the contact edge (x=0), the contact resistance R_c appearing in equation 3.30 corresponds to the input resistance of the transmission line given by equation 3.40. Using equation 3.38, R_c can be given by:

$$R_c = \frac{R_{sk} L_t}{Z} \coth\left(\frac{W}{L_t}\right) \tag{3.41}$$

If the sheet resistance beneath the contacts, as a practical matter, is assumed to be equal to the sheet resistance between the contacts, $R_{sk}=R_{sh}$, equation 3.41 can be solved numerically with respect to L_t by using the value of R_c as determined by the extrapolation technique mentioned earlier. The determination of the transfer length can be further simplified in the case of electrically long contacts, that means if $d \gg L_t$. In that case equation 3.41 can be reduced to $R_c \approx R_{sh} L_t / Z$. The total resistance R_T between a pair of identical contacts separated by a distance d then becomes:

$$R_T = \left(\frac{R_{sh}}{Z}\right)(2L_t + d) \tag{3.42}$$

The transfer length is then determined by a linear extrapolation of the experimental data to the point $R_T = 0$ as shown in equation 3.42. According to this equation the negative x-axis intercept L_x, hence, $L_t = L_x/2$. Once L_t, is determined, the specific contact resistance can be calculated using equation 3.36:

$$\rho_c = R_{sk} L_t^2 \tag{3.43}$$

where $R_{sh}=R_{sk}$.

3.4.1.5 Circular TLM

As we mentioned in the previous section that LTLM measurements are often performed by using a mesa etching of the epitaxial layer to achieve an one-dimensional current flow pattern and omit current spreading. As this mesa etching step requires additional steps in the fabrication process, it has been tried to exc1ude them and hence simplify the fabrication process. This can be done by choosing a different geometry of the test structures. The use of a circular contact geometry eliminates the need for the mesa etch of the epitaxial layer. Furthermore it can be noted that the use of circular TLM (CTLM) structures eliminates the errors that are introduced by the lateral current crowding and gap effect, which are always present in the linear TLM structures. Over the past decades, many different configurations for circular test patterns were developed. In 1979, Reeves

[191] proposed a test pattern consisting of a central disc contact and two concentric ring contacts to determine the specific contact resistance. In 1981, Marlow and Das [193] used a configuration were the inner disc contact is defined by removing circular rings with varying diameter from a metal plate. In 1999, Rechid and Heime [194] refined Reeves' configuration by increasing the number of concentric ring contacts from two up to seven. This expansion is needed for the case that the resistivity of the metal contacts cannot he neglected. Since Reeves used only three contacts (one disc and two rings), he was not able to see the influence of the metallayer resistivity [194]. In order to calculate the total resistance $R_{T,circ}$ of any circular contact configuration, first the resistance of the annular contact will be calculated. According to Reeves [191] this can he done using the nonuniform transmission line model of the planar circular metal-semiconductor contact. In this case, the usual resistances and conductances which describe the transmission line model for a rectangular contact (equation 3.33) have to be modified to account for the circular contact geometry. However, according to Cohen [179], it is also possible to arrive at the same expression for $R_{T,circ}$ using a two-dimensional current continuity equation. For the general case of an annular contact, the contact resistance is given by:

$$R_{T,circ} = \frac{R_{sh}}{2\pi}\left[\ln\left(\frac{R_1}{R_1 - s}\right) + L_t\left(\frac{1}{R_1 - s} + \frac{1}{R_1}\right)\right] \tag{3.44}$$

where R_1 and R_2 is the inner and outer radius respectively, s is the gap spacing between the annular contact. The transfer length L_t can now be determined by a least squares fit of experimental data to equation 3.44. This fit also yields a value for R_{sh}. The specific contact resistance ρ_c can then be calculated using equation 3.43. In addition, it can be observed that for $2\pi R_1 \gg$s equation 3.44 can be further simplified to obtain the same form as equation 3.42 with Z=$2\pi R_1$ and d=s.

3.4.1.6 Current-Voltage (I-V) method

Current-Voltage (I-V) characteristics were carried out using a Keithely Source Measure Unit 2602 (see figure 3.20). The rectifying properties of the Schottky barrier diodes are evaluated by using the (I-V) measurements. Effective Schottky barrier height ϕ_e, saturation current J_s, series resistance R_s and ideality factor n can be extracted from I-V measurements. Figure 3.21 illustrates the I-V characteristics of an ideal (solid red line) and typical (dashed line) Schottky barrier diode. For an ideal Schottky diode, n=1, while for typical it is above unity (n>1), depending on transport mechanisms. In determining I-V parameters, it is assumed that the current transport is dominated by thermionic emission. The current-voltage relationship of a Schottky diode has already

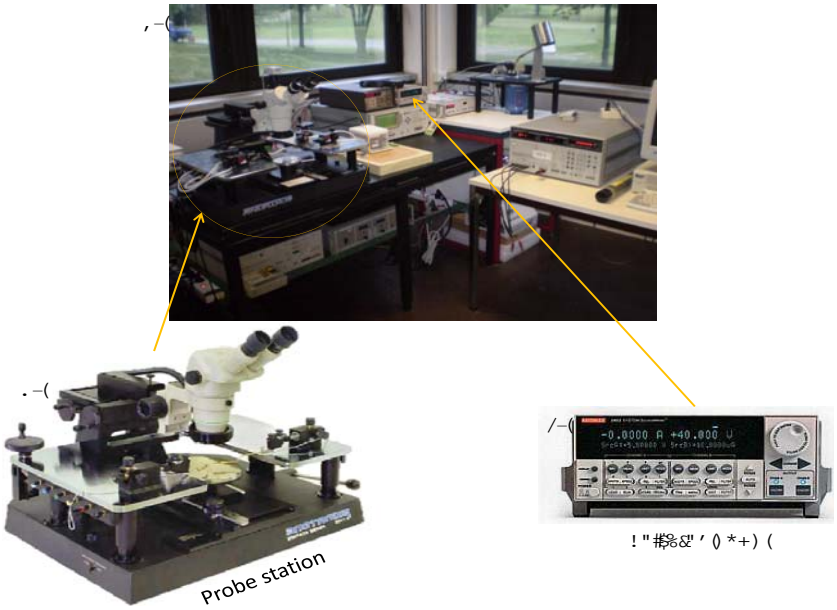

Figure 3.20: *Probe station for IV measurements (b) connected to Keithely Source Measure Unit 2602 (c)*

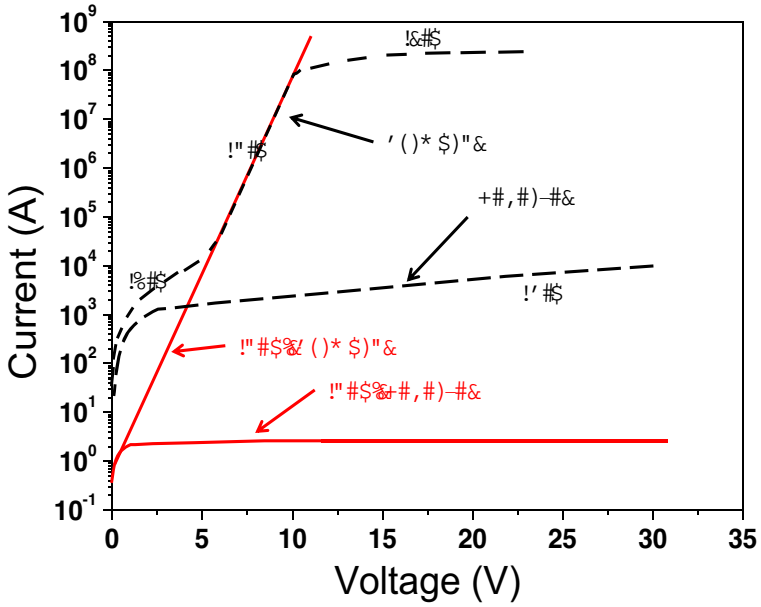

Figure 3.21: *I-V characteristics of an ideal and typical Schottky barrier diode. Generation-Recombination current region (a), diffusion current (b), series resistance (c), reverse leakage current due to generation-recombination and surface effects (d) [12]*

been discussed in section metal semiconductor contact. The universal expression that describes this current-voltage relationship is given by equation 3.18. A plot of ln(J) versus the applied forward bias (V) ideally yields a straight line with a slope that is equal

to q/nk$_B$T and a ln(J)-axis intercept that is equal to ln(J$_s$). After the determination of the slope of the forward I-V plot from the linear fit of region (b), the ideality factor n can be calculated using equation 3.16. After the determination of the value of J$_s$ from the ln(J)-axis intercept, the effective barrier height Φ_e=ϕ_{Bn}-$\Delta\Phi$ can be calculated by using equation 3.6. In practice however, the Schottky diode will not be ideal and the plot will show noticeable deviations from linearity due to among others the presence of an interfacial layer and surface states and the series resistance of the semiconductor material. The series resistance is determined from region (c), where the voltage is high. The plot assumes a flat state and R_s is extracted from the I-V plot. The leakage current is defined as the current flowing when an ideal current is zero. In particular, leakage occurs when electrons or holes tunnel through an insulator and increases exponentially as the insulating region becomes small [195]. In the case of Schottky contact, tunneling of carriers occurs between the metal and the semiconductor at the interface. A high leakage current (region (d)) leads to a failure device, it is of vital importance to measure it.

3.4.2 Van der Pauw and Hall effects

The Hall Effect, after Hall (1879), describes the behavior of the free carriers in a semiconductor when applying an electric as well as a magnetic field. If an electric current flows through a conductor in a magnetic field, it exerts a transverse force on the moving charge carriers which tends to push them to one side of the conductor. The basic principle behind the Hall effect is the Lorentz force. When an electron or hole is subjected to an electric field it experience a force, causing the electron to move. When it moves in a plane perpendicular to an applied magnetic field it experiences an additional force perpendicular to both the electric and magnetic field, called Lorentz force. From Drude's theory of DC conductivity, the Hall coefficient for an n-type samples is derived as:

$$R_H = \frac{E_y}{j_x B_z} = -\frac{1}{q.n} \tag{3.45}$$

where E_y is the electric field balancing the Lorentz force imposed by the magnetic field B_z and the current j_x. The voltage related to the electric field E_y is the Hall voltage V_H. For and applied current I in the x-direction, the corresponding Hall coefficient for a square sample with a thickness t and a width w, equation 3.46 can be written in the simple form:

$$R_H = \frac{E_y}{j_x B_z} = \frac{t.V_H}{I_z} = -\frac{1}{q.n} \tag{3.46}$$

where E_y and V_H are negative quantities, which give a negative Hall coefficient in the case of n-type carriers. Figure 3.22 shows the accumulation of charges due to the electric and magnetic fields. The charges drift under the influence of the Lorentz force towards the edge of the sample until the electric field is compensated by the built up voltage from the accumulated charges. This is the Hall voltage and its magnitude is IB/qnd, where q is the elementary charge, n is the charge density and t the thickness of the sample. It is sometimes convenient to express the sheet density (n_s=n_d) instead of the bulk density:

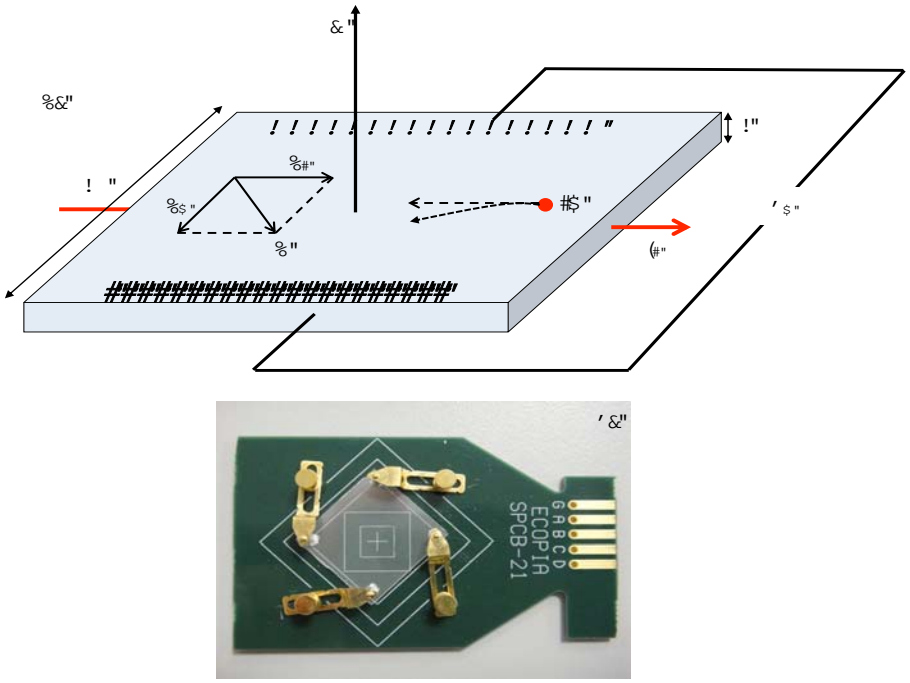

Figure 3.22: *Schematic diagram of the carriers in an orientation perpendicular to the current and magnetic field (a), A typical simple contact configuration for Hall meausrements (b).*

$$n_s = \frac{IB}{qV_H} \tag{3.47}$$

By measuring the Hall voltage, from known values of I, B and q, the sheet charge of a semiconductor can be determined. The Van der Pauw technique can be used to determine the carrier mobility and sheet carrier density for which a combination of both resistivity and Hall measurement is needed. Once the sheet resistance and the Hall voltage known, the Hall mobility can be calculated using the following:

$$n_s = \frac{|V_H|}{R_s IB} \tag{3.48}$$

For a constant Hall coefficient the IV-characteristics must be linear. The Van der Pauw measurements require four small terminal contacts at the circumference of a uniform thickness sample

3.4.3 Schottky contacts

This section deals with the second of the two limiting cases of metal-semiconductor contacts: the Schottky contacts. Their excellent rectifying properties are used to form Schottky diodes, which are majority carrier devices and hence have very short switching times typically in the picoseconds range. It is this property that makes Schottky diodes very suitable for high frequency applications. Therefore, the Schottky contacts should have a high breakdown voltage V_{break} and a low reverse current I_s. Also we will provide a brief overview of the Schottky contact parameters that can be used to indicate their quality. Furthermore, the different characterization methods that can be used to determine them will be briefly discussed.

3.4.3.1 Choice of metal contact

Making a Schottky contact is relatively easy. Depositing a metal on a semiconductor is sufficient to create it. Unfortunately, it is not possible to make a perfect Schottky barrier contact with just any metal placed on a certain semiconductor. Some metals tend to diffuse into the semiconductor and eventually the rectifying behavior of the contact disappears. Good Schottky contact should exhibit a high barrier height and and ideality factor close to unity. Pd, Ni, and Pt are proved to be good Schottky metals for n-type GaN because of their high work function. The Schottky contact on GaN is still far from ideal, because the large variation of Richardson's constant from theoretical value, the barrier height measured by I-V is lower than that measured by C-V, and the ideality factors of the Schottky diodes are observed to be much larger than one [17]. Fang et al. [196] reported that the deposition of Schottky metal onto Ga face is preffered over N face for higher barrier height. Contact with low contact resistance is also required for high quality GaN and AlGaN devices specially photodiodes. A better contact helps improve the quantum efficiency. Lin et al. [197] have reported that the typical contact for n-type GaN is Ti due to its low work function as well as the cubic TiN formation layer resulting in a large excess of four vacancies in the GaN close to the interface after thermal annealing. It is well known that N vacancies are acting as donors and are formed at the contact interface. The contact region at the interface would be highly doped to help

direct tunneling, which is considered to be the reason for the low resistance of the contact. Motayed et al. [198] has shown that Ti/Al alloy can provide the lowest contact resitance to n-type GaN, due to the close of the Al work function value with the GaN's electron affinity value. Usually the contact has a multi-layer structure. Due to the rapid oxidation of the Al layer, a metal/Au bi-layer is used to prevent this oxidation which can increase the contact resistance. The most commonly used metal to prevent the interdiffusion of Ti/Al are Pd,Ti,Pt,Mo,Re,Ir,Ni and Nb [199].

3.4.3.2 Barrier height and ideality factor

Two very important parameters for the characterization of Schottky contacts, the barrier height (ϕ_{Bn}) and the ideality factor (n), respectively, have already been discussed in the previous section, which presents the basic theory of metal-semiconductor contacts. It has been shown that in the case of an ideal Schottky contact the barrier height is bias independent and the current is only determined by thermionic emission (TE). In that case, the forward current-voltage characteristics are linear and the ideality factor is equal to unity. In practice, however, the Schottky contact will generally be far from ideal. This could among others be due to the bias dependency of the barrier height, the presence of an interfacial layer or due to other current transport mechanisms being more dominant than thermionic emission. As a result, the forward current-voltage characteristics will show noticeable deviations from linearity. In that case, it can be described by equation 3.18 where the ideality factor exceeds unity. Khan et al. [200] showed that there is a linear relationship between Φ_{Bn} and n, which is schematically shown in figure 3.23. The reverse current I_s and the breakdown voltage V_{break}, which is generally defined as the voltage at which the reverse current is 1 mA taking into account the geometrical dimensions of the device, are other very important Schottky parameters. Williams et al. [192] has shown that the breakdown voltage is inversely proportional to the product of the doping concentration N_d (in the case of an n-type semiconductor) and the thickness of the semiconductor contact layer. Furthermore, the breakdown voltage of practical contacts is among others affected by the presence of an interfacial layer and surface states. This makes the breakdown voltage of practical contacts sensitive to process details. In addition, a very irregular line definition of the ohmic and Schottky contacts could modify the electric field configuration in such a way that the breakdown voltage is considerably diminished.

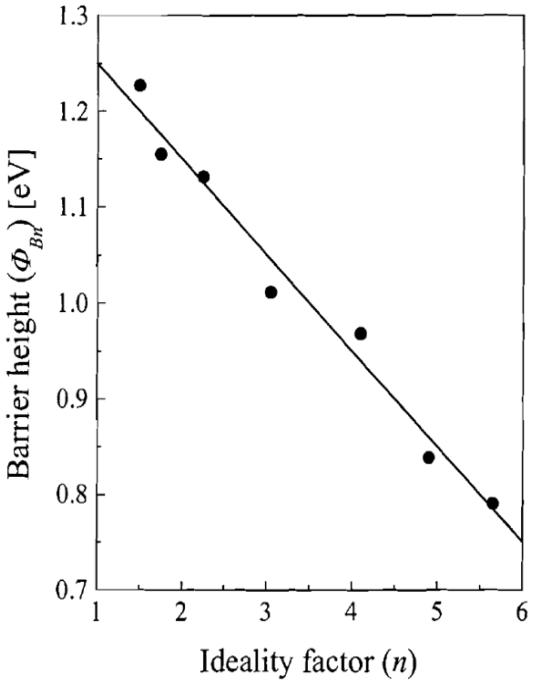

Figure 3.23: *Linear relationship between the barrier height (ϕ_{Bn}) and the ideality factor (n).*

3.4.3.3 Capacitance-Voltage method (case of n-type)

Schottky contacts capacitance is a very important parameter that enables the determination of the doping concentration of the semiconductor contact layer and the value of the built-in voltage V_{bi}. Figure 3.24 shows the energy band diagram of an ideal Schottky diode (without any interfacial layer and surface states) on a n-type semiconductor under reverse bias (V_r). The semiconductor material next to the metal-semiconductor interface is depleted of electrons. What remains is a region containing the ionized donor atoms N_d^+. This region is called the depletion region of a Schottky barrier. Depending on the concentration of the donor atoms N_d, the applied bias V controls the depth W to which the depletion region extends into the semiconductor material. In some respects, the depletion region behaves like a parallel plate capacitor [178, 186, 192], which capacitance is generally given by:

$$C = \frac{\varepsilon_0 . \varepsilon_r . A}{W} \tag{3.49}$$

where ϵ_0 is the permittivity of vacuum, ϵ_r the relative permittivity of the semiconductor material, W the width between the parallel plates and A the area of the Schottky contact. The same result can also be obtained more formally [178, 186, 192] using the fundamental definition of capacitance C = dQ/dV. The potential difference in the depletion region is

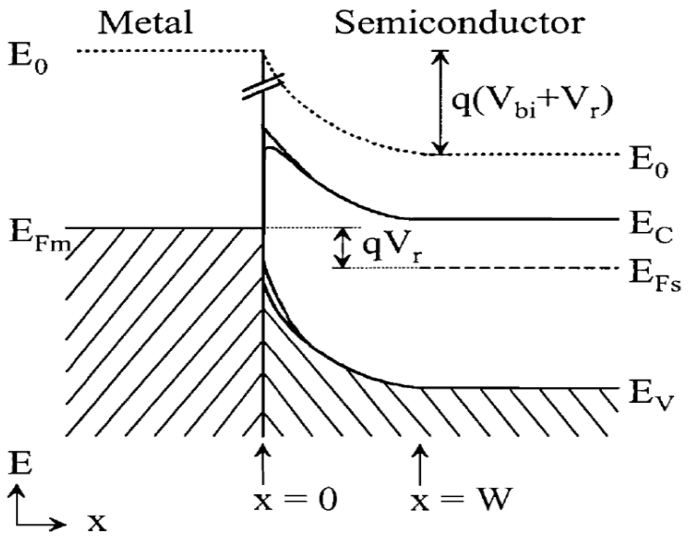

Figure 3.24: *Energy band diagram of an ideal Schottky diode without any interfacial layer and surface states on an n-type semiconductor under reverse bias (V_r).*

equal to:

$$V = V_{bi} - \frac{k_B T}{q} - \frac{q N_d W^2}{2.\varepsilon_0.\varepsilon_r} \tag{3.50}$$

where N_d is the density of the donor atoms that are assumed to be uniformely distributed, V_{bi} the built-in voltage and KT/q the thermal voltage. Combining equation 3.50 with the current-voltage relationship given by equation 3.13 yields:

$$\frac{1}{C^2} = \frac{2\left(V_{bi} - V - \frac{k_B T}{q}\right)}{q.\varepsilon_0.\varepsilon_r.N_d.A^2} \tag{3.51}$$

This expression describes the dependence of the Schottky contact capacitance (C) on the applied bias (V). The basic procedure to obtain a capacitance-voltage profile of a Schottky contact is to apply a reverse DC bias to the contact, which results in the formation of a depletion region with a certain depth and corresponding capacitance. A plot of $1/C^2$ versus the applied voltage (V) would then yield a straight line with a slope determined by N_d as shown in figure 3.25. The modulus value of the built-in voltage ($|V_{bi}|$) can be determined from the negative V-axis intercept, which can be used to calculate the flat band barrier height ϕ_{bFb} by means of the relationship:

$$\Phi_{bFb} = V_{bi} + \frac{k_B T}{q} \ln\left(\frac{N_c}{N_d}\right) + \frac{k_B T}{q} \tag{3.52}$$

where N_c is the effective density of states in the conduction band. It has been observed by many authors [17, 201, 202] that the values for the effective barrier height Φ_e derived by the C-V method are generally higher than those derived by the I-V method. This

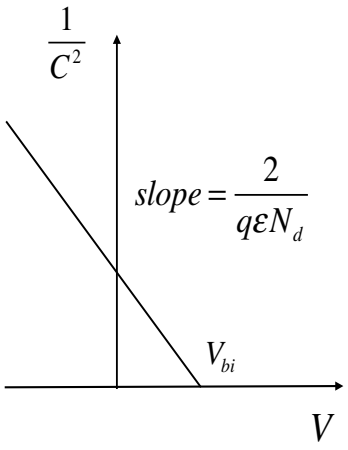

Figure 3.25: *Schematic representation of a plot of $1/C^2$ versus the applied reverse bias (V).*

discrepancy of the experimental results between the different methods may arise among others result from the Schottky effect, from the presence of a thin interfacial layer and surface states, contamination in the interface and deep impurity levels acting as electron traps [12,186,201]. After a derivation of equation 3.51 with respect to V, N_d is given by:

$$N_d = \frac{2}{q.\varepsilon_0.\varepsilon_r.A^2} \frac{-1}{\frac{dC^{-2}}{dV}} \tag{3.53}$$

Equation 3.53 shows that the doping profile of the semiconductor material can be determined from a measurement of the capacitance-voltage profile of a Schottky diode.

3.5 Electro-optical measurements

3.5.1 Quantum efficiency measurements

Quantum-efficiency (QE) measurements quantify the spectral response of a device. The photocurrent response to a monochromatic probe beam is measured with defined QE. QE measurements require a calibrated reference device. Results presented here use as a reference, a crystalline silicon solar cell. It is necessary to distinguish between internal quantum-efficiency and external quantum-efficiency. External QE is the more commonly published result, and can be affected by factors "external" to the diode, such as reflections, and absorption in glass layers. Internal QE considers only the collection of those photons which are incident on the junction (rather than the device). Since internal QE is not reduced by reflection/glass absorption, it always exceeds external QE, and is often close

to unity over a significant spectral range. A schematic diagram of the QE measurement setup is given in figure 3.26. A projector equipped with a 100 W Xenon arc lamp is used as the light source at the input slit of the monochromator. A controlled mechanical chopper

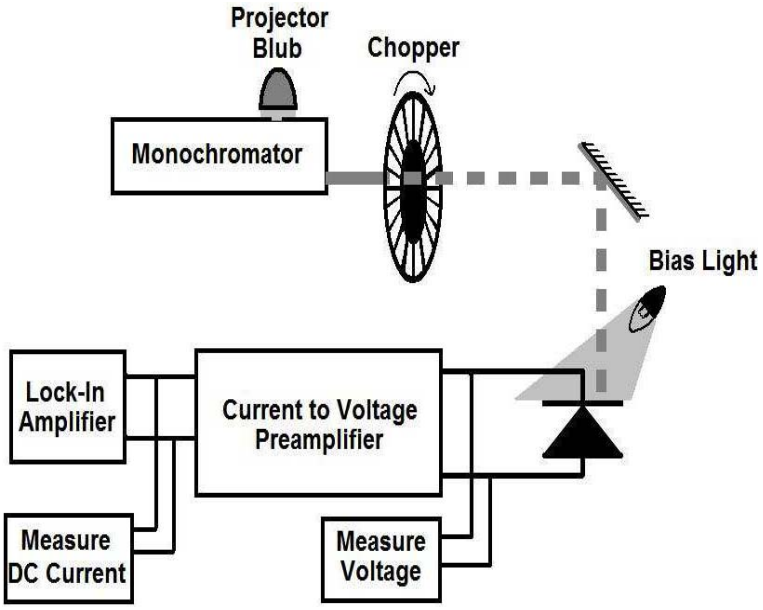

Figure 3.26: *Schematic diagram for QE measurement.*

modulates the probe beam at a specific frequency of 8 Hz, the beam is then collimated and focused into spot on the test device. The device is connected to a voltmeter for voltage monitoring. In parallel with the voltmeter, a current-to-voltage preamplifier converts the AC photocurrent into an oscillating voltage. The preamplifier allows the adjustment of the voltage bias. The oscillating voltage output of the preamplifier is measured by a lock-in amplifier. The lock-in reference frequency comes directly from the chopper controller, and a time-constant of 100 ms is generally used for data acquisition.

The fabricated devices were attached to a specific sample holder with two tips directed to the device (see figue 3.27 (a)) for measuring the photocurrent. The spectral response set-up is shown in figure 3.27 (b). QE data is taken in the range 350-500 nm with 5-nm increments. Temperature control during QE measurement is not necessary, since with monochromatic illumination and relatively weak bias light, devices stay at room temperature during measurement. The continuous output of the Xenon lamp passes through a computer controlled monochromator to produce a single wavelength output. The output of the monochromator is sent to the photodetector which is mounted on the probe station. We apply a DC bias with the Keithley 236 voltage source (see figure 3.28). Furthermore, in order for the device to attain equilibrium a delay of 5 seconds between

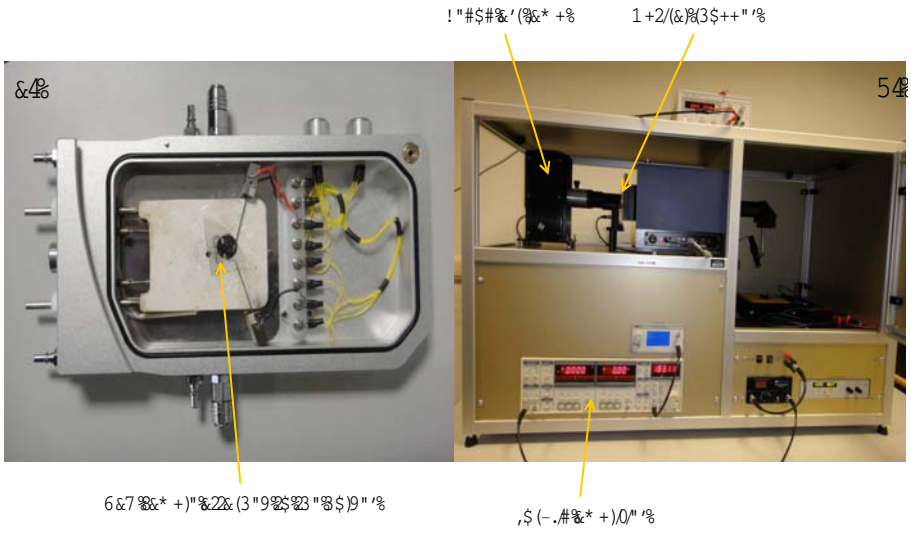

Figure 3.27: *Spectral response measurement set-up*

each wavelength step was used for all spectral response measurements.

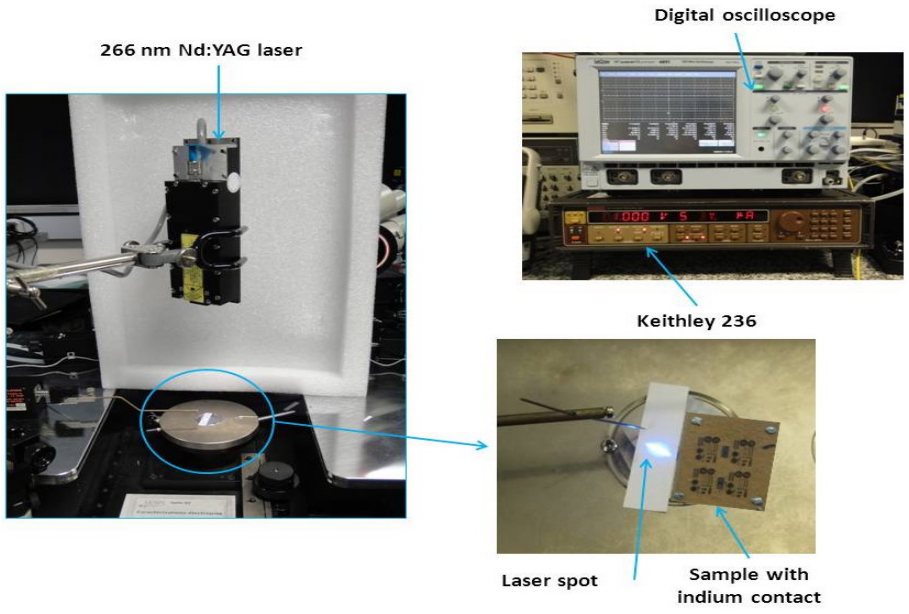

Figure 3.28: *Responsivity measurement set-up.*

Figure 3.29 shows the absorption coefficient of GaN at 300K as a function of the photon energy. Electrons in the valence band of a semiconductor can absorb photons whose energy are higher than the band gap energy E_g and jump to the conduction band. For a direct semiconductor, the absorption coefficient α(E) for an energy E higher than

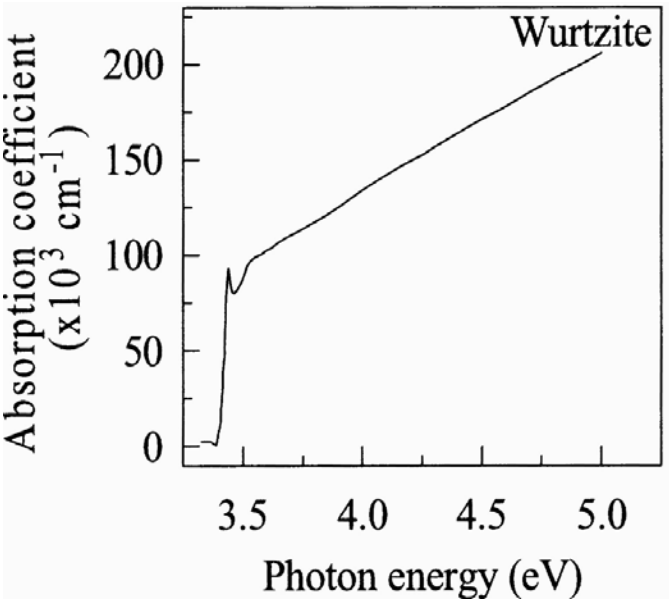

Figure 3.29: *Experimental absorption coefficient of wurtzite GaN at 300 K [203].*

the band gap energy is given by:

$$\alpha(E) = \alpha_0 \sqrt{\frac{E - E_g}{E_g}} \tag{3.54}$$

In addition, the layer thickness play an important role in absorption process. In this study layer thickness used was between 400 nm to 500 nm. However light should be absorbed in the depletion region of the diode formed in the active layer, to ensure that the electrons and holes are separated by the electric field and contribute to the photocurrent. This implies that a depletion region larger than the absorption length must exist in the detector. This is easily assured by making the absorbing layer undoped. Only a very small voltage is required to deplete the undoped region. If a minimum electric field is required throughout the absorbing layer, to ensure a short transit time, it is also the undoped structure, which satisfies this condition with a minimal voltage across the region, because the electric field is constant. The width of the depletion region can be approximated by:

$$W = \sqrt{\frac{2\epsilon_r \times \epsilon_0 \times (V_{bi} - V)}{qN_d}} \tag{3.55}$$

In our case, this calculation leads to an average value of the width which can be assumed to be larger than 300 nm. The length for which 99% of the photons are absorbed in the layer can be calculated using:

$$L_\alpha = -\frac{ln100}{\alpha(E)} \tag{3.56}$$

For our samples, the values of L_α are equal to 260 nm at λ=266 nm and 450 nm at λ=360 nm, respectively. At λ=266 nm, one can consider that all the photons are absorbed within the depletion region. On contrary, this is not totally the case at λ=360 nm. All responsivity measurements were performed by scanning the detector in the x and y directions until the maximum photocurrent at a specific wavelength was found. Since the wavelength range was limited to 350 nm minimum and for doing measurements in deep UV which is not reachable with this setup, we used a separate laser sources, Nd:YAG laser (emitting a wavelength of 266 nm, 0.1 ns pulse width, 10 kHz repetition rates as shown in figure 3.28) attached to a home made holder and mounted directly to the device. The laser spot area is equal to 0.05 cm^2 which is larger than all the devices under test, where the smallest (circular) and largest (interdigitated) device are 3.8x10^{-4} cm^2 and 9x10^{-4} cm^2 respectively. For an accurate measurements we did a simple calculation for obtaining exactly how much does our devices absorb. The output signal, voltage and time dependencies of the responsivity were recorded by a digital oscilloscope with a resolution of 1 ns as shown in figure 3.28. The responsivity measurements used in our study are voltage dependence R(V) and wavelength dependence R(λ). R(V) is obtained by maintaining the laser at a specific wavelength while illuminating the device and applying a variable voltage at the same time. R(λ) is obtained by applying a fixed bias while illuminating the device with variable wavelengths.

3.5.2 Time resolved measurements of the photocurrent

A photodiode takes a certain amount of time to respond to a sudden change in light levels. It is expressed in terms of rise time t_r and fall time t_f as shown in figure 3.30. Rise time is the time required for the output to rise from 10% to 90% of its final value. t_f is the fall time, defined as the time required for the output to fall from 90% to 10% of its value. The response time of a photodiode depends on many factors, like wavelength of incident light, the value of applied voltage across the diode which affects the junction capacitor and the load resistance. Time resolved measurements or time dependence of the photocurrent was divided into two categories long time and short time measurements as shown in figure 3.31. In long time measurements we calibrate the oscilloscope to count average power of the laser pulse. We start by illuminating our devices by specific wavelength for a few seconds and cutting the light immediately by using an automatic shutter (of 10 ms speed) after we see that the current is fully saturated and is not increasing with time. After the shutter blocking the incoming light, the devices is kept in dark while the current decrease

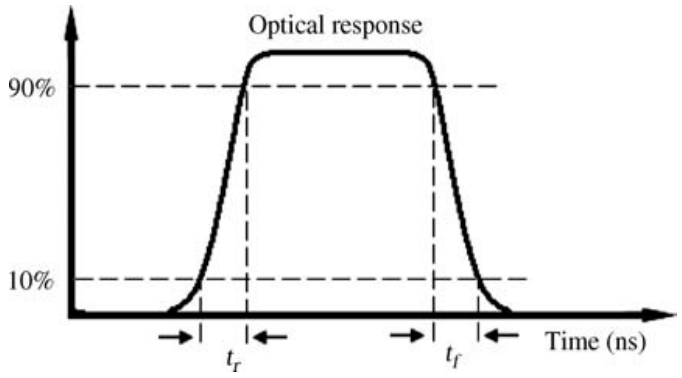

Figure 3.30: *Optical response of the photodiode.*

slowly with time until it reaches a nearly zero value. In short time measurements we calibrate the oscilloscope to take in account all the pulse power. The devices in this case absorbs optical pulse of duration about 1 ns and peak power of 11W.

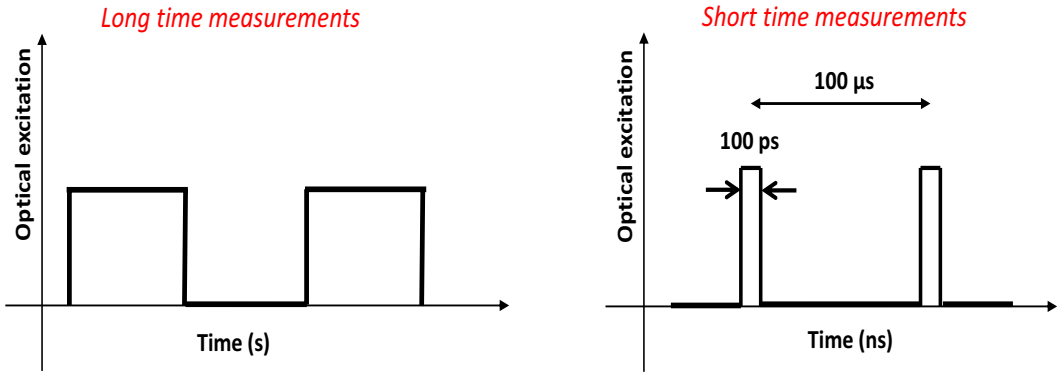

Figure 3.31: *Long and short time dependence of the photocurrent.*

Chapitre 4

Composants référence à base de GaN et AlGaN

Sommaire

4.1 Contacts ohmiques 103

4.2 Contacts Schottky 109

4.3 Photodétecteur Schottky 119

4.4 Photodétecteurs MSM 121

4.4.1 Mesures des courants d'obscurité 122

4.4.2 Mesures de la sensibilité 123

4.4.3 Réponse spectrale 124

4.5 Conclusions 126

Chapter 4

GaN and AlGaN devices as a reference

Contents

4.1 Ohmic contact 103

4.2 Schottky contact 109

4.3 Schottky photodetector 119

4.4 MSM photodetectors 121

4.4.1 Dark currents measurements 122

4.4.2 Responsivity measurements 123

4.4.3 Spectral response 124

4.5 Conclusions 126

4.1 Ohmic contact

In this chapter we will present the results obtained from our experiment on GaN and AlGaN devices in order to compare them to the new BAlGaN devices. Due to its wide band gap, III-Nitrides pose a problem in the development of low resistance ohmic contacts. Several attempts have been made over the past few years to obtain low resistance ohmic contacts on GaN [197, 204–206]. Foresi et al. [204] used Au or Al after annealing at 575°C, leading to contacts with a specific contact resistance ρ_c=$10^{-6}\Omega cm^2$. Tungsten (W) ohmic contacts on highly doped n-GaN with ρ_c=$10^{-4}\Omega cm^2$ have been obtained by Lin et al. [207]. Later, ohmic contacts on n-GaN were significantly improved [197] by using Ti/Al bilayer on GaN epitaxial layer followed by rapid thermal annealing (RTA) at 900C for 30s in an N_2 ambient, yielding ρ_c=8x$10^{-6}\Omega cm^2$. But Ti/Al metallization suffered from Ga outdiffusion and the subsequent reaction with Al leads to surface metal which is discontinuous with high resistivity. To overcome this problem and minimize the resistivity Wu et al. [206] added a second set of Ti/Al layer, following the annealing step, leading to a lowered resistivity ρ_c=3x$10^{-6}\Omega cm^2$. Despite the high metal resistivity and oxidation problem, the commonly accepted ohmic contact for n-GaN is the Ti/Al based metallization schemes, which have been investigated extensively [208–211]. However, the most frequently reported metallization schemes for ohmic contacts on $Al_xGa_{1-x}N$/GaN heterostructures were formed by Ti/Al/Ti/Au, Ti/Al/Ni/Au and Ti/Al/Pt/Au [209,212, 213]. These metallization schemes have shown the lowest contact resistances (0.04 Ω [212] $< R_c <$ 0.6 Ω [214]) and corresponding specific contact resistances ($5\times10^{-8}\Omega cm^2 < \rho_c < 3\times10^{-6}\Omega cm^2$ [214]). ρ_c was showed to depend on the Al content in the $Al_xGa_{1-x}N$ layers. Kim et al. [215] have reported an ohmic contact resistivity on AlGaN/GaN of about 7.5x$10^{-7}\Omega cm^2$ on Ti/Al/Ti/Au contacts annealed at 900°C which is lower than our value on AlGaN. The various metal layers in the metallization schemes described above, have their specific role in the formation of an ohmic contact to the $Al_xGa_{1-x}N$/GaN structures. Ti is the first layer that is deposited on the top and is believed to serve as an adhesion layer in order to provide good mechanical stability [209], dissolve the native oxide on the surface of the $Al_xGa_{1-x}N$ material [17, 212] and create nitrogen vacancies (V_N) by reacting with nitrogen atoms from the $Al_xGa_{1-x}N$ material at the interface and hence rendering this $Al_xGa_{1-x}N$ layer highly n-type doped [209, 212]. The followed Al metal layer is applied in order to react with Ti and form an Al_3Ti layer which is assumed to reduce the oxidation of the contracting Ti layer at the bottom [209, 212] and serves as a diffusion barrier for Ni or Pt because these metals form high Schottky barriers to n-type

$Al_xGa_{1-x}N$ [17]. Ni and Pt are used to form a diffusion barrier for the Au top layer. Furthermore, the Ni/Au or Pt/Au layers on top of the Ti/Al layers prohibit the Al to form drops or to smear out during high temperature annealing. From this overview of the literature we can notice that the actual mechanism of ohmic contact formation is still subject of discussion and yet to be understood. In this work we have used Ti/Al/Ti/Au (15/200/15/200nm) as ohmic contact on several GaN and AlGaN samples see (table 4.1). The fabrication process has been described in chapter 2.

Table 4.1: Different types of GaN and AlGaN samples used in our experiment. * GaN on sapphire, ** GaN on GaN-template

Materials	Thickness (μm)	Doping	Supplier	N_D (cm^{-3})	Label
GaN*	0.4	NID	TDI	$4.83x10^{18}$	GaN-A
GaN*	2	NID	TDI	$4.9x10^{17}$	GaN-B
GaN*	2	Fe-doped	TDI	$1.72x10^{17}$	GaN-C
GaN*	2.2	Si-doped	TDI	$1.18x10^{18}$	GaN-D
GaN*	3.5	NID	LUMILOG	$3x10^{18}$	GaN-E
GaN/GaN**	0.4/3.5	NID	LMOPS	$5.93x10^{18}$	GaN-F
AlGaN	1	Si-doped (∼20% Al)	TDI	—-	AlGaN-A
AlGaN/GaN**	0.14/3.5	undoped (∼20% Al)	LMOPS	$2.61x10^{18}$	AlGaN-B
AlGaN/GaN**	0.3/3.5	undoped	LMOPS	$2.61x10^{18}$	AlGaN-C

All the samples mentioned in table 4.1, were prepared according to the procedure described in chapter 3. Figure 4.1 shows an example of I-V measurements on the different samples. These measurements indicate that the variation of the current with voltage is perfectly linear with high current level up to 16 mA at low applied voltage. Contact resistances were derived from the plot of measured resistance versus gap spacing by TLM. From the I-V measurements the specific contact resistance is calculated and is repeated for contacts with same area and different spacing. By using a least squares linear regression fit to the experimental data, the specific contact resistance ρ_c, sheet resistance R_{sh} and transfer length L_t are calculated and deduced from the plot. This process is repeated for contacts of different areas.

Figure 4.2 shows the plot of the total resistance R_T versus the gap spacing d obtained in different samples. The sheet resistance is calculated from the slope of the line, the

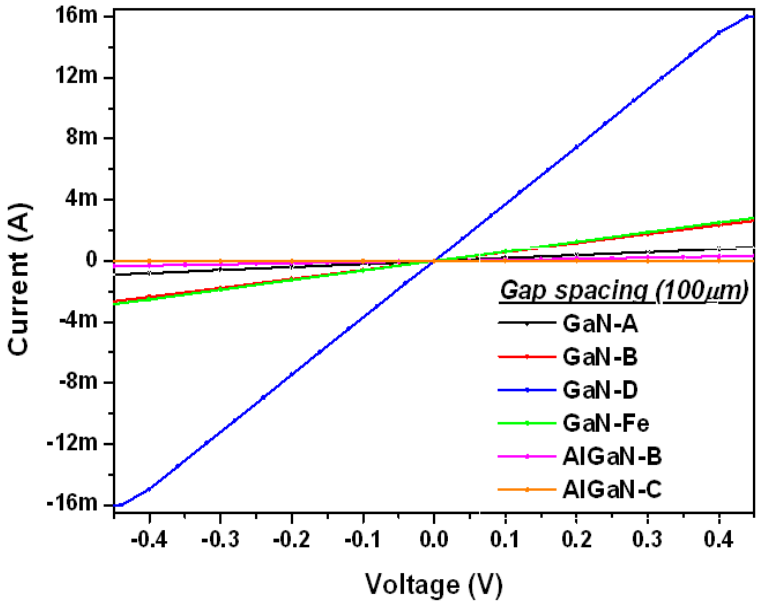

Figure 4.1: *An example of I-V measurements on various GaN and AlGaN samples.*

tranfer length L_T is extracted from the x-intercept of the line, and the total contact resistance is obtained from the y-intercept. The specific contact resistance is calculated using equation 3.43 in chapter 3. The determination of the specific contact resistances obtained for different contacts areas on different GaN and AlGaN samples is based on the assumption that the semiconductor sheet resistance R_{sh} underneath the contacts remains unchanged. This procedure has been used to the different samples under test. The results are summarized in the tables 4.2 to 4.6. Patterns with small gap spacings (patterns III, IV and V) leads to values of R_c, ρ_c, L_T and R_{sh} that are different from those obtained using patterns with larger spacing (I, II). This is probably due to the limitation of our photolithography process, for which the lift-off process is not always successful for removing all the residual between the pad gap, leading to pad connecting to each other and failure structure. Table 4.7 and 4.8 gives the average values of the different parameters extracted from table 4.2-4.6 according to the two sets (I-II and III-IV-V) of different spacing distance between electrodes. For a given patterns some values are out of the range of the others. These values have been excluded for the calculation of the average values. For example, in GaN-B, GaN-D and AlGaN-B the values of R_{sh} of patterns V is not in agreement with the rest of the values, which indicates that this may be due to a technical problem during the lithography process or due to a too small area of the contact pad compared to patterns I and II. In contrary, for GaN-D and GaN-F the results are in good agreement for both set of patterns I-II and III-IV-V. In both cases (I-II and

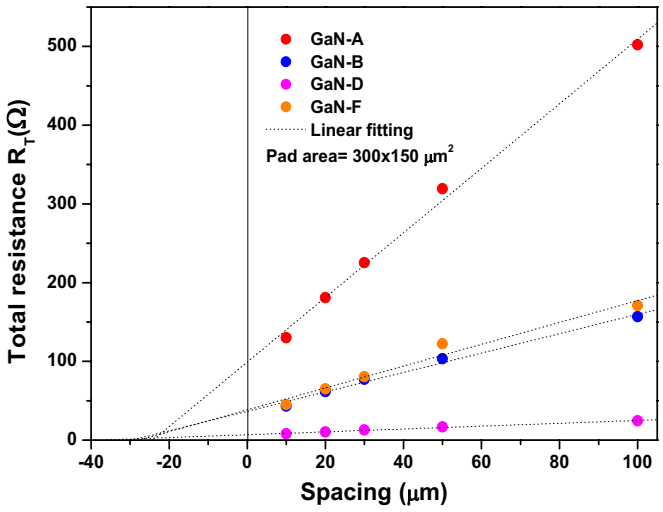

Figure 4.2: *Total resistance versus spacing as deduced from I-V measurements in the different devices.*

Table 4.2: Values of R_c, L_T, R_{sh} and ρ_c obtained on GaN-A and TLM analysis.

GaN-A	Pattern I	Pattern II	Pattern III	Pattern IV	Pattern V
R_c (Ω)	49.5	44.7	26.2	45.9	39.4
L_T (μm)	12	9.6	4.4	4.4	3.1
R_{sh} ($\Omega/\square$)	1230	1395	1800	1569	1887
ρ_c (Ω.cm^2)	1.77x10^{-3}	1.28x10^{-3}	3.42x10^{-4}	3x10^{-4}	1.8x10^{-4}
Pad surface (μm^2)	300x150	300x80	300x80	150x100	150x150
Pad spacing (μm)	10-20-30-50-100			5-10-15-20-25	

III-IV-V), AlGaN-B sample exhibits the largest values of R_{sh} and ρ_c. This is due to its large electrical resistivity, as extracted from Hall measurements and reported in table 4.9, since AlGaN material is known to be highly resistive due to the AlN composition. Among GaN samples, in both cases (I-II and III-IV-V), GaN-A exhibits the largest values of R_{sh} and ρ_c. This is due again to its large electrical resistivity (see table 4.9). The GaN-D sample shows, in a good agreement with its resistivity value, the lowest value of R_{sh} and ρ_c. Surprisingly, the value of R_{sh} for GaN-B sample, which has the largest resistivity, is relatively low and nearly equal to the corresponding value of the GaN-F sample for which the resistivity is the lowest one and two order of magnitude lower than the one of the

Table 4.3: Values of R_c, L_T, R_{sh} and ρ_c obtained on GaN-B and TLM analysis.

GaN-B	Pattern I	Pattern II	Pattern III	Pattern IV	Pattern V
R_c (Ω)	18.3	18	14.5	22.4	37.7
L_T (μm)	14.9	13	8.4	7.6	15.7
R_{sh} ($\Omega/\square$)	369	414	516	441	721.5
ρ_c ($\Omega.cm^2$)	$8.13x10^{-4}$	$6.9x10^{-4}$	$3.6x10^{-4}$	$2.54x10^{-4}$	$1.76x10^{-3}$
Pad surface (μm^2)	300x150	300x80	300x80	150x100	150x150
Pad spacing (μm)	10-20-30-50-100			5-10-15-20-25	

Table 4.4: Values of R_c, L_T, R_{sh} and ρ_c obtained on GaN-D and TLM analysis.

GaN-D	Pattern I	Pattern II	Pattern III	Pattern IV	Pattern V
R_c (Ω)	3.5	3.4	2.8	3.6	4.6
L_T (μm)	17.5	18.8	13.4	9.7	8.1
R_{sh} ($\Omega/\square$)	60	53.7	63	56.6	85
ρ_c ($\Omega.cm^2$)	$1.83x10^{-4}$	$1.89x10^{-4}$	$1.12x10^{-4}$	$0.5x10^{-4}$	$0.55x10^{-4}$
Pad surface (μm^2)	300x150	300x80	300x80	150x100	150x150
Pad spacing (μm)	10-20-30-50-100			5-10-15-20-25	

Table 4.5: Values of R_c, L_T, R_{sh} and ρ_c obtained on GaN-F and TLM analysis.

GaN-F	Pattern I	Pattern II	Pattern III	Pattern IV	Pattern V
R_c (Ω)	19.5	18.9	7.66	18.7	11.7
L_T (μm)	13.9	15	3.4	6.4	3.6
R_{sh} ($\Omega/\square$)	416	375	336	435	393
ρ_c ($\Omega.cm^2$)	$8x10^{-4}$	$5.77x10^{-4}$	$8.35x10^{-5}$	$1.8x10^{-5}$	$6.3x10^{-5}$
Pad surface (μm^2)	300x150	300x80	300x80	150x100	150x150
Pad spacing (μm)	10-20-30-50-100			5-10-15-20-25	

GaN-B sample. It is also to be noticed that the GaN-D and GaN-F, which have nearly the same resistivity, exhibit a large difference in their values of R_{sh}. This two facts could be attributed to the thickness difference of the layers (see table 4.9).

The reproducibility of the ohmic contact fabrication process and its results are ex-

Table 4.6: Values of R_c, L_T, R_{sh} and ρ_c obtained on AlGaN-B and TLM analysis.

AlGaN-B	Pattern I	Pattern II	Pattern III	Pattern IV	Pattern V
R_c (Ω)	110	106.6	11.7	76.3	82.8
L_T (μm)	6.2	5.4	7	1.7	1.7
R_{sh} ($\Omega/\square$)	5280	5943	5011	6684	7215
ρ_c (Ωcm^2)	2x10^{-3}	1.72x10^{-3}	2.4x10^{-4}	1.9x10^{-4}	2.1x10^{-4}
Pad surface (μm^2)	300x150	300x80	300x80	150x100	150x150
Pad spacing (μm)	10-20-30-50-100			5-10-15-20-25	

Table 4.7: Average values of N_D, R_{sh}, ρ_c, R_c, L_T and d of patterns I and II of gap spacing 10 μm.

	N_D (cm^{-3})	R_{sh} ($\Omega/\square$)	ρ_c (Ω.cm^2)	R_c (Ω)	L_T (μm)	d (μm)
GaN-A	4.8x10^{18}	1310±80	(1.5±0.25)x10^{-3}	47.1±2	10.8±1	0.4
GaN-B	4.9x10^{17}	390±20	(7.5±0.2)x10^{-4}	18.2±0.2	13.95±0.95	2
GaN-D	1.2x10^{18}	57±3	(1.86±0.03)x10^{-4}	3.45±0.05	18.15±0,65	2.2
GaN-F	6x10^{18}	395±20	(6.9±1.3)x10^{-4}	19.1±0.2	14.5±0.6	0.4
AlGaN-B	4.5x10^{18}	5610±300	(1.86± 0.14)x10^{-3}	108.3±1.7	5.8±0.4	0.14

Table 4.8: Average values of N_D, R_{sh}, ρ_c, R_c, L_T and d of patterns III, IV and V of gap spacing 5 μm.

	N_D (cm^{-3})	R_{sh} ($\Omega/\square$)	ρ_c (Ω.cm^2)	R_c (Ω)	L_T (μm)	d (μm)
GaN-A	4.8x10^{18}	1750±120	2.74±0.54 x10^{-4}	37.1±6.5	3.9±0.43	0.4
GaN-B	4.9x10^{17}	480±40	7.9±5 x10^{-4}	24.9±7	10.6±2.7	2
GaN-D	1.2x10^{18}	57±3	7.3±0.2 x10^{-5}	3.7±0.6	10.4±1.8	2.2
GaN-F	6x10^{18}	390±40	5.5±2.2 x10^{-5}	12.7±3.7	4.6±0.9	0.4
AlGaN-B	4.5x10^{18}	6950±300	2.2±0.16 x10^{-4}	57±23	3.47±1.76	0.14

tremely important for a reliable implementation of the photodetector fabrication process. We are convinced that our systematic approach of the optimization procedure has re-

Table 4.9: Link between electrical resistivity and R_{sh} and ρ_c values in GaN and AlGaN samples.

	μ (cm^2/v.s)	N_D (cm^{-3})	ρ (Ωm)	R_{sh} ($\Omega/\square$)	ρ_c ($\Omega.cm^2$)	d (μm)
GaN-A	46	4.8x10^{18}	23x10^{-3}	1310 - 1750	(0.27 - 1.5)$\times 10^{-3}$	0.4
GaN-B	71	4.9x10^{17}	17x10^{-2}	390 - 480	(7.5 - 7.9) $\times 10^{-4}$	2
GaN-D	248	1.2x10^{18}	28x10^{-4}	57	(7.3 - 18.6) $\times 10^{-5}$	2.2
GaN-F	50	6x10^{18}	21x10^{-4}	390 - 395	(5.5 - 69) $\times 10^{-5}$	0.4
AlGaN-B	33	4.5x10^{18}	4.16x10^{-2}	5610 - 6950	(2.2 - 18.6) $\times 10^{-4}$	0.14

sulted in ohmic contacts with as low as possible values for R_c and ρ_c as compared to literature [214, 215]. A contact resistance as low as 3.45 Ω and 57 Ω and specific contact resistance of values 5.5x$10^{-5}\Omega cm^2$ and 2.2x$10^{-4}\Omega cm^2$ on GaN and AlGaN respectively have been achieved.

4.2 Schottky contact

Schottky contacts on n-GaN play a vital role and is a critical step for the realization of a lot of electronic devices [201, 216–224]. The ideality factor n and more especially the barrier height ϕ_{Bn} are the most important characteristics of metal-semiconductor Schottky barrier contacts, both in researching their properties and in device applications. There are still large variations in barrier heights reported by different authors for standard metals (Ti, Pt, Au, Pd and Ni) on GaN. Pd appears to produce the lowest consistent values (0.51-0.97 eV) with Pt producing the highest values (0.99-1.08 eV) as reported in table 4.10. This variation appears due to the presence of different transport mechanisms, and to materials and process factors such as defects present in the active layer, the effectiveness of surface cleans prior to metal deposition, and variations in surface roughness which could affect uniformity of the results. Schmitz et al. [201] have reported different values on barrier heights and on the ideality factor that are independent of the metal type used. An increase in the value of ϕ_{Bn} with increasing temperature [219, 223, 225, 228] has been reported in various studies. This unexpected temperature dependence was attributed to some inhomogeneities of the Schottky barrier [225, 228] or to the tunneling effect in a highly defective material [219]. The debate is still open, despite all these numerous

Table 4.10: The different values of the Schottky barrier and ideality factor in GaN according to literature. Different growth techniques have been used: LPMOCVD [201], MOVPE [221], MOCVD [223, 225, 226], MBE [217].

Metal	Barrier height ϕ_b (eV)	Ideality factor n
Pt	1.08 [201], 0.88 [221], 0.99 [225]	1.04 [201], 1.1 [221], 1.42 [225]
Au	0.88 [201], 0.82 [223], 1.1 [217]	1.04 [201], 1.15 [223], 1.4 [217]
Ni	0.99 [201], 0.61–0.69 [219], 0.75 [225],0.82 [226]	1.04 [201], 1.19 [219], 1.98 [226]
Pd	0.92 [201], 0.69 [225], 0.51 and 0.97 [227]	1.04 [201], 1.58 [225], 2 [227]

studies for the realization of electrical contacts on GaN materials.

Schottky diode

We have then undertaken a larger study on the realization of Schottky diode on different GaN and AlGaN achieve layers. In this section we will address the Schottky diode which is the Schottky contact by applying Pt metallization scheme. I(V) measurements will be fully studied on this part of the diode on various GaN and AlGaN samples.

I-V characterization

A schematic structure of Schottky circular diodes used in this measurements are shown in figure 4.3. I-V measurements are used to evaluate the rectifying properties of the Schottky barrier diodes. I-V measurements were performed at room temperature on all the samples mentioned in the table 4.1 except for GaN-C omitted from this study due to its high resistivity that iron-doped caused. Figure 4.4 shows the typical (I-V) characteristics of circular Ti/Al/Ti/Au-GaN-Pt contacts on different GaN samples. A positive voltage has been applied to the Pt-Schottky contact, and a negative voltage has been applied to the Ti/Al/Ti/Au-Ohmic contact. The I-V characteristic shows a diode-like behavior for all GaN samples except for AlGaN samples (not shown here) the shape of the curves was not expected and its probably due to the high Al concentration. In order to find the values of n and ϕ_{Bn} of the GaN and AlGaN materials, we plotted a graph of ln(I) against V as shown in figure 4.5. The slope and the intercept from the linear fit to the log plot yield the ideality factor (n) and the barrier height ϕ_{Bn}. The values of the Schottky barrier height ϕ_{Bn} and ideality factor n are deduced from the I-V measurements

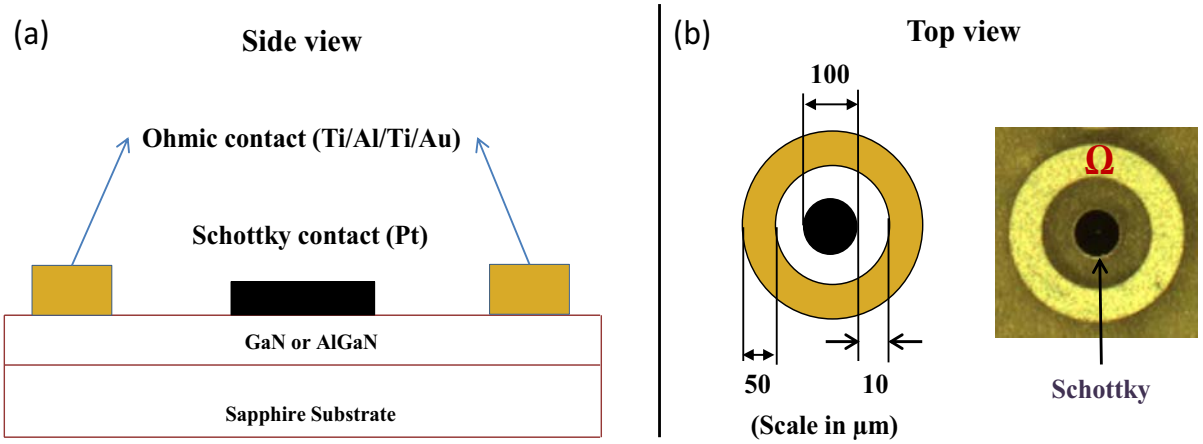

Figure 4.3: *Cross-sectional view (a), Optical microscope image (b)*

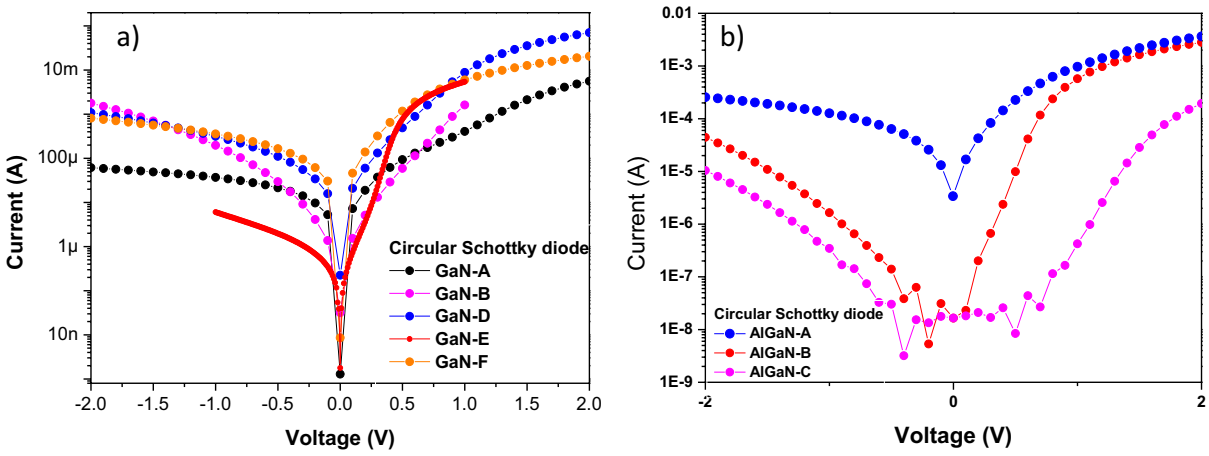

Figure 4.4: *I-V characteristics of Pt-Schottky contacts on different samples of GaN and AlGaN*

of figure 4.4 according to equation 3.6 in chapter 3, and reported in table 4.11. Since we applied the same conditions on whole the samples (chemical treatment, lithography, metal contact and annealed temperature) the output result yields high values of ideality factor and low values of barrier height and it is clear that the diodes ideality factor are much higher than the expected values (between 1 and 2) in GaN and AlGaN except for GaN-E. But these high values of n observed in our case are still in agreement with many cases reported in literature [229–234]. The high value of ideality factor is still not fully understood in GaN diodes. There are a lot of authors who have observed a high ideality factor ranging between 2 to 7 [230, 231, 235, 236]. For example, in GaN-based LEDs the high ideality factors (n$\gg$2) was attributed to deep level assisted tunneling [230, 231, 235]. Ideality factors close to 2 were attributed to space charge region recombination, consistent

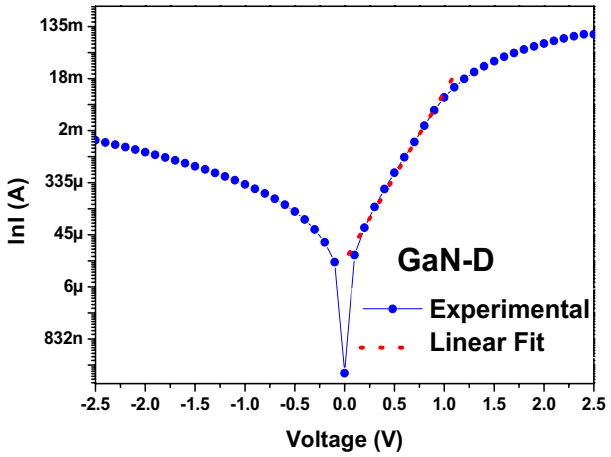

Figure 4.5: *Semilogarithmic plot of the current as a function of the bias voltage.*

with the theory proposed by Sah-Noyce-Schokley [237] due to temperature dependent slopes of (logI)-versus-V plots. Furthermore, Dumin and Pearson [238] stated that the excess currents in GaAs diodes were attributed to tunneling. However, the authors did not state the exact tunneling mechanism and suggested that the excess current could be due to band-to-band tunneling, band-impurity, or a cascade process. Since the only results obtained on GaN-E was in good agreement and comparable with state-of-the-art, therefore, we decided to go through further study on GaN-E.

Table 4.11: Barrier height and ideality factor of Schottky diode.

Sample (Circular diode)	Ideality factor n	Barrier height ϕ_b (eV)
GaN-A	10.2	0.255
GaN-B	4.5	0.32
GaN-D	5.7	0.24
GaN-E	1.3	0.74
GaN-F	5	0.23
AlGaN-A	6.8	0.34
AlGaN-B	2.9	0.42
AlGaN-C	4.4	0.56

Further study on GaN-E

I-V-T

Figure 4.6 shows an example of I-V curves obtained in a Pt-GaN-E Schottky diode at different temperature. For relatively large voltage (>0.7 V) the current saturates due to the effect of the series resistance [186]. For lower voltage, the characteristic exhibits two regimes characterized by two different slopes corresponding to different transport mechanisms. The one taking place in the intermediate voltage range (0.2-0.6 V) was shown [216] to be driven by thermionic emission (TE) and is preponderant at high temperature. In contrary, in the low voltage range (0 - 0.45 V), the current flow is dominated by the thermionic field emission (TFE), the total current is then the sum of both (see equation 3.19 and 3.20).

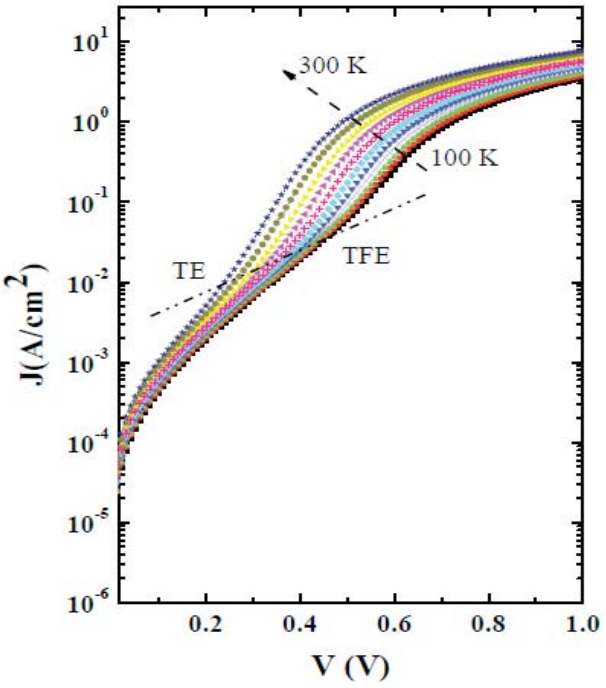

Figure 4.6: *Temperature dependence of the $J-V$ characteristics in a Pt/N-GaN Schottky diode. Temperature increases by step of $20K$ in the arrow direction. The dot-line indicates the separation between the two regimes: behind this line the TFE is preponderant, above this line the TE takes place.*

Ideality factor

Figure 4.7 shows that the values of n are ranging between 1.9 and 1.3 in the temperature range 180–300 K, and become larger than 2 for lower temperatures. The same dependence

of n with temperature has been reported for (Au, Pt, Pd, Ni)/N-GaN Schottky diodes [223, 225] with values of n in a rather good agreement with our results. This decrease of n with temperature has been interpreted in several ways. It has been described as a T_0 problem by Rhoderick [186], and attributed to fluctuations of the barrier height by Werner and Güttler [188] and Tung [239], as well as to the presence of a high interface states density by Levine [240] and Crowell [241]. The value of n obtained at room temperature ($n = 1.3$)

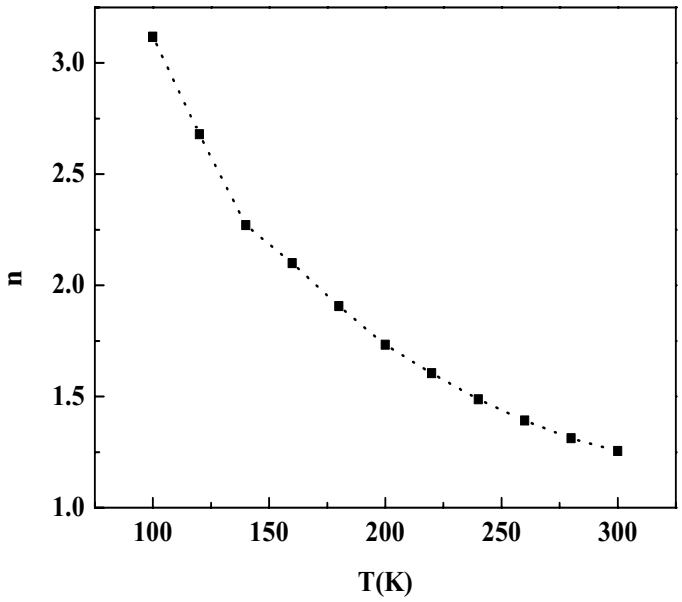

Figure 4.7: *Temperature dependence of the ideality factor in Pt/N-GaN Schottky structures*

is in a good agreement with the values reported in the literature [201, 216, 221, 224] for Pt/N-GaN Schottky diodes. Its higher-than-unity value can also be attributed to a higher doping concentration ($3.9\text{x}10^{18}\text{cm}^{-3}$), since it is well known that the ideality factor departs substantially when doping is increased [12].

Zero bias Schottky barrier height

The value of the Schottky barrier height has been deduced from the data of figure 4.6 according to equation 3.6, by extrapolating the logarithmic $I - V$ plot to $V = 0$. As shown in figure 4.8, the value of ϕ_{Bn} increases linearly with increasing temperature, in opposite to what could be expected for an ideal diode: the barrier height should decrease with temperature, owing to lattice expansion [186]. This increase of ϕ_{Bn} has also been reported for (Au, Pt, Pd, Ni)/N-GaN Schottky diodes [223,225]. TFE mechanism, which is a tunneling through the top of the barrier, can induce barrier height and ideality factor

changes with temperature. Using the values of $V_{bi}(T)$ as deduced from the intercept

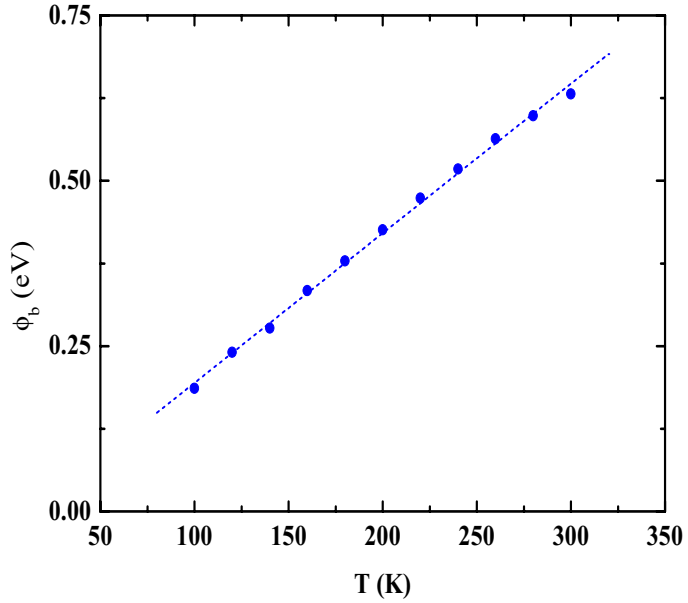

Figure 4.8: *Effective barrier height versus temperature as deduced from $I-V$ measurements.*

of the $1/C^2$ plot (not shown here), the barrier height variation has been estimated and plotted on figure 4.9. It shows that $\Delta\phi_{tunn}$ increases linearly with temperature, and that the contribution of this tunnel effect to the barrier height variation is equal to a ten of meV. This low value cannot explain the large variation of 0.4 eV observed in figure 4.8 between 100 K and 300 K. Thus the TFE effect cannot be responsible for the variations of ϕ_{Bn} shown in figure 4.8. This is reenforced by the calculated temperature dependence, according to equation 3.24, of the ideality factor which is plotted on figure 4.9. It results in a linear increase of the value of n_{tunn} from 1.1 to 1.3 for temperature varying between 77 K to 300 K, in contrast with our experiment which show a decrease of the ideality factor (see figure 4.7). Here we assume that this unexpected temperature dependence of ϕ_{Bn} is due to an unintentional interfacial layer, which can appear at the surface of the sample during the fabrication process or which can be due to an interface states effect linked to structural defects in the active layer such as nitrogen antisite or vacancies, for example. Thus we suggest an additional tunneling effect via the interface states, acting as an interfacial layer, as being responsible for these behavior of ϕ_{Bn} and n versus temperature.

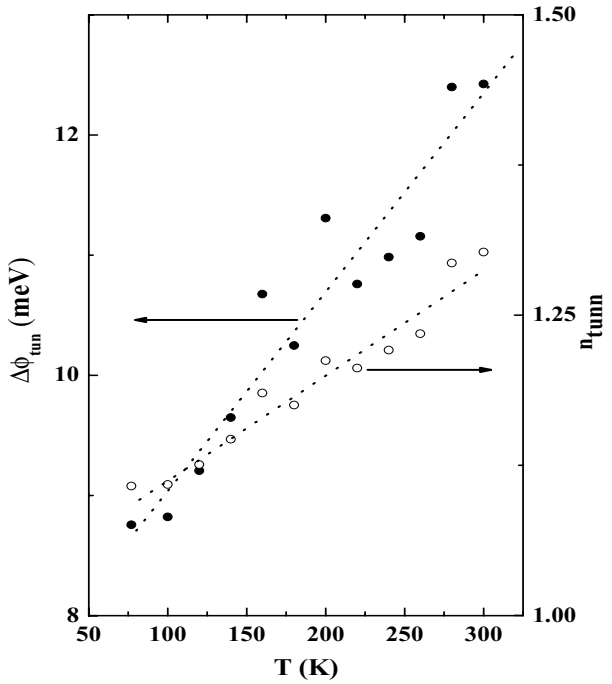

Figure 4.9: *Temperature dependence of the TFE contribution to the Schottky barrier height variation and ideality factor for the studied structures*

Interface states effects

The changes in the slope of the I-V curves observed on figure 4.6 reveal a change in the ideality factor n as a function of the voltage. These variations, as deduced from equation 3.19, and given by equation 3.16 are shown on figure 4.10. For each temperature, n increases with the increase of the voltage, up to a maximum and then decreases. Such behavior has been reported elsewhere on oxidized surfaces of GaAs [242] and InP [243] and has been attributed to interfaces states effects. Using equation 3.17 and data of figure 4.10, the voltage dependence $N_{ss}(V)$ can be determined. According to the relationship E_c-E=ϕ_{Bn0}-qV [225], where ϕ_{Bn0} is the room temperature value of the barrier height, the energy dependence of the interface states distribution $N_{SS}(E_c\text{-}E)$ has been derived and plotted on figure 4.11. This approach has been used in the case of GaAs [242] and InP [243], showing results in a good agreement with those obtained via DLTS measurements. This technique has the advantage to give a rapid way to get a correct estimation of the states density involved in the conduction mechanism since, these states being in equilibrium with the semiconductor, they allow charge transfer to, or from, the conduction band by capture and emission mechanism. As shown in figure 4.11, the energy dependence of N_{ss} exhibits the same behavior whatever the temperature. The interface states density

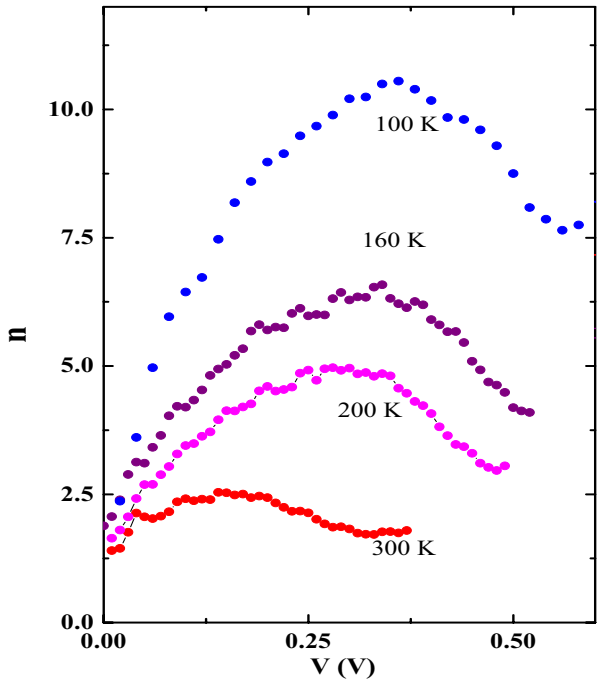

Figure 4.10: *Variations of the ideality factor n versus bias voltage V of Pt/N-GaN structures*

shows a broad peak centered at an energy which depends on the temperature. These energy values, ranging between 0.35 eV and 0.55 eV according to the temperature, are in a good agreement with those obtained by Cho et al. [244] (0.5-0.6 eV), Gotz et al. [245] (0.49 eV), and Tsarova et al. [246] (0.6 eV) using DLTS in GaN Schottky diodes, and are attributed to nitrogen anti-sites. These peaks can also originate from an unintentional surface oxidization which can occur during the fabrication process steps. Additional work is needed to precisely determine its origin.

The interface states play a major role in the charge transfer to or from the conduction band by capture and emission mechanisms or with the metal by tunneling. Those states behave like an interfacial layer through which carriers can move to the metal by tunneling and are responsible for the linear variation of ϕ_{Bn} and n versus temperature. As shown from the temperature dependence of the interface states density (see inset of figure 4.11), a temperature decrease leads the Fermi level to move into a higher interface states density, which makes it difficult to move, and consequently partially or completely pins the surface potential variations under an applied voltage. This results in an apparent higher ideality factor (see figure 4.10). The interface states acts as a low barrier height and thus, assist the tunneling of carriers to the metal and result in a higher current flow through the structure. In the opposite, when temperature increases, the interface states are partially

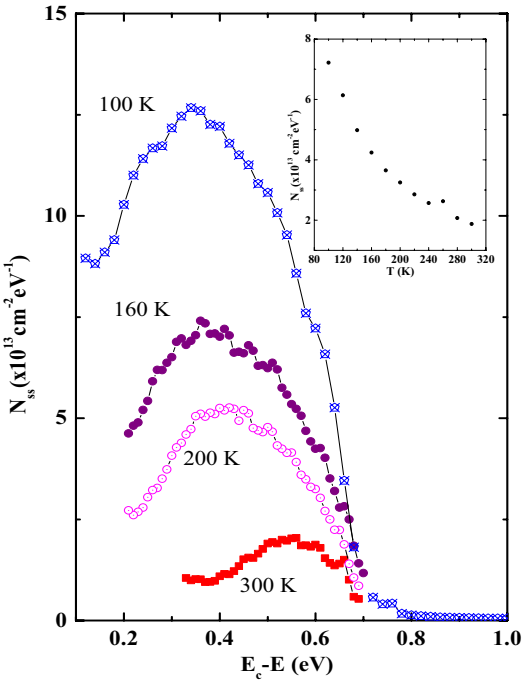

Figure 4.11: *Interface states distribution below the conduction band edge in the studied structures*

or completely filled, making the surface potential variations easier, and the corresponding ideality factor smaller. The current then follows the thermionic emission behavior and the measured barrier height is thus closer to the theoretical expected values.

These interfaces defects can also be responsible for some inhomogeneities of the Schottky barrier height as reported by Mamor et al. [225] and Mtangi et al. [228]. To confirm this interpretation, according to the data of figure 4.8a) and figure 4.7, we have plotted both the variations of ϕ_{Bn} and (n^{-1}-1) versus $\frac{1}{2k_BT}$ (see figure 4.12), and ϕ_{Bn} versus n (see inset of figure 4.12). The results show a quasi linear variation in both cases indicating a Gaussian barrier height distribution and a laterally inhomogeneous distribution of barrier heights as shown by Werner et Güttler [188] and Schmitsdorf et al. [247], respectively. From the data of the inset of figure 4.12 (extrapolated to $n = 1$), we can derive the value of the real barrier height which is equal to 0.74 eV in a rather good agreement with values obtained at room temperature. However, data of figure 4.12 (extrapolated to $\frac{1}{2k_BT}$ gives a zero bias barrier height value of 0.9 eV. This value is higher than all the measured values, but as reported by Werner et al. [188] the values of ϕ_{Bn} derived from I-V measurements are always smaller than this zero bias value.

Therefore, all these results show that, in accordance with Roccaforte et al. [248], the distribution of the interface states density can be pointed out as responsible for the

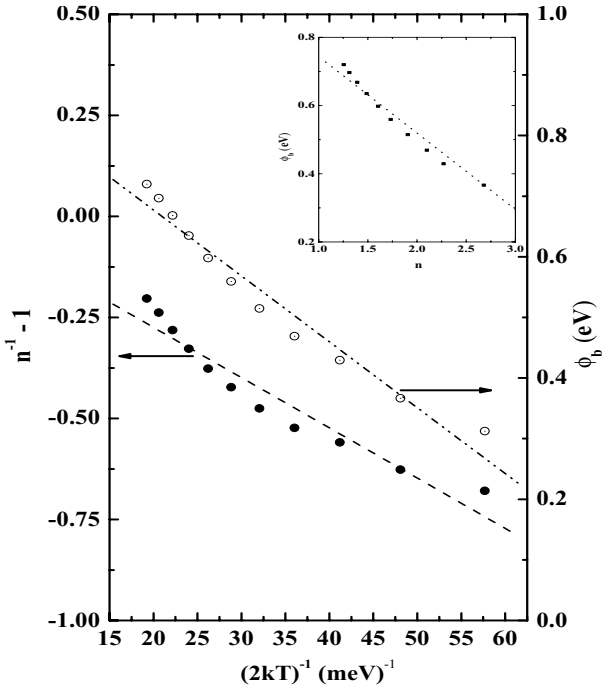

Figure 4.12: Barrier height ϕ_{Bn} and (n^{-1}-1) versus $\frac{1}{2k_BT}$ in the Pt/n–GaN Schottky diodes. The inset shows the barrier height ϕ_b as a function of n for the structure under test.

temperature dependence of ϕ_{Bn} and n. The interface states density is linked to the high dislocation density, generally observed in the GaN near surface region, which acts as defect traps, leading to a high interface defects density. The latter can partially pin the Fermi level, resulting in the wide variability of the Schottky barrier height values found in the literature, which are generally lower than the theoretically predicted ones.

4.3 Schottky photodetector

All the Schottky structures have been thus characterized for their electro-optical response. In this section we will thus report the optical properties of the Schottky photodetectors. For this, dark and photo-current have been measured and voltage and wavelength dependencies of the responsivity have been derived for the different samples.

Voltage and wavelength dependencies of the responsivity

Figure 4.13 shows a typical example of the voltage dependence of R as we have measured on the whole set of samples. This dependence indicates the presence of an internal gain and is in a good agreement with the one which is described by the model proposed by Katz et al. [162] (see section 2.2.6). As shown in figure 4.14, the best value of the SBH

decrease $\Delta\phi_b$ to correctly fit the experimental data is equal to 1.2 meV. A variation of 0.1 meV in the value of $\Delta\phi_b$ yields a non correct fit of the voltage dependence. This allow us to estimate the error on the $\Delta\phi_b$ parameter. In the following, the reported values of all the SBH decrease will be based on the same estimation obtained here and in all next analysis for Schottky and MSM based PDs.

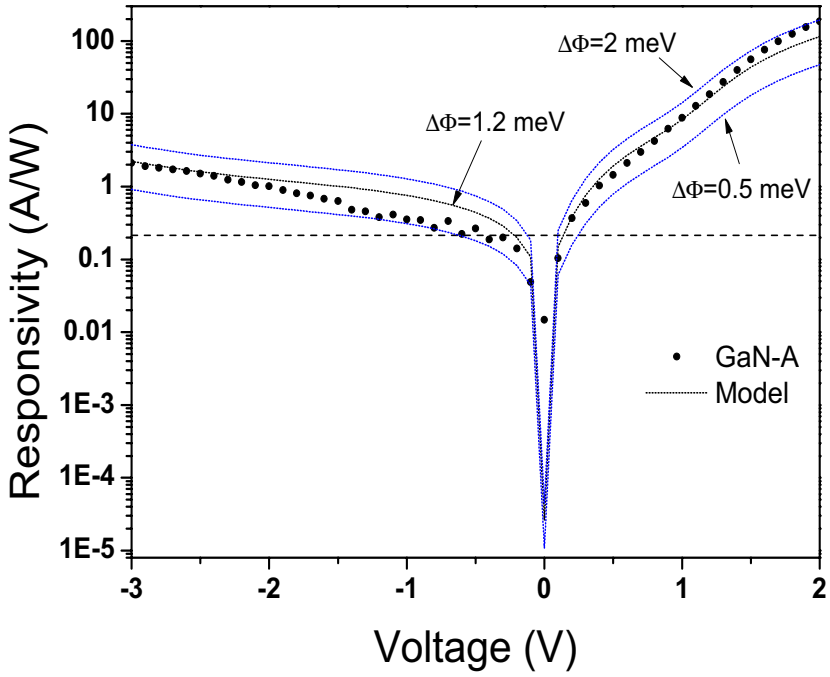

Figure 4.13: *Example of the model by Katz et al [162] applied to the voltage dependence of the responsivity with different values of the SBH decrease in the GaN-A based Schottky PD at λ=266nm.*

Figure 4.14 shows the voltage dependence of R obtained for the Schottky PD devices realized on GaN-A, GaN-D, GaN-F and AlGaN-A at λ=266nm with an optical power of 31.5 μW. This figure shows also the corresponding curves obtained with the model by Katz et al [162]. Internal gain is observed in GaN-A, GaN-D, GaN-F and AlGaN-A PDs for reverse applied voltage larger than 0.43V, 0.075V, 0.049V and 0.14V respectively. In order to discuss these results, the responsivity, dark current, SBH decrease and internal gain are reported in table 4.12. As expected, in the GaN-based PDs, since the SBH decrease values are nearly the same, the larger is the dark current, the larger are the responsivity and internal gain. In AlGaN-based PD, even if $\Delta\phi_b$ is rather large, the weak dark current (the dark current density is high because of the small area of the Schottky contact, but actually the dark current value is low) leads to a lower value of the responsivity and internal gain than in GaN-based PDs.

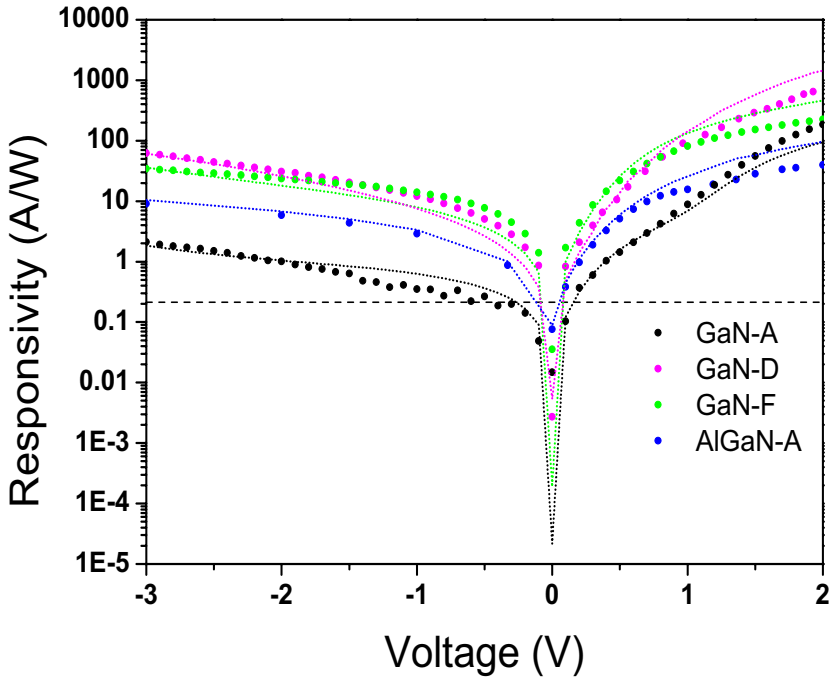

Figure 4.14: *Voltage dependence of the responsivity in GaN and AlGaN Schottky PDs at λ=266nm. The small doted lines and dashed line corresponds respectively to the model proposed by Katz [162] and theoretical value of R for 100% of Q.E. at λ=266nm.*

Table 4.12: Comparison between GaN and AlGaN Schottky photodetectors.

Sample	R (A/W) at λ=266nm, -3V	I_d (A) at -3V	J_d (A/cm^2) at -3V	$\Delta\phi_b$ (meV)	Gain at -3V
GaN-A	2.2± 0.1	61× 10^{-6}	1.4	1.2± 0.1	10
GaN-D	62± 3	1× 10^{-3}	32.4	1.4± 0.2	290
GaN-F	34± 1.7	8.2× 10^{-4}	20.6	1.3± 0.1	160
AlGaN-A	9± 0.5	2.6× 10^{-4}	50.4	20± 1	42

4.4 MSM photodetectors

In this section we will address the electrical and electro-optical characterizations of the GaN and AlGaN-based MSM PDs in order to obtain their voltage and wavelength responsivity dependences. The interdigitating PDs structures were fabricated with finger width equal to 300 μm and finger separation of 10μm. The fabrication process is obtained by using photolithography techniques outlined in chapter 3. This width and finger separation were chosen in accordance with the results of Monroy et al. [249] and Blue et al. [250],

who showed that width and finger separations $\leq$10 μm are required to maximize the measurable quantum efficiency of a MSM photodetector. Figure 2.12 shows fabricated MSM structure with detailed scale dimension. The overall dimension of the MSM was 300 $\times$300 μm^2. This 10 μm finger spacing design has an active area of $4\times10^4 \mu m^2$.

4.4.1 Dark currents measurements

Dark current measurements of the fabricated MSM photodiodes were performed up to a bias of $\pm$ 10V. All I-V measurements were performed in a dark environment at room temperature and are shown in figure 4.15. As expected, the detectors exhibited a sym-

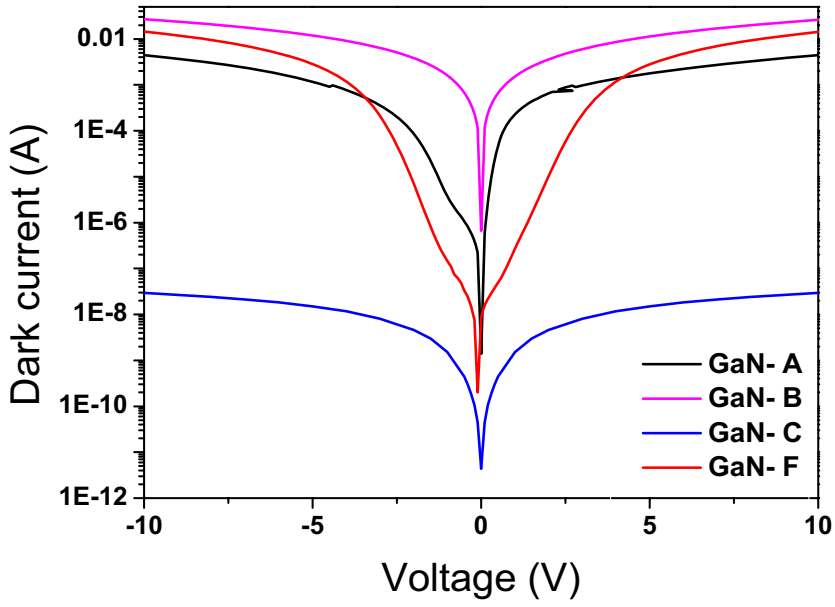

Figure 4.15: *Dark current versus voltage of different types of GaN based MSM photodiode*

metrical Schottky behavior with an equal current value in forward and reverse bias. This is because the structure has two diodes connected back to back so that the current cannot pass through in each direction. As expected, due to the Fe doping and thus a high electrical resistivity, the MSM photodiode fabricated on GaN-C has the lowest dark current. On contrary, the other MSM photodiodes exhibit rather large dark currents, with the largest one in GaN-F sample. This large dark current probably originates from a high-density threading dislocations and high background carrier concentration present in these samples.

4.4.2 Responsivity measurements

Figure 4.16 shows a typical example of the voltage dependence of R as we have measured on the whole set of samples. This dependence indicates the presence of an internal gain and is in a good agreement with the one which is described by the model proposed by Katz et al. [162] (see section 2.2.6). As shown in figure 4.14, the best value of the SBH decrease $\Delta\phi_b$ to correctly fit the experimental data is equal to 6 meV. A variation of 0.3 meV in the value of $\Delta\phi_b$ yields a non correct fit of the voltage dependence. As in the previous section, this allow us to estimate the error on the $\Delta\phi_b$ parameter. Figure 4.14

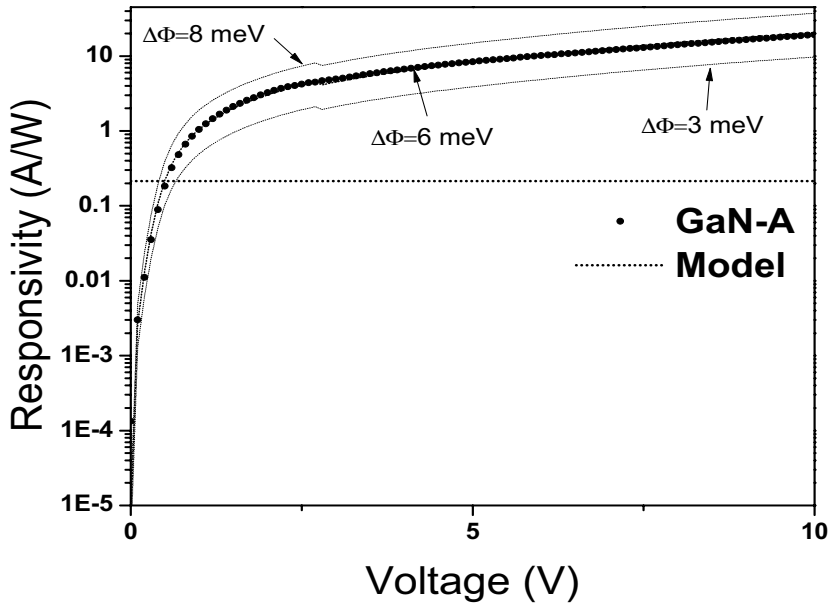

Figure 4.16: *Example of the model by Katz et al [162] applied to the voltage dependence of the responsivity at λ=266 nm with different values of the SBH decrease in the GaN-A based MSM PD.*

shows the voltage dependence of R obtained for the MSM PD devices realized on GaN-A, GaN-B, GaN-C and GaN-F at λ=266nm with an optical power of 56 μW. This figure shows also the corresponding curves obtained with the model by Katz et al [162]. As expected no internal gain is observed in GaN-C based PD whatever the applied bias due to the iron doping which limits the dark current. On contrary, internal gain is observed in GaN-B, GaN-A, and GaN-F for reverse applied voltage larger than 0.4V, 0.5V and 2.3V respectively. In order to discuss these results, the responsivity, dark current, SBH decrease and internal gain are reported in table 4.13. In contrary to Schottky PDs, the GaN-based PDs exhibit relatively different values of the SBH decrease. GaN-A and GaN-F based MSM PDs show close values of R. In this case, the effect on the internal gain

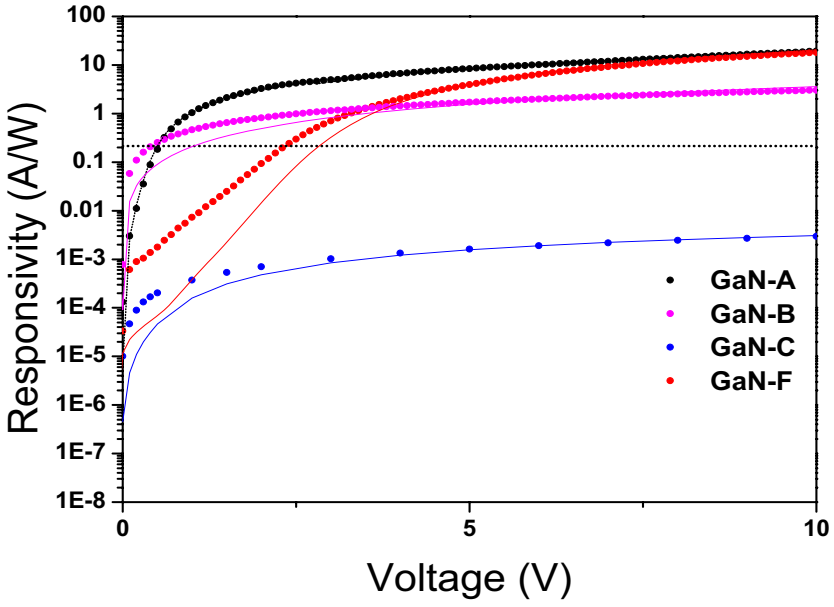

Figure 4.17: *Voltage dependence of the responsivity of the MSM photodetector with the model at λ=266 nm and P=56 μW. The small doted lines and dashed line corresponds to the model proposed by Katz [162] and theoretical value of R for 100% of Q.E. respectively.*

of the three times higher dark current in the GaN-F sample compared to the GaN-A, is counterbalanced by a three times lower SBH decrease. In the same way, the highest value of the dark current, which is obtained for the GaN-B sample, leads to a weak value of the internal gain since the SBH decrease is very low.

Table 4.13: Comparison between GaN MSM photodetectors under a bias of 10V.

Sample	R (A/W) at λ=266nm	I_d (A)	J_d (A/cm^2)	$\Delta\phi_b$ (meV)	Gain	UVVR
GaN-A	19± 1	4.4×10^{-3}	11.1	6± 0.3	90	2230
GaN-B	3± 0.15	26×10^{-3}	7.5	0.2± 0.01	15	570
GaN-C	(3± 0.15) $\times 10^{-3}$	29.4×10^{-9}	735 $\times 10^{-7}$	50± 3	–	550
GaN-F	18± 1	14.2×10^{-3}	35.5	2± 0.1	84	500

4.4.3 Spectral response

Normalized spectral response scans were made from 350 nm to 500 nm with a 1 nm wavelength step. Figure 4.18 shows the spectral response curves of the MSM GaN pho-

todetectors at an applied bias of 17 V. All the spectral response curves exhibit a photopeak located at 360 nm, 361 nm, 366 nm and 370 nm for GaN-A, GaN-F, GaN-B , and GaN-C based MSM PDs, respectively. These peaks correspond to the cut-off wavelengths λ_c. For wavelengths larger than λ_c the photocurrent drops by several orders of magnitude and the response of the detector is cut-off. This red-shift of the wavelength cutoff is due, in the case of GaN-C based PD, to the absorption introduced by the density of states tails, and the Fe^{3+}-ions incorporated in the GaN-lattice [251]. In contrary, the wavelength cutoff of GaN-A are very close to GaN-F and far from GaN-B. The reason for this wavelength cutoff shift is probably related to the difference in GaN layer thickness and maybe due to a variation in threading dislocations from one sample to other. It is important to notice that the decrease of R after the cut off wavelength in the case of the GaN-F sample is less pronounced than for the others samples. This could be attributed to a higher dislocation density existing in this sample. Due to the same reason the UV/Visible contrast ratio (calculated as a ratio of the photocurrent at 266 nm divided by the photocurrent at 500 nm) reported in table 4.13 is higher for GaN-A than for GaN-B, GaN-C and GaN-F based PDs.

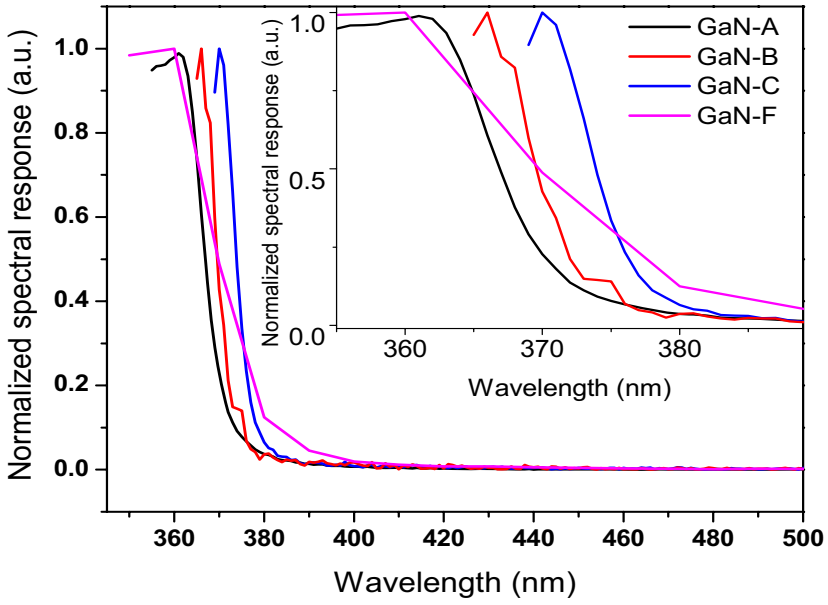

Figure 4.18: *Spectral response curves measured at a bias of 17 V in the MSM GaN PDs*

4.5 Conclusions

We have designed, fabricated, and characterized GaN and AlGaN based Schottky and MSM photodetectors. These studies have arrived at different conclusions with some of the results obtained on both Schottky and MSM PDs supporting the literature and the state-of-the-art achievements while other findings were inconsistent with published results and displayed high variation. This inconsistency in part of our results could probably relate to the various origins of GaN and AlGaN layers (thickness, carrier concentration, dislocations, surface quality and etc...) used and supplied by three different laboratory LUMILOG, LMOPS and TDI. Among all the samples used in our study, we have succeeded in developing excellent Schottky diode on GaN (GaN-E, LUMILOG) and AlGaN (AlGaN-A, TDI) and in obtaining low ohmic contact resistance, low dark current, high responsivity and gain on almost all the devices. We have presented herein a full study on Schottky and MSM PDs, covering complete analysis of the electrical measurements of the ohmic contact by using the linear TLM model. In this work, we have achieved a metallization scheme of Ti/Al/Ti/Au with low contact resistance on GaN and AlGaN. Furthermore, low dark current of Pt contact on the second part of the Schottky diode has been obtained on various GaN and AlGaN. Since all GaN materials showed high ideality factor and low barrier height except for GaN-E which resulted in ideality factor and Schottky barrier values highly consistent with state-of-the-art studies and therefore further studies are being carried out on GaN-E to elucidate the underlying reason.

Chapitre 5

Photodétecteur à base de BAlGaN

Sommaire

5.1 Introduction 128

5.2 Contact ohmique sur BGaN 130

5.3 Diodes Schottky $B_xGa_{1-x}N$ 132

5.4 Photodétecteur Schottky à base de $B_xGa_{1-x}N$ 134

5.5 Photodétecteurs MSM à base de BGAN et BAlGaN 135

5.5.1 Caractérisation I-V 135

5.5.2 Dépendance en tension de la sensibilité 137

5.5.3 Dépendance en puissance optique de la sensibilité 139

5.5.4 Réponse spectrale 139

5.5.5 Temps de réponse 142

5.6 Conclusions 144

Chapter 5

BAlGaN UV Photodetector

Contents

5.1 Introduction 128

5.2 Ohmic contact on $B_xGa_{1-x}N$ 130

5.3 $B_xGa_{1-x}N$ Schottky diodes 132

5.4 $B_xGa_{1-x}N$ Schottky photodetector 134

5.5 BGaN and BAlGaN superlattice MSM photodetectors 135

5.5.1 I-V characterization 135

5.5.2 Voltage dependence of the responsivity 137

5.5.3 Optical power dependence of the responsivity 139

5.5.4 Spectral response 140

5.5.5 Response time 142

5.6 Conclusions 145

5.1 Introduction

In an attempt to improve the reliability and performance of UV photodetectors, we have thus incorporated boron in GaN materials. The lattice-mismatch reduction with AlN substrate leads to better structural and morphological qualities, optimized electronic transport properties is expected. In this chapter we are going to fabricate and characterize electrically and optically the Schottky and MSM PDs on $B_xGa_{1-x}N$ material. To study the electrical and optical transport properties of this material two steps are initially required. The first step is to realize and optimize ohmic and Schottky contacts and the second step is illuminating these diodes by specific wavelengths. Ohmic and Schottky contact used in this study consist of the same recipe (Ti/Al/Ti/Au-ohmic and Pt-Schottky) used on GaN and AlGaN material as already shown in chapter 4. The BGaN material-based PDs are fall in two categories the design of the samples used in this work are schematically shown in figure 5.1. The first category are the BGaN monolayers with several boron incorporation rates varying from 0% (GaN-F) up to 0.82% grown on GaN and AlN templates. The

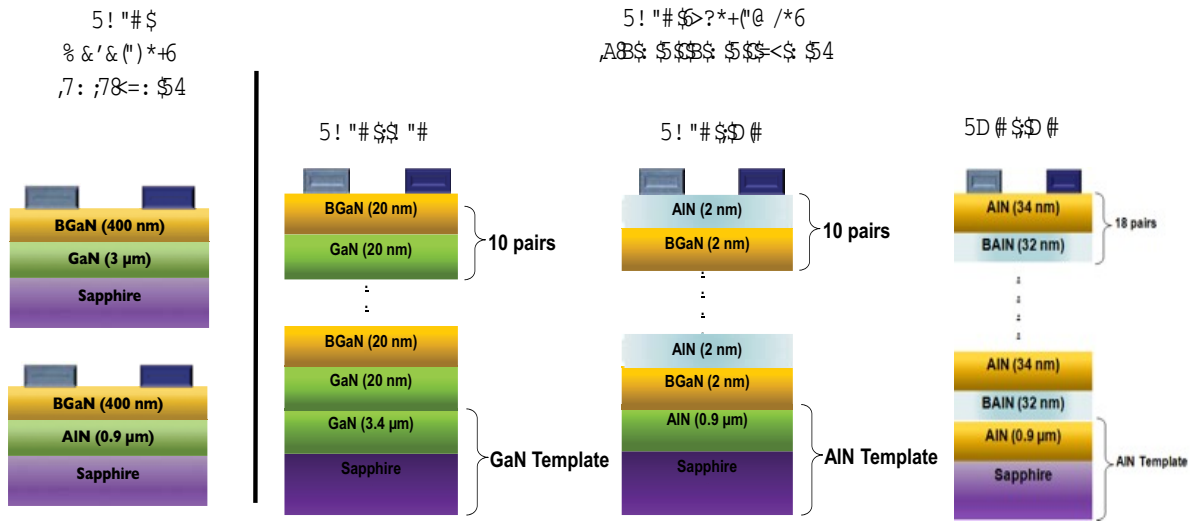

Figure 5.1: *Schematic structure of the BGaN supper lattice on GaN and AlN templates*

second category are BGaN supperlattices structures which is divided into three parts:

1. part one is BGaN-GaN consisting of 10 pairs of 20 nm thick BGaN with 3.6% B and 20 nm thick GaN.

2. part two is BGaN-AlN consisting of 10 pair of 2nm thick BGaN with 6% B and 2 nm thick AlN and finally.

3. part three is BAlN-AlN consisting of 18 pair of 34 nm(AlN) and 32nm (BAlN) thick with 28% B grown on GaN and AlN templates respectively.

All the samples used in this work are reported in table 5.1 below. It is not easy to obtain good quality ohmic contacts in large band gap semiconductors such as BGaN and specially with high boron concentration (BGaN-SLs) which exhibits moreover a large electrical resistivity even for low boron concentration [106]. Since BGaN supperlattices exhibit high resistivity there were no possibility to obtain ohmic contacts on them. Therefore, Schottky PDs are only fabricated on BGaN monolayers and MSM PDs are fabricated on both BGaN monolayer and supperlattices. All the BGaN structures (monolayers and

Table 5.1: BGaN monolayer and quasi-alloy with different boron (%) composition

Material	Boron composition (%)	Type
GaN-F	0	Monolayer
$B_xGa_{1-x}N$/GaN	0.05	Monolayer
$B_xGa_{1-x}N$/GaN	0.48	Monolayer
$B_xGa_{1-x}N$/AlN	0.5	Monolayer
$B_xGa_{1-x}N$/AlN	0.6	Monolayer
$B_xGa_{1-x}N$/AlN	0.7	Monolayer
$B_xGa_{1-x}N$/AlN	0.82	Monolayer
BGaN/GaN-SL	3.6	SupperLattice
BGaN/AlN-SL	6	SupperLattice
BAlN/AlN-SL	28	SupperLattice

SLs) were grown by MOVPE using a T-shape reactor. TMG, TEB and NH_3 were used as source for gallium, boron, and nitrogen, respectively. Details on the growth conditions, boron incorporation, and layers morphology are mentioned in previous works [92, 93]. As we already mentioned in chapter 4, a large variety of GaN and AlGaN samples have been studied. Among all these GaN samples we chose our home-made GaN-F sample as a reference for Schottky PDs and GaN-A sample as a reference for MSM PDs due to their convenient layer thicknesses and performances.

5.2 Ohmic contact on $B_xGa_{1-x}N$

In this section, ohmic contact study will address the $B_xGa_{1-x}N$ monolayer with boron composition up to 0.7%. The fabrication of the ohmic contact on BGaN of 0.82% was almost impossible due to the high layer resistivity. Figure 5.2 shows an example of current-voltage measurements in the BGaN samples for different boron concentrations. All the I-V dependencies are linear, indicating a perfect ohmic behavior of the electrical contact. As expected, for a same value of the applied voltage, higher is the boron concentration, lower is the injected current. Figure 5.3 shows an example of the dependence of the total

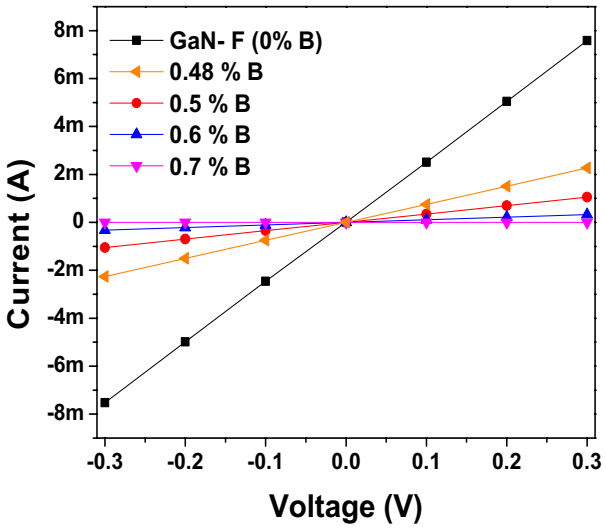

Figure 5.2: *Example of I-V measurements in BGaN samples for different boron concentrations*

resistance R_T, as it can be derived from I-V meaurements in BGaN with 0.5% of boron and for different pad lengths. The values of the sheet resistance R_{SH} and the specific contact resistance ρ_c derived from data of figure 5.3 are reported in table 5.2. All these values are obtained by using the different set of pads distributed on the whole surface of the samples. For boron concentrations up to 0.48%, the value of ρ_c is in the range of $10^{-4}\Omega cm^2$, increases to $10^{-3}\Omega cm^2$ for boron concentration up to 0.6% and reaches tens of Ωcm^2 for higher concentrations. This increase is expected since, as seen in table 5.2, the resistivity, and thus the sheet resistance R_{SH}, of the BGaN films increases with the boron concentration leading to less efficient ohmic contacts. Table 5.2 and figure 5.4 show also a spreading of the values of both R_{SH} and ρ_c for boron concentration higher than 0.6%, revealing inhomogeneous properties of the BGaN layer for high boron concentrations, which was evidenced by our group by using transmission electronic microscopy [95]. We

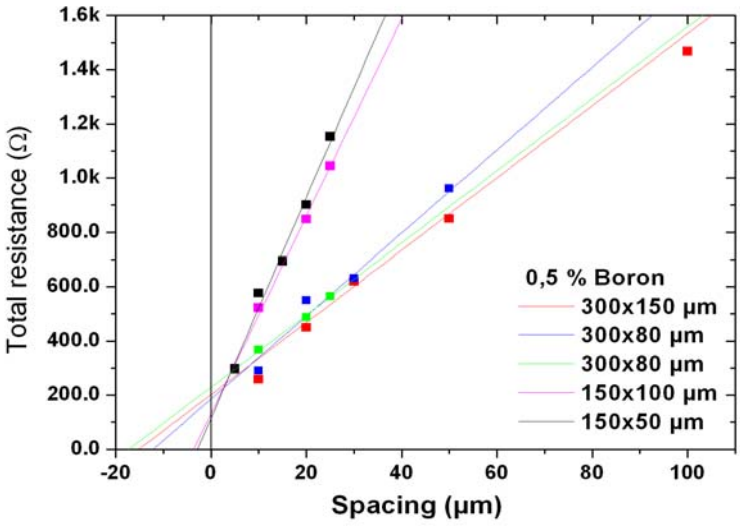

Figure 5.3: *Plot of the total resistance R_T as function of the spacing d between two pads in BGaN with boron concentration of 0.5%.*

have shown that for high boron concentration, nanometer sized zinc-blend BGaN clusters, containing about 20% of boron and representing a few percent of the total volume, appear in the BGaN matrix. These clusters, if not homogeneously distributed in the matrix, can affect the transport properties and lead to variations of the sheet resistance in the BGaN layer.

Table 5.2: Values of the sheet resistance R_{SH} and the specific contact resistance ρ_c in BGaN for different boron concentrations

Boron concentration (%)	Specific contact resistance (Ω.cm^2)	R_{SH} ($\Omega/\square$)
0	1x10^{-4}-3x10^{-4}	53±1
0.48	2x10^{-4}-6x10^{-4}	445±50
0.5	1x10^{-3}-2x10^{-3}	(4.3±0.6)x10^3
0.6	0.6x10^{-3}-6x10^{-3}	10x10^3-30x10^3
0.7	2-40	80x10^3-285x10^3

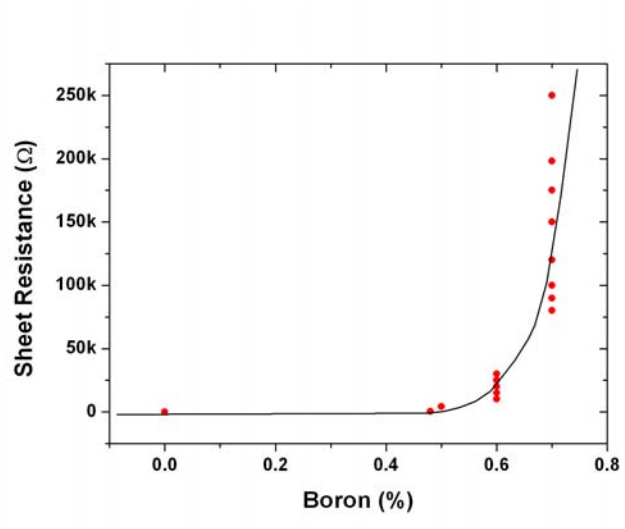

Figure 5.4: *Dependence of the sheet resistance R_{SH} with the boron concentration in BGaN.*

5.3 $B_xGa_{1-x}N$ Schottky diodes

I-V characteristics

As we mentioned above, due to the large resistivity of the BGaN layer, Schottky barrier diodes are only fabricated on BGaN monolayer with B concentration up to 0.7%. The I-V characteristics for $B_xGa_{1-x}N$ Schottky diodes with as deposited Schottky Pt (150nm) and annealed ohmic contacts Ti/Al/Ti/Au (10/250/8/150nm) are shown in figure 5.5. All the measurements were undertaken in dark condition for the whole set of BGaN devices (from x=0% to x=0.82%) and a Schottky diode like behavior is obtained. The dark current in the BGaN monolayers decreases as expected, down to a few μA at high reverse bias (I_d=0.51 μA at -100V for x=0.82%B) due to the large increase of the layer resistivity caused by the increase of the boron concentration. It is clear that the boron composition control the BGaN layer resistivity since, at -5V for x=0% I_d=27 mA, and by adding a small amount of x=0.05% of B the dark current is slightly decreased to I_d=21 mA. By continuing adding B up to 0.82%B the layer become very resistive and the dark current reaches 2.8 nA. In Schottky barrier diodes, the barrier height depends on the voltage and surface conditions prior to metal deposition. The surface condition includes the thickness of the interfacial oxide, which affects the current-transport mechanisms. These include the thermionic emission, which is characterized by ideality factor close to unity and thermionic field emission and field emission. These mechanisms are affected by series resistance, tunneling

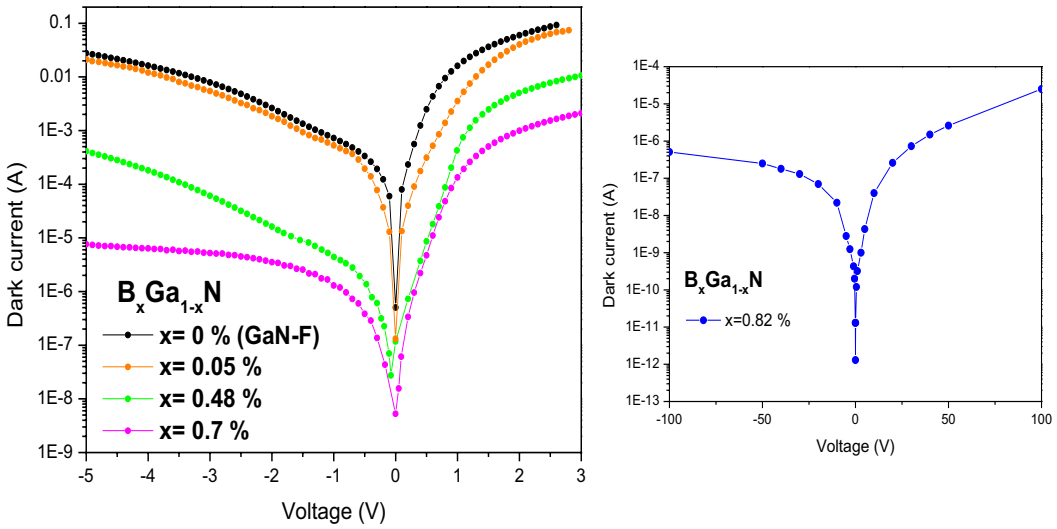

Figure 5.5: *The dark current-voltage (I-V) characteristics for $B_xGa_{1-x}N$ Schottky photodetectors.*

and generation recombination in the depletion region. By using the data of figure 5.5, the values of the Schottky barrier height ϕ_{Bn}, ideality factor n are deduced from equation 3.6 (based on the same analysis done on GaN and AlGaN material in chapter 4) and the carrier concentration from Hall measurements are reported in table 5.3. It is obvious

Table 5.3: Barrier height and Ideality factor for circular photodiode

$B_xGa_{1-x}N$	Ideality factor n	Barrier height ϕ_{Bn} (eV)	Carrier Concentration (cm^{-3})
x=0 % (GaN-F)	4.5	0.4	$5.9x10^{18}$
x=0.05 %	6	0.5	$4.7x10^{18}$
x=0.48 %	4.4	0.42	$2.4x10^{18}$
x=0.7 %	2.9	0.47	$3x10^{17}$
x=0.82 %	6	0.83	$1x10^{17}$

that the ideality factors n for BGaN is above unity and it is attributed to, interface states due to thin oxide layer between the metal and the semiconductor, including other contaminations, tunneling currents in highly doped semiconductors, image-force lowering of the Schottky barrier in electric field at the interface, and generation-recombination currents within the depletion region [177]. The barrier height ϕ_{Bn} varies between 0.4 to 0.8 eV while the carrier concentration decrease with B concentration increase. Seemingly,

as the boron concentration increase the carrier concentration decrease, which also provide us with an additional explanation for why the dark current decrease with the increase of the boron concentration.

5.4 $B_xGa_{1-x}N$ Schottky photodetector

Voltage dependence of the responsivity

We first have studied the photocurrent and thus the responsivity at a bias of 0 V. Figure 5.6 shows the dependence of the responsivity at a bias of 0 V with the boron concentration for Schottky-based PDs. Under this condition, no internal gain is expected and the photocurrent is given by:

$$I_\lambda = qSP\left\{1-\exp\left(-\alpha d\right)\right\} = qSP\left\{1-\exp\left[-\alpha\sqrt{\frac{2\varepsilon(V_{bi}-V)}{qN_D}}\right]\right\} \tag{5.1}$$

where S is the device area, P is the optical power, d is the active layer thickness, and α is the absorption coefficient. Since the B incorporation yields a decrease of N_D, according to the previous equation, the responsivity should increase with the B incorporation. As shown in figure 5.6, this is the case for B incorporation ranging between 0.05% and 0.82 %. Nevertheless, a large decrease in the responsivity is observed between the pure GaN sample and the one with 0.05 % B. This could be attributed to a higher recombination center number in the BGaN sample than in the GaN sample, since BGaN material exhibits higher structural defects than GaN material.

Figure 5.7 shows the voltage dependence of the responsivity for the different BGaN devices at λ= 266 nm and an optical power of 31.5 μW. This figure shows also the corresponding curves obtained with the model by Katz et al [162]. An internal gain is observed for an applied reverse voltage larger than 0.072V (0%B), 0.38V (0.05%B), 1.2V (0.48%B) and 1.5V (0.7%B) and for direct voltage larger than 0.077 V (0%B), 0.34 V (0.05%B), 0.51 V (0.48%B) and 0.46 V (0.7%B). In contrary, in the BGaN(0.82%B) PD, no internal gain is observed whatever the applied reverse bias voltage. In order to discuss these results, the responsivity, dark current, SBH decrease and internal gain for all PDs are reported in table 5.4. It is obvious that the incorporation of B in GaN leads to a high resistive material and consequently decrease the dark current as well as the gain. The variation of the responsivity from one PD to the other is closely related to the value of the dark current. It is also to be noticed that the SBH decrease increases with the B incorporation up to 0.7%.

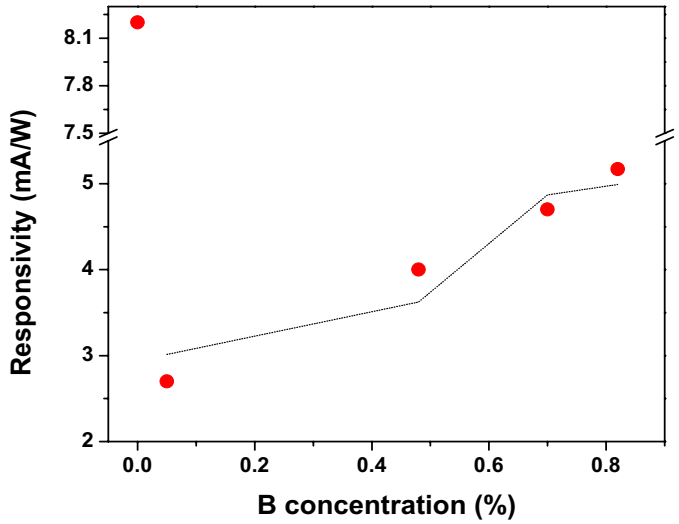

Figure 5.6: *Responsivity as function of the boron concentration at zero bias for Schottky photodetector illuminated at 266 nm with an optical power of 31.5 μW. The doted line corresponds to values obtained via the equation 5.1*

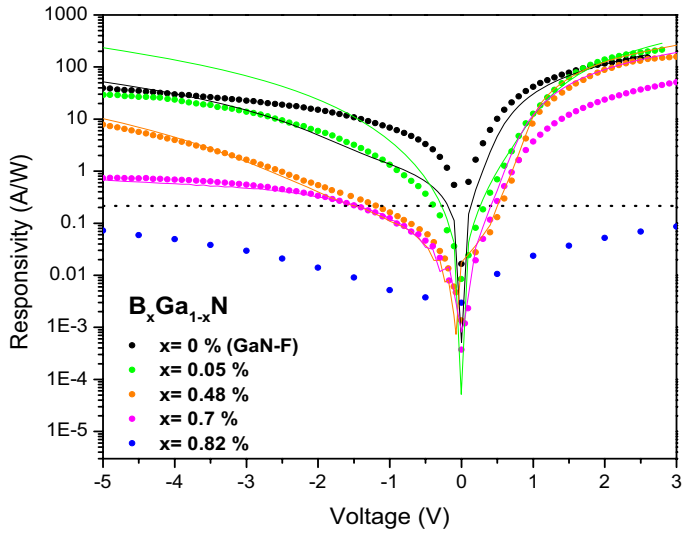

Figure 5.7: *Voltage dependence of the responsivity in BGaN based Schottky photodetectors measured at 266 nm and with an optical power of 31.5 μW.*

5.5 BGaN and BAlGaN superlattice MSM photodetectors

5.5.1 I-V characterization

Figure 5.8 shows the I-V characteristics for the whole set of BGaN devices measured in dark condition. A symmetrical rectifying behavior is obtained, indicating back-to-back

Material	R(A/W)	I_d (A)	$\Delta\Phi_b$	Gain
GaN-F(x=0%B)	39	27 mA	2meV	182
BGaN(x=0.05%B)	29	21 mA	2.5meV	135
BGaN(x=0.48%B)	7.8	420 μA	15meV	36
BGaN(x=0.7%B)	0.73	7.61 μA	35meV	3.5
BGaN(x=0.82%B)	0.072	2.8 nA	—	—

Table 5.4: Responsivity, dark current and SBH decrease at 266 nm with an optical power of 56 μW and at a bias voltage of -5 V in the different BGaN Schottky PDs of surface area 3.4x10^3 μm^2.

Schottky contacts. With the increase of the boron concentration and thus large increase of the layer resistivity, the dark current in the BGaN monolayers decreases, as expected, down to a few nA for a B concentration of 0.82%. In the case of the SL structures,

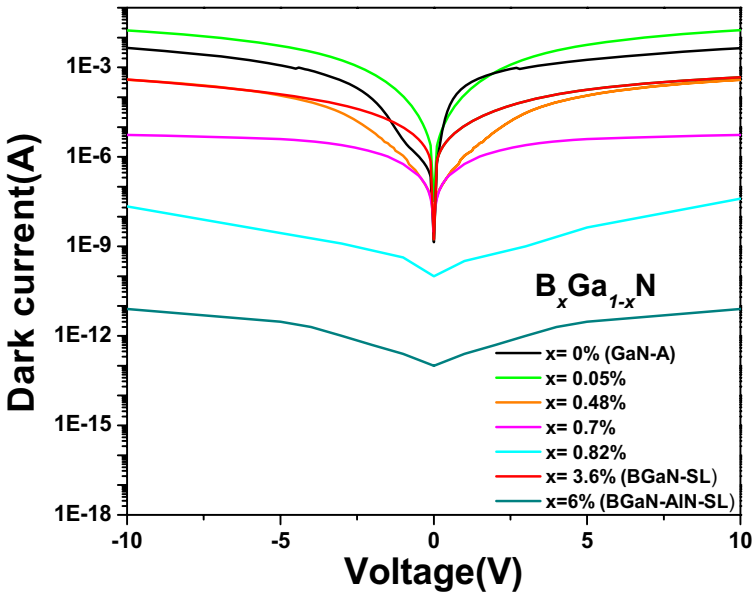

Figure 5.8: *I-V characteristics for the whole set of BGaN devices measured in dark condition.*

the BGaN-AlN SL-based PD exhibits very low dark current (few pA) while the BGaN-GaN SL-based PD shows a relatively high value of the dark current (few hundreds of μA) although the high B concentration (3.6%). This probably originates from the GaN interlayers, which, in contrary to AlN interlayers, possess low value of resistivity and thus allow large current flow.

5.5.2 Voltage dependence of the responsivity

Figure 5.9 shows the voltage dependence of R obtained, for the MSM PDs, at $\lambda = 266$ nm corresponding thus to a photon energy well above the band gap of the different PDs except in the case of the BGaN-AlN SL structure (this will be discussed in the next section), and for an optical power of 31.5 μW. This figure shows also the corresponding curves obtained with the model by Katz et al [162]. In contrary to BGaN-AlN SL-based PDs for which

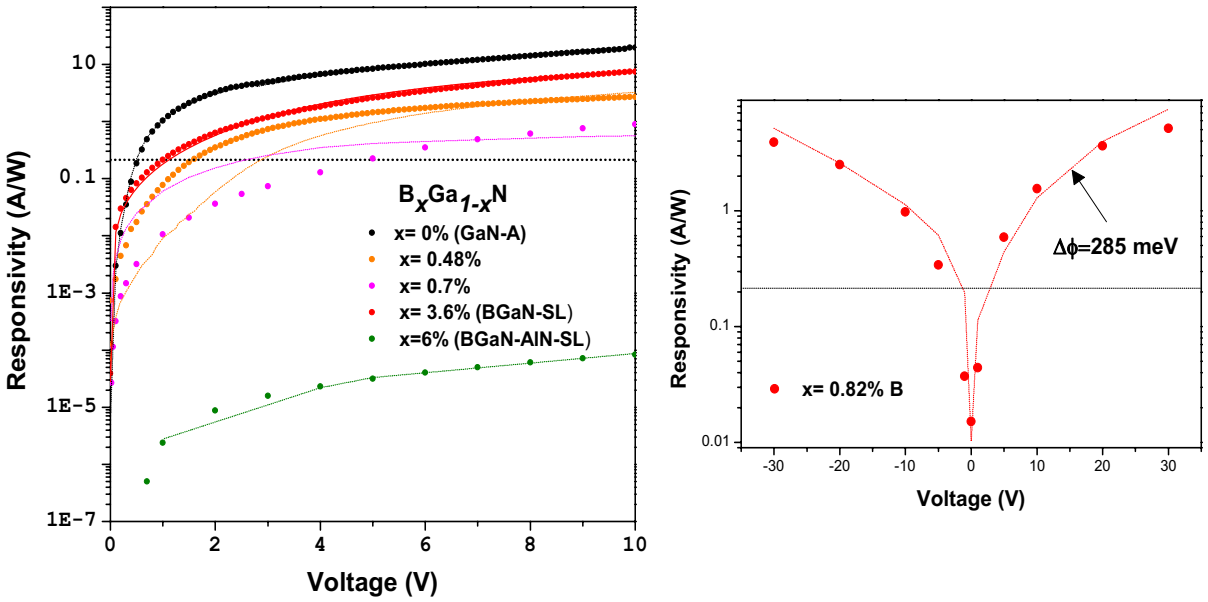

Figure 5.9: *Voltage dependence of the responsivity of the different MSM PDs at λ=266nm and P=56μW. The small doted lines and dashed line corresponds to the model proposed by Katz [162] and theoretical value of R for 100% of Q.E. respectively.*

no internal gain is observed whatever the bias voltage since the measurements are done at a wavelength above its cut off wavelength, all the BGaN-, BGaN-GaN SL- and GaN-based PDs exhibit internal gain for applied voltages above 5V (0.7%B and 0.82%B), 2V ((0.05%B), 1.5V (0.48%), 1V (BGaN-GaN), and 0.5V (GaN). In order to discuss these results, the responsivity, dark current, SBH decrease and internal gain for all PDs are reported in table 5.5. As it was mentioned before the variation of R from one PD to the other is closely related to the value of the dark current, which mainly controls the internal gain. According to the data of table 5.5, figure 5.10 shows the B concentration dependence of the dark current density (red dots), Schottky barrier decrease (black dots) and low optical power gain (gray line) in BGaN monolayer-based and BGaN SL-based UV photodetectors. In the case of the BGaN monolayer-based PD, the B concentration increase leads to the increase of the active layer resistivity and thus to the decrease of

the dark current density. As the BGaN monolayers are thick (400 nm), they exhibit a high-density threading dislocations leading to a large number of trapping states at the active layer-metal interface, and thus to an enhancement of the SBH decrease under illumination yielding large internal gain PD if the dark current is not too weak. In the case of BGaN-GaN SL-based PD, even for large B concentration, due to leakage current in the GaN interlayers, the dark current density is higher than the one of BGaN monolayer-based PD. As the BGaN monolayers in the SL structure is thin (20 nm), they exhibit a lower-density threading dislocations leading to a lower number of trapping states at the active layer-metal interface, and thus to a decrease of the SBH decrease under illumination yielding large internal gain PD since the dark current is relatively large. In the case of BGaN-AlN SL-based PD, the large B concentration, and the high resistivity of the AlN interlayers, leads to a very weak dark current density. Even if the BGaN monolayers in the SL structure is very thin (2 nm), the large B concentration yields a high-density threading dislocations leading to a large number of trapping states at the active layer-metal interface, and thus to an enhancement of the SBH decrease under illumination yielding large internal gain PD if the dark current is not too weak. It is to be noted that for this last structure, the value of the SBH decrease under illumination has been obtained at a wavelength of 266 nm far away from the maximum absorption of the structure.

5.5.3 Optical power dependence of the responsivity

Figure 5.11 presents the optical power dependence of the responsivity for three types of PDs, It is to be noted that with the decreasing optical power P, responsivity increases for each PD as $P^{\frac{1}{2}}$ relationship. This relationship suggests [172] the existence of traps in the band gap acting as recombination centers with an acceptor character, supporting the explanation of the existence of internal gain described above. Thus, when operating at low optical power (nW range), the internal gain, of GaN- and BGaN-GaN SL-based PDs for instance, which is equal to 90 and 35, respectively, for an optical power of $56\,\mu$W (case of the data plotted in figure 5.9), becomes very high and reaches values equal to 10^5 and 3×10^4, respectively. Table 5.6 reports the comparison of the responsivity and gain at high (W range), medium (μW range) and low (nW range) optical power for two types of PDs.

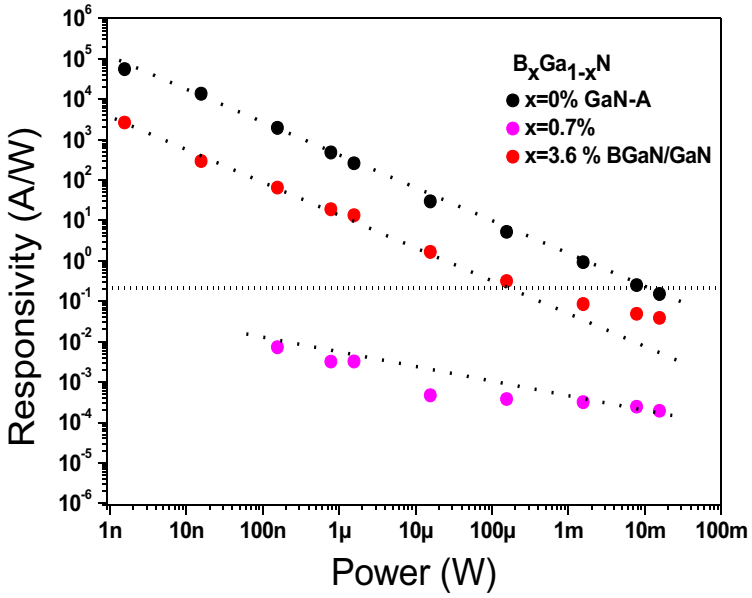

Figure 5.11: *Optical power dependence of the responsivity of three type of PDs measured at λ=355 nm.*

Material	High optical power (W range)		Medium optical power (μW range)		Low optical power (nW range)	
	R (A/W)	Gain	R (A/W)	Gain	R (A/W)	Gain
GaN-A	0.024	-	19.2	90	6×10^4	10^5
BGaN-SL (x=3.6 %B)	0.03	-	7.4	35	3×10^3	3.5×10^4

Table 5.6: Values of the responsivity and gain at high (W range), medium (μW range) and low (nW range) optical power for two types of PDs

5.5.4 Spectral response

The normalized spectral responsivity of the whole set of PDs measured under a bias of 10V are shown in figure 5.13. It is to be noticed that in the case of the BGaN-AlN SL-based PD, in order to determine the cutoff wavelength of the BGaN-AlN SL-based PD, since the wavelength cutoff of the xenon arc lamp is equal to 350 nm, the photocurrent under 212 nm, 244 nm, and 266 nm laser irradiations have been measured and reported in figure 5.12. Unfortunately, the data of figure 5.12 do not allow any accurate conclusions to be drawn and only indicate that the wavelength corresponding to the maximum value of the photocurrent ranges between 212 nm and 266 nm. Additional measurements for intermediate wavelengths are needed to clarify this point. From the data of the figure 5.13,

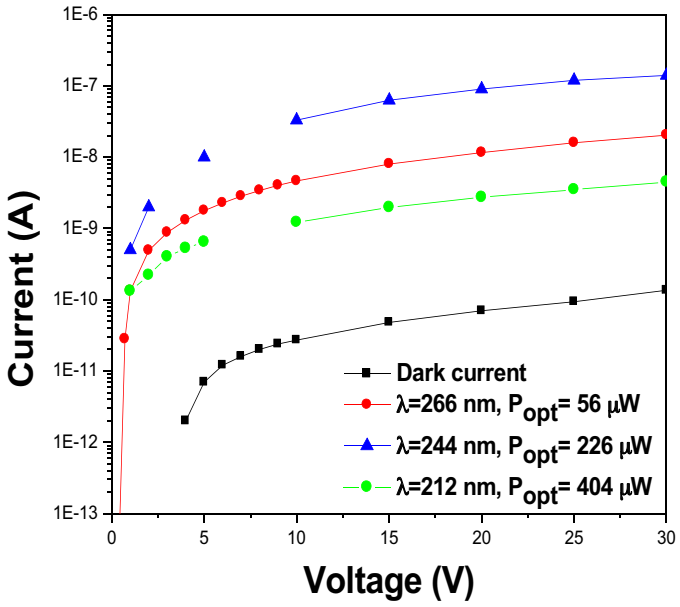

Figure 5.12: *I-V characteristics of the BGaN-AlN SL-based PD measured under different UV radiations.*

the cutoff wavelength and UV visible rejection ratio can be deduced and are reported in table 5.7. The wavelength cutoff, corresponding to the value of the wavelength at which the responsivity is maximum, is found to be equal to 360 nm for the GaN-based PD, and increases to values equal to 361 nm (0.05% B), 367 nm (0.48% B), 373 nm (0.7% B), and 380 nm (0.82% B) for the BGaN-based PDs, respectively. This red-shift of

Device	Cutoff (nm)	UVRR
GaN-A	360	$2x10^5$
x=0.05 %B	361	$1.54x10^3$
x=0.48 %B	367	322
x=0.7 %B	375	10^2
x=0.82 %B	380	39
BGaN/GaN-SL (x=3.6 %B)	365	$1.3x10^2$
BGaN/AlN-SL (x=6 %B)	$\sim$ 260	$>10^3$

Table 5.7: Summarized value of cutoff wavelength and UVRR of MSM photodetector.

the wavelength cutoff is due, as expected, to the band gap bowing induced by the boron incorporation [105]. In the case of the BGaN-GaN SL-based PD, and according to this band gap bowing, a wavelength cutoff equal to 387 nm should be observed. In contrary,

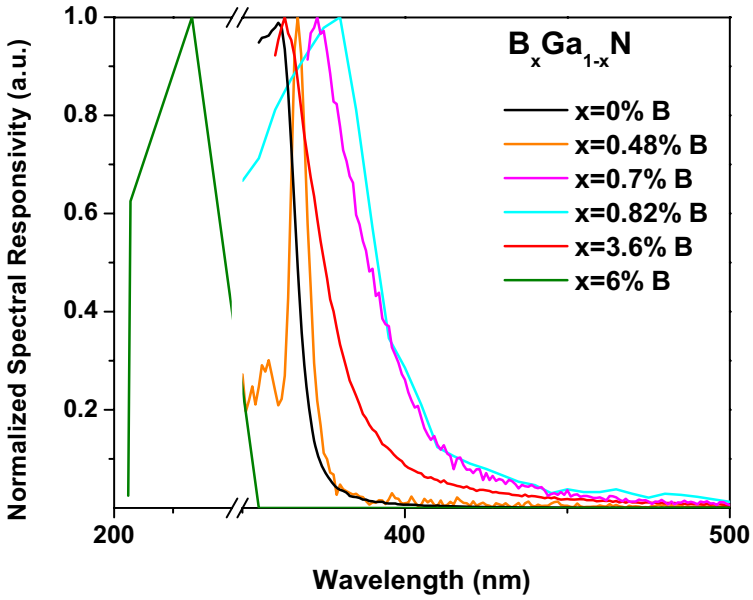

Figure 5.13: *Normalized spectral responsivity for the different UV PDs under a bias of 10V.*

the wavelength cutoff is found to be equal to 365 nm, very close to the one of the GaN-based PD. This discrepancy could probably be attributed to the extrapolation procedure for the calculation of the wavelength cutoff for BGaN materials with B composition equal to 3.6%, which is based on a value of the bowing coefficient determined according to band gap measurements in BGaN materials for B composition up to only 1.8% [105]. Further studies need to be performed to clarify this point. It is also to be noted that the decrease of R with increasing wavelength above the cutoff is less sharp for both BGaN- and BGaN-GaN SL-based PDs than for the GaN-based PDs. This is probably due to the higher dislocation density existing in the BGaN material. Due to the same reason, the value of the UV/VIS rejection ratio is more than one order of magnitude higher for the GaN based PD ($2x10^3$) than for the BGaN- and BGaN-GaN SL-based PDs.

5.5.5 Response time

The records of the photocurrent transients of the three PDs, at $\lambda = 266$ nm, V = 10V, and for optical pulse duration of 0.1ns (11 W of optical peak power) and several tens of seconds (56 μW of optical peak power), respectively, are shown in figure 5.14. The values of the 10% to 90% rise and fall times as well as those of the peak responsivity, which can be deduced from the data of figure 5.14, are reported in table 5.8. At high optical power, all PDs exhibit low values of the rise time (less than 15 ns). BGaN-GaN

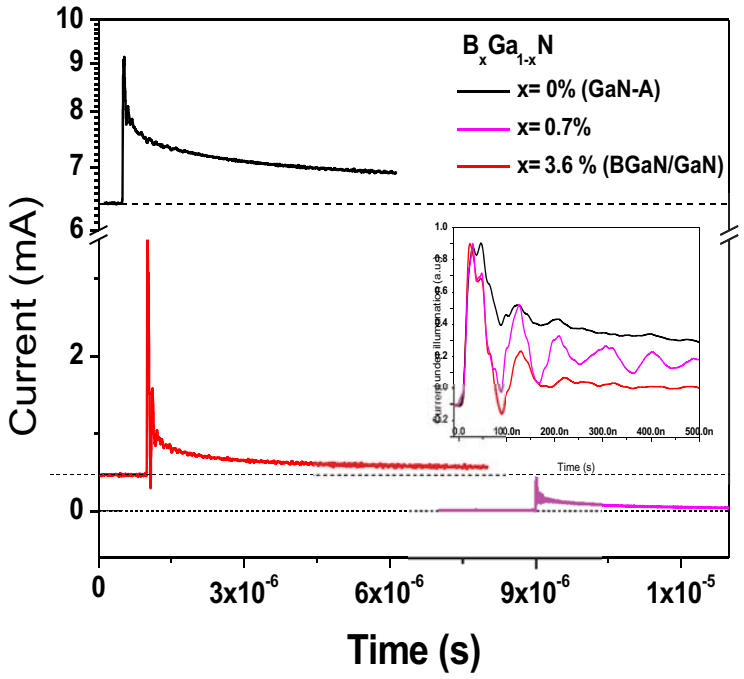

Figure 5.14: *Time dependence of the photocurrent in the three MSM PDs recorded at λ=266 nm, for V=10 V, and for an optical pulse duration of 0.1ns with a peak power of 11W.*

SL-based PDs exhibit relatively low photocurrent time-decays (90% of the response is reached after 45 ns and 15 ns, respectively), whereas more than hundred times higher time-decays are observed in the GaN- and BGaN monolayer-based PDs (90% of the response is reached after 15 μs and 6.7 μs, respectively). These relatively slow time-decays (the initial current value before illumination is recovered within less than 100 μs after the optical power is turned off) can be attributed to a persistent photoconductivity effect caused by trapping/detrapping processes of photo-generated carriers at deep level defects in the band gap of the material [174]. As it has been discussed above, at such high optical power,

	High optical power		Low optical power	
Material	τ_r	τ_f	τ_r	τ_f
GaN-A	15ns	15μs	42ms	4s
x=0.7 %B	15ns	6.7μs	4s	60s
BGaN-SL (x=3.6 %B)	15ns	44ns	0.56s	20s

Table 5.8: 10% to 90% rise τ_r and fall τ_f times of the different PDs, measured at λ=266 nm and V=10 V, for low (56μW) and high (11W) optical power.

much lower internal gain is expected and R is in the mA/W range for all PDs. The highest value of R, equal to 30mA/W, is obtained in the BGaN-GaN SL-based PD, and is 25%, and 710% higher than those of the GaN-, and BGaN monolayer-based PD, respectively. The low value of R for the BGaN monolayer-based PD can be explained by the relatively poor structural quality of the 400 nm thick BGaN monolayer [93], yielding low values of the photo-carrier mobility and diffusion length. In contrary, the higher structural quality of the 20 nm thick BGaN layers [93] in the BGaN-GaN SL-based PD leads to higher values of the photo-carrier mobility and diffusion length and, thus, responsivity. BGaN-GaN SL- and GaN-based PDs exhibit relatively low photocurrent time-decays (see figure 5.14), whereas more than hundred times higher time-decays are observed in the GaN- and BGaN-based PDs. At low optical power (see figure 5.15), and thus higher internal gain, for all PDs, R is in the A/W range and the rise times and recovering times of the initial current value are much longer and reach several tens of ms and seconds, respectively, as reported in table 5.8.

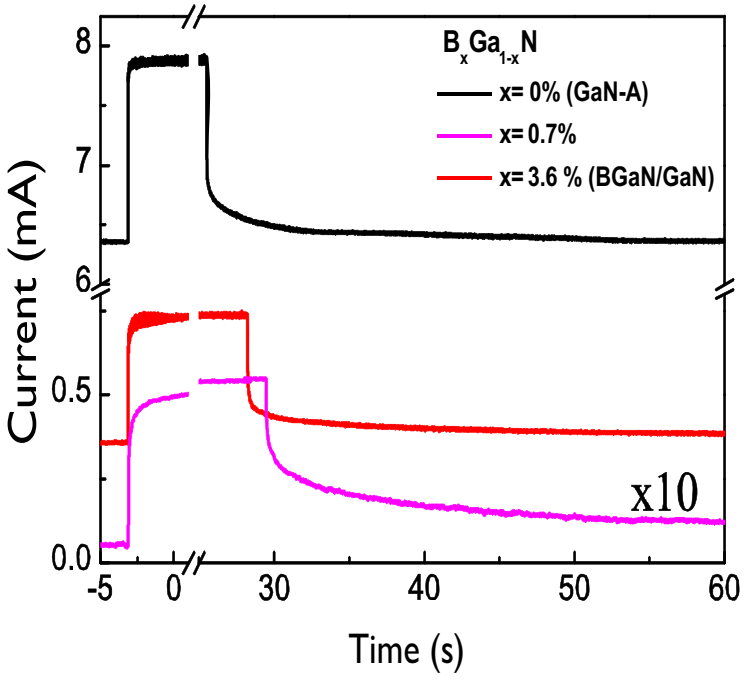

Figure 5.15: *Time dependence of the photocurrent for an optical pulse duration of several tens of seconds with a peak power of 56μW.*

5.6 Conclusions

MSM solar-blind ultraviolet PDs were fabricated using BGaN monolayers and quasi-alloy of BGaN/GaN SLs as the active layer. Table 5.9 compiles the summarized values of dark current, SBH, gain in nano and micro watt range, wavelength cut-off and UV visible rejection ratio of MSM PDs.

Device	I_d	$\Delta\Phi$ (meV)	Gain		Cut off (nm)	UVRR
			(nW)	(μW)		
GaN-A	4.4mA	6	10^5	90	360	$2x10^3$
BGaN (0.7%B)	5.4μA	20	10^3	5	375	10^2
BGaN-Sl(3.6%B)	0.47mA	16	$3.5x10^4$	35	365	$1.3x10^2$
BAlGaN-SL(6%B)	8pA	133	–	–	280	$>10^3$

Table 5.9: Summarized values of various GaN and BGaN devices.

Compared to the GaN-based MSM PD:

- in the BGaN monolayer (0.7% B) based MSM PD, the dark current is reduced by 3 orders of magnitude with still a large gain but with a larger cut off wavelength and a decrease of the UVRR,
- in the BGaN-AlN SL (6% B), the dark current is reduced by 9 orders of magnitude but without any internal gain

The best trade off [252] is thus obtained with the BGaN-GaN SL (3.6% B) based PD in which the dark current is reduced by 1 order of magnitude while maintaining a large gain. It allows also to tune the cut-off wavelength of the PD and, in the high optical power regime, it exhibits more than two orders of magnitude lower time response and 25% higher responsivity than GaN-based PD. The improvement of the UV/VIS rejection ratio and sharpness of the wavelength cutoff is in progress and relies on the optimization of the crystal quality of the active layers which could be obtained by the growth of thinner layers of the BGaN material.

General conclusion and perspectives

The aim of this work was to improve actual solar blind ultraviolet photodetectors by introducing new active layers into these devices. We targeted the realization of low dark current, high electro-optical response, low response time and more robust in harsh environment photodetectors, for which the wavelength cut off can be tuned in the UV range. For this, we fabricated, developed and achieved of a new category of solar-blind ultraviolet photodetectors fabricated using monolayers and superlattices of BAlGaN semiconductor alloys. The main idea lied on the role of the boron incorporation in GaN material, which increases drastically the electrical resistivity and the strength of the bonds, helps to decrease the mismatch with the substrate (and thus could increase the structural quality of the active layer), and finally allows to tune the wavelength cut off.

To reach this goal, several GaN, AlGaN, and BGaN monolayers as well as BGaN-GaN, BGaN-AlN and BAlN-AlN superlattices were first grown using MOVPE technique. Then, both Schottky and ohmic contacts on GaN, AlGaN and BAlGaN alloys were realized and optimized. For this, a full process using photolithography, metal deposition and thermal annealing was developed. Finally, the electrical and electro-optical properties were characterized using a set of experimental techniques such as, from one part, Hall effect, Van der Paw, I-V, C-V, and TLM methods for the study of the electrical transport mechanism and, from the other part, photocurrent spectroscopy, external quantum efficiency, and photocurrent time response measurements for the characterization of the photodetectors.

During this work, we succeeded to obtain ohmic contact with low specific contact resistance as well as Schottky diodes in nearly all the different layers. We also evidenced the existence of an interfacial layer between the metal and the semiconductor which is present in all the devices. This interfacial layer plays an important role in the appearance of a large internal gain in the photodetectors via the trapping of the photo generated holes. As expected, the boron incorporation in the GaN material leaded to photodetectors with a decrease of the dark current up to nine orders of magnitude compared to a GaN-based photodetector, and cut off wavelength tunable in the range 260 nm - 380 nm.

Unfortunately, in the device based on a BGaN monolayer, the internal gain was shown to simultaneously decrease with the boron incorporation. This was not the case in devices using BGaN-GaN superlattices, which are the best trade off, and for which the internal gain is maintained while the dark current is reduced by one order of magnitude.

This work also allowed to show that the internal gain exhibited by the different devices is largely dependent on the optical power and pulse duration of the radiation impinging on the photodetector. At low optical power and long pulse duration the internal gain is huge and the response time is long. The performances of BGaN-GaN superlattices-based photodetectors are comparable to those of the GaN-based photodetectors, even if the dark current is reduced by one order of magnitude. On contrary, at high optical power and short pulse duration, the internal gain becomes very low and the response time short. In this regime, the BGaN-GaN superlattices-based photodetector exhibits large improvements compared to the GaN-based photodetector. Its responsivity is 25% larger than the one of the GaN-based photodetector and its response time is reduced by more than two order of magnitude.

This work provides valuable insight into the properties of photodetectors, but a myriad of steps can be taken to add to the merit of this study. A great deal of development and optimization in the field of material growth, process technology, and device characterization is required and is the focus of our future research. There is also a great need for physical models required for the optimization of material growth and evaluation of new device structures by simulations. This work can also be improved by deep investigation of the high internal gain reported in this study. The use of alternative ohmic contacts (Ti/Al/Ni/Au) instead of Ti/Al/Ti/Au and semi-transparent Schottky contact in order to let more light reach the active layer provides a mechanism to further explore this finding. Wire bonding may also be another method used to avoid device contact damages and scratches. Mesa structures should be used to isolate ohmic contacts, and Circular Transmission Lime Model (CTLM) should be used instead of the Linear-TLM (TLM) to investigate accurately the specific contact resistance.

The concept laid out in this work and the current findings open the doors to numerous improvements in the field of photodetectors and other disciplines. One major impact of this work could be in the field of neutron detector development. While most neutron detectors are ^{3}He based with a detection efficiency of 80%, in reality, their efficiency is reduced to 30% due to their long term instability (leakage, buildup of electronegative poison) apart from the inconveniences associated with the maintenance of such gas-based detectors. By moving to solid state semiconductors, considerable gain in material density,

low operating voltage, small device footprint and excellent stability can be achieved. Moreover, despite the prevalence of Si-based detectors, GaN-based materials show two advantages over the latter; GaN has two orders of magnitude higher radiation hardness than Si and has a much wider bandgap and hence we propose the use of BGaN and BAlN superlattices for the development of more robust devices.

Bibliography

[1] Jun HU et al. *4H-SiC Detectors for Low Level Ultraviolet Detection*. Rutgers The State University of New Jersey-New Brunswick., 2008.

[2] G. Parish et al. High-performance (Al,Ga)N-based solar-blind ultraviolet p-i-n detectors on laterally epitaxially overgrown GaN. *Appl. Phys. Lett.*, 75:247, 1999.

[3] P. T. Landsberg et al. *Handbook of Geophysics and the Space Environment*, volume 27. Eidor: A. S. Jursa, Springfield BVA 22161, 1988.

[4] D. M. Brown et al. SiC flame sensors for gas turbine control systems. *Solid-State Electronics*, 42:755–760, 1998.

[5] P. Schreiber et al. Solar-blind UV region and UV detector development objectives. *Photodetectors: Materials and Devices IV, San Jose, CA, USA.*, pages 230–248, 1999.

[6] G. A. Shaw et al. Nlos UV communication for distributed sensor systems. *Integrated Command Environments, San Diego, CA, USA.*, pages 83–96, 2000.

[7] J. P. Grant. Thesis: GaN radiation detectors for particle physics and synchrotron applications, 2007.

[8] P. N. K. Deenapanray et al. Electric-field-enhanced emission and annealing behaviour of electron traps introduced in n-si by low-energy he ion bombardment. *Semiconductor science and Technology*, 14:41, 1999.

[9] H. S. Ogawa et al. First-year continuous solar euv irradiance from soho by the celias/sem during 1996 solar minimum. *Journal of Geophysical Research-Space Physics.*, 103, 1996.

[10] M. razeghi et al. Semiconductor ultraviolet detectors. *Journal of Applied Physics*, 79:7433, 1996.

[11] Rogalski Antoni et al. Infrared detectors: Status and trends. *Progress in Quantum Electronics*, 27:59–210, 2003.

[12] S.M Sze et al. *semiconductor Devices, physics and Technology*. Wiley, New york, 2nd and 3rd edition, 1981.

[13] J.I. Pankove et al. Symp. proc. *Mater. Res. Soc.*, 162:515, 1990.

[14] Z.C. Huang et al. Characterization of GaN using thermally stimulated current and photocurrent spectroscopies and its application to UV detectors. *Journal of Crystal Growth*, 170:362, 1997.

[15] C.H. Cehn et al. GaN metal-semiconductor-metal ultraviolet photodetectors with transparent indium-tin-oxide schottky contacts. *Chen, IEEE Photon. Technol. Lett.*, 13:848, 2001.

[16] D. Walker et al. High-speed, low-noise Metal-Semiconductor-Metal ultraviolet photodetectors based on GaN. *Appl. Phys. Lett.*, 74:762, 1999.

[17] Q. Z. Liu et al. A review of the metal GaN contact technology. *Solid-State Electron*, 42:677–691, 1998.

[18] A. C. Schmitz et al. Metal contacts to n-type GaN. *Journal of electronic materials*, 27:255–260, 1998.

[19] L. L. Smith et al. *in Properties of Group III Nitrides*. IEEE, london, 1994.

[20] S. E. Mohney et al. *GaN and Related Materials II, eds. S. J. Pearton*. Gordon and Breach Science Publishers, 2000.

[21] S. N. Mohammad et al. Near-ideal platinum-GaN schottky diodes. *Electronics Letters 32*, 32:598–559, 1996.

[22] M. R. H. Khan et al. The barrier height and interface effect of Au-n-GaN schottky diode. *Journal of Physics D*, 28:1169, 1995.

[23] F. Fichter et al. *Z. Anorg. Chem.*, 54:332–327, 1907.

[24] F. Fichter et al. *Berichet der deutschen Chemischen Gesellschaft*, 43:1465, 1910.

[25] Johnson W.C. et al. Nitrogen compounds of gallium. III. *The journal of physical chemistry*, 36:2561–2654, 1932.

[26] R. Juza et al. *Anorg. Allgem. Chem.*, 234:248, 1938.

[27] H.P. Maruska et al. The preparation and properties of vapor-deposited single-crystal-line GaN. *Appl. Phys. Lett.*, 15:327, 1969.

[28] J.I. Pankove et al. Luminescence in GaN. *Journal of Luminescence*, 7:114, 1973.

[29] H. Amano et al. P-type conduction in mg-doped GaN treated with low-energy electron beam irradiation (LEEBI). *J. J. Appl. Phys.*, 28:L2112, 1989.

[30] H. Amano et al. Metalorganic vapor phase epitaxial growth of a high quality GaN film using an AlN buffer layer. *Appl. Phys. Lett.*, 48:353–355, 1986.

[31] I. Akasaki et al. Effects of ain buffer layer on crystallographic structure and on electrical and optical properties of GaN and. *J. Crystal Growth*, pages 209–219.

[32] Van Vechten et al. Defeating compensation in wide gap semiconductors by growing in h that is removed by low temperature de-ionizing radiation. *Japanese Journal Applied Physics*, 31:3662, 1992.

[33] D. Walker et al. AlGaN ultraviolet photoconductors grown on sapphire. *Phys. Lett.*, 68:2100, 1996.

[34] B. W. Lim et al. High responsitivity intrinsic photoconductors based on AlGaN. *Appl. Phys. Lett.*, 68:3761, 1996.

[35] A. Osinsky et al. Schottky barrier photodetectors based on AlGaN. *Applied Physics Letters*, 72:742, 1998.

[36] T. Tut et al. High bandwidth efficiency solar-blind AlGaN schottky photodiodes with low dark current. *Solid state electronics*, 49:117, 2005.

[37] U. chowdhury et al. High-performance solar-blind photodetector using an AlGaN n-type window layer. *Journal of crystal growth*, 248:552, 2003.

[38] M.M. Wong et al. High quantum efficiency AlGaN/GaN solar-blind photodetectors grown by mocvd. *Phys. Status Solidi A*, 188:333, 2001.

[39] T. Li et al. Solar-blind AlGaN based metal semiconductor metal ultraviolet photodetectors. *Electron Letters*, 36:1581, 2000.

[40] N. Biyikli et al. High speed solar-blind AlGaN-based metal-semiconductor-metal photodetectors. *Phys. Status Solidi C*, 7(2314), 2003.

[41] Qing Xia et al. Pressure induced rocksalt phase of aluminum nitride: A metastable structure at ambient condition. *Journal of Applied Physics*, 73:8198, 1993.

[42] Perlin P. et al. Raman scattering and x-ray-absorption spectroscopy in gallium nitride under high pressure. *Physical Review B: Condensed Matter*, 45:83, 1992.

[43] Ueno M. et al. Stability of the wurtzite-type structure under high pressure: GaN and inn. *Physical Review B: Condensed Matter*, 49:14, 1994.

[44] Hadis Morkoc. *Handbook of Nitrides Semiconductor and Devices*, volume 1. Wiley-VCH Verlag GmbG and Co. KGaA, Weinheim, 2008.

[45] Harrison W.A. et al. *Electronic Structure and Properties of Solids.* Dover, New York, 1980.

[46] Yeh C.Y. et al. *Physical Review B: Condensed Matter*, 46:10086, 1992.

[47] S. Nakamura et al. InGaN/GaN/AlGaN-based laser diodes with modulation-doped strained-layer superlattices grown on an epitaxially laterally overgrown GaN substrate. *Applied Physics Letters*, 72:211, 1998.

[48] J.T. Torvik et al. Optical characterization of GaN/SiC n-p heterojunctions and p-SiC. *Applied Physics Letters*, 72:945, 1998.

[49] D.D. Koleske et al. Influence of AlN nucleation layer temperature on GaN electronic properties grown on SiC. *Applied Physics Letters*, 80:4372, 2002.

[50] S. Nakamura et al. *The Blue Laser Diode: GaN based light emitters and lasers*, volume 2. Springer Verlag Berlin Geidelberg New York, 1997.

[51] Rudiger Quay et al. *Galluim Nitride Electronics*. Springer, 2008.

[52] W.H. Goh et al. Structural and optical properties of nanodots,nanowires,and multi-quantum wells of III-nitride grown by movpe nano-selective area growth. *journal of cyrstal growth*, 315:160–163, 2011.

[53] J. Park et al. Selective-area and lateral epitaxial overgrowth of III-n materials by metal organic chemical vapor deposition. *App. Phys. Lett.*, 73:333, 1998.

[54] C. Monier et al. Simulation of npn and pnp AlGaN/GaN heterojunction bipolar transistors performances: limiting factors and optimum design. *IEEE Transactions on Electron Devices*, 48:427–432, 2001.

[55] Eastman L.F. et al. Undoped AlGaN/GaN hemts for microwave power amplification. *IEEE transactions on electron devices*, 48:479, 2001.

[56] A. Chini et al. 12 w/mm power density AlGaN/GaN hemts on sapphire substrate. *Electronics Letters*, 40:73–74, 2004.

[57] Masataka Higashiwaki et al. High-performance short-gate InAlN/GaN heterostructure field-effect transistors. *Jpn. J. Appl. Phys.*, 45:L843–L845, 2006.

[58] G. Simin et al. *Appl. Phys. Lett.*, 40:L1142–1144, 2001.

[59] J. Kuzmik et al. Power electronics on InAlN/(In)GaN: Prospect for a record performance. *IEEE Electron Device Lett.*, 22:510–512, 2001.

[60] Davydov V.Yu. et al. Band gap of inn and in-rich inxga1-xn alloys ($0.36 < x < 1$). *Physica Status Solidi B: Basic Research*, 230:R4–R6, 2002.

[61] Araki T. et al. Radio frequency-molecular beam epitaxial growth of inn epitaxial films on (0 0 0 1) sapphire and their properties. *Journal of Vacuum Science and Technology B: Microelectronics and Nanometer Structures*, 22:2139–2143, 2004.

[62] Y. K. Su et al. In0.11ga0.89n-based p-i-n photodetecto. *Physica Status Solidi C*, 6:S811, 2009.

[63] I. Akasaki et al. *Properties of Group III Nitrides, No. 11 in EMIS Data reviews Series*. IEE INSPEC, London, 1994.

[64] M. Levinshtein et al. *Properties of Advanced Semiconductor Materials: GaN, AlN, InN, BN, SiC, SiGe*. New York: Wiley, 2001.

[65] H. Morkoc. *Nitride Semiconductors and Devices*. No. 32 in Springer Series in Materials Science, Springer, Berlin Heidelerg New York, 1999.

[66] W. Meng. *Properties of Group III Nitrides*. No. 11 in EMIS Data reviews series IEE INSPEC, London, 1994.

[67] T. Tansley et al. *Properties of Group III Nitrides*. Institution of Engineering and Technology, 1994.

[68] T. Tansley et al. *in Properties, Processing and Applications of GaN Nitride and Related Semiconductors*. IEE INSPEC, London, 1999, 1999.

[69] M. Drory et al. *J. Appl. Phys*, 69:4044, 1996.

[70] I. Yonenaga et al. *J. Nitride Semicond. Res.*, 7:6, 2002.

[71] V. W. L. Chin et al. Electron mobilities in gallium, indium, and aluminum nitrides. *J. Appl. Phys.*, 75:7365, 1994.

[72] J. Miragliotta. *In Properties of Group III Nitrides*. No. 11 in EMIS Data reviews Series, IEE INSPEC, London, 1994.

[73] C. Kisielowski et al. *Phys. Rev. B*, 17745:54, 1996.

[74] J.I. Pankove et al. *RCA Review*, 36:163, 1995.

[75] R. J. Molnar et al. Electron transport mechanism in gallium nitride. *Appl. Phys. Lett.*, 62:72, 1993.

[76] P. Boguslavski et al. Native defects in gallium nitride. *Physical Review B: condensed matter*, 51:17255, 1995.

[77] T.L. Tansley et al. Point-defect energies in the nitrides of aluminum, gallium, and indium. *Physical Review B: solid state*, 45:10942, 1992.

[78] P. Boguslavski et al. *MRS, Symp. Proc.*, pages 693–698, 1994.

[79] M. A. Reshchikov et al. Luminescence properties of defects in GaN. *J. Appl. Phys.*, 97:061301, 2005.

[80] W. Lambrecht et al. *Properties of Group III Nitrides, No. 11 in EMIS Data reviews Series*. INSPEC, The Institution of Electrical Engineers, London, 1994.

[81] S. Yoshida et al. Properties of $Al_xG_{1-x}N$ films prepared by reactive molecular beam epitaxy. *Journal of Applied Physics*, 53:6844, 1982.

[82] M.R.H. Khan et al. Edge emission of $Al_xG_{1-x}N$. *Solid State Communications*, 60:509, 1986.

[83] Zoroddu A. et al. Firstprinciples prediction of structure, energetics, formation enthalpy, elastic constants, polarization, and piezoelectric constants of AlN, GaN, and

inn: comparison of local and gradientcorrected density-functional theory. *Physical Review B: Condensed Matter*, 64:208, 2001.

[84] Ambacher et al. Pyroelectric properties of al(in)GaN/GaN heteroand quantum well structures. *Journal of Physics: Condensed Matter*, 14:3399–3434, 2002.

[85] Amano H. et al. *Materials Research Society Symposium Proceedings*, 449:1143–1150, 1997.

[86] Yoshida et al. Epitaxial growth of GaN/AlN heterostructures. *Journal of Vacuum Science & Technology B: Microelectronics and Nanometer Structures*, 1:250, 1983.

[87] K. D. Cummings et al. A monte carlo simulation of damage to the gate oxide of metal-oxide-silicon field-effect transistors from electron beam lithography. *Applied Physics Letters*, 65:2024, 1994.

[88] Y. Koide et al. Energy band-gap bowing parameter in an $Al_xGa_{1-x}N$ alloy. *Journal of Applied Physics*, 61:4540, 1987.

[89] Yun F. et al. Energy band bowing parameter in AlGaN alloys. *Journal of Applied Physics, Rapid Communications*, 92:4837–4839, 2002.

[90] M. Asif Khan et al. High electron mobility $GaN/Al_xG_{1-x}N$ heterostructures grown by low-pressure metalorganic chemical vapor deposition. *Applied Physics Letters*, 58:2408, 1991.

[91] Tanaka T. et al. p-type conduction in mg-doped GaN and al0.08ga0.92n grown by metalorganic vapor phase epitaxy. *Applied Physics Letters*, 65:593, 1994.

[92] S. Gautier et al. Movpe growth study of BGaN on GaN template substrate. *superlattices and microstructures*, 40:233, 2006.

[93] A. Ougazzaden et al. BGaN materials on GaN/sapphire substrate by movpe using n2 carrier gas. *J. Crystal Growth*, 298:316, 2007.

[94] S. Gautier et al. Movpe growth study of $B_xGa_{1-x}N$ on GaN template substrate. *Superlattices and microstructures*, 40:233, 2006.

[95] S. Gautier et al. Deep structural analysis of novel BGaN material layers grown by movpe. *Journal of crystal growth*, 10:1016, 2010.

[96] M. Haruyama and T. Shirai et al. Proceeding of the international. symp. blue laser and light emiting diodes.

[97] M. Kurimoto et al. Growth of BGaN/AlGaN multi-quantum well structure by metalorganic vapor phase epitaxy. *J. of crystal Growth*, 221(378), 2000.

[98] S. Sakai et al. *Japanese journal of applied physics*, 32:4413, 1993.

[99] T. Takano et al. Epitaxial growth of high quaility BAlGaN quaternary lattice matched to AlN on 6h SiC substrate by lp-movpe for deep UV emission. *Journal of Crystal Growth*, 237:972–977, 2002.

[100] C.H.Wei et al. Unstable composition region in the wurtzite bgaaln system. *Journal of Crystal Growth*, 179:179–182, 2000.

[101] C. H. Wei et al. Thermodynamic analysis of BGaN grown by MOVPE. *J. of Crystal Growth*, 217:109–114, 2000.

[102] L.K. Teles et al. Spinodal decomposition in BGaN and BAlN alloys. *Appl. Phys. Lett.*, 80:1177–1179, 2002.

[103] G. B. Stringfellow et al. *Organometallic vapor-phase epitaxy: theory and practice.* Academic press, San Diego, 2nd edition, 1999.

[104] G. Orsal et al. Effect of boron incorporation on growth behavior of BGaN/GaN by movpe. *Crystal Growth*, 310:5058–5062, 2008.

[105] A. Ougazzaden et al. Bandgap bowing in BGaN thin films. *Appl. Phys. Lett.*, 93:083118, 2008.

[106] T. Baghdadli et al. Electrical and structural characterizations of BGaN thin flims by metal-organic vapor phase epitaxy. *Phys. Stat. Sol. C*, 6:S1029, 2009.

[107] J. A. Freitas et al. Shallow donors in GaN. *Phys. Status Solidi B: Basic research*, 240:330, 2003.

[108] Stampfl C. et al. Doping of $Al_xG_{1-x}N$. *Materials Science and Engineering: B*, 59:253–257, 1999.

[109] A.Y. Polyakov et al. Growth of gabn ternary solutions by metallorganic vapor phase epitaxy. *E. materials*, 26:3, 1997.

[110] Gupta W. K. et al. Molecular beam epitaxy of boron-containing nitrides. *J. Vac. Sci. Technol B*, 17:1246, 1999.

[111] C. H. Wei et al. Growth and characterization of $B_xGa_{1-x}N$ on 6h-SiC (0001) by movpe. *MRS Internet J. Nitride Semicond.*, 4S1:G3.79, 1999.

[112] Simon Gautier. *Thesis: Elaboration Par MOVPE des nouveaux materiaux B(Ga,Al)N pour les applications dans l'Ultra Violet et l'electronique de puissance.* 2007.

[113] T. Honda et al. Excitonic emission of BGaN grown on (0 0 0 1) 6h-SiC by metal-organic vapor-phase epitaxy. *Journal of Luminescence*, 89:1274–1276, 2000.

[114] V.V. Ilyasov et al. Electronic energy structure and x-ray spectra of GaN and BGaN crystals. *Crystals. Phys. Stat. Sol.*, 48:654, 2006.

[115] S. Watanabe et al. Refractive indices of $B_xAl_{1-x}N$ (x=0-0.0012) and $B_yGa_{1-y}N$ (y=0-0.023) epitaxial layers in ultraviolet region. *Phys. Stat. Sol.*, 7:2691–2694, 2003.

[116] Pallab Bhattacharya. *Semiconductor optoelectronic devices.* Prentice-Hall, Inc., 2 edition, 1997.

[117] R. D. Nelson et al. *Optical engineering*, 16:275, 1977.

[118] Dereniak E. L. et al. *Optical radiation detectors.* Wiley New york, 1984.

[119] Hadis Morkoc. *GaN-based optical and electronic devices*, volume 3. Wiley-VCH, 2008.

[120] John Wilson et al. *Optoelectronics an introduciton*, volume 3rd. Printice Hall Europe, 1998.

[121] Didier Decoster et al. *Optoelectronic Sensors.* ISTE Ltd and John Wiley and Sons, Inc., 2009.

[122] Monroy E. et al. Visible-blindness in photoconductive and photovoltaic AlGaN ultraviolet detectors. *J. of Electronic Materials*, 28:238, 1999.

[123] Garrido J.A. et al. Photoconductive gain modelling of GaN photodetectors. *Semiconductor Science and Technology*, 13:563, 1998.

[124] Yang B et al. Li T. *SPIE Optoelectron. Tech. Digest*, 3948:304–10, 2000.

[125] Brown J. D. et al. *Journal of Nitride Semiconductor Research.*, 59, 2000.

[126] E.Munoz et al. III-nitrides and UV detection. *J. Phys. Condens. Matter*, 13:7115–7137, 2001.

[127] J.B. Limb et al. GaN ultraviolet avalanche photodiodes with optical gain greater than 1000 grown on GaN substrates by movcd. *Applied Physics Letters*, 89:11112–1, 2006.

[128] M. C. Chen et al. Improved performance of planar GaN-based p-i-n photodetectors with mg-implanted isolation ring. *Applied Physics Letters*, 89:183509–1, 2006.

[129] B. Butun et al. High-performance visible-blind GaN-based p-i-n photodetectors. *Applied Physics Letters*, 92:033507–1, 2008.

[130] Cyril Peronot et al. Solar-blind UV photodetectors based on GaN p-i-n photodiodes. *Jpn. J. Appl. Phys.*, 39:L387–L389, 2000.

[131] F. Capasso et al. *Physics of avalanche photodiode in light wave communication technology.* R.K. Willardson and A.C. Beer et al., 1985.

[132] J. C. Carrano et al. GaN avalanche photodiode. *Applied Physics Letters*, 76:924, 2000.

[133] B. Yang et al. Low dark current GaN avalanche photodiodes. *IEEE journal of quantum electronics*, 36:1389, 2000.

[134] Omnes F. et al. Movpe grown AlGaN materials for visible blind ultraviolet photodetector applications. *Applied Physics Letters*, 86:9, 1999.

[135] Pau J. L. et al. High visible rejection AlGaN photodetectors on si(111) substrates. *Appl. Phys. Lett.*, 76:19, 2000.

[136] Binet F. et al. Properties of a photovoltaic detector based on an n-type GaN schottky barrier. *R.L.*, 1997.

[137] F. Omnes et al. *GaN based UV photodetectors, in Nitride Semiconductors-Handbook on Materials and Devices.* Wiely-VCH GmbH and CO. KGaA, 2003.

[138] Z. Yi et al. Fabrication and device characteristics of schottky type bulk GaN based visible blind ultraviolet photodetectors. *Applied Physics Letters*, 90:121118, 2007.

[139] M. L. Lee et al. Photodetectors formed by and indium tin oxide/zinc oxide/p-type GaN heterojunction with high UV to visible rejection ratio. *Applied Physics Letters*, 94:13512, 2009.

[140] T. Tut et al. $Al_xG_{1-x}N$-based avalanche photodiodes with high reproducible avalanche gain. *Applied Physics Letters*, 90:163506, 2007.

[141] S. Senda et al. AlN based UV photodiode grown by metal organic chemical vapor deposition. *Applied Physics Letters*, 92:203507, 2008.

[142] D Y Jiang et al. Hybrid AlN–SiC deep ultraviolet schottky barrier photodetectors. *Applied Physics Letters*, 90:263505, 2007.

[143] Gang Cheng et al. Zno nanowire schottky barrier ultraviolet photodetector with high sensitivity and fast recovery speed. *Applied Physics Letters*, 99:203105, 2011.

[144] K. H. Lee et al. GaN msm photodetectors with and anactivated mg-doped GaN cap layer and sputtered ito electrodes. *Journal of the Electrochemical Society*, 155:165–167, 2008.

[145] K. T. Lam et al. Nitride-based photodetectors with unactivated mg-doped GaN cap layer. *Sensors and Amp Actuators A. Physical*, 143:191–5, 2008.

[146] A. Ahaitouf et al. Interface states effects in pt/n-GaN schottky diodes. *Paper submited to Thin Solid Films*, 2012.

[147] L. Sang et al. High-performance metal-semiconductor-metal InGaN photodetectors using caf2 as the insulator. *Appl. Phys. Lett.*, 98:103502, 2011.

[148] M. L. Lee et al. GaN Schottky barrier photodetectors with a low-temperature GaN cap layer. *Appl. Phys. Lett.*, 82:2913, 2003.

[149] F. W. Simth et al. Picosecond gaas-based photoconductive optoelectronic detectors. *Appl. Phys. Lett.*, 54:890–892, 1989.

[150] P. Bhattacharya et al. *Semiconductor Optoelectronic Devices*. Prentice Hall, New Jersy, 1994.

[151] M. Ito et al. Monolithic integration of a metal-semiconductor-metal photodiode and a gaas preamplifier. *IEEE Electron Device Letter EDL*, 5:531–532, 1984.

[152] T. Nishida et al. 346nm emission from AlGaN multi quantum well light emitting diodes. *Phys. Stat. Sol. A*, 176:45, 1999.

[153] J. C. Carrano et al. Very low dark current metal-semiconductor-metal ultraviolet photoconductors fabricated on single-crystal GaN epitaxial layers. *Applied Physics Letters*, 70:1992, 1992.

[154] Bahttacharya P. et al. *Semiconductor Optoelectronic Devices.* Prentice-Hall., 1994.

[155] Monroy E. et al. AlGaN metal-semiconductor-metal photodiodes. *Applied Physics Letters*, 74:3401, 1999.

[156] Monroy E. et al. Effect of bias on the responsivity of GaN metal-semiconductor-metal photodiodes. *Physica Status Solidi a: Applied Research*, 176:157–161, 1999.

[157] Soares et al. Photoconductive gain in a Schottky barrier photodiode. *Japanese Journal of Applied Physics*, 31:210, 1992.

[158] Klingenstein M. et al. Photocurrent gain mechanisms in metal-semiconductor-metal photodetectors. *Solid-State Electronics*, 37:333, 1994.

[159] Monroy E. et al. Assessment of GaN metal-semiconductor-metal photodiodes for high-energy ultraviolet photodetection. *Applied Physics Letters*, 80:3198–3200, 2002.

[160] J. C. Carrano et al. Comprehensive characterization of msm ultraviolet photodetectors fabricated on single crystal GaN. *Journal of Applied Physics*, 83:6148, 1998.

[161] C. L. YU et al. GaN Metal-Semiconductor-Metal UV photodetectors with Ir/Pt contact electrodes. *Journal of the Electrochemical Society*, 154:71, 2007.

[162] O. Katz et al. GaN mechanism in GaN schottky ultraviolet detectors. *Appl. Phys. Lett.*, 79(10):1417, 2001.

[163] J.S. Liu et al. High responsivity ultraviolet photodetector realized via a carrier trapping process. *Appl. Phys. Lett.*, 97:251102, 2010.

[164] M. Martens et al. High gain ultraviolet photodetectors based on AlGaN/GaN heterostructures for optical switching. *Applied Physics Letters*, 98:211114, 2011.

[165] K. H. Lee et al. InGaN metal-semiconductor-metal photodetectors with triethylgallium precursor and unactivated mg-doped GaN cap layers. *Applied Physics Letters*, 110:083113, 2011.

[166] D Y Jiang et al. A high-speed photoconductive UV detector based on an MgZnO thin film. *Semicond. Sci. Technol.*, 22:687, 2007.

[167] Mose Bevilacqua et al. Extreme sensitivity displayed by single crystal diamond deep ultraviolet photoconductive devices. *Applied Physics Letters*, 95:243501, 2009.

[168] Feng Zhang et al. High-performance 4H-SiC based Metal-Semiconductor-Metal ultraviolet photodetectors with al2o3/sio2 films. *Applied Physics Letters*, 92:243501, 2008.

[169] Z. Zhang et al. Wavelength selective Metal-Semiconductor-Metal photodetectors based on (Mg,Zn)O-heterostructures. *Appl. Phys. Lett.*, 99:083502, 2011.

[170] A. Sciuto et al. Photocurrent gain in 4h-SiC interdigit schottky UV detectors with a thermally grown oxide layer. *Appl. Phys. Lett.*, 90:223507, 2007.

[171] Y.N. Hou et al. Mg0.55zn0.45o solar-blind ultraviolet detector with high photoresponse performance and large internal gain. *Appl. Phys. Lett.*, 98:103506, 2011.

[172] S.K. Zhang et al. Backilluminated GaN/AlGaN heterojunction ultraviolet photodetector with high internal gain. *Appl. Phys. Lett.*, 81:4862, 2002.

[173] J. Li et al. High performance schottky UV photodetectors based on epitaxial AlGaN thin film. *Physica B: Condensed Matter*, 405:996, 2010.

[174] M. Martens et al. High gain ultraviolet photodetectors based on AlGaN/GaN heterostructures for optical switching. *Appl. Phys. Lett.*, 98:211114, 2011.

[175] L. Sang et al. High-temperature ultraviolet detection based on InGaN schottky photodiodes. *Appl. Phys. Lett.*, 99:031115, 2011.

[176] Manijeh R. et al. *Technology of Quantum Devices*. Springer New York Dordrecht Heidelberg London, 2010.

[177] E. H. Rhoderick et al. *Metal-Semiconductor Contacts.* Oxford, Clarendon, 2nd edition, 1988.

[178] H. K. Henisch et al. *Semiconductor contacts: An approach to ideas and models*. Oxford Science Publications, Clarendon Press, Oxford, 1984.

[179] S. S. Cohen et al. Metal- semiconductor contacts and devices. *VLSI Electronics Microstructure Science, Academic Press, London*, 13, 1986.

[180] A. Rogalski et al. Temperature dependence of the r0a product for lead chalcogenide photovoltaic detectors. *Infrared Physics*, 21:191–199, 1981.

[181] J. C. Bose et al. *US. Patent 775,840*, 1904.

[182] A. H. Wilson et al. The theory of electronic semiconductors. *Proc. R. SOC. Lond. Ser: A*, 133:458, 1931.

[183] W. Schottky et al. *Halbleitertheorie der Sperrschicht,Naturwissenschaften*, 26:843, 1938.

[184] H. A. Bethe et al. Theory of the boundary layer of crystal rectifiers. *MIT Radiation Laboratory Report No.43-12*, 1942.

[185] Kramer M. Fabrication and characterization of metal-semiconductor contacts for application in al$_x$ga$_{1-x}$n/GaN hfets. *Master Thesis*, Dec.1999-Oct.2000.

[186] E. H. Rhoderick et al. *Metal Semiconductor contact*. Clarendon press, Oxford, 1988.

[187] DIETER K. et al. *Semiconductor material and device characterization*, volume 3. A John Wiley and Sons, INC., Publication, 2006.

[188] H.J.Werner et al. Barrier inhomogeneities at schottky contacts. *J. Appl. Phys.*, 69:1522–1533, 1991.

[189] W. Shockley et al. Rep al-tdr-64-207. *Air Force Avionics Laboratory, Wright Patterson AFB, OH.*, 1964.

[190] Murrmann H. et al. *Solid-state electronics*, 12:879, 1969.

[191] Reeves G.K. et al. Obtaining the specific contact resistance from transmission line model measurements. *IEEE Electron Device Letters*, 3:111–113, 1982.

[192] R. Williams et al. *Modem GaAs processing methods*. Artech House, London, 1990.

[193] G. S. Marlow et al. The effects of contact size and non-zero metal resistance on the detennination of specific contact resistance. *Solid State Electronics*, 25:91–94, 1982.

[194] J. Rechid et al. Concentric ring contacts used for the determination of contact resistances. *Solid State Electronics*, 44:451–455, 2000.

[195] Y. Tsividid et al. *Operation and Modeling of the MOS Transistor.* McGraw Hill, New york, 2nd edition, 1999.

[196] Z. Q. Fang et al. Deep centers in a free standing GaN. *Applied Physics Letters*, 78:2178, 2001.

[197] M. E. Lin et al. Low resistance ohmic contacts on wide band gap GaN. *Applied Physics Letters*, 64:1003, 1994.

[198] A. Motayed et al. Electrical, thermal, and microstructural characteristics of ti/al/ti/au multilayer ohmic contacts to n-type GaN. *J. Appl. Phys.*, 93:1087, 2003.

[199] F. M. Mohammed et al. The role of barrier layer on ohmic performance of ti/al-based contact metalliztions on AlGaN/GaN heterostructures. *J. Appl. Phys.*, 100(023708), 2006.

[200] M.R.H. Khan et al. A study on barrier height in au-$Al_xGa_{l-x}N$ schottky diodes in the range $0 \leq x \leq 0.2$. *Solid State Electronics*, 42:470–471, 1998.

[201] A.C. Schmitz et al. Schottky barrier properties of various metals on n-type GaN. *Semicond. Sci. Technol.*, 11:1464–1467, 1996.

[202] D. Qiao et al. Dependence of ni/$Al_xGa_{1-x}N$ schottky barrier height on al mole fraction. *Applied Physics*, 87:801–804, 2000.

[203] Nsm archive-physical properties of semiconductors. ioffe institute (http://www.ioffe.ru/sva/nsm/semicond/GaN/index.html).

[204] Foresi J. S. et al. Metal contacts to gallium nitride. *Applied Physics Letters*, 62:2859, 1993.

[205] Lin M.E. et al. Non-alloyed ohmic contacts on GaN using inn/GaN short-period superlattices. *Applied Physics Letters*, 64:2557–2559, 1994.

[206] Wu Y. et al. Low resistance ohmic contact to n-GaN with a separate layer method. *solid state electronics*, 41:165, 1997.

[207] Lin C. F. et al. W ohmic contact for highly doped n-type GaN films. *Solid State Electronics*, 44:757, 2000.

[208] Luther B. P. et al. Investigation of the mechanism for ohmic contact formation in al and ti/al contacts to n-type GaN. *Applied Physics Letters*, 70:57–59, 1997.

[209] Ruvimov S. et al. Microstructre of ti/al ohmic contacts for n AlGaN. *Applied Physics Letters*, 73:2852–2854, 1998.

[210] Kawak J.S. et al. Low resistance al/ti/n-GaN ohmic contacts with improved surface morphology and thermal stability. *Semiconductor science and Technology*, 15:756–760, 2000.

[211] Pelto C.M. et al. Issues concerning the preparation of ohmic contacts to n-GaN. *Solid-state electronics*, 45:1597, 2001.

[212] Q.Z. Liu et al. Study of contact formation in AlGaN/GaN heterostructures. *Applied Physics Letters*, 71:1658–1660, 1997.

[213] S.J. Cai et al. High performance AlGaN/GaN hemt with improved ohmic contacts. *Electronics Letters*, 34:2354–2356, 1998.

[214] K. K. Chu et al. High speed high power AlGaN/GaN heterostructure field effect transistors with ohmic contacts. *IEEE*, 6:399–406, 1997.

[215] Kim K.H. et al. Microstructural analysis of au/ni/al/ti/ta ohmic contact on AlGaN/GaN heterostructure. *Physica Status Solidi c*, 1:223–226, 2002.

[216] S. N. Mohammad et al. Progress and prospects of group-III nitride semiconductors. *Prog.Quant. Elect.*, 20:361–525, 1996.

[217] Y. Kribes et al. Investigation of au schottky contacts on GaN grown by molecular beam epitaxy. *Semicond. Sci. Technol.*, 12:913–915, 1997.

[218] S. J. Pearton et al. GaN: Processing, defects and devices. *J. Appl. Phys*, 86:1–78, 1999.

[219] L.S. Yu et al. The role of the tunneling component in the current-voltage characteristics of metal-GaN schottky diodes. *J. Appl. Phys*, 84:2099–2014, 1998.

[220] M. Jang et al. Analysis of schottky barrier height in small contacts using a thermionic-field emission model. *ETRI journal*, 24:455–461, 2002.

[221] S. Oyama et al. Mechanism of current leakage through metal/n-GaN interfaces. *Appl. Surf. Sci.*, 19:323–325, 2002.

[222] Yuanping Sun et al. Thermal annealing behavior of ni/au n-GaN Schottky contacts. *J.APL*, 35:2648–2651, 2002.

[223] B. Akkal et al. Electrical characterization of au/n-GaN schottky diodes. *Materials Chemistry and Physics*, 85:27–31, 2004.

[224] J. S. Jang et al. Schottky barrier characteristics of pt contacts to n-type inGaN. *Japanese Journal of Applied Physics*, 99:(73704)1–4, 2006.

[225] M. Mamor et al. Interface gap states and schottky barrier inhomogeneity at metal/n–type GaN schottky contacts. *J. Phys: Condens. Matter*, 21:335802(1–12), 2010.

[226] N. Yildirim et al. On temperature–dependent experimental I–V andC–V data of Ni/n–GaN schottky contacts. *J. Appl. Phys*, 108:114506–1–8, 2010.

[227] H. Kim et al.. Metallization contacts to nonpolar a-plane n-type GaN. *Appl. Phys. Lett.*, 93:(032105)1–3, 2008.

[228] W. Mtangi et al. Analysis of current–voltage measurements on Au/Ni/n–GaN Schottky contacts in a wide temperature range. *Mat. Sci. Eng. B*, 171:1–4, 2010.

[229] J. M. Shah et al. *Applied Physics Letters*, 94:2627, 2003.

[230] H. C. Casey et al. Dominance of tunneling current and band filling in InGaN/AlGaN double heterostructure blue light-emitting diodes. *Applied Physics Letters*, 68:2867–2869, 1996.

[231] P. Perlin et al. Low-temperature study of current and electroluminescence in inGaN/AlGaN/GaN double-heterostructure blue light-emitting diodes. *Applied Physics Letters*, 69:1680, 1996.

[232] X. A. Cao et al. Diffusion and tunneling currents in GaN/inGaN multiple quantum well light-emitting diodes. *IEEE Electron Device Letters*, 23:535–537, 2002.

[233] K. Mayes et al. High-power 280 nm AlGaN light-emitting diodes based on an asymmetric single-quantum well. *Applied Physics Letters*, 84:1046, 2004.

[234] T. Li et al. Low-noise back-illuminated $Al_xG_{1-x}N$-based pin solar-blind ultraviolet photodetectors. *Quantum Electron*, 37:538, 2001.

[235] V. A. Dmitriev et al. *J. Nitride Semicond. Res.*, 1:29, 1996.

[236] A. Chitnis et al. High-quality p-n junctions with quaternary AlInGaN/InGaN quantum wells. *Applied Physics Letters*, 77:3800, 2000.

[237] C. Sah et al. *Proc. IRE 45*, 45:1228, 1957.

[238] D. J. Dumin et al. *Applied Physics Letters*, 36:3418, 1965.

[239] R.T.Tung et al. Electron transport at metal-semiconductor interfaces: General theory. *Phys. Rev. B*, B45:13509–13523, 1992.

[240] J.D. Levine et al. Schottky barrier anomalies and interface states. *J. Appl. Phys.*, page 3991, 1971.

[241] C.R. Crowell et al. The physical significance of the t_0 anomalies in schottky barriers. *Sol. Stat. Electr.*, 20:171–, 1977.

[242] K. Maeda et al. Current-voltage characteristics and interface state density of gaas schottky barrier. *Applied Physics Letters*, 62:2560–, 1993.

[243] A. Ahaitouf et al. Stability of sulfur-treated n-inp schottky structures, studied by current–voltage measurements. *Mat. Sci. Eng. B*, B 52:208–, 1998.

[244] H. K. Cho et al. Electron traps and growth rate of buffer layers in unintentionally doped GaN. *Journal of crystal growth*, 223:38–42, 2001.

[245] W. Gotz et al. Deep level defects in n–type GaN. *Appl. Phys. Lett.*, 65:463–465, 1994.

[246] T. Tsarova et al. Deep–level defects in mbe-grown GaN–based laser structure. *Acto Physica Polonica A*, 112:331–337, 2007.

[247] R. F. Schmitsdorf et al. Explanation of the linear correlation between barrier height and ideality factors of real metal-semiconductor contacts by laterally nonuniform schottky barriers. *J. Vac. Sci. Technol. B*, 15:1221–1226, 1997.

[248] F. Roccaforte et al. Surface and interface issues in wide band gap semiconductor electronics. *Appl. Phys. Lett.*, 56:5727–5737, 2010.

[249] E. Monroy et al. Assessment of GaN metal-semiconductor-metal photodiodes for high-energy ultraviolet photodetection. *Appl. Phys. Lett.*, 80:3198, 2002.

[250] A. Blue et al. GaN UV detectors for synchrotron-base protein structure studies. *Nuc. In-str. and Meth A.*, 546:131–134, 2005.

[251] P. Gladkov et al. Effect of fe doping on optical properties of freestanding semi-insulating hvpe GaN:fe. *J. Cryst. Growth*, 312:1205, 2010.

[252] H. Srour et al. Solar blind metal-semiconductor-metal ultraviolet photodetectors using quasi-alloy of BGaN/GaN superlattices. *Applied Physics Letters*, 99:221101, 2011.

List of Figures

1 *Solar irradiation at the top of the atmosphere and at the sea level on the earth. The stratospheric ozone layer strongly absorbed the UV emission with the wavelengths from 200 nm to 290 nm [2].* 2

1.1 *Top figures depict the three-dimensional view. Bottom figures indicate the projections on the (0 0 0 1) and (1 1 1) planes for wurtzitic and cubic phases, respectively. Note the rotation in the zincblende case along the* $\langle 111 \rangle$ *direction. [44].* 10

1.2 *Labeling of planes in hexagonal symmetry [44].* 11

1.3 *Magnified view of labeling of planes in hexagonal symmetry in the (tuvw) coordinate system with w representing the unit vector in the c-direction. The lines are simply to show the symmetry only [44].* 12

1.4 *The orientations which are commonly used in nitrides, namely the* $(11\bar{2}0)$*and* $(1\bar{1}00)$ *planes and associated directions are shown as projections on the (0001) basal plane [44].* 12

1.5 *Schematic illustration of the lattice mismatch for GaN(0001) grown onto an* Al_2O_3*(0001) surface [50]* 13

1.6 *Selected defect levels in GaN.* V_{Ga} *and* V_N *denote Ga and N vacancies respectively. Ga is a Ga atom on an N atom site (that is a Ga antisite)* [7]. 18

1.7 *Experimental data of energy band gap of AlGaN* $0 \leq x \leq 1$ *, plotted as a function of Al composition (solid circle), and the least squares fit (solid line) giving a bowing parameter of b=1.0 eV. The dashed line shows the case of zero bowing [44].* 20

1.8 *Comparison of III-N semiconductors band gap energy at T=300K as a function of lattice constant with III-V semiconductors.* 22

1.9 *BGaN surface images taken with SEM. Each of the figures represents different BGaN thicknesses grown with various TEB/III ratios [104].* 23

1.10 *(a) Nomarsky optical contrast microscopy image of thick relaxed strain BGaN layer. The marker line represents 10 mm. (b) Nomarsky optical contrast microscopy image of 20/20nm of BGaN/GaN multi layer [93].* . . 24
1.11 *HRXRD rocking curves of three BGaN films grown on 4-m-thick GaN layer. The shift of the BGaN peak increases from top to the bottom spectrum with boron incorporation [93].* 25
1.12 *Mapping of BGaN surface morphology as a function of TEB/III ratio for two different growth pressures. The lines delimitate good (left side) and poor (right side) morphology regions [93].* 26
1.13 *SIMS profile of 350nm BGaN monolayer grown on GaN substrate [93].* . . 26
1.14 *SIMS profile of BGaN superlattice of 10 periods of 20/20nm BGaN/GaN [93].* 27
1.15 *Dependence of the electrical resistivity on boron composition in BGaN alloy at room temperature. Inset table shows the carrier density and mobility dependence on boron content with layers thickness varies from 0.3 μm to 0.6 μm [106].* 28
1.16 *Refractive index versus boron composition [112].* 29
1.17 *Absorbtion coefficient versus wavelength [112].* 30

2.1 *Photodiode equivalent circuit [120].* 34
2.2 *Response of a p-n junction detector to a narrow optical pulse. The effects arising from the relatively long time it takes for carriers generated away from the depletion region to diffuse to the junction [120].* 36
2.3 *Characteristic I-V curves of the photodiode.* 37
2.4 *Schematic structure of different types of photodetectors.* 40
2.5 *Schematic structure of AlGaN-based photoconductor* 40
2.6 *(a) Schematic structure of a reverse-biased p-i-n diode, with the incident light arriving on the p-type side; (b) the absorption of photons creates electron-hole pairs in the ptype, n-type and the i-region where they then become spatially separated through the electric field across the space charge region.* 42
2.7 *Spectral responses of $Al_xGa_{1-x}N$ p-i-n photodiodes. The dotted line represents the theoretical limit for an external quantum efficiency of 100% [126].* 44
2.8 *Schematic representation of the multiplication process in an avalanche photodiode.* 45
2.9 *Current-voltage and gain-voltage plots for a GaN avalanche photodector [132]* 46

2.10 *Equilibrium energy band diagram of Schottky contacts: (a) metal-(n-type) semiconductor ($\phi_m > \phi_s$); (b) metal-(p-type) semiconductor ($\phi_m < \phi_s$). A Schottky contact is obtained in each case because the majority carriers in the semiconductor experience a potential barrier which prevents their free movement across the metal-semiconductor junction. (c) Optical top view image of Schottky diode after realization.* 47

2.11 *Normalized room-temperature spectral response of $Al_xGa_{1-x}N$ Schottky barrier photodiodes for different values of the Al mole fraction. The inset shows the dependence of the photocurrent on the incident light power [137]* 48

2.12 *Schematic representation of a typical MSM detector structure, (a) Side view, (b) Top view, (c) Energy band diagram of MSM photodiode under bias.* 50

2.13 *Current-voltage characteristics of Schottky diodes fabricated on GaN epitaxial layers of different thicknesses. The upper curve is for the case of 1.5 mm thick GaN while the lower is for 4.0 mm thick GaN. The dashed lines represent calculations [153].* 51

2.14 *Spectral response of AlGaN MSM photodiodes, measured under different bias. Triangles were obtained with the 458 and 488 nm lines of an Ar^+ laser [155].* 52

2.15 *Responsivity dependence on bias for GaN MSM photodiodes, measured with an excitation wavelength of 325 nm, which is above the band gap. Performances of three sizes of devices with finger widths and spacings of 2x2, 4x4, and 7x7 μm^2 in an active area of 250x250 μm^2 are shown. The model calculations of the responsivity for the 4x4 μm^2 active area are also shown with the solid line [137, 156].* 53

2.16 *Calculated time response of GaN MSM photodiodes as a function of finger separation for devices with various active areas. A saturation velocity v_{sat} of 107 cm s^{-1} is assumed [159]. The experimental data points are from Ref. [160].* 54

2.17 *Trapping states at the active layer-metal interface, which under illumination, can trap photogenerated holes, leading to a Schottky barrier height decrease $\Delta\Phi_B$ and producing a secondary photocurrent.* 55

2.18 *Voltage dependence of the responsivity in Schottky and MSM PDs based on the model proposed by Katz et al. [162].* 56

3.1 *Energy band diagrams of a metal-semiconductor contact without an interfacial layer and surface states before (a) and after (b) intimate contact under thermal equilibrium.* 59
3.2 *Energy band diagrams of a metal-semiconductor contact with a thin interfacial layer δ and a large density of surface states before (a) and after (b) intimate contact under thermal equilibrium.* 59
3.3 *Four basic transport processes under forward bias.* 62
3.4 *Normalized current-voltage characteristic predicted by equation 3.15.* . . . 66
3.5 *Energy band diagrams in the case of field emission (FE) (a) and thermionic field emission (TFE) (b) under forward bias for a metal-n-type semiconductor contact.* 66
3.6 *Depletion-type contacts to n-type substrates with increasing doping concentrations. The electron flow is schematically indicated by the electrons and their arrows.* 67
3.7 *E_{00} and $k_B T$ as a function of doping density [187].* 69
3.8 *a) Laminar air flow system, directly filter downward air in a constant stream towards filters located on walls near the cleanroom floor. b) Turbulent air flow which uses both laminar air flow hoods and non-specific velocity filters to keep air in a clearoom in constant motion* 70
3.9 *Minalor cleanroom facilities and equipments used in our device processing and fabrication. To the right is the "salle rouge" for doing lithography and to the left is the sputtering and thermal evaporator for doing metal deposition.* 70
3.10 *Effect of the chemical treatment on the ohmicity, (a) I(V) characteristic of contacts before and after chemical treatment. (b) Effect of acetone and HCL on the surface before and after cleaning.* 72
3.11 *Photolithography process sequence. When using positive resist, the exposed regions are dissolved in the developing solution, while the unexposed areas remain intact. (a) The positive photoresist is exposed using a source of intense ultraviolet light. (b) The wafer is removed from the alignment station and areas exposed are dissolved in a solution.* 73
3.12 *(a) when the metal is deposited it will stick to the substrate. (b)The lift-off layer is removed the metal contact stuck to the substrate will remain.* . . . 74
3.13 *Cross-section of a typical vacuum evaporation system which includes a vacuum chamber, a sample holder, a metal filament, and a thickness monitor.* 75

3.14 *Cross-section schematic diagram of a typical sputtering, which is enclosed in a vacuum chamber and includes the substrate which are placed on a heater, and a set of electrodes, one of which is made from the target material to be sputtered. Argon gas is supplied and ionized so that ions can impact the target to release atoms of the material to be deposited.* 76
3.15 *General overview of the furnace (a), infrared halogen lamps heat up the substrate through a quartz window located on the topside of the process chamber (b). Temperature versus time profile, yellow line represent the power, green line represent the realtime temperature of the sample and the white line shows the rise, steady and fall time (c).* 77
3.16 *Schematic diagrams showing the sequence in the ultrasonic wire bonding process (a). One of our samples connected to sample holder and ready for characterization (b), Example of wire bonded device viewed under electron and optical microscopy taken from our current work (c)* 78
3.17 *Flow of the current density in a planar contact.* 82
3.18 *Schematic diagram of a semiconductor material with contact pads prepared for LTLM analysis (a), schematic structure of all the pattern with the rectangular pads dimension (b).* 84
3.19 *Equivalent circuit of the rectangular metal-semiconductor contact pad.* . . 85
3.20 *Probe station for IV measurements (b) connected to Keithely Source Measure Unit 2602 (c)* 89
3.21 *I-V characteristics of an ideal and typical Schottky barrier diode. Generation-Recombination current region (a), diffusion current (b), series resistance (c), reverse leakage current due to generation-recombination and surface effects (d) [12]* 89
3.22 *Schematic diagram of the carriers in an orientation perpendicular to the current and magnetic field (a), A typical simple contact configuration for Hall meausrements (b).* 91
3.23 *Linear relationship between the barrier height (ϕ_{Bn}) and the ideality factor (n).* 94
3.24 *Energy band diagram of an ideal Schottky diode without any interfacial layer and surface states on an n-type semiconductor under reverse bias (V_r).* . . 95
3.25 *Schematic representation of a plot of l/C^2 versus the applied reverse bias (V).* 96
3.26 *Schematic diagram for QE measurement.* 97

3.27 *Spectral response measurement set-up* 98
3.28 *Responsivity measurement set-up.* 98
3.29 *Experimental absorption coefficient of wurtzite GaN at 300 K [203].* . . . 99
3.30 *Optical response of the photodiode.* 101
3.31 *Long and short time dependence of the photocurrent.* 101

4.1 *An example of I-V measurements on various GaN and AlGaN samples.* . . 105
4.2 *Total resistance versus spacing as deduced from I-V measurements in the different devices.* 106
4.3 *Cross-sectional view (a), Optical microscope image (b)* 111
4.4 *I-V characteristics of Pt-Schottky contacts on different samples of GaN and AlGaN* 111
4.5 *Semilogarithmic plot of the current as a function of the bias voltage.* . . . 112
4.6 *Temperature dependence of the $J-V$ characteristics in a Pt/N-GaN Schottky diode. Temperature increases by step of $20K$ in the arrow direction. The dot-line indicates the separation between the two regimes: behind this line the TFE is preponderant, above this line the TE takes place.* 113
4.7 *Temperature dependence of the ideality factor in Pt/N-GaN Schottky structures* 114
4.8 *Effective barrier height versus temperature as deduced from $I-V$ measurements.* 115
4.9 *Temperature dependence of the TFE contribution to the Schottky barrier height variation and ideality factor for the studied structures* 116
4.10 *Variations of the ideality factor n versus bias voltage V of Pt/N-GaN structures* 117
4.11 *Interface states distribution below the conduction band edge in the studied structures* 118
4.12 Barrier height ϕ_{Bn} and (n^{-1}-1) versus $\frac{1}{2k_BT}$ in the Pt/n–GaN Schottky diodes. The inset shows the barrier height ϕ_b as a function of n for the structure under test. 119
4.13 *Example of the model by Katz et al [162] applied to the voltage dependence of the responsivity with different values of the SBH decrease in the GaN-A based Schottky PD at λ=266nm.* 120

4.14 *Voltage dependence of the responsivity in GaN and AlGaN Schottky PDs at λ=266nm. The small doted lines and dashed line corresponds respectively to the model proposed by Katz [162] and theoretical value of R for 100% of Q.E. at λ=266nm.* 121
4.15 *Dark current versus voltage of different types of GaN based MSM photodiode* 122
4.16 *Example of the model by Katz et al [162] applied to the voltage dependence of the responsivity at λ=266 nm with different values of the SBH decrease in the GaN-A based MSM PD.* 123
4.17 *Voltage dependence of the responsivity of the MSM photodetector with the model at λ=266 nm and P=56 μW. The small doted lines and dashed line corresponds to the model proposed by Katz [162] and theoretical value of R for 100% of Q.E. respectively.* 124
4.18 *Spectral response curves measured at a bias of 17 V in the MSM GaN PDs* 125

5.1 *Schematic structure of the BGaN supper lattice on GaN and AlN templates* 128
5.2 *Example of I-V measurements in BGaN samples for different boron concentrations* 130
5.3 *Plot of the total resistance R_T as function of the spacing d between two pads in BGaN with boron concentration of 0.5%.* 131
5.4 *Dependence of the sheet resistance R_{SH} with the boron concentration in BGaN.* 132
5.5 *The dark current-voltage (I-V) characteristics for $B_xGa_{1-x}N$ Schottky photodetectors.* 133
5.6 *Responsivity as function of the boron concentration at zero bias for Schottky photodetector illuminated at 266 nm with an optical power of 31.5 μW. The doted line corresponds to values obtained via the equation 5.1* 135
5.7 *Voltage dependence of the responsivity in BGaN based Schottky photodetectors measured at 266 nm and with an optical power of 31.5 μW.* 135
5.8 *I-V characteristics for the whole set of BGaN devices measured in dark condition.* 136
5.9 *Voltage dependence of the responsivity of the different MSM PDs at λ=266nm and P=56μW. The small doted lines and dashed line corresponds to the model proposed by Katz [162] and theoretical value of R for 100% of Q.E. respectively.* 137

5.10 *B concentration dependence of the dark current density (red dots), Schottky barrier (black dots) and μW range optical power (λ=266nm) gain (gray line) in BGaN monolayer-based and BGaN SL-based UV photodetectors.* . 138
5.11 *Optical power dependence of the responsivity of three type of PDs measured at λ=355 nm.* 140
5.12 *I-V characteristics of the BGaN-AlN SL-based PD measured under different UV radiations.* 141
5.13 *Normalized spectral responsivity for the different UV PDs under a bias of 10V.* 142
5.14 *Time dependence of the photocurrent in the three MSM PDs recorded at λ=266 nm, for V=10 V, and for an optical pulse duration of 0.1ns with a peak power of 11W.* 143
5.15 *Time dependence of the photocurrent for an optical pulse duration of several tens of seconds with a peak power of 56μW.* 144

List of Tables

1.1 Mismatch comparison for the III-N binary materials for [0001] directions at 300K [51]. 14
1.2 Material properties of binary compounds at 300K [51]. 16
1.3 Mass density, Vickers hardness H, refractive index and fracture toughness K_c of III-N comparing with other semiconductor materials [51]. 16
1.4 Dielectric constants ϵ_r^t, ϵ_r^s and e^- saturated velocity of III-N and other semiconductor materials [51]. 17
1.5 BGaN band gap values as deduced from photoluminescence measurements [112]. 29

2.1 Major progress of III-Nitride p-i-n photodiodes. 44
2.2 Comparing major progress of III-Nitride with ZnO, SiC, Diamond Schottky photodiodes 49
2.3 Comparing the major progress of III-Nitride with ZnO, SiC, and Diamond MSM photodiodes. 54

4.1 Different types of GaN and AlGaN samples used in our experiment. * GaN on sapphire, ** GaN on GaN-template 104
4.2 Values of R_c, L_T, R_{sh} and ρ_c obtained on GaN-A and TLM analysis. 106
4.3 Values of R_c, L_T, R_{sh} and ρ_c obtained on GaN-B and TLM analysis. 107
4.4 Values of R_c, L_T, R_{sh} and ρ_c obtained on GaN-D and TLM analysis. 107
4.5 Values of R_c, L_T, R_{sh} and ρ_c obtained on GaN-F and TLM analysis. 107
4.6 Values of R_c, L_T, R_{sh} and ρ_c obtained on AlGaN-B and TLM analysis. . . 108
4.7 Average values of N_D, R_{sh}, ρ_c, R_c, L_T and d of patterns I and II of gap spacing 10 μm. 108
4.8 Average values of N_D, R_{sh}, ρ_c, R_c, L_T and d of patterns III, IV and V of gap spacing 5 μm. 108

4.9 Link between electrical resistivity and R_{sh} and ρ_c values in GaN and AlGaN samples. 109
4.10 The different values of the Schottky barrier and ideality factor in GaN according to literature. Different growth techniques have been used: LP-MOCVD [201], MOVPE [221], MOCVD [223,225,226], MBE [217]. 110
4.11 Barrier height and ideality factor of Schottky diode. 112
4.12 Comparison between GaN and AlGaN Schottky photodetectors. 121
4.13 Comparison between GaN MSM photodetectors under a bias of 10V. . . . 124

5.1 BGaN monolayer and quasi-alloy with different boron (%) composition . . 129
5.2 Values of the sheet resistance R_{SH} and the specific contact resistance ρ_c in BGaN for different boron concentrations 131
5.3 Barrier height and Ideality factor for circular photodiode 133
5.4 Responsivity, dark current and SBH decrease at 266 nm with an optical power of 56 μW and at a bias voltage of -5 V in the different BGaN Schottky PDs of surface area 3.4x10^3 μm^2. 136
5.5 BGaN monolayer and superlattices responsivity dependence on boron concentration at 266 nm with an optical power of 31.5 μW and at a bias voltage of 10 V for MSM-based PDs. *For the BGaN/AlN-SL PD no gain is observed since the measurements are done at a wavelength above its cut off wavelength.* 138
5.6 Values of the responsivity and gain at high (W range), medium (μW range) and low (nW range) optical power for two types of PDs 140
5.7 Summarized value of cutoff wavelength and UVRR of MSM photodetector. 141
5.8 10% to 90% rise τ_r and fall τ_f times of the different PDs, measured at λ=266 nm and V=10 V, for low (56μW) and high (11W) optical power. . . 143
5.9 Summarized values of various GaN and BGaN devices. 145

Publications linked to this work

Papers

[1] A. Ahaitouf, **H. Srour**, S. Hamady, N. Fressengeas, A. Ougazzaden, J.P. Salvestrini, "Interface states effects in GaN Schottky diodes", Submitted to Thin Solid Films (2012).

[2] **H. Srour**, J.P. Salvestrini, A. Ahaitouf, S. Gautier, T. Moudakir, M. Aarkan, B. Assouar and A. Ougazzaden, "Solar blind metal-semiconductor-metal ultraviolet photodetectors using quasi-alloy of BGaN/GaN superlattices". Appl. Phys. Lett. 99, 221101 (2011).

[3] A. Ahaitouf, J.P. Salvestrini, **H. Srour**, "Accurate surface potential determination in Schottky diodes by use of correlated current and capacitance voltage measurements. Application to InP", J. Semicond. 32 104002 (2011).

[4] H. Mortada, M. Derivaz, D. Dentel, **H. Srour**, J.L. BIischoff, "Si epitaxial growth on LaAlO3 (001)" Surface Science Vol. 603, 9, 2009, L66-L69.

Proceedings of international conferences

[1] J.P. Salvestrini, **H. Srour**, A. Ahaitouf, S. Gautier, T. Moudakir, B. Assouar and A. Ougazzaden, "Tuning of internal gain, dark current and cut off wavelength in UV photodetectors using quasi-alloys of BGaN-GaN and BGaN-AlN superlattices", Quantum Sensing and Nanophotonic Devices IX, SPIE Photonics West, San Francisco, CA (USA), 2012, *Invited Paper* n°8268-99.

[2] F. Genty, S. Margueron, S. Ould Saad Hamady, J.C. Petit, **H. Srour**, J. Jacquet, "Low temperature transparent ITO-based contacts for Mid-Ir applications", MRS Spring Meeting proceedings: 6 pages, San Francisco, CA USA (2011).

Oral presentation of international conferences

[1] **H. Srour**, A. Ahaitouf, S. AMOR, A. Ougazzaden, and J.P. Salvestrini "Role of carrier traps and interface states in large internal gain uv photodetectors based on bgan monolayers and superlattices". The symposium 6C, Advances in Semiconducting Materials at the XXI International Materials Research Congress, to be held in Cancun-Mexico in August 12 - 17, 2012. *Invited Paper*.

[2] J.P. Salvestrini, **H. Srour**, S. Gautier, A. Ahaitouf, T. Moudakir, B. Assouar and A. Ougazzaden, "Tuning of internal gain, dark current and cut off wavelength in UV photodetectors using quasi-alloys of BGaN-GaN and BGaN-AlN superlattices", Quantum Sensing and Nanophotonic Devices IX, SPIE Photonics West, San Francisco, CA (USA), 2012, *Invited Paper*

[3] A. Ahaitouf, J.P. Salvestrini **H. Srour**, 11th International Conference on Condensed Matter and Statistical Physics 20-21 October 2011, Agadir-Morocco.

[4] **H. Srour**, S. Ould Saad Hamady, J.P. Salvestrini, G. OrsalL, N. Tarchichi, B. Assouar, P. Miska, S. Gautier, T. Moudakir and A. Ougazzaden, The 37th International Symposium on Compound Semiconductors, Takamatsu Symbol Tower, Kagawa, Japan May-31 to June-4, 2010.

[5] **H. Srour**, S. Ould Saad Hamady, B. Assouar, L. Bouvot, P. Miska, J.P. Salvestrini, T. Baghdadli, A. Ahaitouf, S. Gautier, T. Moudakir, A. Ougazzaden, The International conference on Innovations in Thin Film Processing and Characterizations, November 17-20, 2009 Nancy -France.

[6] **H. Srour**, S. Ould Saad Hamady, B. Assouar, P. Miska, J.P. Salvestrini, T. Baghdadli, A. Ahaitouf, S. Gautier, T. Moudakir, A. Ougazzaden, The 8th International Conference on Nitride Semiconductors ICNS-8, Oct. 18-23, 2009, Jeju, Korea.

Poster presentations of international conferences

[1] **H. Srour**, J.P. Salvestrini, B. Assouar, A. Ahaitouf, G. Orsal, S. Gautier, T. Moudakir, A. Ougazzaden, "Ohmic and Schottky contacts for BGaN based UV photo- and alpha, beta-detectors". E-MRS Spring 2011 and Bilateral Energy Conference 9-13 May 2011 Nice-France.

[2] **H. Srour**, J.P. Salvestrini, B. Assouar, A. Ahaitouf, G. Orsal, S. Gautier, T. Moudakir, A. Ougazzaden, "Investigation of specific contact resistance of optimized

ohmic contacts in BGaN/AlN/GaN heterostructures for solar blind UV photodetector". Mediterranean Conference on Innovative Materials and Applications, 15-17 March 2011 Beirut-Lebanon.

Résumé

Les développements récents des techniques de fabrication de matériaux semiconducteurs de type III-N comme GaN et AlGaN permettent le développement de photo-détecteurs Schottky et métal-semiconducteur-métal opérant dans le domaine de l'ultraviolet. Alors que les photo-détecteurs à base de GaN et AlGaN ont un faible bruit et un temps de réponse rapide, l'absence de gain interne est un obstacle majeur à leur utilisation dans des applications qui nécessitent des photodétecteurs à haute sensibilité. Dans ce travail, nous avons conçu et fabriqué des photo-détecteurs à base d'alliage BAlGaN sous forme de monocouches et de super réseaux réalisés par MOVPE et photo-lithographie. Une caractérisation complète de leurs propriétés électriques et électro-optiques a ensuite été réalisée. Nous montrons que ces nouveaux alliages BAlGaN ont un impact majeur sur les performances des photo-détecteurs étudiés. Nous avons pu réaliser des détecteurs présentant un important gain interne (jusqu'à $3x10^5$) donc avec une sensibilité améliorée, un courant d'obscurité faible (jusqu'à 9 ordres de grandeurs plus faible que dans les détecteurs à base de GaN réalisés), une longueur d'onde de coupure ajustable dans la gamme 260-380, et un temps de réponse deux fois plus rapide que dans les détecteurs à base de GaN réalisés. Finalement, nous proposons une interprétation du mécanisme de gain dans ces nouvelles structures reposant sur l'existence de pièges profonds à électrons et à trous .

Recent developments in III-N material growth technology such as GaN and AlGaN made possible to fabricate high performance solar-blind Schottky, and metal-semiconductor-metal based photodetectors operating in the ultraviolet range -based photodetectors. While GaN and AlGaN have low noise and fast response times, the lack of high internal gain is a limitation for their use in applications that require high sensitivity photodetectors. In this work, we have designed and fabricated BAlGaN-based photodetectors. For this, several BGaN monolayer and superlattices were grown using MOVPE and lithography processes followed by a full characterization of their electrical and electro-optical properties. We show that these new BAlGaN alloys have tremendous impact on the performance of these photodetectors. We were able to achieve photodetectors with large internal gain (up to $3x10^5$) and thus improved sensitivity, low dark current (up to nine orders of magnitude lower compared to our own GaN-based photodetectors), tunable cut-off wavelength in the 260-380 nm range, and more than two orders of magnitude reduction in the response time compared to our own GaN-based photodetectors. Finally, we propose an interpretation, based on the existence of deep level electron and hole traps, to explain the different mechanisms at the origin of the internal gain in these new structures.